Swansea University E-Theses

_____

Minimising variability in steel / weld fatigue data and developing robust durability design for automotive chassis applications.

Bright, Gary W

How to cite:
_____

Use policy:
_____

Minimising Variability in Steel/Weld Fatigue Data and Developing Robust Durability Design for Automotive Chassis Applications

ENGINEERING DOCTORATE THESIS

Thesis submitted in candidature to

Swansea University for the

Degree of Doctor of Engineering

G.W. Bright

September 2013

ProQuest Number: 10805426

ProQuest 10805426

ABSTRACT

Engineers often make use of component safety factors in order to ensure reliability and robustness of new products. To truly define a suitable safety factor for a given component, an understanding of the variability in the structural performance of the component is required, in addition to the variability in conditions of use. A large variation in either of these two factors can give rise to an overlap between the structural capability of a component and the limits of its service conditions. This may result in a situation where the component's structural capability fall below the in-service requirements, which could lead to catastrophic failure.

Accurately defining the variability in the mechanical behaviour of High Strength Low Alloy (HSLA) steels used for automotive chassis & suspension applications can help design engineers decide on appropriate safety factors to avoid over-engineering products. By investigating the root-causes of this variability, the steel industry can also benefit from this research, as its findings can assist in reducing the variability of its steel products that arise during production. Variability in steel mechanical behaviour can be due to numerous factors including chemistries, processing temperatures, cooling patterns, and the strip thickness etc.

By analysing the variability that exists in the mechanical properties, fatigue behaviour and thickness of strip steel, a prediction of the overall effect of variations within these parameters on manufactured components is possible. Understanding the relationship between material variability and the consistency of component structural capability is paramount for achieving robust and reliable designs. The current research attempts to uncover and present some of these relationships.

DECLARATION

This work has not previously been accepted in substance for any degree and is not being concurrently submitted in candidature for any degree.

Signed: .... ~~~~~~~~~~~~~~~~~~~~~~~~~ (candidate)
Date: ....20/09/13..........

Statement 1

This thesis is the result of my own investigations, except where otherwise stated. Where correction services have been used, the extent and nature of the correction is clearly marked in a footnote(s). Other sources are acknowledged by footnotes giving explicit references. A bibliography is appended.

Signed: .... ~~~~~~~~~~~~~~~~~~~~~~~~~ (candidate)
Date: ....20/09/13..........

Statement 2

I hereby give consent for my thesis, if accepted, to be available for photocopying and for inter-library loan, and for the title and summary to be made available to outside organisations.

Signed: .... ~~~~~~~~~~~~~~~~~~~~~~~~~ (candidate)
Date: ....20/09/13..........

I hereby give consent for my thesis, if accepted, to be available for photocopying and for inter-library loans after expiry of a bar on access approved by the Swansea University.

Signed: .... ~~~~~~~~~~~~~~~~~~~~~~~~~ (candidate)
Date: ....20/09/13..........

ACKNOWLEDGMENTS

LIST OF CONTENTS

Chapter 1 – Background

Chapter 2 – Literature review

Chapter 3 – Tensile and fatigue specimen geometry

Chapter 4 - Variability of HSLA steel mechanical properties

Chapter 5 – Fatigue properties of Tenform steel

Chapter 6 – Weld performance

Chapter 7 – Effect of material variability on a top hat structure

Chapter 8 – Conclusions and further work

List of references

Chapter 1 – Background

1.1 Background

An important aspect of the design for automotive chassis structures is to ensure that their durability targets are met. Currently, durability (fatigue lives) of metal and welds in new chassis products are assessed by a combination of computer-aided fatigue analysis and physical testing in laboratories and on vehicle proving grounds.

One major challenge concerning durability design is variability. Variability in fatigue life of a vehicle structure arises from many factors. Variability in material and manufacturing conditions is one of those factors. Material variability may result from variations in the sheet steel properties and thickness (gauge), in particular statistical scatters of metal and weld fatigue data. Fatigue data scatter may result from fluctuations in the control signals of fatigue test machines, and uncertainties in specimen gripping conditions such as loading misalignment etc.

With increased emphasis on product reliability and design robustness, vehicle manufacturers and suppliers are turning their attention to understanding and controlling product performance variability, concerning that of durability in particular, and developing a systematic design analysis approach to achieve this.

Reliability refers to the ability to develop a product having a low probability of failure in service. Reliability can normally be achieved by over-design, which may result in a heavy and costly vehicle product. Design robustness, on the other hand, requires a product to have a narrow range of performance variation. In other words, the product performance is consistent and insensitive to such factors as the material variability. A robust design, if achieved, permits an efficient and cost-effective product to be developed. An automotive chassis system needs to be both reliable and robust.

The need for efficient designs is greater than ever before, with increasingly tougher legislation on vehicle emissions, manufacturers are under pressure to produce vehicles that are more fuel efficient yet still meet customer demands for comfort, safety, performance and many other qualities. The pressure for efficiency does not

only come from government legislation, consumers also desire vehicles that are both inexpensive on fuel and are in low tax brackets, which are governed by CO_2 emissions. Thus reducing vehicle mass is a key concern for all automotive manufacturers in today's market climate.

Previous studies carried out to date by Tata Steel suggests a strong link between the overall durability variability of a chassis structure and the level of scatter in the fatigue data of steel products and their welds. Therefore, it is essential to improve understanding on the sources of the fatigue data scatter, through an EngD research programme, with a view to minimising or eliminating their influences.

1.2 Project aims and objectives

The EngD programme aims at establishing a full understanding of the fatigue life variability of automotive chassis structures, especially contributions from variability in steel/weld static and fatigue properties, from variations in sheet steel thickness within the specified tolerance bands, and other factors that may be of relevance. Particular emphasis will be placed on identifying and understanding the sources of metal/weld fatigue data variations during the data generation (testing) process. Recommendations on minimising fatigue data variability will be developed.

In the second stage of the EngD programme, the research will turn to developing a robust design methodology, as well as a computer-aided engineering (CAE) capability, for minimising and controlling fatigue life variability in automotive chassis systems. The focus will be on how to design chassis structures of the most consistent durability, for a given level of material fatigue data scatter. In turn, using this capability, acceptance criteria will be developed for steel producers, such as Tata, to help define the appropriate level of scatters in their fatigue data to be supplied to automotive customers.

Benefits and relevance to the steel and automotive industries include: a better understanding of the fatigue data variability, the ability to minimise its negative impact, and an effective robust-design methodology will equip steel producers and their automotive customers with the ability to reliably design automotive chassis

systems, especially to promote the confident and efficient use of Tata Steel materials. In turn, the understanding and knowledge from the EngD programme will help guide steel producers in better definition for the development of current and new steel products suitable for future chassis applications.

The EngD programme plan will be devised from the following range of activities, in conjunction with the academic supervisor and Tata Steel industrial supervisors:

- Investigate, identify and isolate sources of metal/weld fatigue data scatter, through a comprehensive metal and weld fatigue testing and statistical analysis programme.
- Propose recommendations on minimising metal/weld fatigue data variations during fatigue testing.
- Review and master engineering statistics theories relating to reliable and robust design. Summarise and critique design variability studies already carried out within and outside Tata Steel.
- Conduct case studies on durability variability of selected automotive chassis components or assemblies, taking account of the metal/weld fatigue property and sheet thickness (gauge) variations. Draw conclusions on the main contributors to the overall chassis durability variability.
- Review and evaluate existing techniques and CAE-based software tools for design robustness. Apply the techniques/tools to laboratory-scale components and/or real automotive chassis structures, then assess their effectiveness.
- Develop an effective robust-design CAE capability, together with procedure and guidelines, for the applications of hot-rolled sheet steel products to automotive chassis systems.
- Produce recommendations on steel property and thickness (gauge) tolerance windows for future steel products suitable for automotive chassis applications.

Chapter 2 - Literature Review

2.0 Introduction

Material variability has long been an issue across all engineering industries. Manufacturers often introduce large safety factors to account for unknown variations in the mechanical properties of materials in order to ensure reliable products. The focus of this thesis is to accurately define the variability of steel grades used extensively in the automotive industry and to analyse its effect on the structural performance of chassis & suspension components. Such components are lower control arms, sub frames and other suspension components. The decision to focus on chassis and suspension rather than other areas such as body in white is due to Tata Steels' customer requests and the fact that chassis components suffer greater loading regimes and are therefore more susceptible to fatigue failure.

The information gathered and presented as part of this project can be used to aid in the design of robust new products through a partnership with Jaguar Land Rover (JLR). Variability in tensile strength, fatigue performance and elongation to failure are of particular interest. TSSP-UK performs a tensile test for every coil produced, therefore obtaining variability data for these mechanical properties is a relatively straight-forward procedure. Other data, such as fatigue data, is however a more costly and time-consuming affair.

As well as considering variability in delivered strip products, it must also be considered that, post-delivery, materials can deteriorate through excessive heat caused by welding or other procedures. Welds in particular require analysis, as they will inevitably have different properties to the parent material(s) [1]. Weld quality may adversely affect fatigue performance through poor fit up, control, shielding or other factors. Careful consideration of weld start/stop locations as well as pre-weld preparation can improve component life, as the start/stop section of a weld will have different mechanical properties to the continuous mid-weld section. There may also be benefits in selecting alternate geometries of mating the two edges, such as overlap, butt weld, "v" prepared joint, etc. Understanding the optimum method for any given circumstance could greatly enhance the performance of new products and must therefore be considered in this project.

In addition to manufacturing processes affecting the performance of the material, the physical shape of the component can also influence fatigue strength. Small radii can induce stress concentrations and are locations where cracks initiate and propagate, thus leading to failure. There are other geometrical factors to be considered, such as analysing the stress distribution within each component and influencing how stress is passed on from one component to the next. Finite Element Analysis/Method (FEA/FEM) now plays a major role within automotive manufacturing in order to consider such factors.

When assessing variability in fatigue results, numerous factors must be considered. As fatigue testing is a lengthy process, experiments are not carried out as frequently as tensile tests, and as such the range of variability in fatigue data from one coil to another within one particular steel grade is difficult to quantify. Fatigue life intrinsically demonstrates a great deal of variability and can be influenced by numerous parameters. The quality of cut edges can have a significant effect on the fatigue life of specimens [2], small defects on the surface act as stress raisers, from which cracks can initiate and propagate. Care must be taken when comparing test results from different sources, even if the results are from the same grade of material and specimens are prepared in an identical fashion, coil to coil variability will have a bearing on the final fatigue properties.

Gathering reliable data on fatigue performance is arguably the most important aspect of this research, since it has been stated that at least 90% of mechanical failures are due to fatigue [3]. It is therefore of the utmost importance to establish the extent of scatter in fatigue performance within the grades of steel assessed, whilst taking into consideration the manufacturing processes the material is likely to experience.

Once the statistical distribution of all factors that affect the performance of automotive structures are assessed and understood, the final part of the project can begin. This section aims to investigate the effect of numerous mechanical performance & geometrical tolerance variability data on the performance of chassis & suspension components manufactured by TSSPUK's automotive customers. Once the statistical variation in performance transmitted from the material to the final

5

component is understood, analysis of this information will help design engineers construct future designs to be more robust and reliable.

2.1 Automotive chassis and suspension overview

2.1.1 Chassis and suspension design

Automotive chassis & suspension covers a broad spectrum of components, with various types of designs and assemblies in existence. The use of sub-frames is now much more common in modern chassis systems compared to the vehicles of yesteryear. Sub-frame and suspension assemblies (most often with the engines) are typically assembled off line and bolted onto the vehicle quickly and easily during assembly of the vehicle. By far the most common type of assembly for the front of a front wheel drive passenger vehicle is a MacPherson strut suspension with a peripheral subframe, as shown in figure 2.1 below:

Fig. 14.8
Audi '50' rear suspension (1974)
(courtesy Audi AG)

Figure 2.1. MacPherson Strut Suspension Assembly   Figure 2.2. H-Frame Rear Suspension

Steel is by far the most predominant material used for this type of design where the two main applications of strip steel are for the control arms and sub-frame, with strip thicknesses of 2-3mm commonly being used. As for the rear setup on a front wheel drive passenger car, most european vehicles use a torsion axle/H-Frame design, as shown in figure 2.2. Steel once again is the most popular material for this type of design, this is due to its high resistance to failure modes such as creep and fatigue, unlike alternative materials such as aluminium. For rear and four wheel drive vehicles double wishbone and multi-link suspension are popular designs. Within these systems steel is still the most commonly used material, however, aluminium is increasing its market share, especially so for multi-link suspension types. Examples of these assemblies can be seen in figures 2.3 & 2.4. Between these four designs,

6

they cover most assemblies used in modern vehicles, though it is worth noting that other systems such as live axles, trailing arm, blade types and others are used in some vehicles, with live axles still popular in rear wheel drive commercial vehicles.

Figure 2.3. Example of a double wishbone suspension   Figure 2.4. Example of a multi link type suspension unit
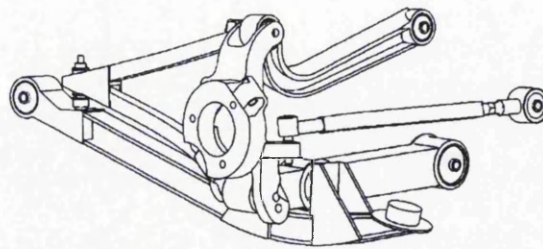
2.1.2 Basic structural considerations

Apart from engine components, chassis & suspension components are the most susceptible components to fatigue failure within a vehicle. This is due to the high levels of cyclic loading they encounter during regular use. As such they need to be designed to withstand numerous loading conditions from multiple sources. These forces can be lateral cornering forces, longitudinal acceleration and braking forces, vertical suspension forces, as well as combinations of all three. The advantage of steel over competitor materials is that the fatigue strength usually levels off between 10^6 and 10^8 cycles [3], as shown in figure 2.5, thus providing engineers with confident data limits to work within.
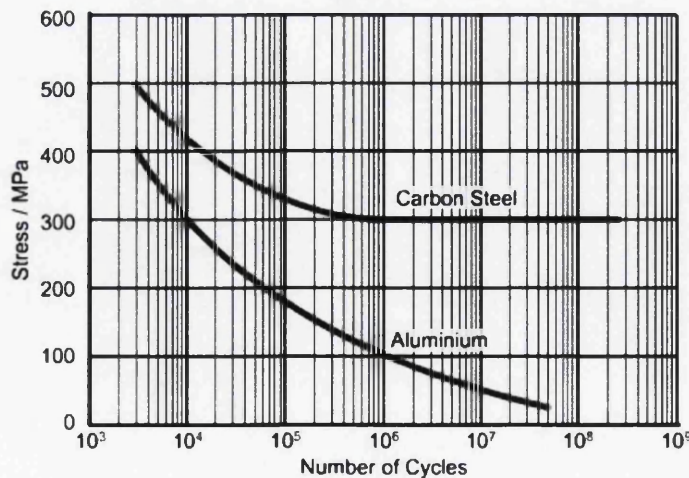
Figure 2.5. Typical fatigue curves for steel & aluminium

7

As well as being able to withstand fatigue failure from regular use, chassis & suspension components are also required to withstand occasional large abusive loads, with manufacturers testing under conditions such as pothole braking, etc., in order to simulate such scenarios. These are not conditions you would expect to encounter on a regular basis. Thus absolute strength is an important consideration, as well as other factors such as stiffness. These factors not only affect durability, but also ride and handling characteristics.

Buckling is a failure mode associated with stiffness and is a prominent concern when assessing the structural performance of chassis & suspension systems, especially so with some multi-link systems which have slender connecting rods. The Swiss physicist/mathematician Leonhard Euler derived a formula to calculate the slenderness ratio of a rod/strut, this is sometimes denoted by the Greek letter lambda (λ) and is the ratio of the strut length (L) to the least radius of gyration (R) i.e. $\lambda=L/R$. His work also enabled engineers to determine the force required to cause buckling of struts depending on the loading conditions. For the loading conditions shown in Figure 2.6, which describe most multi-link type loading conditions, the minimum required load can be calculated as follows:

$$F = \frac{\pi^2 EI}{L^2}$$

Where:

    F = minimum load required to cause buckling (N)

    E = modulus of elasticity (MPa)

    I = polar moment of inertia (m^4)

    L = strut length (m)

PINNED   FIXED   FREE   PINNED
PINNED   FIXED   FIXED   FIXED
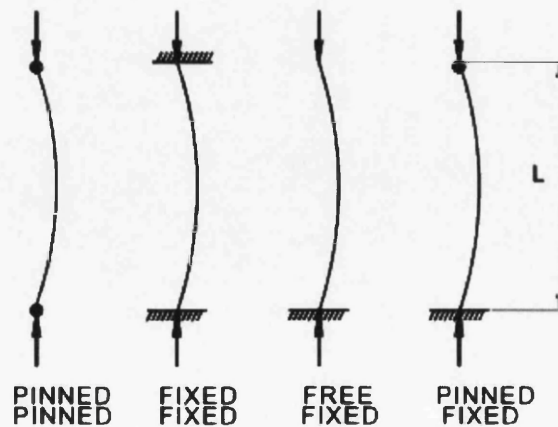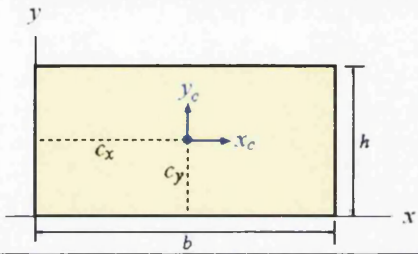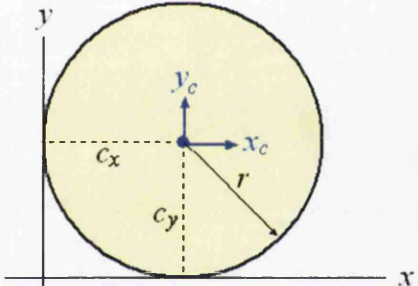
Figure 2.6. Loading conditions relating to Euler's buckling theorem

Properties of areas are important factors that need to be assessed when considering the stiffness and buckling resistance of components. The two properties that are of interest are the second moment of area (I) and the polar moment of inertia (J) [4], where the former is associated with loading perpendicular to a cross sectional plane and the latter is associated with torsion loading. The stiffness and buckling resistance of materials are directly proportional to the relevant area property. These properties are shown below for two common cross-sectional profiles:

Table 2.1. Second moment of area and polar moment of area of cross sections

Cross-section	Second moment of area $I = \int y^2 .dA$	Polar moment of Inertia $J_{xc} = I_{xc} + I_{yc}$
	$I_{xc} = bh^3/12$ $I_{yc} = hb^3/12$	$J_{xc} = (bh^3 + hb^3)/12$
	$I_{xc} = \pi D^4/64$ $I_{yc} = \pi D^4/64$ (where D = 2r)	$J_{zc} = \pi D^4/32$ (where D = 2r)

The information in table 2.1 is designed to illustrate the effect of altering certain design parameters, such as doubling the diameter of a circular bar. It can be shown that doubling this dimension only increases the cross-sectional area by 4x, though increases the buckling resistance by 16x. Further benefits can be made by the use of hollow rods, where the area properties can be calculated in a similar fashion, except by subtracting the properties of the vacated area. Sheet-metal based chassis & suspension components rely on a combination of stiffness acquired from the strip thickness and the cross-sectional design.

Properties for more elaborate shapes can be calculated by use of the parallel axis theorem, which is documented in the literature. It can be seen from this information how materials that are not as stiff as steel, though have a lower density can be used

to produce both stiff and lightweight structures by careful consideration of these geometrical area properties. Aluminium is one such material where the trade-off between density and the modulus of elasticity causes continuous debate when proposing new designs.

2.2 Steels for chassis and suspension applications and their properties

2.2.1 Steels and families of steels

Numerous families of steels have been used for vehicle chassis & suspension systems over the years, with automotive manufacturers continually seeking higher strength steels in order to down gauge, thus reducing mass and CO_2 emissions. Unfortunately there is a general trend that steels with high yield points and UTS tend to be more brittle and prove to be less formable. This is illustrated in figure 2.7, which shows how elongation values tend to reduce as yield strength increases.

High Strength Low Alloy (HSLA) steels are currently the most popular family for use in chassis & suspension applications, though there has been a recent push towards Advanced High Strength Steels (AHSS), in particular Dual Phase (DP) steels.
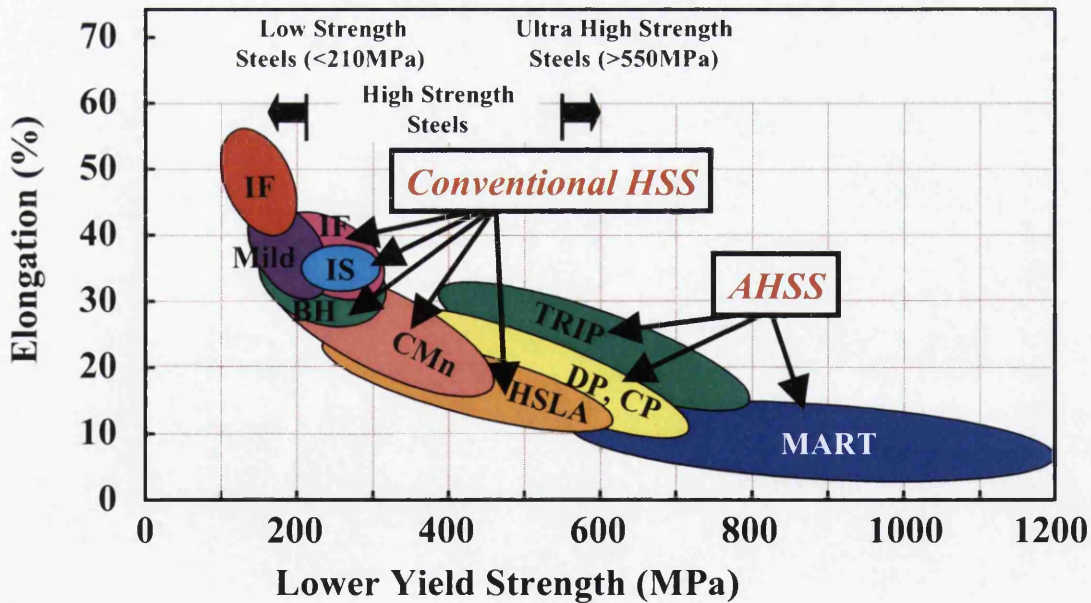
Figure 2.7. Families of steels

In order to ensure that the work carried out is relevant both now and in the future, it is essential to identify the main grades of steel within these families that are currently

used for structural vehicle components, and also any emerging steel grades that could be used as eventual successors. By far the most common grade manufactured by Tata Steel Strip Products, UK (TSSPUK) for automotive chassis applications is the Tenform XF family. This family is a High Strength Low Alloy (HSLA) steel with reduced sulphur content. The grade combines excellent mechanical properties with good formability. Many grades exist within the Tenform family, though the grade that is manufactured and sold in the largest quantity is XF350, with XF450 claiming a smaller market share. The chemical composition of these grades of steel, along with their euronorm equivalents are displayed in table 2.2 below.

Table 2.2. Chemical composition of XF & equivalent euronorm grades

Chemical Composition

Grade	C	Mn	Si	P	S	Al	Nb	V	Ti	Micro Alloys
XF350	≤0.10	≤1.20	≤0.04	≤0.025	≤0.010	≥0.020	-	-	-	≤0.30
XF450	≤0.10	≤1.50	≤0.35	≤0.025	≤0.010	≥0.020	-	-	-	≤0.30
S355MC	≤0.12	≤1.50	≤0.50	≤0.025	≤0.020	≥0.015	≤0.09	≤0.20	≤0.15	-
S460MC	≤0.12	≤1.60	≤0.50	≤0.025	≤0.015	≥0.015	≤0.09	≤0.20	≤0.15	-

Note: Values are in weight percentages.

Note that XF350 and XF450 have a minimum Yield Strength of 350 and 450 MPa respectively. Although these materials are marketed as having a yield strength of 350 or 450 MPa these values are the minimum accepted values for each respective grade. Initial data suggests that many coils of steel are supplied with a far higher strength than the minimum specified.

An emerging grade of steel, which is still under trial within TSSPUK is DP600, a Dual Phase steel with a minimum Ultimate Tensile Strength (UTS) of 600MPa. Since it is a trial material exact specifications cannot be given, though the microstructure, by definition is a combination of ferrite and martensite, although some retained austenite also exists. As reducing vehicle mass is becoming increasingly important it is obvious why this Advanced High Strength Steel (AHSS) grade deserves consideration for automotive chassis applications.

This grade of material is however widely commercialised in its cold rolled variant and is increasingly popular for body in white applications. One example of a vehicle

that uses cold rolled DP material is the latest Ford Fiesta – a car that has been praised for its innovative use of materials to achieve a light yet class-leading structure in terms of safety. Bernd Liesenfelder, Body Engineering Manager for Ford of Europe commented on the benefits of this material for strength and work hardenability: "Mapping the strength of the structure improves our understanding of the benefits of these dual-phase steels and increases our ability to predict structural behaviour accurately. It's this kind of attention to detail that has gone into defining the new Fiesta and its safety performance."

The two most predominant phases (martensite and ferrite) of dual phase material can be seen in the micrograph in figure 2.8. This micrograph is from a Tata Steel hot rolled material and shows some retained austenite as well as the clear martensitic and ferritic regions.
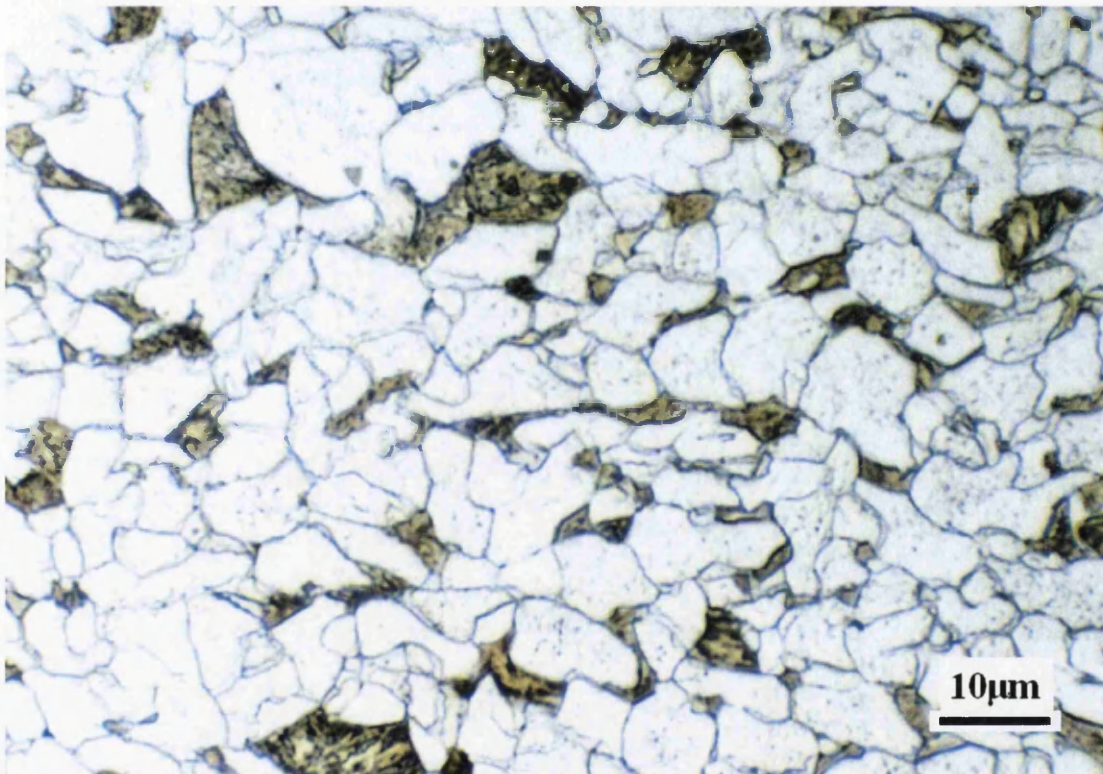
Figure 2.8. Microstructure of Hot-Rolled DP 600

2.2.2 Mechanical properties and testing

Numerous tests can be carried out on strip steel to establish its mechanical properties. These properties can be linked to tensile performance, formability, hardness, fatigue performance etc., though typically only three properties are

specified to characterise the delivery condition of each coil. These three are the UTS, yield stress and elongation to failure, where each property has a specified minimum value in the relevant euronorm standard, i.e. S355MC has clearly defined delivery conditions [5]. These three properties are of great interest for this project.

Some mechanical properties may not be so applicable for chassis & suspension applications, for example there are numerous tests which could be carried out to measure properties such as hardness and formability. These properties can generally be estimated reasonably well from studying the tensile data, and as such are not really necessary for this type of project. High cycle fatigue is also of particular interest, more so than low cycle fatigue, as manufacturers obviously intend to build structures that survive beyond the typical 1,000-100,000 cycles that low cycle tests are run to. Thus the main properties of interest are the tensile properties and high cycle fatigue.

The tensile properties of materials dispatched will continue to change after they are supplied to the customer as they are formed and fabricated. They may become harder and stronger through work hardening [6, 7]. As shown in figure 2.9. Knowing the extent of cold working after the material has been supplied will help engineers understand the true mechanical properties of the material and component.
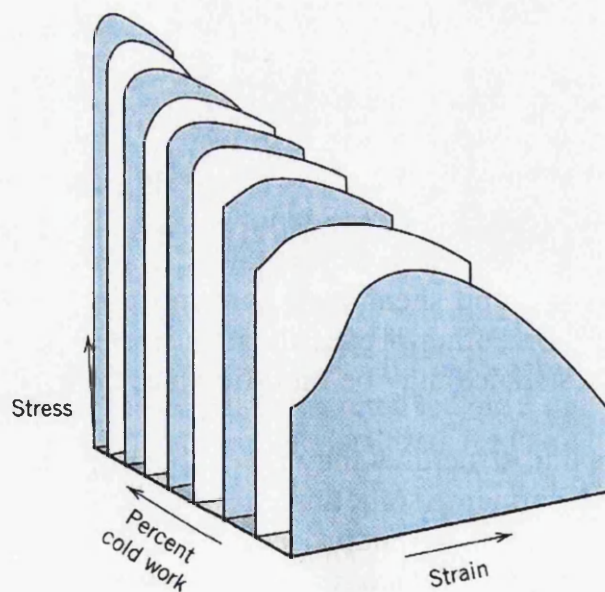
Figure 2.9. Effect of cold working steels

Certain properties can be calculated that help define the work or strain hardening properties of a given steel grade, these are n and K values. Unfortunately the way these are calculated throughout industry is not consistent, though all are based upon similar theory. The most prominent theory is based on the work of Ramberg & Osgood hence the Ramberg-Osgood theory to define the total true strain of a material:

$$\varepsilon = \varepsilon_e + \varepsilon_p = \frac{\sigma}{E} + \left(\frac{\sigma}{K}\right)^{1/n}$$

Where:

σ = True Stress

E = Young's Modulus

ε = Total Strain (true)

ε_e = Elastic Strain

ε_p = Plastic Strain (true)

K = Work/Strain hardening coefficient

n = Work/Strain hardening exponent

This expression comes from the relationship between stress and elastic strain as defined by Thomas Young, as well as the plastic strain element as shown below:

$$\sigma = K\varepsilon_p^{\ n}$$

By curve fitting tensile data to the equation above it is possible to define both K and n. Other methods, while not as accurate, use the total strain i.e.

$$\sigma = K\left(\varepsilon_e + \varepsilon_p\right)^n$$

Fortunately both methods give very similar values for K and n since the plastic strain is usually much greater than the elastic strain.

Essentially, the n-value is derived from the gradient of the log-log true stress-strain curve at strain levels typically between 10-20%. Many steels will display a straight line on a log-log graph for these strain levels. Once plotted, the gradient can be calculated using the least squares method as described later on. Some steels, such as

dual-phase steels do not return a straight line on a log-log plot, and as such an instantaneous n-value graph better illustrates the strain hardening properties of the material [8].
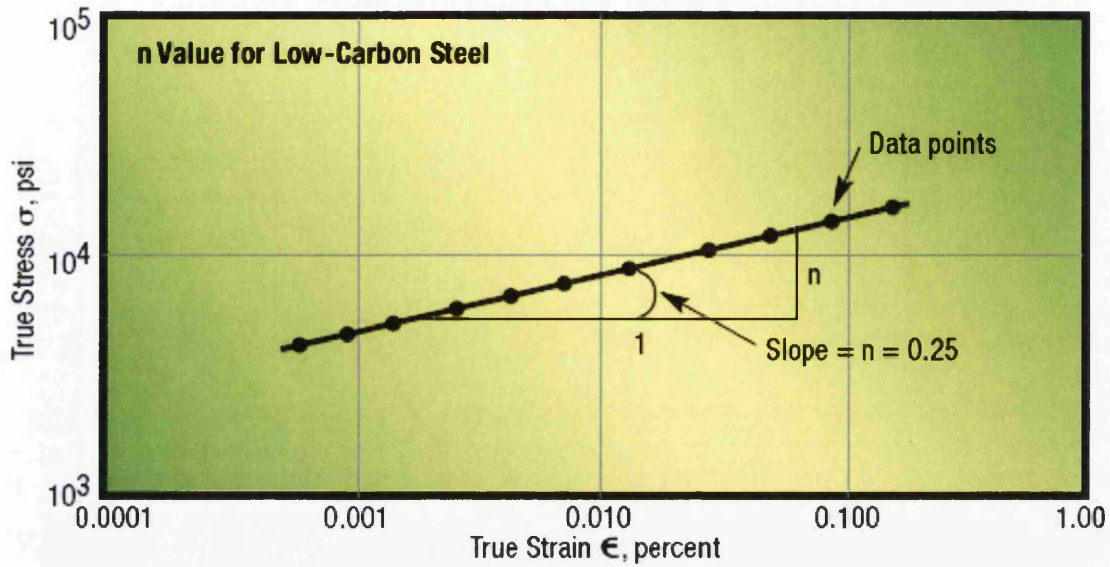
Figure 2.10. Calculating the n-value of metallic materials
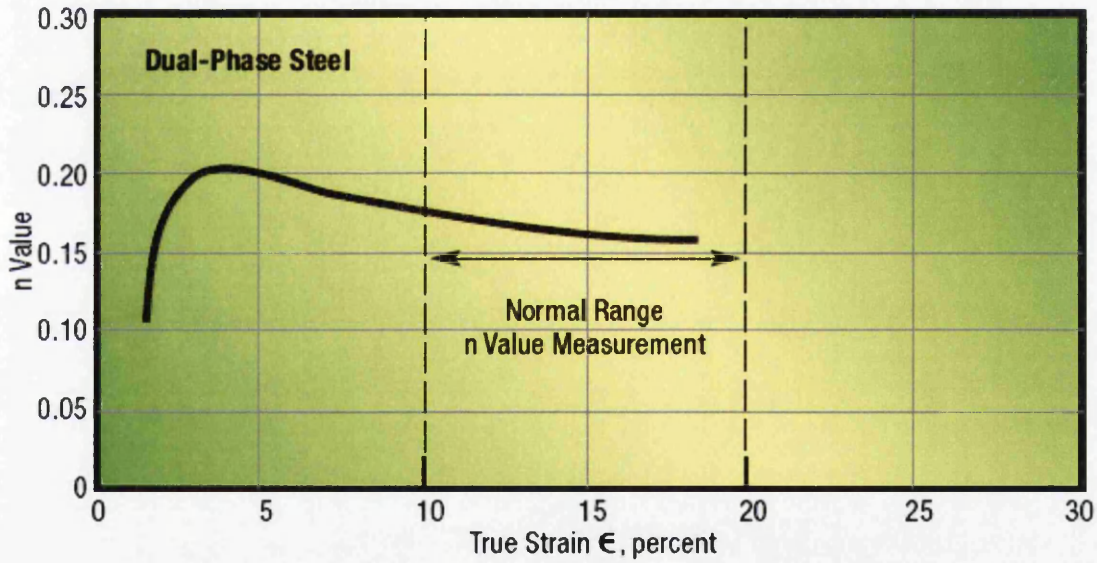
Figure 2.11. Non consistent n-value in DP material

Note that the stresses and strains shown above are true stresses/strains. More often than not the stresses obtained from testing are engineering stresses and as such need to be converted. The following hypothesis demonstrates how engineering stress and strain can be converted to true stress and strain:

15

$$\varepsilon_t = \int_{L_o}^{L_i} \frac{dL}{L} = \ln\left(\frac{L_i}{L_o}\right)$$

$$\varepsilon_{eng} = \frac{\Delta L}{L_o} = \frac{L_i - L_o}{L_o} = \frac{L_i}{L_o} - 1 \quad \therefore \quad \frac{L_i}{L_o} = \varepsilon_{eng} + 1$$

Hence true strain can be calculated by:

$$\varepsilon_t = \ln\left(\varepsilon_{eng} + 1\right)$$

And for the stress aspect:

$$A_o L_o = A_i L_i \quad ; \quad \sigma_{eng} = \frac{F}{A_o} \quad ; \quad \sigma_t = \frac{F}{A_i}$$

$$A_i = \frac{A_o L_o}{L_i} \quad ; \quad \sigma_t = \frac{F L_i}{A_o L_o} = \frac{\sigma_{eng} L_i}{L_o}$$

Hence true stress can be calculated by:

$$\sigma_t = \sigma_{eng}\left(\varepsilon_{eng} + 1\right)$$

Where:

L_i = Instantaneous length

L_o = Original length

A_i = Instantaneous area

A_o = Original area

ε_t = True Strain

ε_{eng} = Engineering Strain

σ_t = True Stress

σ_{eng} = Engineering Stress

Another basic property associated with strain is the r-value, often called Rankford value or also Plastic Anisotropy. It is often calculated as the ratio of strain along the width of a specimen to its thickness at 10-20% strain:

$$r - value = \frac{\varepsilon_w}{\varepsilon_{th}} = \frac{\ln {W_o}/{W}}{\ln {L_i W}/{L_o W_o}}$$

Where:

W = Instantaneous width

W_o = Original width

ε_w = Strain along specimen width

ε_{th} = Strain along specimen thickness

2.2.3 Basics of metal fatigue

As mentioned previously, understanding the fatigue properties of materials is an essential part of ensuring designs are both robust & reliable. Fatigue testing can be undertaken in a number of different fashions, with various tests being carried out utilising both temperature and loading variations. Most fatigue tests are carried out at room temperature with typical R ratios of R = 0.1, -1.0 & -0.5 where:

$$R = \frac{\sigma_{min}}{\sigma_{max}}$$

An illustration representing the equation above is given in BS 3518-1 (1993), and is shown in figures 2.12 & 2.13:
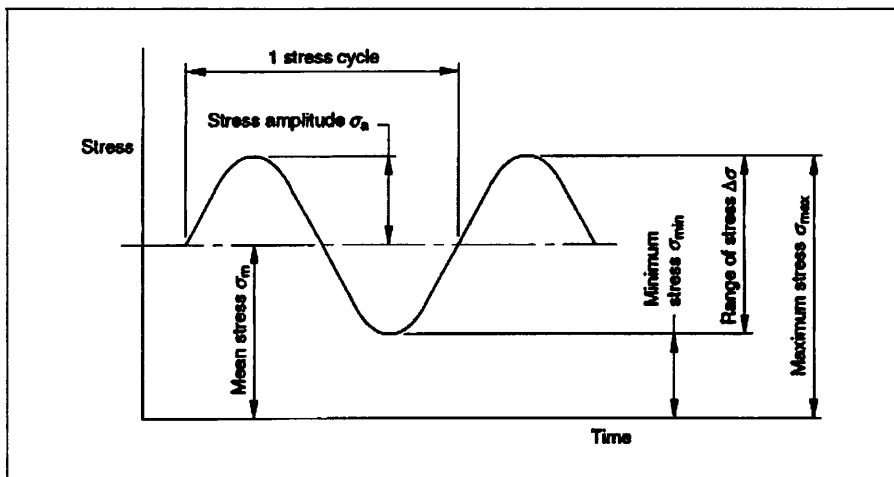
Figure 2.12. Fatigue stress cycle
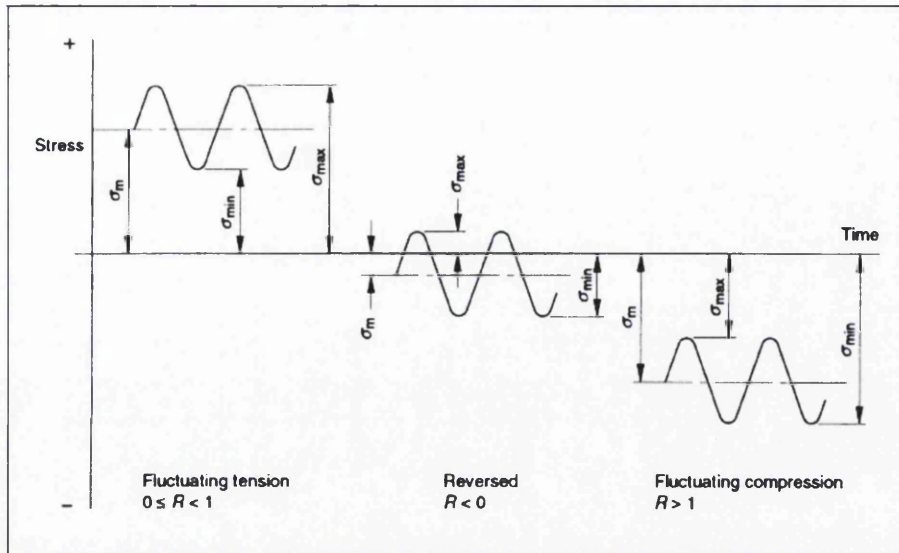
Figure 2.13. Types of stress cycle

To construct data that is to be of value to the automotive industry, it would be wise to perform tests with a wide range of R values. With this type of information it is then possible to estimate the fatigue performance at any stress ratio. The best way of processing data from a wide range of R values is by using a Goodman diagram [3, 4, 9]. There are two ways of representing a Goodman diagram and there have been a number of suggestions as to how the true shape of the curve within the diagram should appear. As well as the Goodman line we also have the Gerber and Soderberg lines. The Gerber line is a curved version of the Goodman line, while the Soderberg line uses Yield instead of UTS. These lines are seen in figure 14. What all three lines agree on is that as the mean stress increases, the material will not be able to withstand such a wide range of stresses.
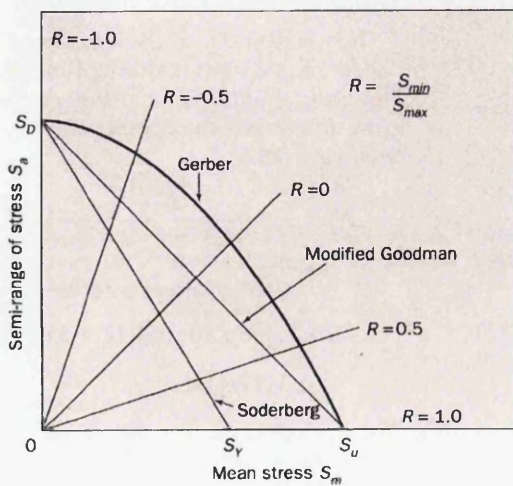
Figure 2.14. Goodman diagram
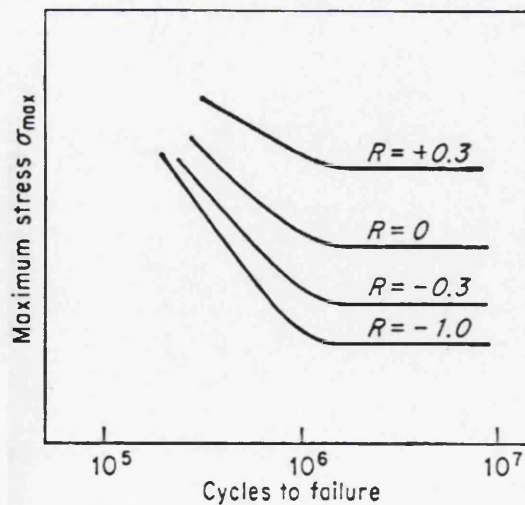
Figure 2.15. S-N curves for different R values

18

The diagram in figure 2.14 is drawn by using the fatigue limit values for each curve shown in figure 2.15. This means that although there may have been 8 to 12 separate tests for each curve shown in figure 14, giving a total of 32 to 48 tests in total, only four values are be used to create the Goodman diagram, i.e. the four values for the fatigue limit at each specified R-value. From this it is evident that obtaining sufficient data to create a Goodman diagram for a specified steel grade is an expensive and time consuming affair. It is generally accepted that the Gerber line provides the most accurate representation for most materials. However, since there is usually a large amount of scatter associated with fatigue data the Goodman line is still the most commonly used method.

The Goodman diagram is not always represented in the format shown in figure 2.14, with the y-axis representing the range of stress. The original Goodman diagram had the working stress representing the y-axis, therefore two converging lines had to be drawn to illustrate that the range of stress narrows as the mean stress increases. Figure 2.16 shows the data represented in this manner. Note that John Goodman drew dashed lines predicting increasingly large stress ranges for materials in mean compressive stress. The method shown in figure 2.14 is preferred as only one line is required to represent as much data as the original form of the Goodman diagram provides. The range of stress at any given mean is represented by the length of the vertical line drawn intersecting both upper and lower lines. Plastic deformation occurs at σ_0.
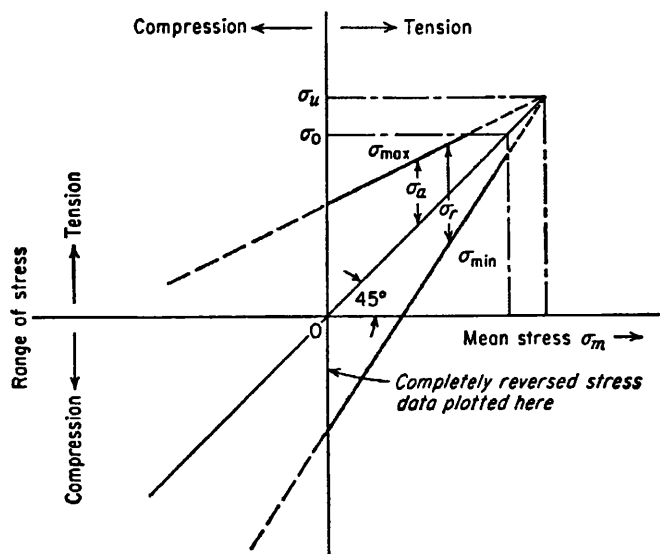
Figure 2.16. Original form of Goodman diagram

Looking back again at the more modern diagram shown in figure 2.14, the three lines each have their own distinctive equation to describe the relationship between alternating stress and mean stress. It is a topic of much debate as to which is most accurate, with most now believing that the Gerber curve most accurately describes the effect of mean stress with regard to predicting fatigue performance. Despite this it is generally accepted that the simple Goodman line is a perfectly sufficient tool.

Goodman line:

$$S_a = S_D \left(1 - \frac{S_m}{S_u} \right)$$

Gerber curve:

$$S_a = S_D \left[1 - \left(\frac{S_m}{S_u} \right)^2 \right]$$

Soderberg line:

$$S_a = S_D \left(1 - \frac{S_m}{S_Y} \right)$$

Where:

S_a = applied alternating stress

S_D = applied alternating stress for completely reversed loading

S_m = mean applied stress

S_u = ultimate tensile strength of the material

S_Y = yield stress

All three equations are very similar, the only difference being between the Goodman and Gerber is the square relation, this is what makes the Gerber relation a curve, while Soderberg uses S_Y instead of S_u.

Although much of this work is accredited to Gerber, Goodman and Soderberg, it is worth pointing out that the theory as it is presented today is somewhat different to the original theory. This is well documented by Sendeckyj [10] who researched

many different types of constant life diagrams and also helped make light of the unlabelled graphs drawn by Goodman [9]. John Goodman used fatigue data gathered by Wohler's "experiments on the repetition of stress". The results of Wohler's experiments can be seen in figure 2.18.

Goodman plotted an unlabelled graph shown in figure 2.17 and strangely dubbed the horizontal scale "immaterial", though he did state that the y-axis "shows the ratio to the static breaking stress" this can possibly be interpreted as being the applied stress displayed as a fraction of the UTS (S_a/S_u). Since we do not know for certain what the x-axis represents it is difficult to predict why the original diagram drawn by Goodman seems to be shifted to the left compared to figure 2.16. What is clear is that results for completely reversed loading do not lie on intercept with the y-axis, as is the case with figure 2.16.

The knowledge and understanding of these diagrams is important for displaying variability data on fatigue results with varying R ratios since it allows direct comparison of different data sets, which is impossible to do using any other method. The Gerber and Goodman formulae are of particular importance as they can be used to predict performance under a multitude of loading conditions and can therefore be used to robustly design new products.
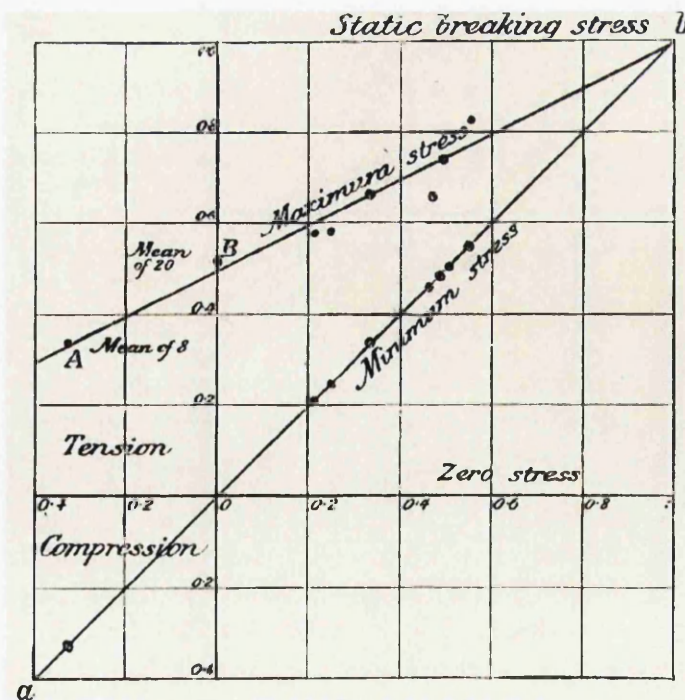
Figure 2.17 Original Goodman diagram

21

MATERIAL.

Krupp's Axle Steel.

Tensile strength, varying from 42 to 49 tons per sq. inch.

Tensile stress applied in tons per square inch		Number of repetitions before fracture.	Nominal bending stress in tons per square inch		Number of repetitions before fracture.
from	to		from	to	
0	38·20	18,741	0	26·25	1,762,000
0	33·40	46,286	0	25·07	1,031,200
0	28·65	170,170	0	24·83	1,477,400
0	26·14	123,770	0	23·87	5,234,200
0	23·87	473,766	0	23·87	40,600,000
0	22·92	13,600,000 (unbroken)			(unbroken)

Nominal bending stress in a revolving axle		Number of repetitions before fracture.
from	to	
20·1	− 20·1	55,100
17·2	− 17·2	127,775
16·3	− 16·3	797,525
15·3	− 15·3	642,675
,,	,,	1,665,580
,,	,,	3,114,160
14·3	− 14·3	4,163,375
,,	,,	45,050,640

MATERIAL.

Krupp's Spring Steel.

Tensile strength, 57·5 tons per sq. inch.

Tensile stress applied in tons per square inch		Number of repetitions before fracture.	Tensile stress applied in tons per square inch		Number of repetitions before fracture.
from	to		from	to	
47·75	7·92	62,000	38·20	4·77	99,700
,,	15·92	149,800	,,	9·55	176,300
,,	23·87	400,050	,,	14·33	619,600
,,	27·83	376,700	,,	,,	2,135,670
,,	31·52	19,673,000 (unbroken)	,,	19·10	35,800,000 (unbroken)
42·95	9·55	81,200	33·41	4·77	286,100
,,	14·33	1,562,000	,,	9·55	701,800
,,	19·10	225,300	,,	11·94	36,600,000 (unbroken)
,,	23·87	1,238,900			
,,	,,	300,900			
,,	28·65	33,600,000 (unbroken)			

Figure 2.18. Wohler "experiments on the repetition of stress"

2.2.4 Fatigue crack initiation & propagation

The stages and mechanisms influencing fatigue crack initiation & propagation are distinctive and well defined in literature, Lee et. all [11] covers this topic and describes the fatigue failure mechanism by the following stages:

1) Crack initiation forming from persistent slip bands

2) Stage I crack growth

3) Stage II crack growth

4) Failure

The nucleation & stage I crack growth can occur at multiple locations within a component or test coupon, though are more likely to initiate in areas that exhibit surface defects, stress concentrations or inclusions. Persistent slip bands occur at stress levels in the elastic region of the material, even at stresses which are less than the endurance limit of the material. The formation of these slip bands during cyclic loading, which leads to the formation of microcracks is illustrated documented by Shcijve [12] and can be seen in figure 2.19, where the growth a crack formed as a result of cyclic slip is shown in figure 2.20.
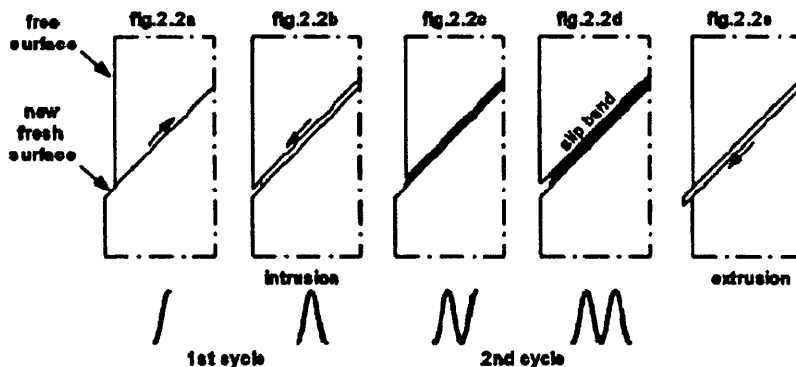
Figure 2.19. Formation of slip bands during cyclic loading
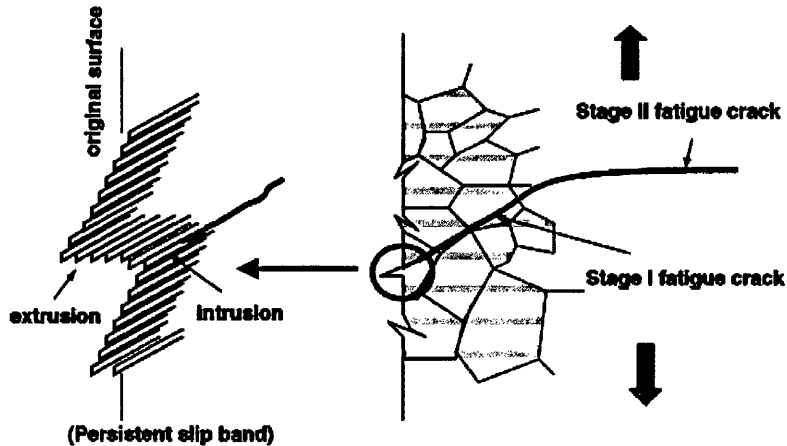
Figure 2.20. Formation of persistent slip bands & nucleation and growth of microcracks.

23

Schijve also suggested that as microcrack growth is dependant on cyclic plasticity, barriers to slip can imply a threshold to crack growth. This is evident in figure 2.21, whereby crack growth rate decreases as the crack nears a grain boundary, in some cases where the energy levels are not sufficient to re-initiate growth, the crack may be impeded altogether, thus giving a run-out reading for that particular stress level. A small average grain size would mean cracks would have less room to grow before being retarded by a grain boundary, thus with everything else being equal, microcracks are more likely to be impaired during stage I with a fine-grained microstructure as compared to a course grained material.
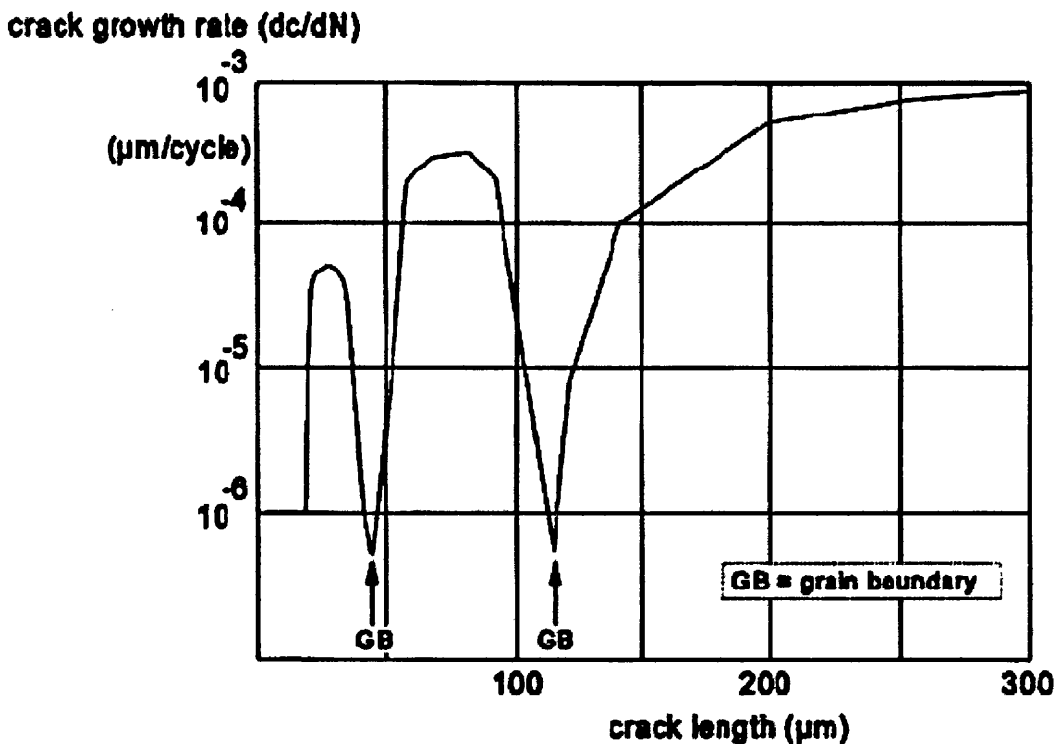
Figure 2.21. Grain boundary effect on crack growth

For high cycle count failures, the crack initiation period may cover a significant portion of the total fatigue life, where for low cycle fatigue it may be governed more by stage I & II crack growth. It is thought that once stage I crack growth has travelled along a significant number of grains, stage II grack growth is initiated and thus the Paris relation for grack growth applies. Figure 2.21 & 2.22 illustrates how microcracks can be formed, but as a result of barriers to growth, such as grain boundary's, these microcracks are prevented from growing and as a result failure does not occur.

This theory is supported by the fact that fatigue cracks grow transgranularly and not along grain boundarys, hence grain boundarys will always become obstacles to crack growth. Fatigue coupons which are identified as having a run-out life may arise from either stress levels at which microcracks are not initited, or where cracks do initiate but there is insufficent energy to overcome barriers during stage I. This is illustrated in figure 2.22.
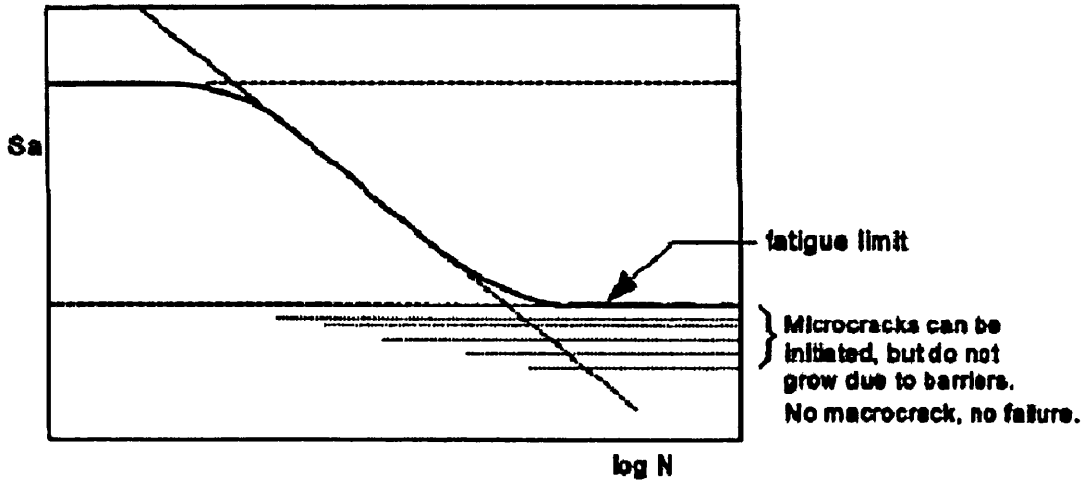
Figure 2.22. Stress levels sufficient to cause microcracks, but not failure

Resistance to slip is highly influenced by crystalline oreientation, where it can be seen that the elastic modulus of steel is fairly anisotropic compared to that of aluminium, and is greatest in the [111] plane (figure 2.23). This anisotropy causes inhomogenous stress distributions within the material (figure 2.24), where slip may readily occur in some crystalline orientations, but is arrested in others. Thus it is reasonable to assume that numerous processing conditions which influence texture will come into play in determining final fatigue properties. These could include the amount of hot and (if applicable) cold reduction, temperature traces, time between processing stages, plus numerous others.

Material	E_{max} [111] (MPa)	E_{min} [100] (MPa)	Ratio max/min
α-Fe	284500	132400	2.15
Al	75500	62800	1.2
Cu	190300	66700	2.85

Figure 2.23. Elastic anisotropy of various materials
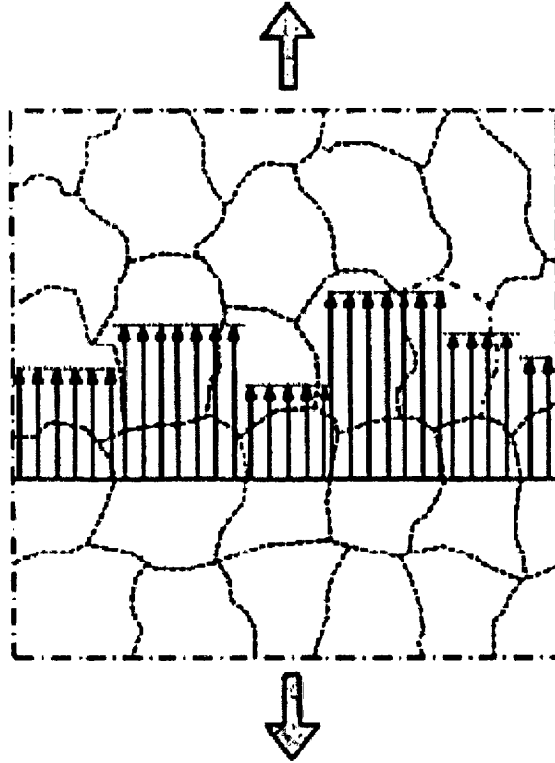
Figure 2.24. Inhomogeneous stress distribution from grain to grain due to elastic anisotropy

Stage II crack growth is more stable and quantifiable than stage I crack growth, where it is governed by the Paris (sometimes called Paris-Erdogan) growth law. Geometrical factors play a large role in the determination of the stress intensity factor, though in plain un-notched fatigue specimens it is the materials properties that will determine this. The Paris equation, along with the definition of the stress intensity factor are shown in the two equations below, followed by graphical representation of Paris crack growth in figure 2.25.

$$da\!\!\Big/\!\!_{dN} = C(\Delta K)^m$$

$$\Delta K = \Delta Y \sigma \sqrt{\pi a}$$

Where:

a = crack length

N = number of cycles

C, m = constants relating to material/geometry

K = stress intensity factor

Y = geometrical factor

σ = axial stress
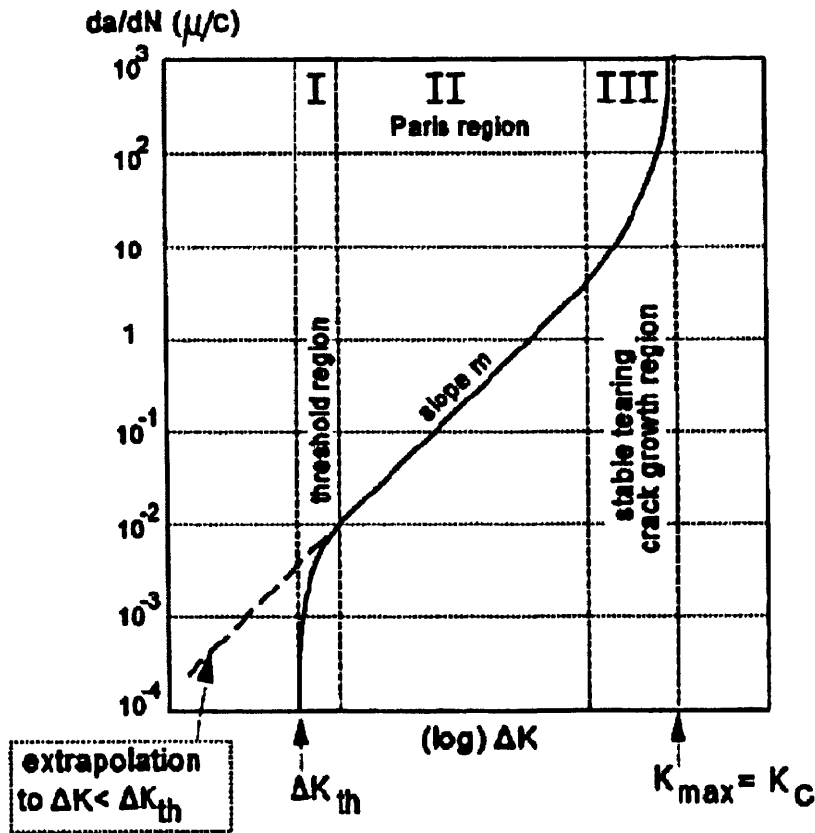
Figure 2.25. Paris crack growth

2.2.5 Graphical representation of fatigue data

Fatigue data by its very nature will always exhibit a great deal of variability, therefore many different mathematical trends have been linked with representing fatigue data. Most of them are based on power laws or exponential curves such as the Weibull distribution. It is still open to debate which type of curve is most accurate. In industry the Basquin relation [13, 14, 15, 16] is now the most preferred and commonly used representation of stress life fatigue data:

$$\frac{\Delta\sigma}{2} = AN_f^{\,b}$$

Where:

$\Delta\sigma/2$ = Stress amplitude

A = Basquin coefficient

b = Basquin exponent

N_f = Number of cycles to failure

27

The terms on the left represent the amplitude of the applied load and A and b are constants. Data is fitted to the relationship using the least squares method, which aims to minimise the function shown below in order to find the values for A and b:

$$Minimize : \sum_{i=1}^{n} \left(y_{act} - f(x_i) \right)^2$$

The following information explains the principles behind this theory and illustrates how the Basquin relationship can be quantified from a data set. Note that on a log-log scale the S-N curve will display as a straight line with a negative gradient. i.e. it has the form:

$$y = A.x^b$$

which becomes:

$$\log(y) = \log(A) + b \cdot \log(x)$$

i.e. It has the straight line form (note the change in case):

$$Y = a + bX$$

Observing figure 2.26, below, where point p shows the value of a result at (x_i, y_i), we aim to minimise the sum of the square of the errors shown by the red lines:
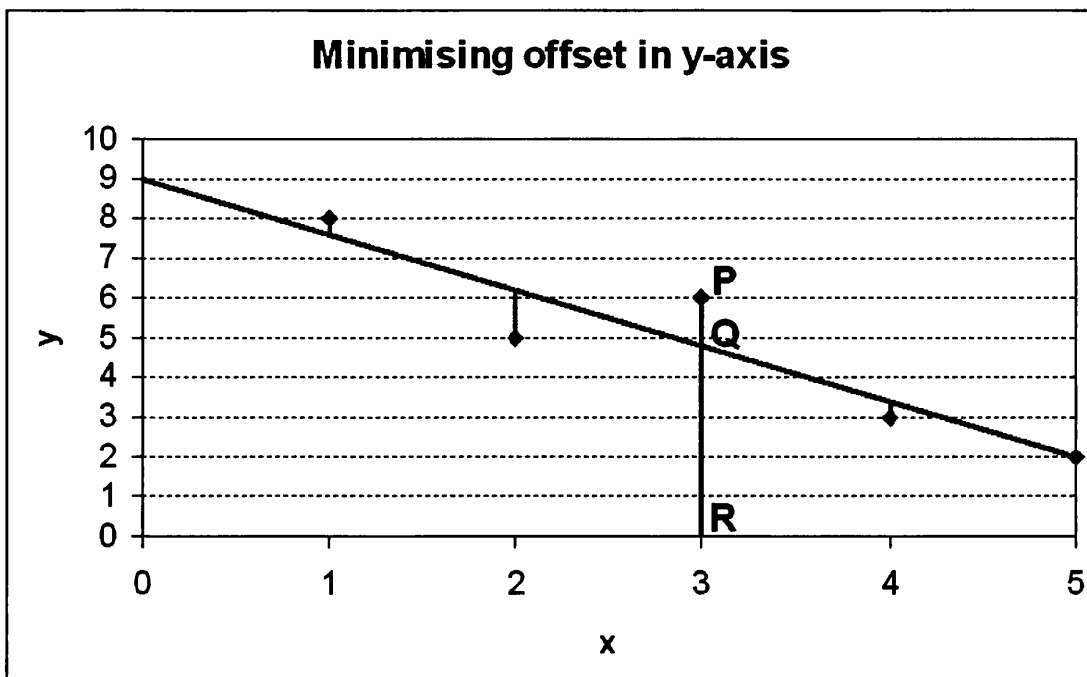
Figure 2.26. Least squares y-axis offsetting.

QR is the value of Y=bX+a at x = x_i i.e X_i or $Y = bX_i + a$

PQ is the difference between PR and QR:

$$PR = Y_i$$

$$PQ = PR - QR = Y_i - (bX_i + a)$$

$$PQ = Y_i - bX_i - a$$

The sum S of the squares of these differences for all n points is given by:

$$S = \sum_{i=1}^{n} \left(Y_i - bX_i - a\right)^2$$

For the sum of the squares to be a minimum:

$$\frac{\partial S}{\partial a} = 0 \quad \text{and} \quad \frac{\partial S}{\partial b} = 0$$

$$\frac{\partial S}{\partial a} = -2\sum_{i=1}^{n} (Y_i - bX_i - a) = 0$$

$$\frac{\partial S}{\partial b} = -2\sum_{i=1}^{n} X_i(Y_i - bX_i - a) = 0$$

The first gives:

$$\sum_{i=1}^{n} Y_i - b\sum_{i=1}^{n} X_i - na = 0$$

And the second gives:

$$\sum_{i=1}^{n} X_i Y_i - b\sum_{i=1}^{n} X^2_i - a\sum_{i=1}^{n} X_i = 0$$

These two give expressions for (a) and (b) respectively:

$$a = \frac{\sum_{i=1}^{n} Y_i - b\sum_{i=1}^{n} X_i}{n} \quad ...(1)$$

29

$$b = \frac{\sum_{i=1}^{n} X_i Y_i - a\sum_{i=1}^{n} X_i - a\sum_{i=1}^{n} X_i}{\sum_{i=1}^{n} X^2{}_i} \quad ...(2)$$

Substituting (1) into (2) gives:

$$b = \frac{n\sum_{i=1}^{n} X_i Y_i - \sum_{i=1}^{n} X_i \sum_{i=1}^{n} Y_i}{n\sum_{i=1}^{n} X_i{}^2 - \left(\sum_{i=1}^{n} X_i\right)^2} \quad ...(3)$$

Remembering that X = log x and Y = log y, equations (1) and (3) gives us two expressions that enable us to calculate (a) and (b):

$$a = \frac{\sum_{i=1}^{n}(\ln y_i) - b\sum_{i=1}^{n}(\ln x_i)}{n}$$

$$b = \frac{n\sum_{i=1}^{n}(\ln x_i \ln y_i) - \sum_{i=1}^{n}(\ln x_i)\sum_{i=1}^{n}(\ln y_i)}{n\sum_{i=1}^{n}(\ln x_i)^2 - \left(\sum_{i=1}^{n}\ln x_i\right)^2}$$

Where:

$$b \equiv b$$

$$A \equiv e^a$$

Often results are then displayed with +/- a number of standard deviations (or standard error) to show i.e. 99% & 1% confidence limits which is approximately 2.6 standard errors from the 50% confidence limit.

While the method illustrated above shows the method with y-axis offsetting, quite often x-axis offsetting is used, since with fatigue the stress is the fixed input value,

with the number of cycles being the result. The least squares method can be used to calculate the values for a and b' as shown below:

$$N_f = a \left(\frac{\Delta\sigma}{2} \right)^{b'}$$

By using the same principles (a) and (b') can be calculated by:

$$a = \frac{\sum_{i=1}^{n} \left(\ln N_i \right) - b \sum_{i=1}^{n} \left(\ln \left(\frac{\Delta\sigma}{2} \right)_i \right)}{n}$$

$$b = \frac{n \sum_{i=1}^{n} \left(\ln \left(\frac{\Delta\sigma}{2} \right)_i \ln N_i \right) - \sum_{i=1}^{n} \left(\ln \left(\frac{\Delta\sigma}{2} \right)_i \right) \sum_{i=1}^{n} \left(\ln N_i \right)}{n \sum_{i=1}^{n} \left(\ln \left(\frac{\Delta\sigma}{2} \right)_i \right)^2 - \left(\sum_{i=1}^{n} \ln \left(\frac{\Delta\sigma}{2} \right)_i \right)^2}$$

Where:

$$b \equiv \frac{1}{b'}$$

$$A \equiv \frac{1}{e^{ab}}$$

For Strain life fatigue graphs results are fitted to the Coffin-Manson equation:

$$\frac{\Delta\varepsilon}{2} = \frac{\Delta\varepsilon_e}{2} + \frac{\Delta\varepsilon_p}{2} = \frac{\sigma'_f}{E} \left(2N_f \right)^b + \varepsilon'_f \left(2N_f \right)^c$$

Where:

E = Young's Modulus

N_f = Number of cycles to failure ($2N_f$ is the number of reversals to failure)

σ'_f = Fatigue strength coefficient

b= Fatigue strength exponent

ε'_f = fatigue ductility coefficient

c = Fatigue ductility exponent

2.2.6 Weld fatigue and structural performance

Weld performance is a large subject area, since so many joining methods exist, ranging from simplistic methods such as oxy acetylene to other more sophisticated processes such as Metal Inert Gas/Metal Active Gas (MIG/MAG), Tungsten Inert Gas (TIG) and laser welding. Resistance spot welding is still popular in the automotive industry, though not for structural chassis components such as lower control arms, etc. By far the most popular method deployed for these purposes is the MIG/MAG method. By only considering this type of welding there is still a huge range of factors that not only affect the weld quality/performance, but also the substrate.

Figure 2.27 Illustrates the MAG welding process. From this it is clear that many factors can contribute to the overall performance of the weld and that optimising these conditions is critical.
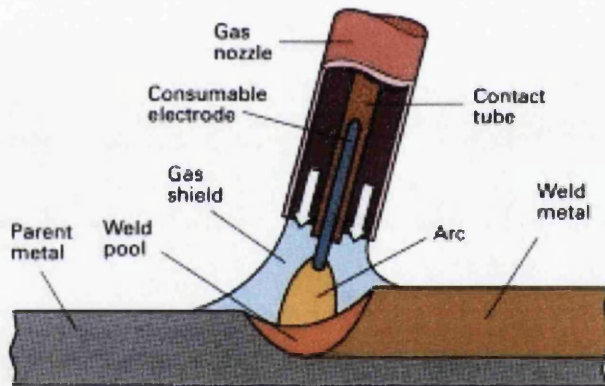
Figure 2.27. MIG/MAG welding schematic

Factors which affect weld quality variability are [17]:

- Wire speed
- Nozzle speed
- Substrate preparation
- Shielding gas
- Welding angle
- Heat
- Stop/start
- Wire gauge
- Wire chemistry

These factors will affect the performance of the weld regardless of whether or not the process is automated. By optimising these conditions the component manufactured will be less susceptible to fatigue failure and prove to be more robust. The three most critical aspects listed are the nozzle control, wire speed and heat/current. Getting the right amount of heat (a function of welding current), the correct nozzle control and the appropriate wire speed are crucial to obtaining a high quality weld.

Factors such as weld toe undercut, sometimes called the Cinderella defect [18] can occur if the heat is too great which may result in a stress concentration point. The effects of the three critical welding factors can be seen in figure 2.28. [19]

| A | B | C | D |
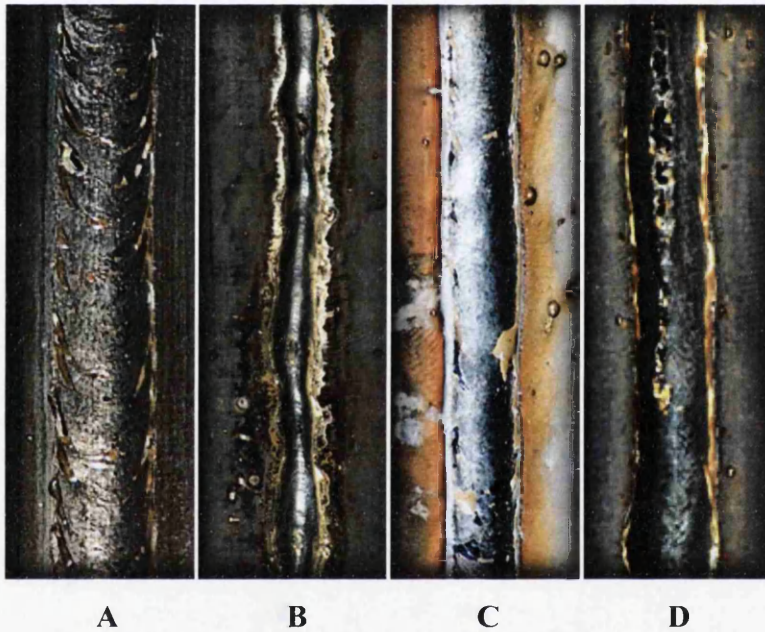
Figure 2.28. Samples of various welding conditions

Weld **A** is a good weld, it can be clearly seen that the weld has penetrated the base material as the weld toe shows good 'tie in' i.e. there is a very slight undercut but not enough to cause the potential fatigue problems discussed by Nguyen & Wahab [20], which is discussed later.

Weld **B** shows a result whereby the nozzle speed is far too high, as a result there has not been sufficient time for heat to build up and penetrate the base material. It is likely that this weld is on the surface only with very little tie in and will break very easily.

Weld **C** has a welding voltage which is set too high, this results in a turbulent weld pool which the operator has poor control over. Often when the voltage is too high there can be weld toe undercut (not in this case), although this phenomenon is also associated with a slow nozzle speed. Blow outs can also occur with thin gauge material. The major problem here, especially when dealing with AHSS is the size of the Heat Affected Zone (HAZ), which will be very large.

Weld **D** shows a weld that may have a combination of excessive amperage as well as a high wire speed. The result of this is a large convex bead with poor tie in at either side of the weld bead. The large amount of material deposited can hide the potentially poor penetration of the weld. Even though there was a large amount of heat applied, much of the energy was used to melt the filler material, and as such not enough energy was dispersed to penetrate the substrate.

A paper by T. Ninh Nguyen and M.A. Wahab [20] discussed the effects of weld geometry on fatigue performance in detail. Weld toe undercut theory developed by Jubb [18] was used in conjunction with the Paris-Edrogan model to predict the effect of small notches on weld toes on fatigue performance:

It is clear from section 2.24 that if weld-toe undercut contains notches or cracks it will increase the rate of crack growth due to geometrical effects increasing stress intensity. Furthermore the two initial stages of metal fatigue, i.e. crack initiation and stage I growth, which can account for a significant proportion of fatigue life will have been bypassed. Experimental procedures were used to validate this theory, however since weld-toe undercut appears in many forms, defining the crack length is not such a simple affair. The model developed by Jubb distinguished 3 main types of defect, shown in figure 2.29.

Type 1: _curved_

Type 2: _crack-like_

Type 3: _micro-flaw_

0.25 mm
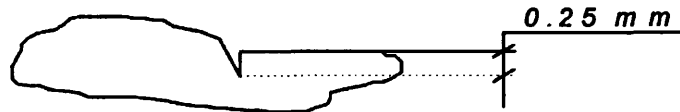
Figure 2.29. Classification of undercuts

Type 1 defects (which are the most common variety) do not have cracks as such, therefore a method of quantifying the scale of the defect was developed and is shown in figure 2.30.
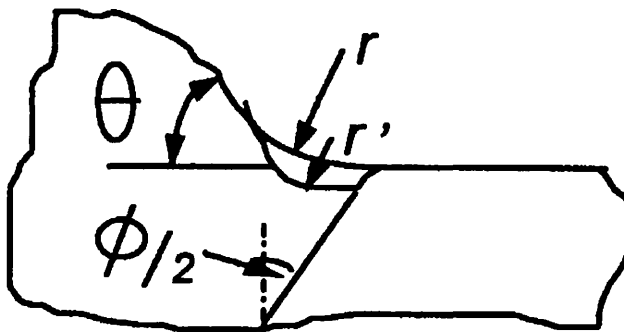
Figure 2.30. Weld toe radii

This method of using radii to define flaws was used to compare the S-N curves of various welds. The pattern is clear and there can be no doubt by comparing the results on figure 2.31 that defects with a small radii (more crack like in appearance) have a reduced fatigue life compared to defect free material.
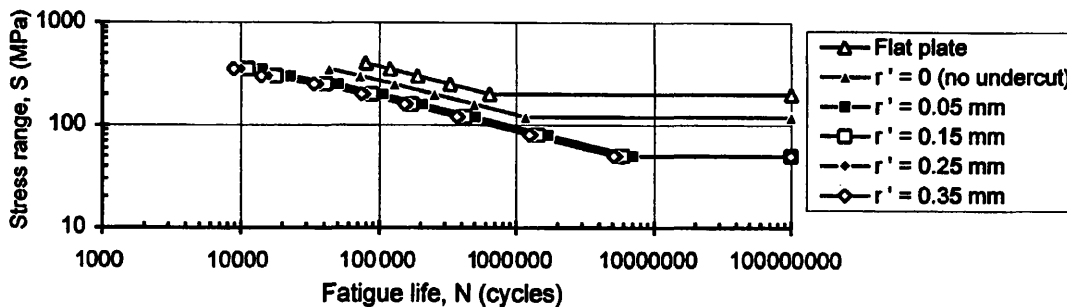
Figure 2.31. Effect of tip radius of the weld toe undercut (r') on the S–N curve ($R=0$)

35

Another measurable factor to consider with welding is the weld toe angle (θ), as shown in figure 2.32. This was not considered by Nguyen & Wahab [20] but was covered in another paper [21] with some interesting results. It seems that welders' natural instinct of preference for flatter welds over more raised welds is backed up by theoretical and experimental data showing that lesser angles have a far improved fatigue performance to welds with steep angles, this can be seen in figure 2.32.
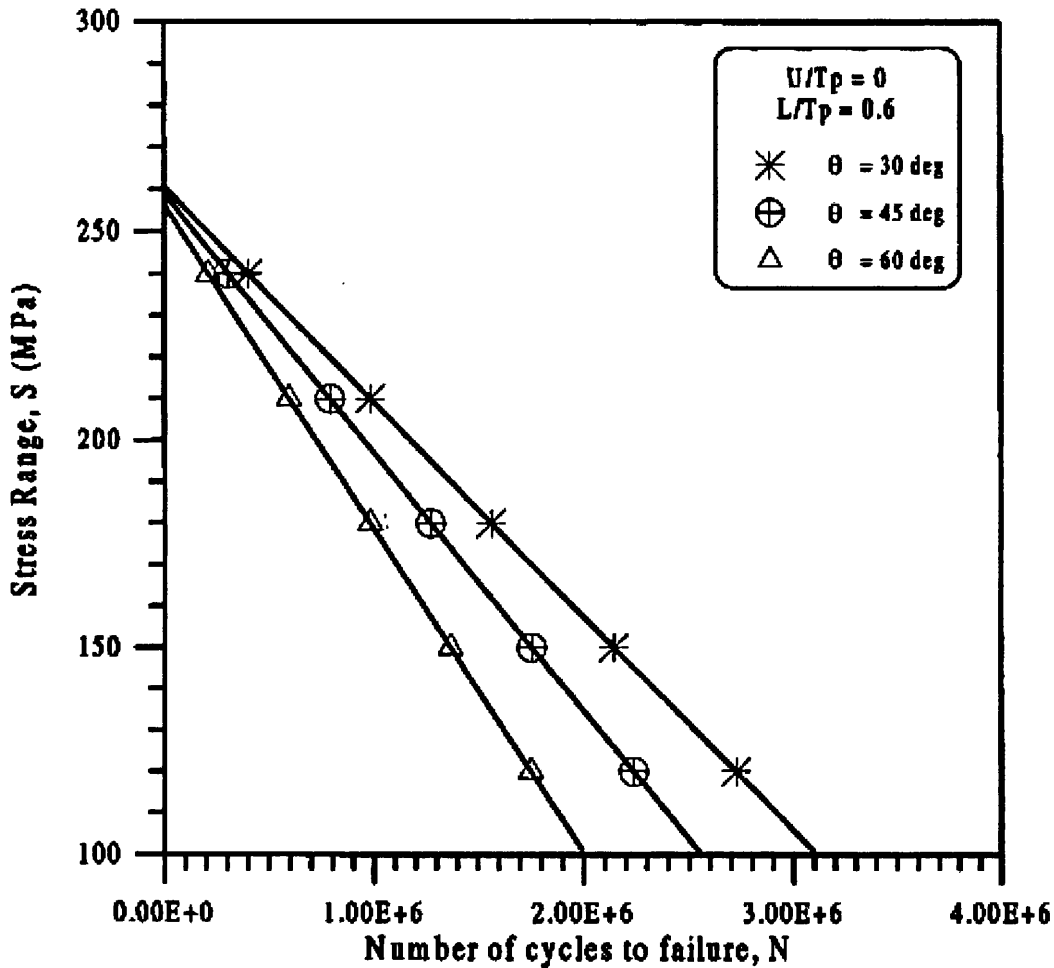
Figure 2.32. Comparing fatigue performance with welds of varying toe angle

What is unclear from this report is whether this is due to the structural integrity of the weld or the influence of the angle itself. Going back to figure 2.28, the weld shown in B has a very steep angle, and would obviously perform poorly in a fatigue test since it surely lacks penetration. Though that is not to say that it is impossible, if unlikely to achieve a good weld with excellent penetration with a high angle. It is clear that differentiation between good and bad welds is needed when comparing weld geometry, so that it is only the geometry itself which is being studied independently of other factors.

2.2.7 Improving the fatigue performance of metals

There are numerous other methods of improving fatigue performance of welded structures, though more research is needed to establish if these methods also minimise the variability. Some of these methods include shot peening, machining burrs and imperfections of the welded areas and plasma and TIG dressing of the weld toe. Dressing involves minimising notch defects as shown earlier in figure 2.29 by re-melting the weld toe and maximising its radius in order to minimise the stress concentration. An example of a dressed weld is shown in figure 2.33.
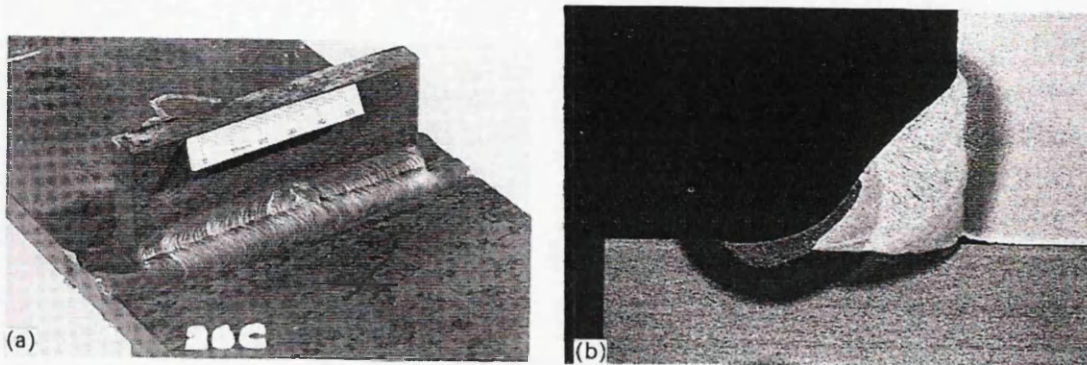
Figure 2.33. TIG dressed weld

The toe of the weld shown in (b) has a shallow curvature leading down to the weld toe and has a very neat tie-in to provide a weld with excellent mechanical properties. The fatigue improvements of this method, as well as other weld fatigue improvement solutions are shown in figure 2.34. This survey by Maddox [22] suggests hammer peening to be the most effective technique to improve performance. Though as this is mainly a manual procedure, large amounts of variability is certainly possible depending on user skill/knowledge.

Essentially all methods of improving the fatigue characteristics shown in figure 2.34 either involve applying compressive residual stress to the surface of the weld or minimising crack like defects mainly at the weld toe. Some of these techniques are easily automated, while others are difficult and are mainly done manually and as such this graph should only be used as a rough guide.
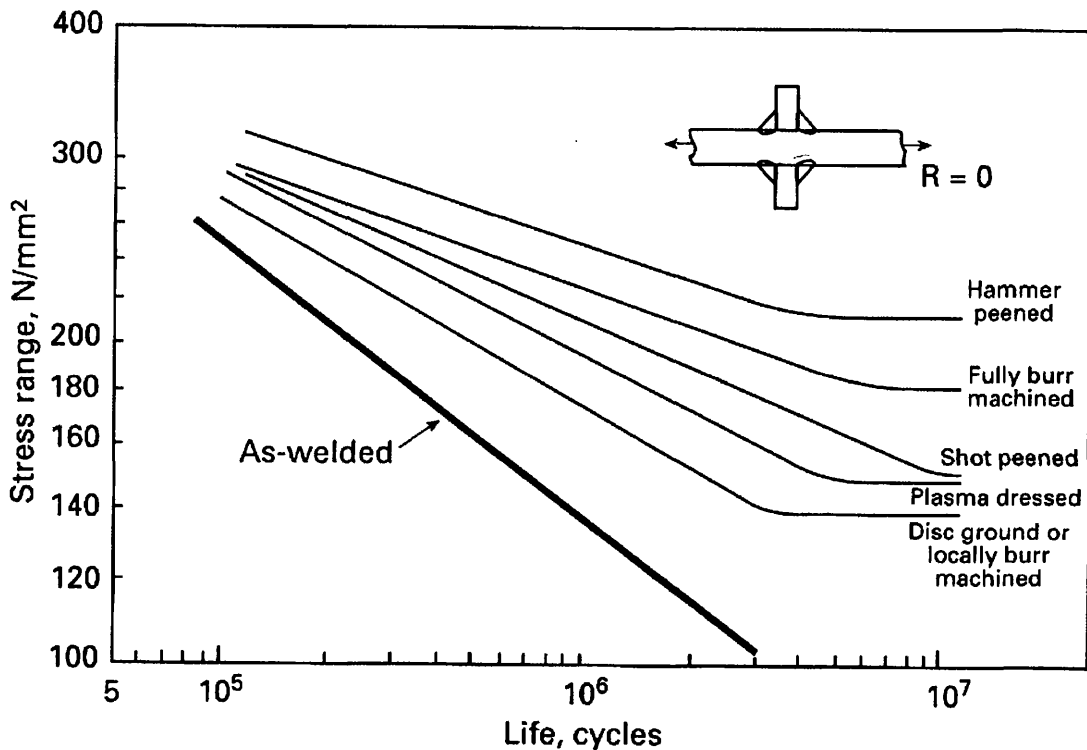
Figure 2.34. Comparison of fatigue improvement techniques for welded structures

Since improving fatigue performance and minimising variability plays a large role in this project, one method worth considering is the effect of shot peening on the mechanical properties and performance of steel. George et. al. [23] described the theory of how shot peening can potentially improve fatigue performance as "since fatigue failures are cracks, and cracks never open unless adjacent particles are pulled apart, it may be assumed that cracks can neither start in a compressive layer nor propagate into it".

Current literature on the peening process indicate that the residual compressive stress levels are of the order of a few hundred MPa or greater [24], this significant amount of stress reinforces the theory of inhibiting crack initiation and propagation. Shot peening in itself is a huge research topic, this is due to the fact that there are so many factors that affect the performance of shot peened parts. The main contributors to the quality of the peening are the shot size, shot intensity, shot hardness, shot speed, shot flow rate, coverage and impact angle. All these factors need to be optimized, as an un-optimized peening process can actually lead to a deterioration in component performance.

Even though shot peening can prove to be damaging if not optimized, there is a huge amount of evidence to support its application for improving fatigue performance in steels and other materials. Tekeli [25] studied the effect of shot peening on SAE 9245 steel, which is widely used for spring manufacture. The results of these tests were that with an optimised peening intensity, giving a surface compressive residual stress of around 400MPa, the fatigue life of the test specimens were around 30% greater than standard. These results can be seen in figure 2.35.
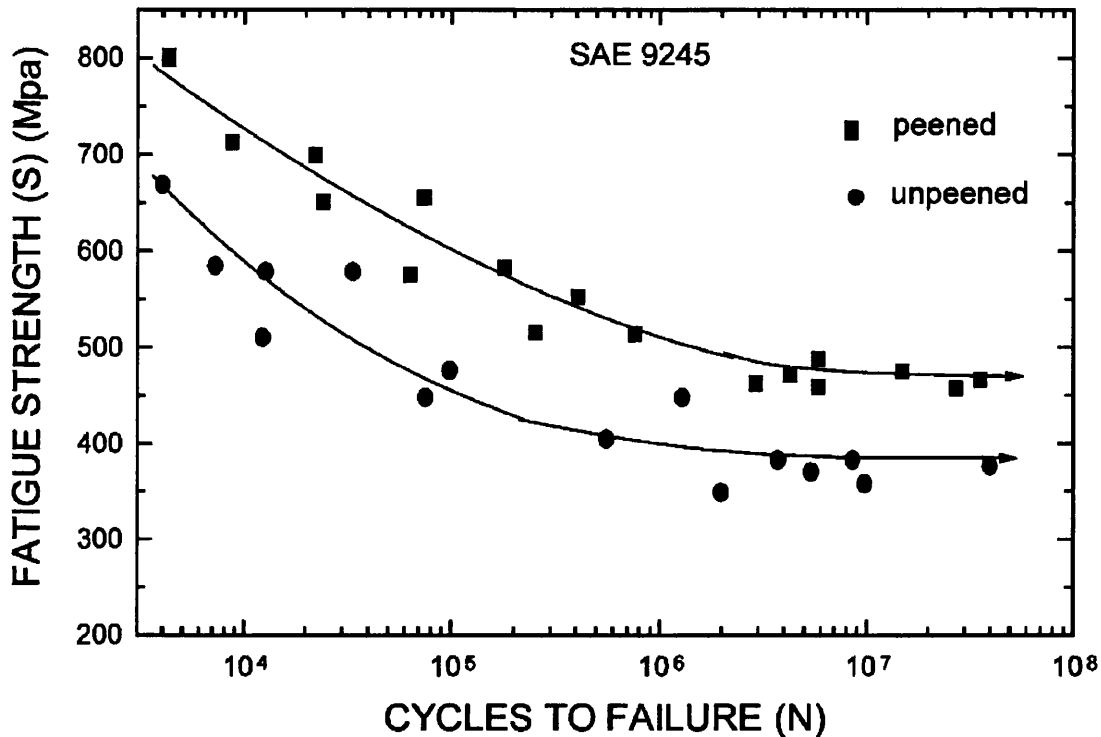
Figure 2.35. S-N curves for shot peened and un-peened specimens

The success of shot peening with this grade of steel is undeniable, even though there is still a considerable amount of scatter, the two sets of results are clearly separated. What is unclear by these results is what R-ratio the tests were performed at and whether or not we should expect this kind of benefit across all loading conditions. These significant unknown factors require careful consideration before suggesting use of shot peening for chassis applications.

Understanding whether or not the benefits these techniques have on as-received material also translate into benefits in welded joints would be of interest. There are also possibilities for future technologies such as laser shock peening [26] to provide fatigue performance enhancements. Typical internal compressive residual stress as a

result of shot peening, published by Asquith et. al. [27] is shown in figure 2.36, as well as a schematic of the process in figure 2.37.
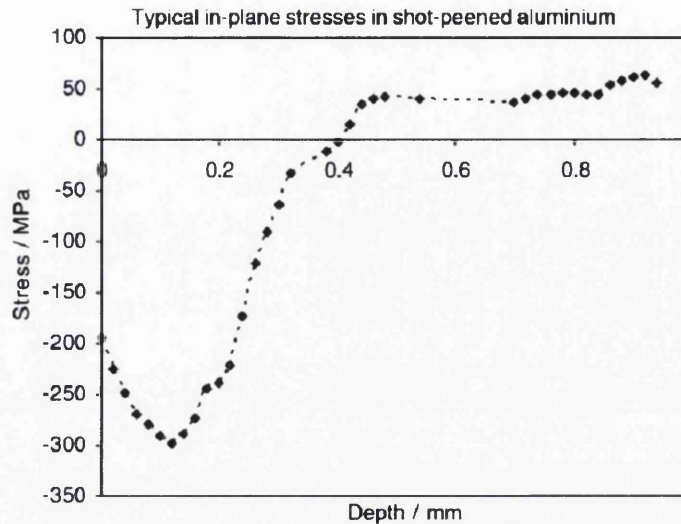
Figure 2.36. Residual compressive stress on surface of shot-peened sample
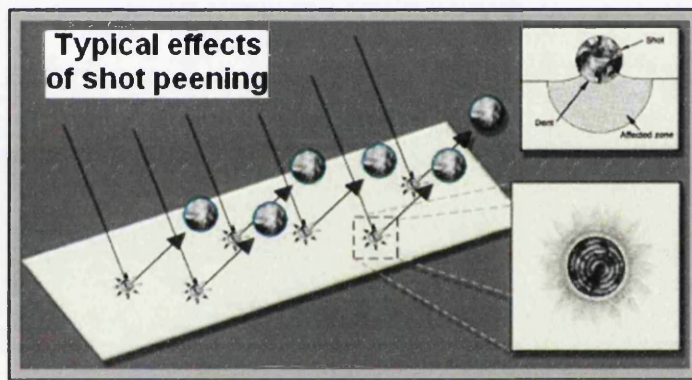
Figure 2.37. Illustration of surface effect due to shot peening

2.3 Methods of evaluating structural performance

2.3.1 Introduction to evaluating structural performance

The methods of evaluating structural performance are numerous and ever evolving. Before the introduction of Computer Aided Engineering (CAE) methods such as Finite Element Analysis (FEA), the use of lengthy hand calculations was the main method used to develop initial designs. Refinement of designs could then be completed after physical experimentation, a process which itself has evolved with the introduction of new technologies.

40

Physical testing may involve measuring stresses & strains derived from strain gauge data, fatigue performance from cyclic testing, and crash performance, as well as many other methods such as non-destructive testing. Physical testing may not be limited to laboratory conditions, the use of proving grounds, such as the one held at MIRA, are also widely used in the automotive industry.

Hand calculations may sometimes be combined with empirical or rule-based calculations for calculating factors such as stress concentrations [28]. The downside of using hand calculations is that it becomes extremely difficult to apply basic principles and theories to complex shapes. Hence the popularity of using FE packages such as Abaqus, MSC Nastran, ANSYS and others in recent times. FE methods do however have their drawbacks, the major problem associated with it is the care required to ensure that predictions are accurate. Many factors can affect the accuracy of these predictions, ranging from the way in which boundary conditions are applied to the meshing details.

2.3.2 Example of hand calculation for comparison with FE models

Before using any FE software it is essential to ensure its accuracy, as FE modelling can often return a wide range of results depending on several factors such as mesh size, boundary conditions, geometrical accuracy, as well as numerous other factors. A common practice to ensure that FE models accurately predict structural performance is to compare the results with other data such as physical test data or hand calculations. By considering a simple cantilever being loaded, the stresses and deflections can be calculated using Macaulay's method [4]. Comparison of these results with FE predictions will aid in the verification and optimisation of CAE procedures.

Consider a cantilever beam, 0.99m long, made of square section tubing with outside dimensions of 19mm and inside dimensions of 16mm. The cantilever is fixed at one end, and has a load of 46.5N at the other end as seen in figure 2.38:
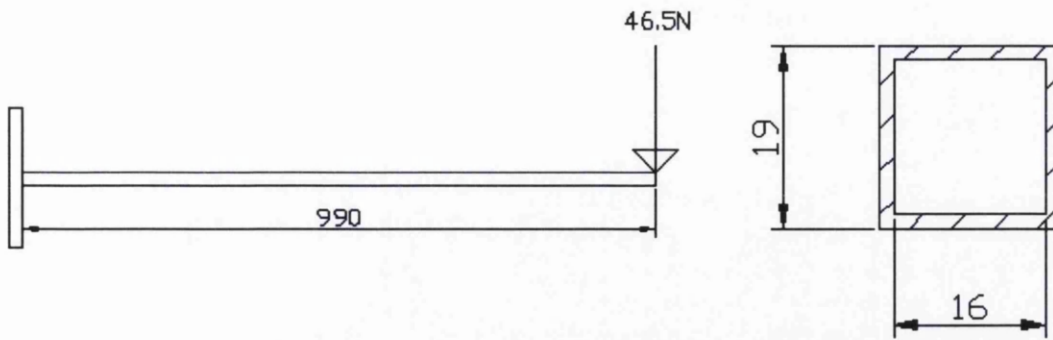
Figure 2.38. Cantilever beam boundary conditions

The maximum stress in this cantilever is at the point where the bending moment is greatest i.e. at the furthest point from the applied load, note that the dimensions given on the illustration above are in millimetres. The equation for this maximum stress is given by the equation shown below, where M represents the applied moment, y represents half the outer dimension of the square cross-section and I is the second moment of area.

$$\sigma_{MAX} = \frac{M \times y}{I}$$

The second moment of area for a hollow square tube is given by the equation:

$$I = \frac{B \times D^3}{12} - \frac{b \times d^3}{12}$$
$$I = \frac{0.019 \times 0.019^3}{12} - \frac{0.016 \times 0.016^3}{12}$$
$$I = 5.4 \times 10^{-9} m^4$$

Inserting all the variables into the first equation gives:

$$\sigma_{MAX} = 81 MPa$$

Using Macaulay's method, the calculation for deflection is as follows:
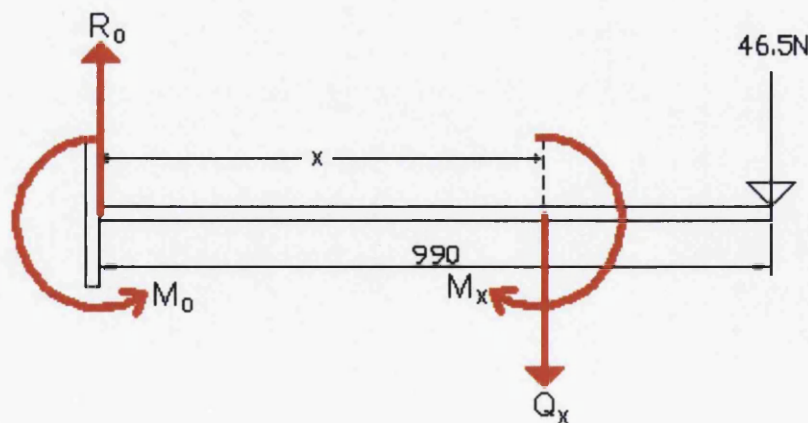
Figure 2.39. Cantilever beam moments & forces

42

Consider the illustration above; the red arrows represent the reaction forces that allow the beam to be in equilibrium. From this diagram it is clear that:

$$R_o = 46.5N$$

$$M_0 = 0.99 \times 46.5 = 46.035 \text{N·m}$$

Taking moments about a point at distance x away from the support, then it is true that:

$$M_0 = M_X + R_0{\cdot}x$$

$$M_X = M_O - R_0{\cdot}x$$

$$M_X = 46.035 - 46.5{\cdot}x$$

Applying bending equation and double integration:

$$E.I\frac{d^2V}{dx^2} = -M_X$$

$$E.I\frac{d^2V}{dx^2} = -46.035 + 46.5x$$

$$E.I\frac{dV}{dx} = -46.035x + \frac{46.5x^2}{2} + C_1$$

$$E.I.V = \frac{-46.035x^2}{2} + \frac{46.5x^3}{6} + C_1 \cdot x + C_2$$

Applying boundary conditions, it can be proven that where x = 0, V = 0 – and therefore dV/dx = 0. Applying these conditions to the appropriate equations above proves that the constants are equal to 0. The second moment of area was calculated earlier as 5.4×10^{-9} m^4. If the cantilever was made of a HSLA steel with a young's modulus of 208Gpa, since all the variables are now defined, we can calculate the deflection (V):

$$V = \frac{1}{(208 \times 10^9) \times (5.4 \times 10^{-9})} \left\{ \frac{-46.035 \times 0.99^2}{2} + \frac{46.5 \times 0.99^3}{6} \right\} = -13.6mm$$

Note that the negative value for deflection indicates that the beam is deflected downwards. These two results for stress and deflection can be used to verify the accuracy of predictions made by FE models. This type of approach help ensure correct data is fed into the model and meshing is appropriate for the component being analysed.

2.4 Causes of variability in steel strip

There are several causes for variability in steel supplied for these components, and even more sources of variability in manufactured components. Variability in strip steel can be due to a chemistry which is not exactly as specified for that particular grade, as well as a non-homogenous chemistry within a batch due to insufficient dispersion of alloying elements during stirring in the secondary steelmaking process [29]. Chemistry problems can also occur when using scrap of unknown origin, scrap metal may contain high levels of tramp elements such as Tin, Copper, Arsenic, Antimony and many others which cannot be removed during steelmaking [30, 31].

There are also several thermo-mechanical processing parameters such as rolling temperature, force, speed, tension between rollers as well as cooling parameters that affect the microstructure and mechanical properties of the material. All these factors have some effect on the supplied strip product, and as such there is often a wide range of mechanical properties for a single grade of steel. The distribution of the statistical variation in these properties may have some pattern, and identifying these patterns is essential in order to design robust new products.

It is highly likely that the factors that affect the mechanical properties of strip steel will also have a direct effect on the fatigue performance of the steel coils. The reason for this presumption lies with the documented correlation that exists between fatigue and mechanical properties [32]. If a correlation can be established and quantified between both these properties for the steel grades under investigation, then the range of fatigue performance can be assessed in a cost-effective manner.

Studying the statistical distribution in the mechanical properties of TSSP-UK products and extrapolating predicted fatigue performance from this data could be one possible method of quantifying such variability. Fatigue testing is an expensive and time consuming process, and as such testing thousands of samples would not be viable. Tensile tests are quick and inexpensive by comparison and as such a relationship between the two would be beneficial for this project.

Grouping and displaying variability data requires careful consideration, as the following questions need to be answered, such as: "Can all gauges of the same grade of steel be grouped together? Does gauge variability depend on the gauge and/or grade being rolled? Does the position within the coil influence mechanical properties?". There are also numerous other factors to consider before grouping data. Traditionally it is generally accepted that the coil end will be harder, stronger and less ductile than the middle of the coil.

This is due to the greater cooling rate applied to this section as it is not surrounded by as much hot material as the centre once coiled up. Aichbhaumik's [33] results did not follow this trend, although the number of samples tested was low. Surprisingly the results also showed that fatigue results for the steel grade tested (not too dissimilar to Tenform grades) was very insensitive to variability of other factors such as chemistry, gauge, etc.

There is some data to suggest that producing data on the variability in gauge is a more straight forward affair. Wang et. al. [34] stated that the extent of variability in the gauge of steel piping is directly proportional to the outside diameter of the pipe, thus standard deviations can be expressed in terms of percentages, and can be used to account for all diameters of tubes instead of standard deviations being described in millimetres and graphs having to be made for every diameter in production.

If a similar scenario is true for strip products then one graph should be able to account for the variability in gauge of all gauges of a particular grade. Taken one step further it needs to be established whether or not it is possible to include more than one grade of steel under the same graphical representation. If so it would be a huge benefit as the graph produced will be constructed from a large amount of data which is always beneficial when dealing with statistical scatter.

An area where grouping is likely to prove difficult is analyzing the strength (UTS and yield) of various gauges of the same grade. During quenching the outer part of the material will always cool more rapidly than the inner part, with very thin gauges the cooling rate is virtually homogenous throughout the whole cross-section. Unfortunately with thicker gauges the material in the centre of the cross-section

45

experiences a lower cooling rate and hence will have a larger grain size and be softer and weaker than the outer most material.

Through integration of basic principles, the distribution of temperature within a workpiece can be described by the following equation [35]:

$$T(x) = T_1 + \left(\frac{T_2 - T_1}{L} \right) x$$

Where:

T(x) = temperature along any point

T_1 = temperature in the centre of the material (in this case)

T_2 = temperature on outside of material

L = the half gauge of the material (in this case)

x = given length of a point along the cross section from centre to outer edge
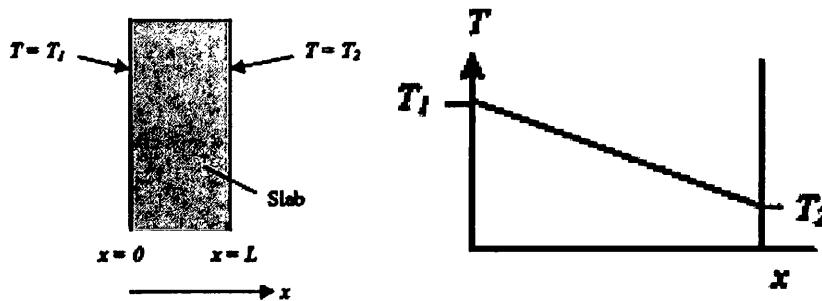
Figure 2.40. Temperature gradient within a material

Thus from the above equation and the diagrams in figure 2.40 we can see that the temperature within the strip product will be far from homogenous and this theory accounts for softer centres within coils of thick gauges. The rate of heat transfer can also be described by a version of Fourier's Law [36], which is adapted to suit these boundary conditions, shown below:

$$\frac{\Delta Q}{\Delta t} = \frac{-kA(T_1 - T_2)}{L}$$

So we see any changes in strip thickness will not have an effect on the heat transfer rate ($\Delta Q / \Delta t$), as changes in L will be offset by the same fractional change in area. Although since there is more heat to remove with thicker material, which will be directly proportional to thickness, and the teat transfer rate is fixed, then the following equation relationship is true:

46

$$\text{Cooling Rate } (°C·s^{-1}) \propto \frac{1}{\text{Thickness}}$$

This raises complications in terms of controlling variability and grouping variability data. Mechanical properties can be heavily dependent on cooling rate, thus an inherent amount of variability will exist due to intentional changes in gauge, unless of course a sophisticated control mechanism for cooling is used.

Since thick gauges that have been under the same processing conditions as thinner gauges tend to have decreased strength, it may be the case that a separate analysis has to be carried out for each gauge manufactured. Once the extent of softening due to the increase in gauge is known, a decision can be made – possibly by grouping several gauges such as 1mm-3mm, 3mm-5mm etc.

Reduction of Yield Strength & UTS as the gauge increases can be seen in figure 2.41, albeit for plate of considerable thickness, and not the types of gauges that are considered for automotive structures. The source of this information, [37] did not unveil the manufacturer of the steel studied, though the amount of variability is quite large, and not many samples were close to the lower specified limit of 490MPa for the UTS. Should this variability resemble TSSP-UK's tenform grades it would allow considerable room for improvement for robustly designing new components with the variability data acquired.
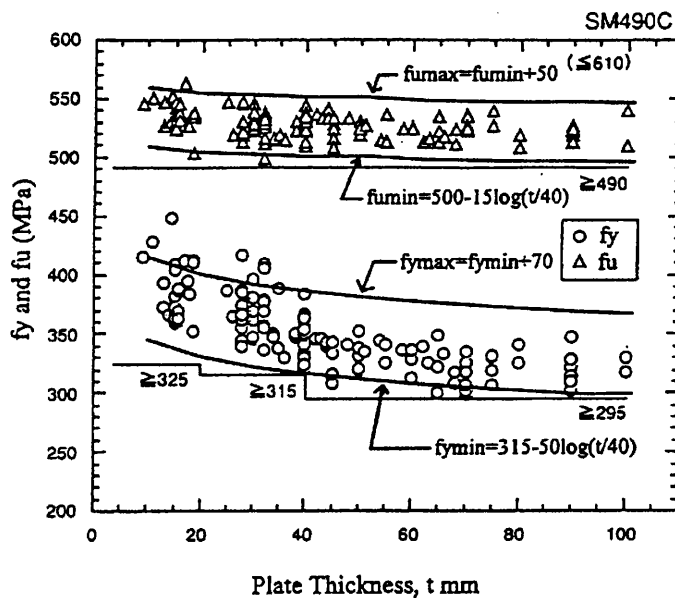
Figure 2.41. Yield strength & UTS variability dependant on plate thickness

47

2.5 Designing robust & reliable structures

In order to design structural components successfully and achieve a reliable product it is paramount that all variables such as material, manufacturing and design, as well as operating condition variations are taken into consideration. Historically, component safety factors are derived from the expected structural performance divided by the expected operating conditions, as illustrated by the graph in figure 2.42 [38].

Unfortunately the expected performance will always have a certain amount of variability, and so will the operating conditions. This is an especially important consideration for automotive chassis components, since some drivers are careful and some drive recklessly. If the standard deviations for these two variables are large then the two curves shown in figure 2.42 could overlap, giving rise to failure. Therefore a significant safety factor does not necessarily mean that there will be no failures unless all variables are considered carefully.
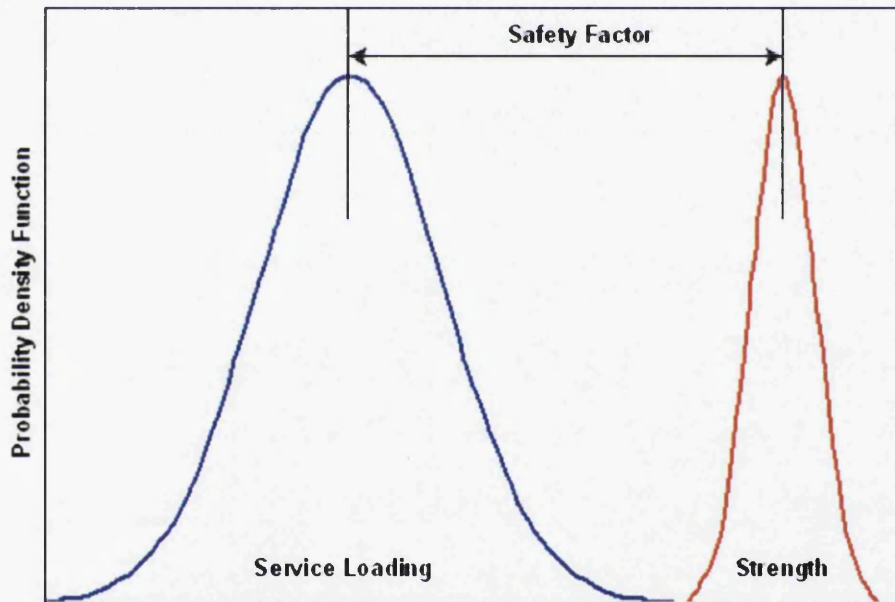
Figure 2.42. Typical method for calculating safety factors

Defining the operating conditions is more complicated than defining the variability in component performance. It is possible to calculate "worst case scenarios" for normal driving, such as hard cornering, braking, etc., though these calculations themselves do not account for the possible abusive worst case scenarios the vehicle

could encounter. Manufacturers commonly define other severe loads, such as 1g pothole braking (PHB) performed by Jaguar Land Rover [38] i.e. an acceleration of -9.81m.s^{-2} over an uneven surface. Abuse of a vehicle from loadings like these are hard to quantify, and it is even harder to define what is acceptable and how many loadings such as these a component should be able to withstand.

Thomas [39] described a method used by Peugeot Citroen (PSA) to define the service conditions expected from an automotive chassis. This system is based on two fictional owners, both of who use their cars differently in terms of time spent on different types of road and vehicle load (passengers, luggage etc.). Figure 2.43 shows how the loading conditions are defined as h_{jkl}, where j, k and l represent the identification of the driver, the load state and the road type respectively. The collection of matrices can be used to define a great portion of expected loading conditions for a future vehicle.

table 1 : Car usage description for two owners

|	Owner (j)	1	2
% kilometers without load		27	15
elementary %	Motorway	10	25
	Good road	25	12
	Mountain	40	50
	City	25	13
% kilometers with half load		58	35
elementary %	Motorway	5	16
	Good road	30	24
	Mountain	30	40
	City	35	20
% kilometers full load		15	60
elementary %	Motorway	15	18
	Good road	25	42
	Mountain	40	10
	City	20	30

table 2 : Owner behaviour with different car usage

	Usage U$_1$ Road % for total kilometers	Usage U$_2$ Road % for total kilometers
Load state 1 (without load)	27	15
% Motorway	[h$_{11A}$]	[h$_{21A}$]
% Good road	[h$_{11R}$]	[h$_{21R}$]
% Mountain	[h$_{11M}$]	[h$_{21M}$]
% City	[h$_{11V}$]	[h$_{21V}$]
Load state 2 (half load)	58	35
% Motorway	[h$_{12A}$]	[h$_{22A}$]
% Good road	[h$_{12R}$]	[h$_{22R}$]
% Mountain	[h$_{12M}$]	[h$_{22M}$]
% City	[h$_{12V}$]	[h$_{22V}$]
Load state 3 (full load)	15	60
% Motorway	[h$_{13A}$]	[h$_{23A}$]
% Good road	[h$_{13R}$]	[h$_{23R}$]
% Mountain	[h$_{13M}$]	[h$_{23M}$]
% City	[h$_{13V}$]	[h$_{23V}$]

Fig. 2.43. Vehicle service loading

So for a simulation of owner 1 behaving like U$_1$ the full matrix would be:

$$H_{11} = N \; (([h_{11A}] \times 0.27 \times 0.1) + ([h_{11R}] \times 0.27 \times 0.25) + ([h_{11M}] \times 0.27 \times 0.4)$$
$$+ ([h_{11V}] \times 0.27 \times 0.25) + (+ \text{ other terms associated with half load and full load}))$$

(Where N is the total mileage the owner will do across the lifetime of the vehicle)

Note that the equation above accounts for all terms associated with the no load fraction that owner 1 drives, which is 27% of total driving time. The complete term will include a further 8 bracketed terms for half and full load. Therefore with the 24 different matrices that are available, the total number of bracketed terms to cover all simulations will be $4 \times 12 = 48$.

Thomas claims that this loading matrix corresponds to up to an equivalent of 50,000 virtual owners, and the combined service loading for this matrix does indeed correspond to a standard distribution curve as shown in figure 2.44.
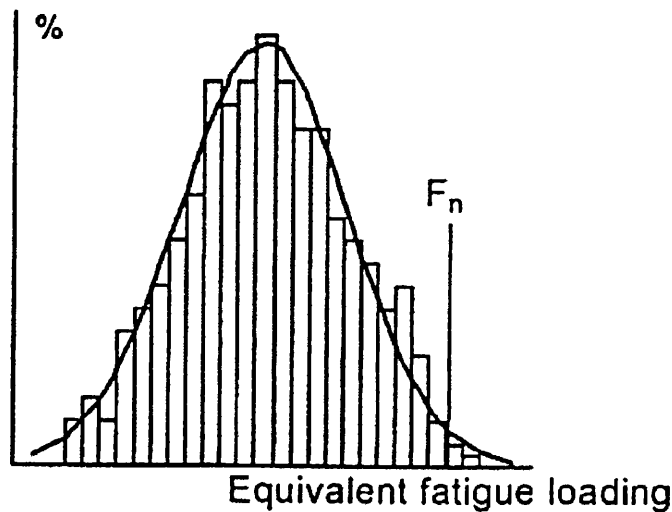
Figure 2.44. Equivalent loading for matrix

F_n represents a 1/50000 possibility of an owner exceeding that particular in service loading condition. Engineers can then decide whether any overlap with both tail ends of the normal distribution curves (loading and component performance) is acceptable, as it is possible to work out what the possibility of an extreme driver being paired with a "poor" vehicle component is. Data such as this can also be used to perform testing on prototypes which is similar to real world conditions, instead of standard sine, square wave or other types inputs used in regular fatigue tests.

Johanssen [40] used measured signals and extrapolated the worst or most demanding section of the data to perform fatigue tests, this is shown in figure 2.45. If the data collected and extrapolated represents the real worst case scenario well, then the fatigue tests performed using this technique can prove a powerful tool in analyzing structural performance.
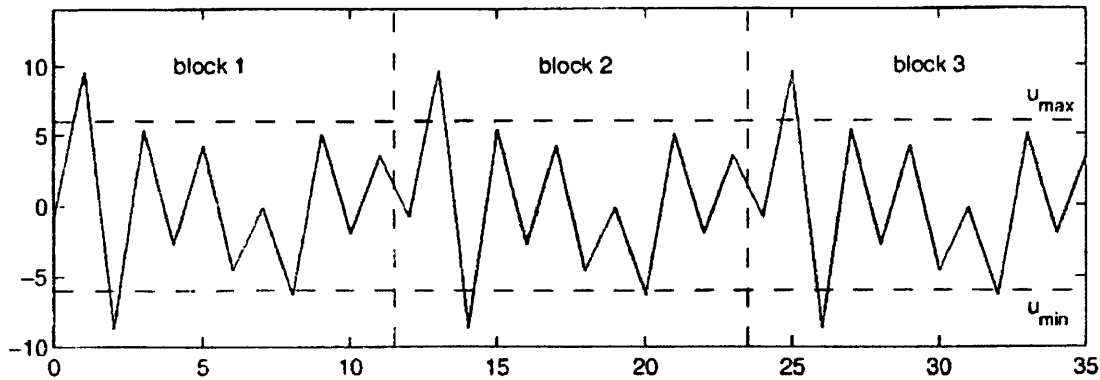
Figure 2.45. Extrapolated loading

Other attempts aimed at improving reliability are also focussed on understanding the "field situation". Klyatis [41] describes this as the first step towards improving performance, this is illustrated by the diagram below:
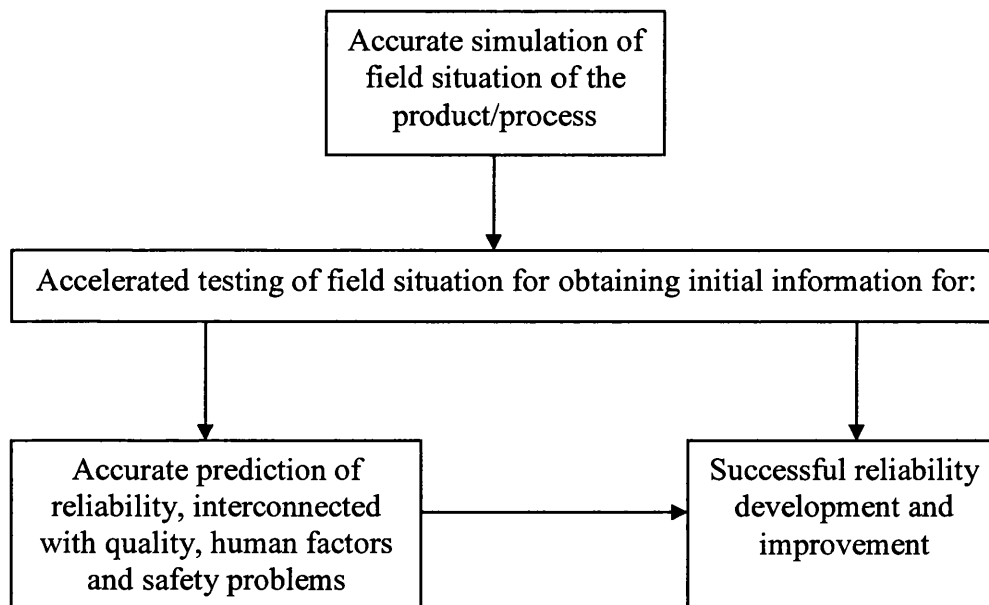
Figure 2.46. Interconnected links for prediction of field reliability and successful reliability development and improvement.

Just as Thomas stated, developing an understanding of the variables is of paramount importance, where the variability of manufactured components are defined by human factors and quality (shown in figure 2.46). The variability in service loading due to different users etc. is described in the first box on the top.

Perhaps the most complete flowchart illustrating one possible modern design process for structural components is the work of Stephens et al. [15], shown in figure 2.47. This model defines all variables that are of interest when designing automotive

51

chassis and suspension components and outlines the process engineers may use to account for such variables in order to design a component that is both robust and reliable.
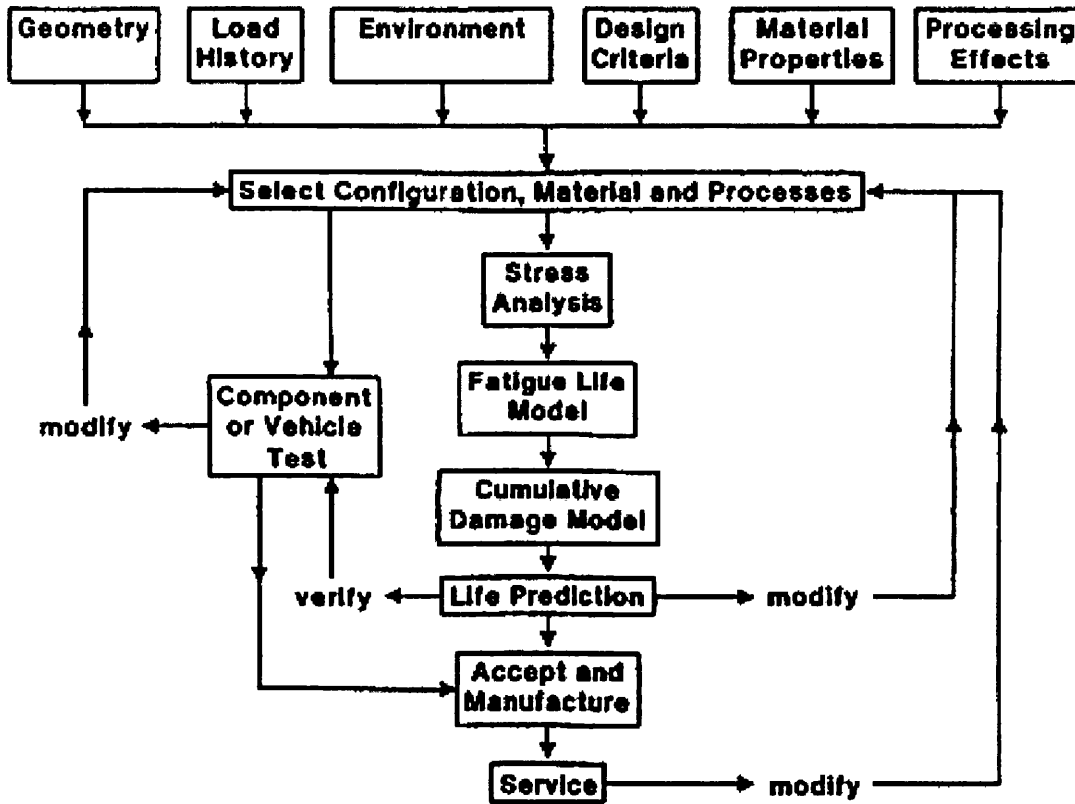
Figure 2.47. Stephens model for developing robust designs

Many of the principles discussed in this chapter regarding robust design are also the principles of the six sigma design approach [42]. The core aspects of 6σ practice are the DMAIC continuous improvement cycle for existing products and DMADV for new products. An explanation of these two acronyms are described by Pyzdec [43] in tables 2.3 & 2.4. The differences between each of these two processes are highlighted in the flow chart in figure 2.47.

Table 2.3. DMADV process

D	**Define** the goals of the design activity.
M	**Measure** customer input to determine what is critical to quality from the customers' perspective. Use special methods when a completely new product or service is being designed. Translate customer requirements into project goals.
A	**Analyse** innovative concepts for products and services to create value for the customer. Determine performance of similar best-in-class designs.
D	**Design** new processes, products and services to deliver customer value. Use predictive models, simulation, prototypes, pilot runs, etc. to validate the design concept's effectiveness in meeting goals.
V	**Verify** that new systems perform as expected. Create mechanisms to ensure continued optimal performance.

Table 2.4. DMAIC process

D	**Define** the goals of the improvement activity, and incorporate into a project charter. Obtain sponsorship and assemble a team.
M	**Measure** the existing system. Establish valid and reliable metrics to help monitor progress toward the goal(s) defined at the previous step. Establish current process baseline performance using metric.
A	**Analyse** the system to identify ways to eliminate the gap between the current performance of the system or process and the desired goal. Use exploratory and descriptive data.
I	**Improve** the system. Be creative in finding new ways to do things better, cheaper or faster. Use project management tools to implement the new approach. Use statistical methods to validate the improvement.
C	**Control** the new system. Institutionalise the improved system by modifying compensation and incentive systems, policies, procedures, MRP (Material Requirements Planning), budgets, operating instructions and other management systems. You may wish to utilise standardisation such as ISO 9000 to ensure that documentation is correct. Use statistical tools to monitor stability of the new systems.

In lean six sigma design, as with all robust design approaches, the foundations for achieving the desired level of reliability & robustness lie with developing an accurate understanding of the demands on the product and the manufacturing process. Both these factors are always subject to variability, where Yang [42] illustrated that the overall variability of a product may be a sum of numerous variables, as shown in figure 2.48. It would not be practical to outline all theories relating to the six sigma design approach within the context of this literature survey. However, an understanding of the statistical tools mentioned earlier as well as knowledge of the DMAIC and DMADV design approaches serves as a good foundation for understanding the fundamental principles of six sigma philosophy.

DMAIC versus DMADV
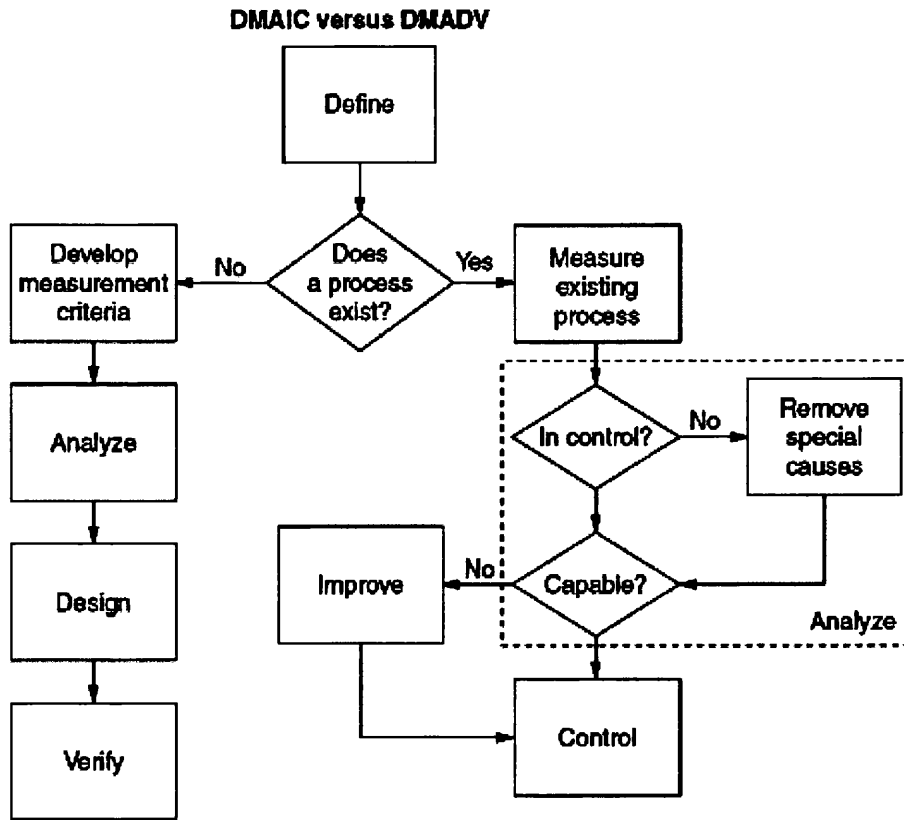
Figure 2.48. DMAIC & DMADV process optimisation flowchart

Inputs   Outputs
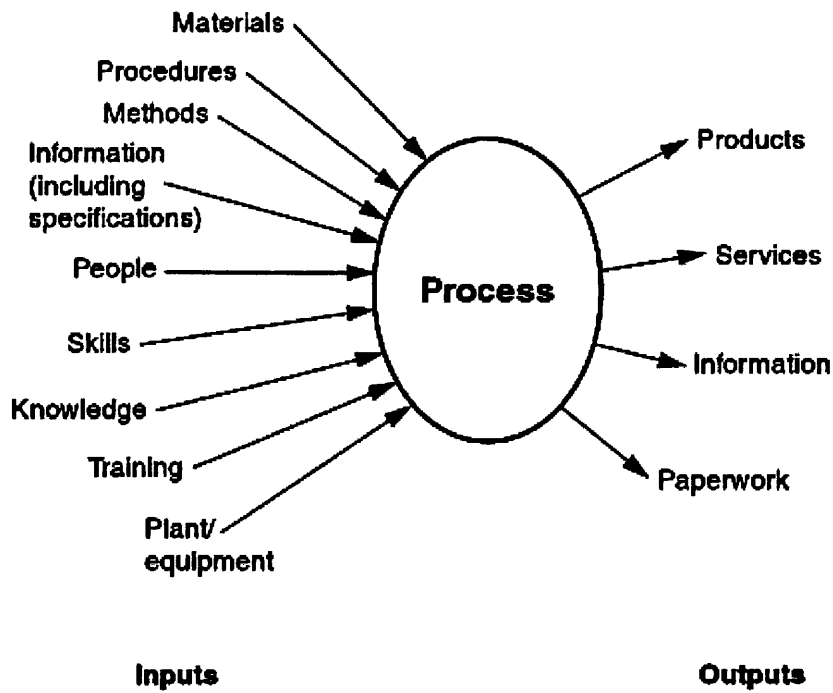
Figure 2.49. Contributors to process variability

54

Another important consideration is that many factors relating to reliability are interrelated, Smith [44] stated: "It is improper to base a design solely on mechanical factors, or environmental factors without considering the fact that they are interrelated. The key to reliability is the understanding of this interdependency combined with the availability of applicable data on which to base decisions". But even though we have to live with the fact that there will always be variability in material properties, it is not to say that the effects of those variations cannot be minimised in the final product.

Hence another one of Smith's quotations: "Material is Key: There are however, ways to reduce the variability resulting from both stresses and environment. For example, welding techniques that produce less severe residual stress patterns can be selected, grinding on surfaces can be minimized, fabrication tolerances can be tightened, high stress lines can be redesigned or rerouted and operational procedures can be changed". Some of these factors have already been discussed in previous chapters, where improving fatigue performance instantly improves the reliability rate of components.

Robust design differs from reliable design as products must not only be able to withstand the rigours of everyday use but also the design must be optimised to reduce weight, variability and cost. Optimizing components according to Parkinson [45] "requires the determination, or choice, of a set of parameters which renders measures of design performances insensitive to such variability" where "for a given design point the variability in actual values gives rise to global maximum and minimum values of the output variable".

The key concept is that variation in random parameters and design variables have to be transferred into performance functions. Thus once again accurately determining the service conditions and the variability in manufacturing processes is key. This is based upon the theory that the performance of a product is a function of many input variables:

$$f(X) = f(x_1 + x_2 + ... x_n)$$

Where x = input variables and f(x) is the overall performance

If each value for x has a nominal value, $\bar{x}_n$, and each is susceptible to a lower and upper specified limit, l_n and u_n, then the following is true:

$$\bar{x}_n - l_n \leq x_n \leq \bar{x}_n + u_n$$

Robust design is essentially using mathematical tools to optimize these variables. Zhang et. al. [46] used robust design principles and identified the variables with the highest sensitivity to overall performance to reverse engineer a current design automotive front side rail. The results showed a 29.96% reduction in the mass of the structure shown in figure 2.50.

Figure 2.50. CAD model of robustly optimized structure

Kumar et. al. [47] used Bayesian Monte Carlo methods to robustly design a compressor blade under manufacturing uncertainty. The flow chart in figure 2.51 illustrates the technique used.
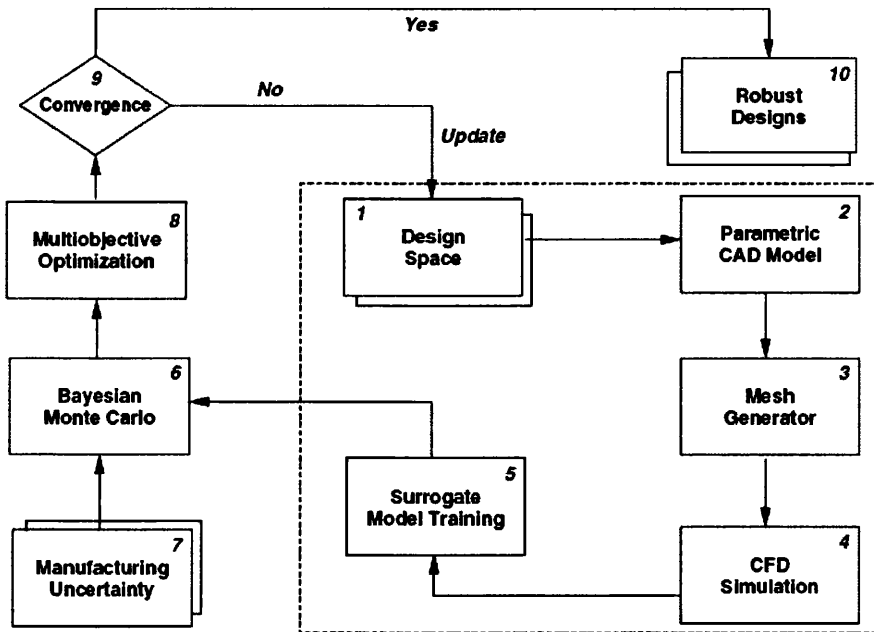
Figure 2.51. Monte Carlo optimization flow chart

Although this model was used for the development of a compressor blade, the theory used here could easily be adapted for other structural applications. Where essentially within the dashed box a FE CAD model would be used to analyse the structural performance, the overall performance would have a range of outcomes depending on the extent of manufacturing/material uncertainty. If there is no convergence in the results obtained, new tests will be carried out with new design variables – this is a cyclic procedure until convergence is achieved. Kumar called the design variables control factors, while unwanted variables such as manufacturing uncertainty are classified noise factors, the range of each control factor needs to be predetermined prior to running the simulation.

Hsu et.al. [48] described the design and noise variables in an experiment to robustly design a vehicle to withstand a side impact. Note that some variables are both design variables (DV) and noise Variables (NV). Each variable is then given a lower and an upper limit as well as a base value, which can be seen in Tables 2.5 & 2.6. The Six Sigma CAE package is then programmed to experiment and search for the optimum value for each of these variables within the specified limits.

Table 2.5. Example of design and random variables

#	DV	RV	Name of Parameter	Description of Parameter
1	●		SideSill_Thk	Thickness of side sill reinforced beam
2	●		ImpactBar_thk	Thickness of impact beam
3	●		Armrest_thk	Thickness of door-trim armrest
4	●	●	ChestPad_SFO	Material property of chest pad
5	●	●	PelvisPad_SFO	Material property of pelvis pad
6	●	●	Vendhole_Size	Vent hole size of airbag
7		●	Inflator_SFO	Pressure of inflator
8		●	AirbagTTF_Offa	Time-to-fire of airbag
9		●	Dummy_PosLong	Dummy position in direction of rear-front
10		●	Dummy_PosVert	Dummy position in direction of up-down
11		●	Barrier_Dz	Crash height of barrier
12		●	Barrier_Initial_Vel	Initial speed of barrier

Table 2.6. Setting limits for Monte Carlo simulation

#	Parameter Name	Lower Boundary	Base Value	Upper Boundary
1	SideSill_Thk	0.745	1.0	1.66
2	ImpactBar_thk	0.75	1.0	1.25
3	Armrest_thk	0.75	1.0	1.25
4	ChestPad_SFO	0.4	1.0	2.1
5	PelvisPad_SFO	0.4	1.0	2.1
6	Vendhole_Size	0.75	1.0	1.25
7	Inflator_SFO	0.90	1.0	1.10
8	AirbagTTF_Offa	-1ms	0	+1ms
9	Dummy_PosLong	-15mm	0	+15mm
10	Dummy_PosVert	-15mm	0	+15mm
11	Barrier_Dz	-25mm	0	+25mm
12	Barrier_Initial_Vel	0.99	1.00	1.01

In essence this is a progression from the Taguchi method, where experiments were physically carried out with typically only a high and a low value for each variable, i.e. if there were 3 variables you would require $2^3 = 8$ experiments for full representation. The '2' value represents the number of values per variable i.e. a high and a low in this case, and the '3' value represents the number of variables. To reduce the number of experiments it is possible to use a $2^{3-1} = 4$, which is termed an L4 array. Once the results are gathered the signal to noise ratio is often calculated to see which variable has the most significant effect. The signal to noise ratio is given by:

$$Z = -10 Log \left(\frac{\sum_{i=1}^{n} 1/y^2}{n} \right)$$

An example of this type of process optimization is a set of experiments by George et. al. [23], which was used to determine optimum shot peening parameters. Georges' experimental design table is shown below, where a '1' illustrates a low value for a given variable and a '2' illustrates a high value.

Table 2.7. Design of Experiments for Taguchi technique

Trial No.	Exposure Time t (min)	Work Height h (mm)	Shot Size d (mm)	Flow Rate Q (kg/min)
1	1	1	1	1
2	1	1	1	2
3	1	2	2	1
4	1	2	2	2
5	2	1	2	1
6	2	1	2	2
7	2	2	1	1
8	2	2	1	2

Note that this is not a full array as a full array with four variables would have $2^4 = 16$ experiments. This illustrates a $2^{3-1} = 8$ experimental lay out, a design that will lose some accuracy but reduce the number of experiments required by half.

The methods discussed in this review outline many statistical tools illustrating how to analyze variability data associated with tensile strength, elongation, fatigue and other factors. Gathering and processing this data is of paramount importance in order to achieve the final target – to use variability data to robustly design new products. In order to achieve this, other data such as loading conditions as well as manufacturing conditions need to be accurately defined. As mentioned, there will be statistical scatter associated with all input variables, that is for both design and noise variables.

As well as defining variables, developing methods of minimising variability in manufactured components to ensure a better overall product with increased performance is also of significant importance. Any method employed will have to be verified by physical experimentation to ensure confidence.

Another method of improving the robustness of a design is through the use of Tailor Welded Blanks (TWB), a fairly recently adopted technique used to optimise structural components. These can be described as [49] "steel sheets of different thickness and grades laser welded into a single flat blank prior to pressing to achieve

the optimal material arrangement and weight reduction for cars, and to increase process efficiency and machine flexibility".

By using TWB's, Fourlaris [50] was able to reduce the mass of a lower control arm by 19% whilst maintaining equal fatigue performance. This was done by substituting sections of mild steel for dual phase steel and testing using CARLOS (CAR Loading Standard) multi [51, 52], which is a load-time history file jointly created by 16 European automotive manufacturers. This file gives engineers the necesarry data to evaluate if a particular design can withstand the loads expected of it.

Once all possible factors that affect the design, operation and performance of a product are defined, and new methods of minimising variability are identified and verified it will then be necessary to use this information to robustly engineer a chassis component. This could be done using CAE packages or by physical experimentation via Taguchi methods outlined earlier. These ideas are based on identifying the sensitivity of the final product to each input variable to establish optimum values for each design input.

Chapter 3 – Tensile and Fatigue Specimen Geometry

3.1 Tensile testing standards & general considerations

Before analysing any of the data contained within this project, it was noticed that a wide range of specimen geometries for fatigue and tensile specimens existed. Despite the fact that the geometry of tensile samples has to comply with ISO standards, upon investigation it was found that the ISO standards only have definitions for certain aspects of the coupon geometry, where the rest is left to the tester's discretion. For fatigue specimens, researchers often use their own design of test piece that they may find compatible with their own test equipment. This is widely accepted as many papers in the field include the geometry of the specimens in the finished publications. Due to the wide range of designs of both tensile and fatigue specimen geometries in existence, research was carried out to establish what effect various geometries have on the results obtained during material testing.

Within TSSP-UK, one tensile test is performed to characterise a whole coil of a Tenform product. As of late 2009 tests are performed in accordance with BS EN ISO 6892-1:2009, before then tests were carried out to BS EN 10002-1:2001 specifications. Within both these standards the exact geometry of the test specimen is largely up to the individual/organisation performing the tests. TSSP-UK uses 80mm extensometers, therefore in accordance with the most recent standard, the geometry of the test piece must comply with the following:
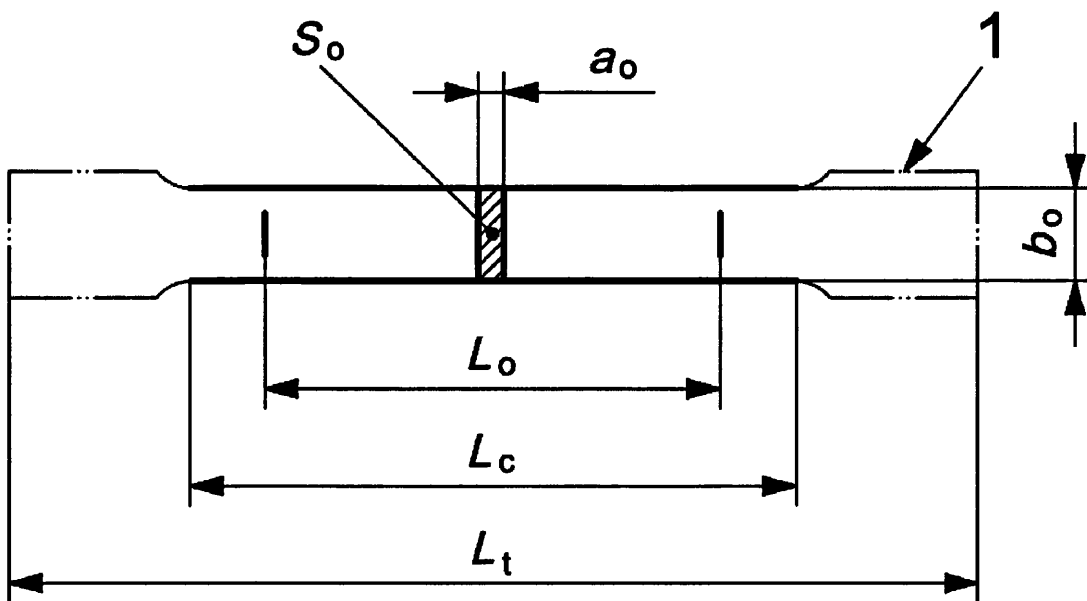

Figure 3.1. BS EN ISO 6892-1:2009 Specimen Geometry.

a_o Original thickness of a flat test piece

b_o Original width of the parallel length of a flat test piece (=20mm±1mm)

L_c Parallel length (90mm min, 120mm recommended)

L_o Original gauge length (80mm)

L_t Total length of test piece (=350mm – for CSPUK HR products)

S_o Original cross-sectional area of the parallel length

1   Gripped ends

The shape of the test piece heads is only given as a guide, some of the constraints are due to the relevant standard, while others (350mm total length & 80mm gauge length) are due to the testing equipment used. Therefore there is a lot of freedom within these constraints to decide upon the best dimensions. For all results documented in Chapter 4, the geometry of the test pieces were as shown in figure 3.2.
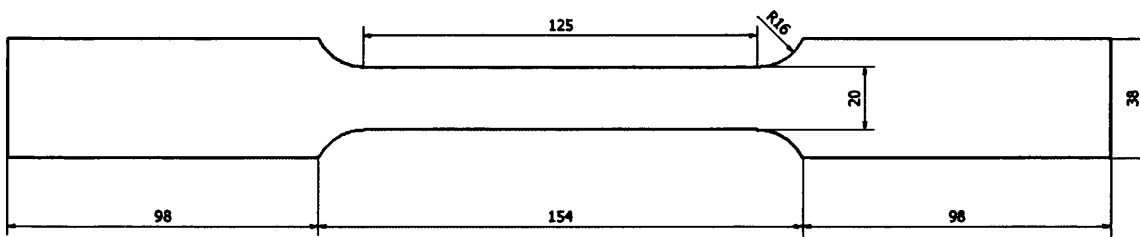
Figure 3.2. TSSP-UK HR Specimen.

Since there is a large amount of discrepancy between tensile geometry, it was deemed necessary to determine if the shape of the tensile sample had any effect on the mechanical properties obtained. This was done by physically testing specimens with different geometries as well as using FE to verify and assess the accuracy of the software, which would be critical for later use in this project.

3.2 Finite element analysis of tensile specimens

From the drawing in figure 2 it is evident that for a 3mm thick specimen of XF350 to reach its UTS of around 430MPa, the sample requires a force of:

$$\sigma = \frac{F}{A}$$

$$F = \sigma A$$

$$F = \left(430 \times 10^6\right) \times \left((20 \times 10^{-3}) \times (3 \times 10^{-3})\right)$$

$$F = 25800 N$$

Applying this load to a model of the specimen in ANSYS did give a stress of around 430MPa in the 20mm parallel region, though it indicated a stress concentration of around 20% at the base of the radius. This can be seen in figure 3.3. This study therefore suggests that due to the stress concentration, failure may also occur around this area, though this may not be the case as the stress concentrated area is quite small and failure during tensile testing does not always occur at the area of highest stress.

In order to see if a larger radius would reduce the degree of stress concentration, a sample with a radius of 70mm, but with otherwise identical geometry was created and modelled. The results in figure 3.4 show a greatly reduced stress – though a stress concentration still exists at the base of the fillet radius. The maximum stress is reduced to 447MPa instead of 515MPa. Even though the stress concentration is greatly reduced, it remains to be seen whether the geometry it has any real effect on results obtained during physical testing.
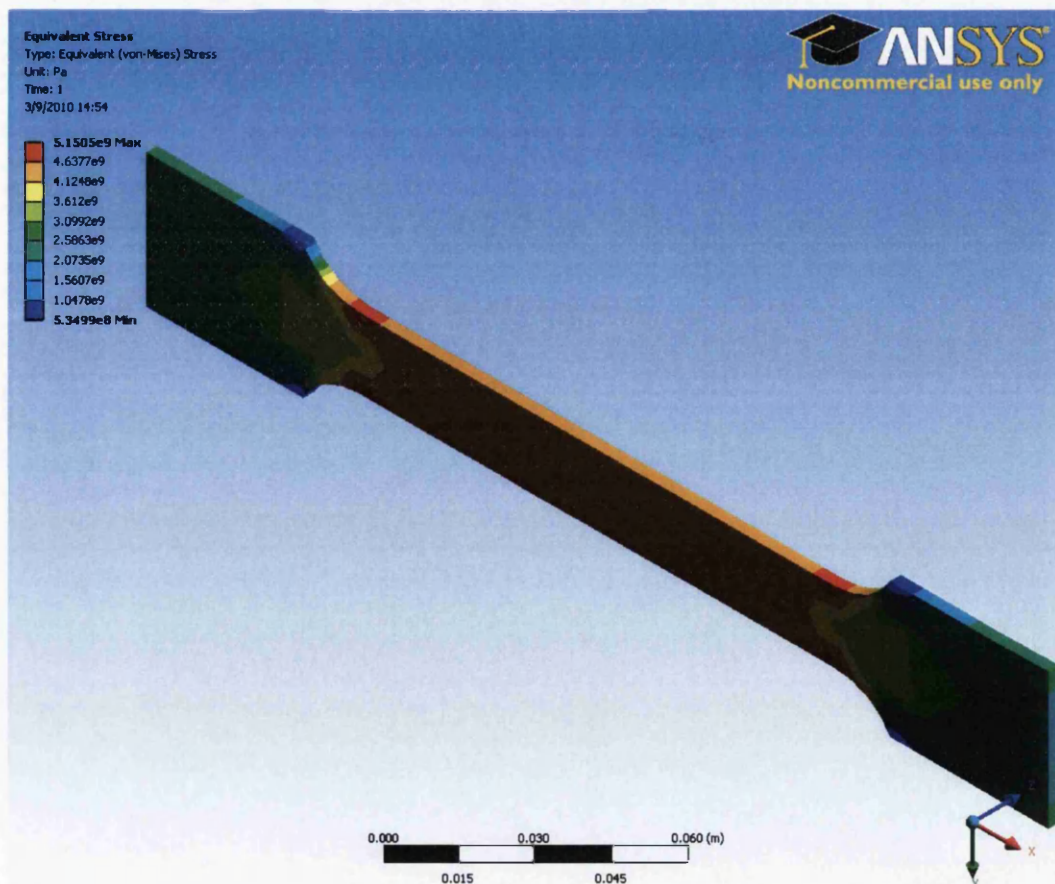
Figure 3.3. 25800N Tensile Test.

The distribution of stress is much more uniform in figure 4 and shows only a 4% stress concentration at the base of the fillet – a huge reduction over the previous design. Deciding upon tensile test geometry cannot be purely academic, and although a stress concentration exists in the first sample that does not mean that it will yield any different results from those of the modified geometry. Much can be learned from analysis of these results, as well as physical testing to analyse failure modes and help predict failures in more complex components later on in this project.
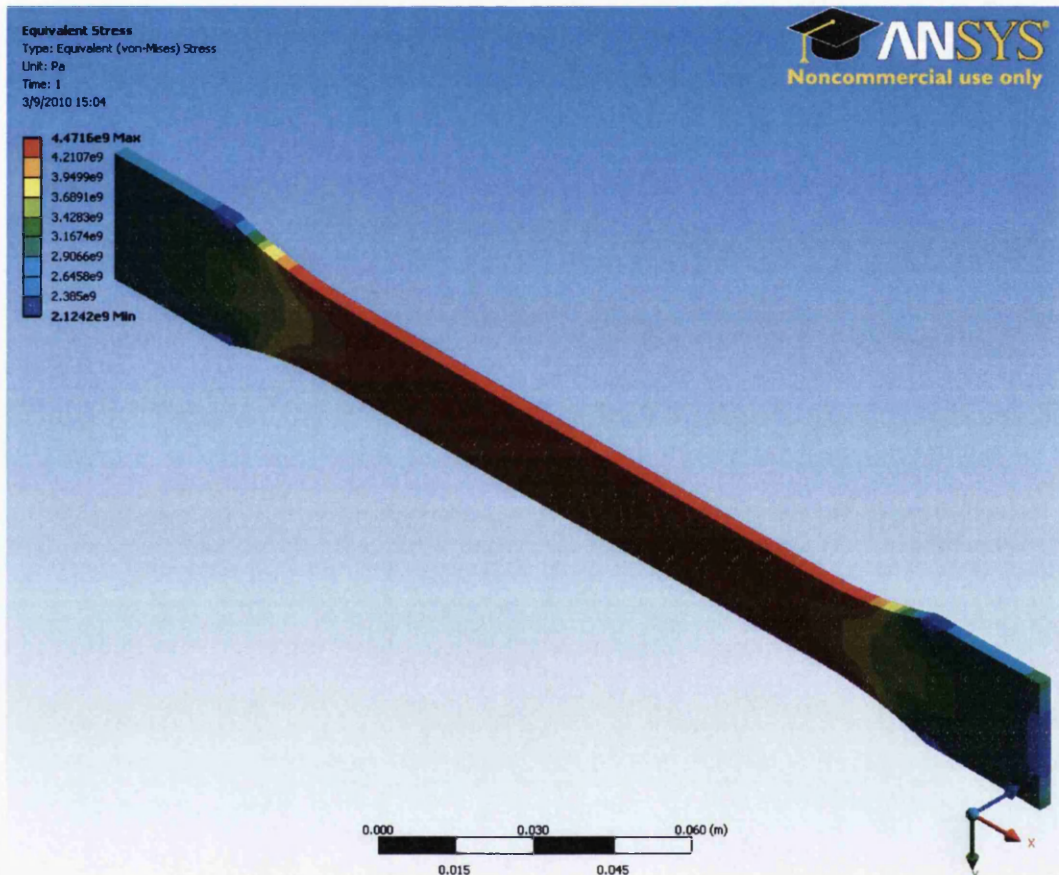
Figure 3.4. 25800N Tensile Test – 70mm Radius.

3.3 Physical testing to determine validity of FE model

It was decided that testing should be carried out at ECM^2 by Testing Solutions Wales, instead of using TSSP-UK's in-house test facility where testing may disrupt production. The only problem being that the tensile tester at this facility can only accommodate a 240mm long sample, although this is not a huge problem as much of the geometry could stay the same as the original sample by reducing only the length of the gripped ends from 98mm to 43mm, thus giving a 240mm test piece with identical critical geometry.

It was determined that the gripped ends only needed to be 30mm long to ensure a good contact, thus a larger radius of 80mm compared to 16mm could be used whilst still maintaining a similar length of around 125mm for the parallel middle section. An even larger radius could be utilised, as BS EN ISO 6892-1:2009 states that this dimension only needs to be 90mm minimum, though it is recommended that it be 120mm min. The extensometer used to measure strain is 80mm long, so a 125mm parallel length gives a good tolerance either side. A technical drawing of the test pieces are shown in figure 3.5.
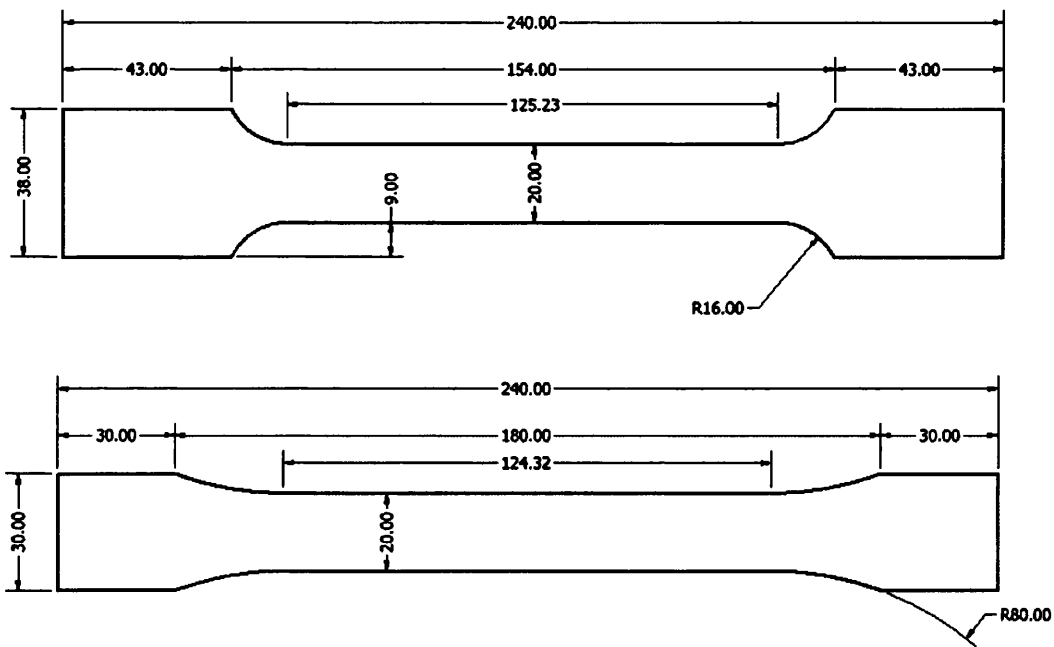
Figure 3.5. Tensile Test Specimens.

Three specimens of each type were machined and tested from one sheet, the yield, UTS and elongation results for each sample are shown in the table below:

Table 3.1. S355MC Tensile Results

	16mm Raduis #1	16mm Raduis #2	16mm Raduis #3	80mm Raduis #1	80mm Raduis #2	80mm Raduis #3
Yield (MPa)	382.67	380.11	376.92	379.18	382.29	381.03
UTS (MPa)	469.21	468.18	465.03	470.41	469.36	468.36
Elongation (%)	26.13	29.43	29.17	27.94	30.18	28.34

It can be clearly seen that results are similar regardless of geometry. Thus the stress concentration zone shown in figure 3 is not large enough to have any effect on the tensile test data. This is echoed by the images in figure 3.6, showing that all specimens failed in the centre i.e. not at the stress concentrated zone. This may be due to the fact that during tensile testing we are obviously exceeding the yield point of the material, thus thinning of the centre occurs and as the cross sectional area is reduced in the middle of the specimen the stress continues to increase and yet more thinning occurs. These results are important as the lessons learned here need to be transferred and studied in later chapters, especially when predicting failure due to fatigue etc. and analysing life of components.

Figure 3.6. Failed S355MC tensile specimens

With harder, more brittle material with lower elongation it is more likely that failure will occur at the stress concentrated regions, where less thinning occurs and thus the material fails at the point that the stress is greatest. Such an example is shown in figure 3.7, which is DP800GI, this specimen had a UTS at the higher end of the

statistical spread (928MPa). Note also that the failure mode is at approximately 45°, which, by applying Mohr's circle to this loading condition coincides with the angle at with the combination of shear and normal stress is greatest:
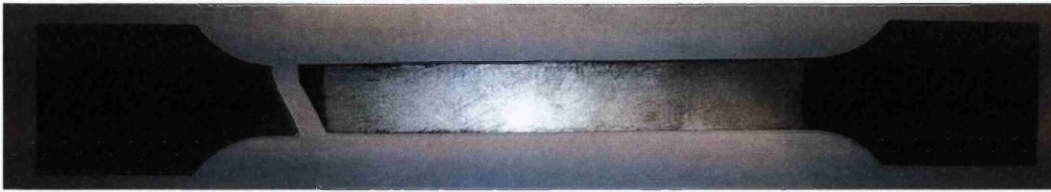
Figure 3.7. Failed DP800GI tensile specimen

3.4 Finite element analysis of fatigue specimens

Despite the previous section concluding that the geometry of test specimens have no effect on tensile results and all samples were found to fail in the centre of the coupons, it was found during fatigue testing that samples failed at the bottom of the fillets. This is true of both types of fatigue specimens used in this research project i.e., the Cardiff University and Swinden Technology Centre coupons. In order to illustrate the difference in failure modes between the low stress level fatigue test and high stress tensile test, two experiments were undertaken and an image of the two failed coupons can be seen in figure 3.8.
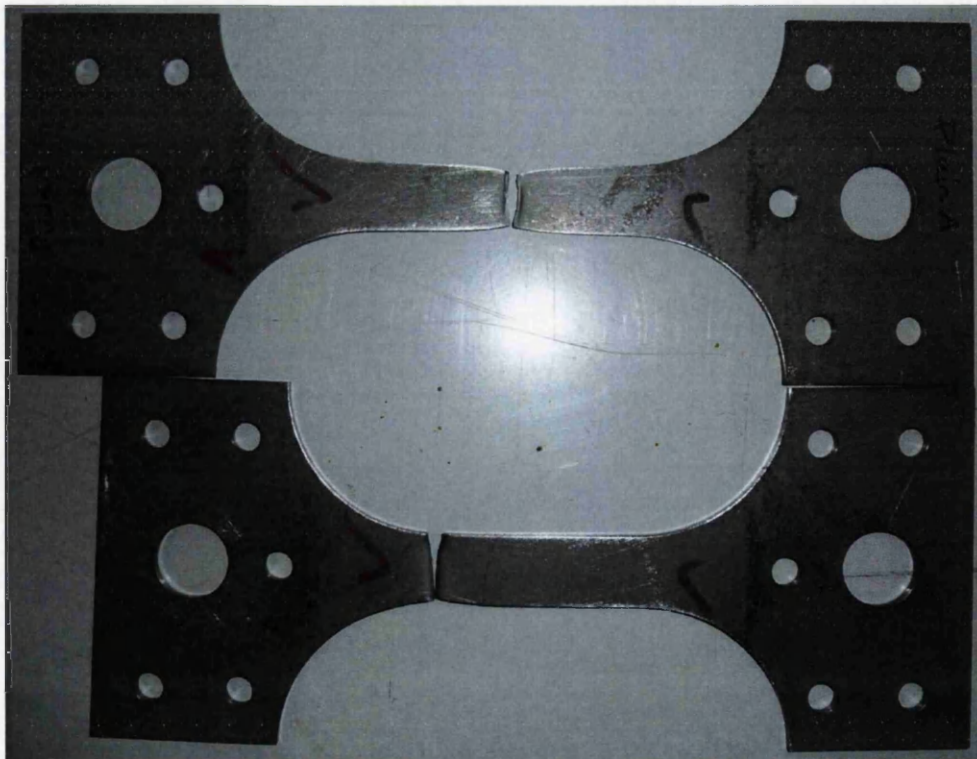
Figure 3.8. Failed tensile and fatigue specimens

Note that the uppermost sample shown in figure 3.8 failed through applying a large load as what was effectively a tensile test, whereas the sample on the bottom was a fatigue specimen that lasted 262,684 cycles. Since exactly the same phenomenon occurred with the STC fatigue samples (i.e. failing at the bottom of the fillets), and those coupons are widely used by TSSP-UK, it was decided that a FE evaluation of the stress concentrations within those coupons would be beneficial. The screenshots of those evaluations are shown in figures 3.10 and 3.11.

After completing the fatigue testing programme, failure of the specimen were shown to be in the same region as that shown in figure 3.8 in all of the coupons bar one. This coupon is shown in figure 3.9, where it can be seen that two fatigue cracks grew concurrently. One crack did grow from the location that was expected, though another grew from a location closer to the centre of the coupon. The growth of the latter could be due to machining roughness that was not fully polished out prior to testing, and highlights the importance of careful specimen preparation in order to ensure that the number of locations in which cracks could initiate and propagate are kept to a minimum. This ensures that samples are as consistent as possible and the statistical scatter shown in the SN curve is a result of the materials properties and not the variable surface quality of the machined edges of each coupon.

Figure 3.9. Two fatigue cracks that grew concurrently

Note that the applied stress for these screenshots, given their cross sectional area are in theory ±204MPa (load of ±2448N), which for these coupons should return a fatigue life of exactly 10,000,000 cycles. This is the fatigue life that the least squares

fit predicts from the results that were obtained from physical testing of these coupons predicts. At first glance, it appears that a stress concentration may not exist at the bottom of the fillets, though this is because it is too small to be noticed by the default stress scale. In fact a significant stress concentration does exist, which was identified by using probes, the central part of the specimen exhibited a stress of nearly exactly 204MPa, and the maximum stress was 216MPa, giving a 9% stress concentration.

Figure 3.10 & 3.11 gives us a clearer illustration of the stress concentration in the sample, where the increased stresses at four locations on the sample resulted in the fatigue life prediction being reduced from 10,000,000 cycles to less than 4,000,000 cycles. Furthermore, the locations where fatigue cracks were initiated during physical testing of the coupons were consistent with the ANSYS FE predictions shown on figure 3.11. The trend of higher than expected stresses with lower than expected fatigue lives also existed at other loading conditions, where FE predictions at other stress levels were undertaken. The results of those experiments are shown in figure 3.12.
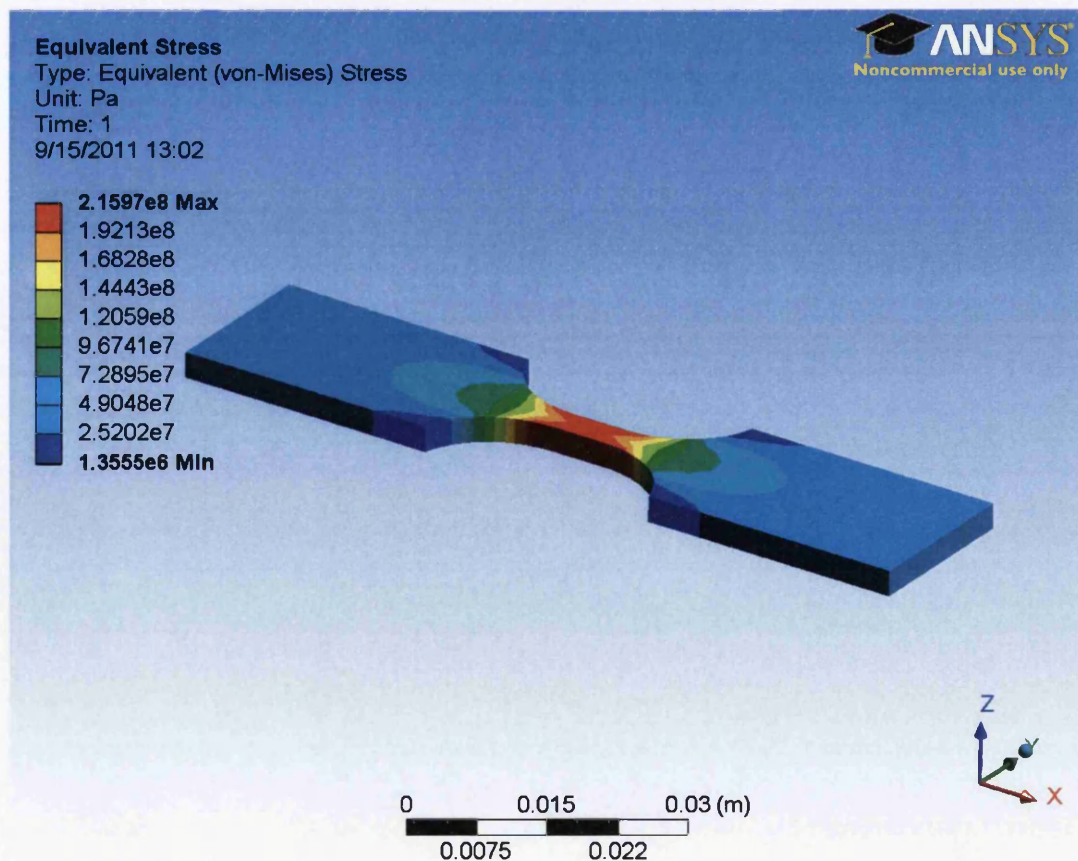

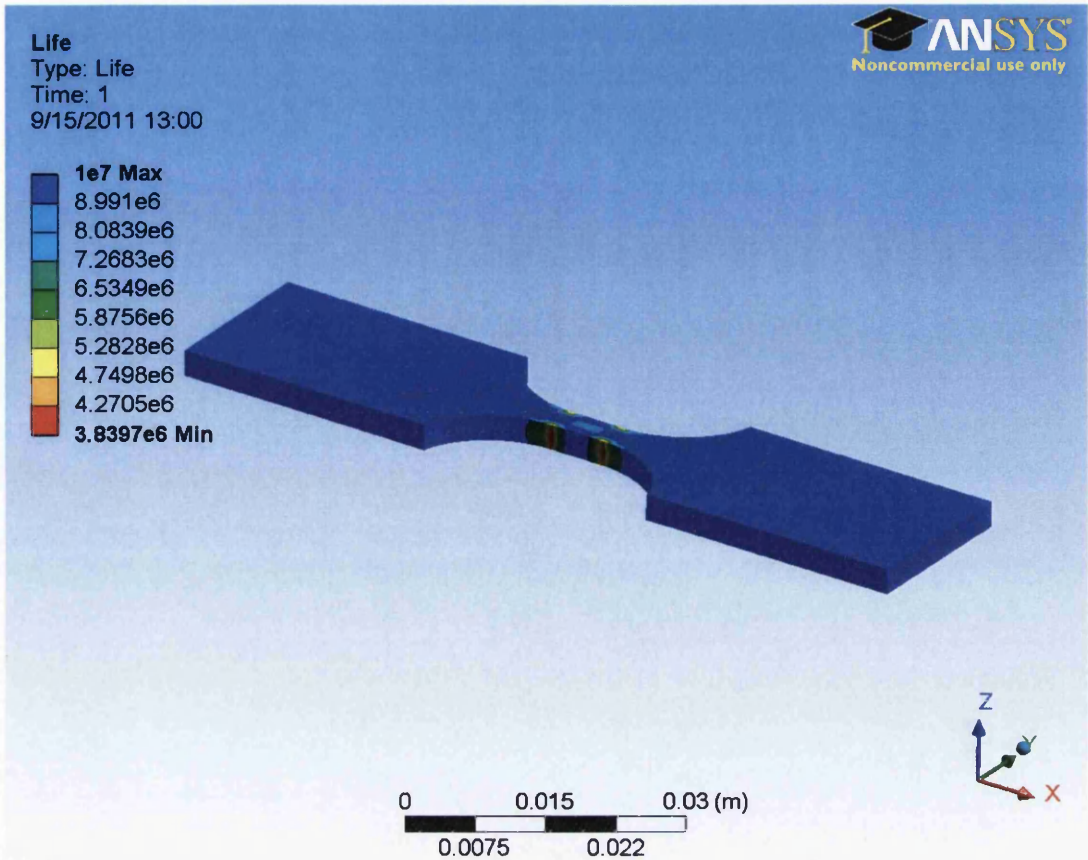Figure 3.10. FE stress evaluation of fatigue specimen

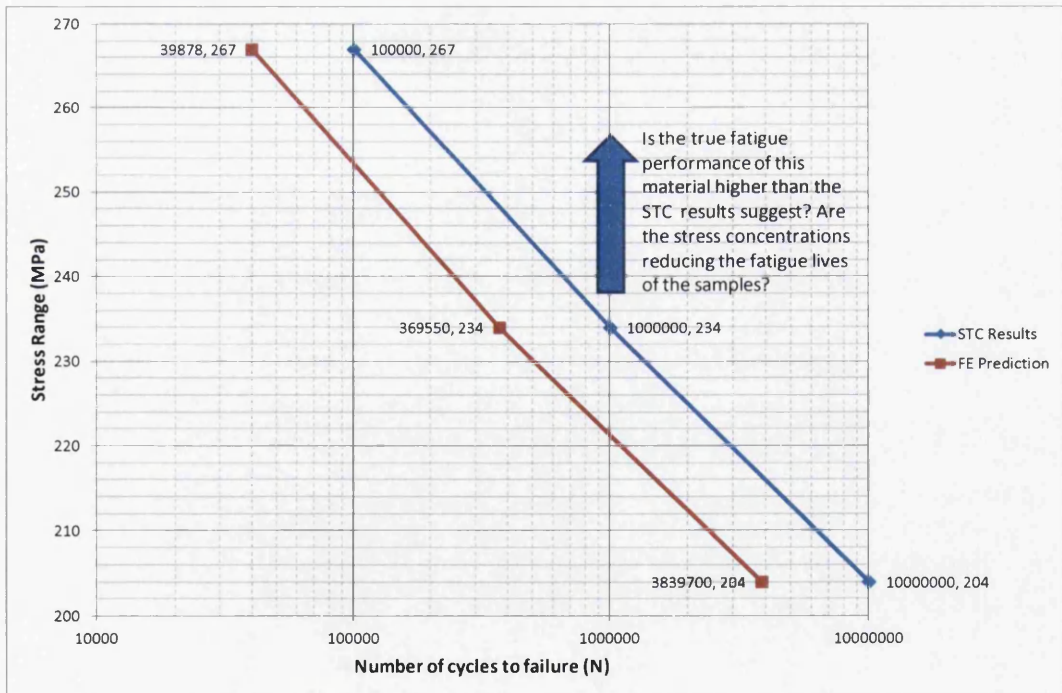Figure 3.11. FE life evaluation of fatigue specimen

Figure 3.12. Potential error in TSSP-UK fatigue curve

Note that both curves seem reasonably parallel, with the FE predicted curve constantly tracking 12-14 MPa below the STC curve, this raises the question of whether the stress concentrations that exist in the samples tested at STC are causing reduced fatigue lives and hence a curve that is very conservative and not a true reflection of the materials capability. There are two ways of attempting to combat this phenomenon, one is to move all our STC tested fatigue curves up by 12-14 MPa and the other one is to test new design samples that have such a large radius for the dog-bones that any stress concentration would be negligible. The second suggestion is not practical since the current design specimens already have a large radius, and there are practical considerations such as the geometry of the test grips etc.

With regards to moving the curves up by 12-14 MPa, this move could potentially be controversial unless extensive testing far beyond the scope of this project were carried out in order to validate and accurately quantify the effects of the stress concentrations. Instead of attempting to quantify the effects of the radii on the fatigue lives of samples, it is much better to consider this phenomenon as a built in safety factor. This is especially desirable since work completed in later chapters may have identified cases where the fatigue performance may have been overestimated slightly. By using this method, at worst we over-engineer by around 5% and at best this phenomenon, combined with the variability in fatigue performance due to manufacturing inconsistencies from coil to coil (see later chapters) cancel each other out.

A similar stress concentration was identified with the welded and un-welded coupons tested at Cardiff University, where the Von-Mises stress for this coupon is shown in figure 3.13, and since many use the normal stress in the direction of applied load to identify stress concentrations, this is also shown in figure 3.14. It can be seen that although they both calculate stress using different methods, the result is almost identical, with stresses of 373MPa at the base of the fillet.

Note that this FE evaluation was carried out with a load of 21kN, which in theory would give a stress of 350MPa. This is true for both simulations in the centre of the specimen, thus giving us confidence that the FE prediction is accurate. This stress concentration is less than 7%, which is better than the stress concentration in the

STC tested samples, therefore we need not worry that the results collected from these tests are overly conservative as they are at least as good as or better than most specimens encountered during the course of this project in terms of stress concentration.
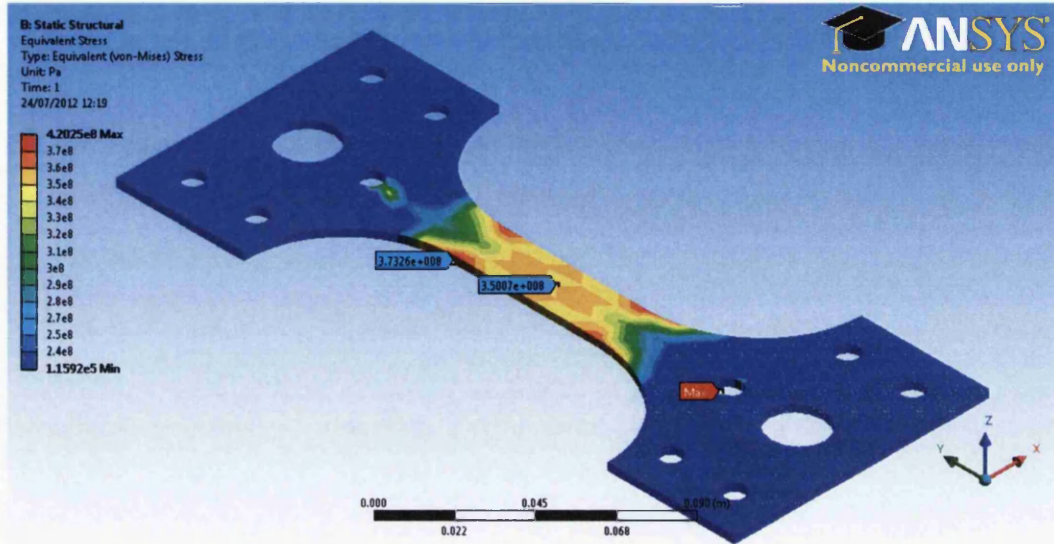
Figure 3.13. Von-Mises stress evaluation of fatigue specimen
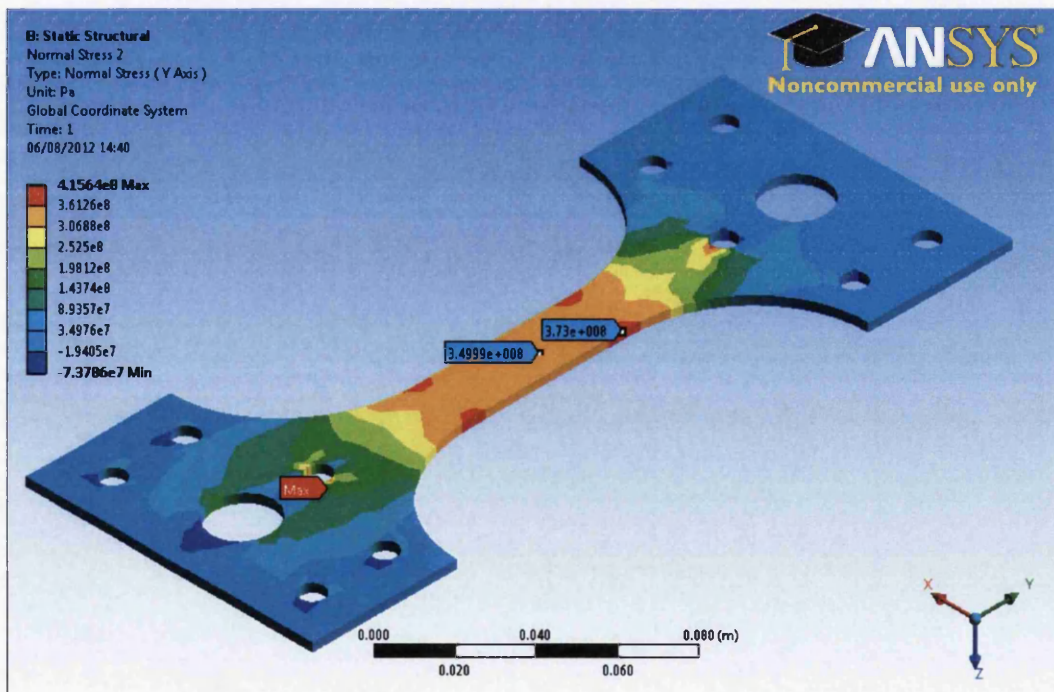
Figure 3.14. Normal stress evaluation of fatigue specimen

Of course it would be desirable to create a fatigue specimen without a stress concentration at all. This would require an extremely large radius that would only be possible by having an end width that is only marginally greater than the test width, or a longer specimen. Since the type of specimen we are using requires clamping plates, and the work carried out in chapter 6 identified that it needed 5 bolts in its design, it would then make it impossible to have a very narrow end width. Increasing the radius would then have to be done by increasing the overall coupon length, which is not desirable in this case due to the machine size restrictions.

Despite identifying stress concentrations during testing and FE evaluations, it is concluded that the magnitude of these concentrations are not great enough to cause concern and are comparable to other specimens in use. Furthermore they are fully compliant with the relevant British and European standards and therefore deemed suitable to give us trustworthy results.

Chapter 4 - Variability of HSLA Steel Mechanical Properties

4.0 Introduction

This chapter provides statistical descriptions of the distributions of mechanical properties within HSLA steel grades currently used by Tata Steels' automotive customers. The steel grades considered are for chassis & suspension applications, typically of the range of 2-4mm in thickness. The European (euronorm) standards that are used to describe the mechanical properties of these steel grades have a wide range of permissible values, and as such a more detailed analysis is required to provide adequate information to achieve robust designs.

As well as studying the statistical distributions, this chapter also considers the root cause of the distributions by analysing the thermo-mechanical processing route and chemical composition of each coil. The statistical distributions are then described by the use of a Classification and Regression Tree (CART).

All coils of steel studied in this chapter (SxxxMC grades) conformed to the delivery conditions set out by BS EN 10149-2:1996 and BS EN 10051:1991+A1:1997, the key aspects of these documents are shown in Tables 4.1, 4.2 and 4.3. Note that XF materials in table 1 do not have to conform to euronorm standards, as they are TSSP-UK grades with their own specifications. However, both steels go through exactly the same processing route and the only differences are the brand names and a slight variation in permissable properties.

Table 4.1. Tenform & euronorm mechanical properties specification

Mechanical properties for thermomechanically rolled steels			
Grade	Yield Stress Range (MPa)	UTS Range (MPa)	Elongation Range (%)
XF350	≥350	≥430	≥23
S355MC	≥355	430 –550	≥19
XF450	≥450	≥500	≥20
S460MC	≥460	520 - 670	≥14

Table 4.2. S355MC ladle chemistry

Chemical Composition of the Ladle Analysis (%)									
Grade	C Max	Mn Max	Si Max	P Max	S Max	Al Min	Nb Max	V Max	Ti Max
S355MC	0.12	1.50	0.50	0.025	0.020	0.015	0.09	0.20	0.15
S460MC	0.12	1.60	0.50	0.025	0.015	0.015	0.09	0.20	0.15

Table 4.3. Category A steels thickness tolerance

Nominal Thickness (mm)	Thickness Tolerances for a Nominal Coil Width (mm)			
	≤ 1200	> 1200 ≤ 1500	> 1500 ≤ 1800	> 1800
≤ 2.00	0.17	0.19	0.21	-
> 2.00 ≤ 2.50	0.18	0.21	0.23	0.25
> 2.50 ≤ 3.00	0.20	0.22	0.24	0.26
> 3.00 ≤ 4.00	0.22	0.24	0.26	0.27
> 4.00 ≤ 5.00	0.24	0.26	0.28	0.29

Note that S355MC and S460MC are classified as group B and C steels respectively, therefore the tolerances shown in table 4.3 are increased by 15% for S355MC and 30% for S460MC. With this in mind the maximum thickness tolerances for these two grades were calculated and are shown in table 4.4.

Table 4.4. Gauge tolerances for S355MC & S460MC

Gauge (mm)	S355MC Tolerance (mm)	S460MC Tolerance (mm)
> 2.0 ≤ 2.5	±0.2875	±0.325
> 2.5 ≤ 3.0	±0.299	±0.338
> 3.0 ≤ 4.0	±0.3105	±0.351
> 4.0 ≤ 5.0	±0.3335	±0.377

These coils were tensile tested to BS EN ISO 6892-1:2009 using an extensometer of 80mm gauge length, as shown below in figure 4.1.
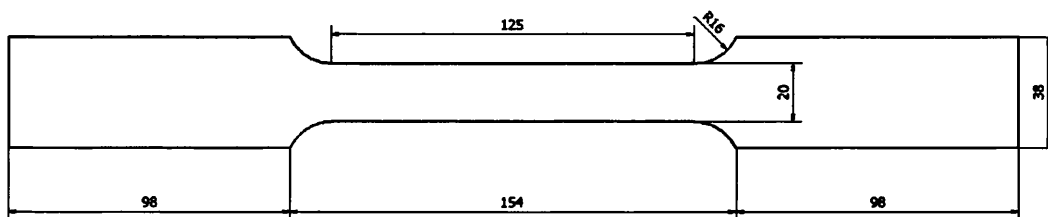

Figure 4.1. Tensile specimen geometry

With regards to defining the statistical distribution of properties & parameters, most were found to be normally distributed and fit the relationship shown in equation 1:

$$p(x) = \frac{1}{\sigma\sqrt{2\pi}} e^{\frac{(x_i - \bar{x})^2}{2\sigma^2}} \qquad \ldots\ldots\ldots\ldots(1)$$

Calculating the mean ($\bar{x}$) for each data set is a straightforward procedure. In order to draw a normal distribution curve, the only other parameter that requires calculating is the standard deviation (σ), as described in equation 2:

$$\sigma = \sqrt{\frac{\sum_{i=1}^{N}(x_i - \bar{x})^2}{N-1}} \qquad \ldots\ldots\ldots\ldots(2)$$

4.1 Variability of hot rolled pickled HSLA steel

For this analysis, data was collected for yield strength, UTS, elongation and gauge variation for all pickled (acid cleaned) coils of XF350 & XF450 produced in 2008. This section outlines the statistical scatter observed for basic material properties for these two grades of steel. Distribution patterns are illustrated and quantified as well as correlation patterns between properties being identified. Since Jaguar Land Rover (JLR) requested this information, much of the data processed comes from coils used to manufacture JLR components. This data set is limited to 1055 coils. Some studies carried out required more samples to distinguish patterns so the whole population of nearly 6000 samples was used.

4.1.1 Yield strength variability

As shown earlier, XF350 has a lower specified limit (LSL) of 350 MPa for yield strength, whereas XF450 has a LSL of 450 MPa. TSSP-UK also manufactures XF400, though this is produced in smaller quantities. What is surprising in this study is the extent of the difference between the statistical scatter of both materials. The difference in scatter between the two highlights the extra difficulty of manufacturing a material with an additional 100 MPa of strength over that of XF350. The two graphs (Figures 4.2 and 4.3) show frequency histograms along with a normal

distribution trend line for S355MC. It is visible that data collected for XF350 fits a normal distribution curve very well. The same cannot be said for XF450, where its distribution appears to be resemble half a normal distribution curve, i.e. with the lower strength end missing.
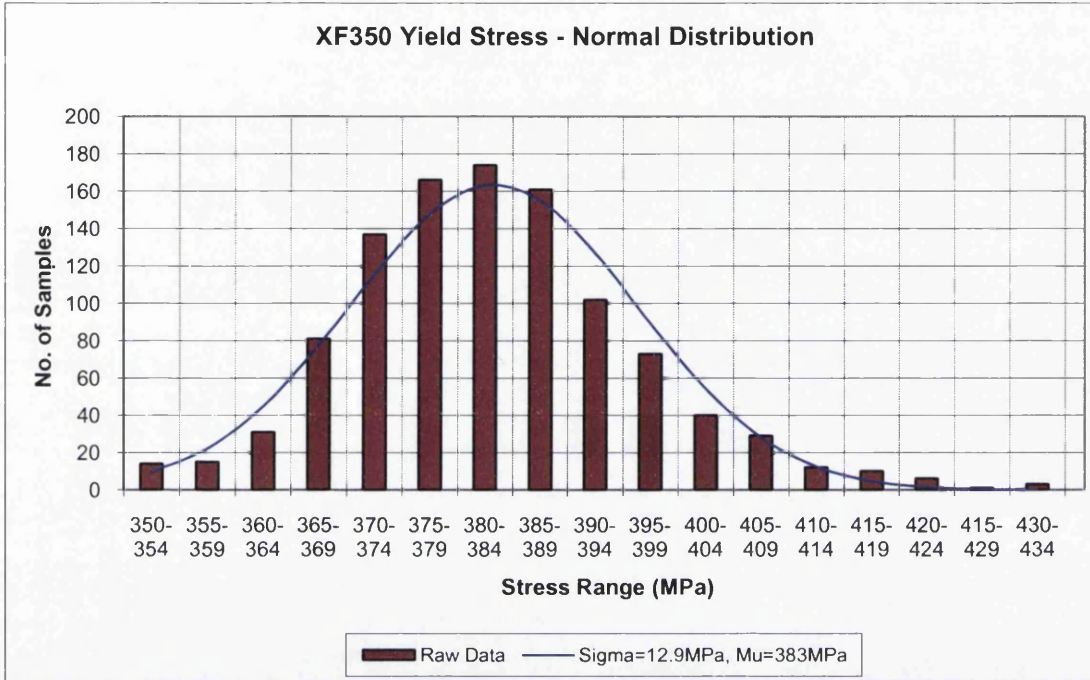

Figure 4.2. XF350 yield stress variability
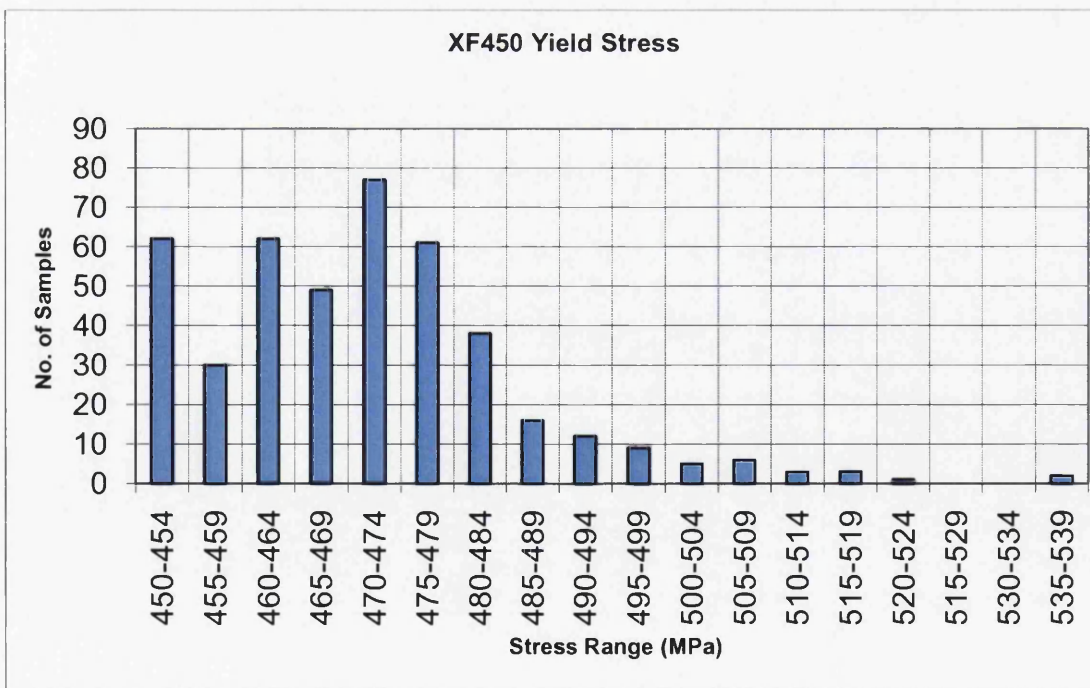
Figure 4.3. XF450 yield stress variability

Although the graph for XF450 appears somewhat unexpected, the nature of the histogram actually makes sound logic. The reason that the histogram appears skewed is that many samples with measured yield strength close to or below the yield LSL of 450MPa and/or those with measured tensile strength close to or below the UTS LSL are excluded and re-branded or downgraded to XF400, or other euronorm grades. By looking at the graph, after the peak of 470MPa, the distribution of the histogram looks like the tail end of a normal distribution curve. By trial and improvement method, i.e. by adding data points of material that may have been downgraded, the nature of the original distribution has been predicted and is shown by the purple bars in figure 4.4.

This effect can also be seen, albeit to a much reduced extent for XF350. Where there are a small number of rejects that are not accounted for, this causes the mean value to be slightly higher than that calculated based on the whole population without any exclusions. This is visible in the graph i.e. the bell curve looks shifted to the right as compared to the histogram.
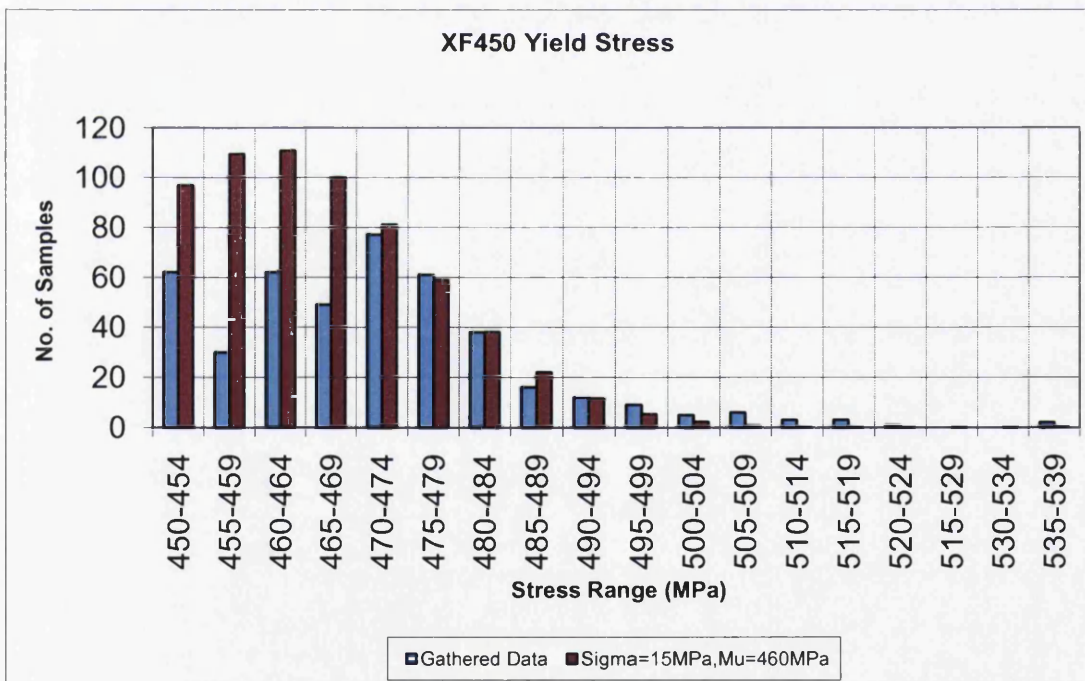
Figure 4.4. XF450 yield stress variability (+predicted data)

The graph in figure 4 shows close tracking for stresses larger than 470MPa. The gap between the red and blue lines for ranges between 450 & 470MPa represents post-calculated missing data. We can therefore assume that the true distribution for the yield of XF450 to be a normal distribution with a mean of approximately 460MPa, and a standard deviation of around 15MPa. Added to this the distribution has a cut off of 450MPa, as well as missing data between 450 & 470MPa.

The cumulative distribution function graphs are displayed in figures 4.5 and 4.6, they are useful as a visual aid to check the closeness of the data to a normal distribution, as well as to establish the percentage of population that falls within any specified limits, i.e. it can be established that about 85% of the population of XF350 has a yield stress greater than 370MPa.
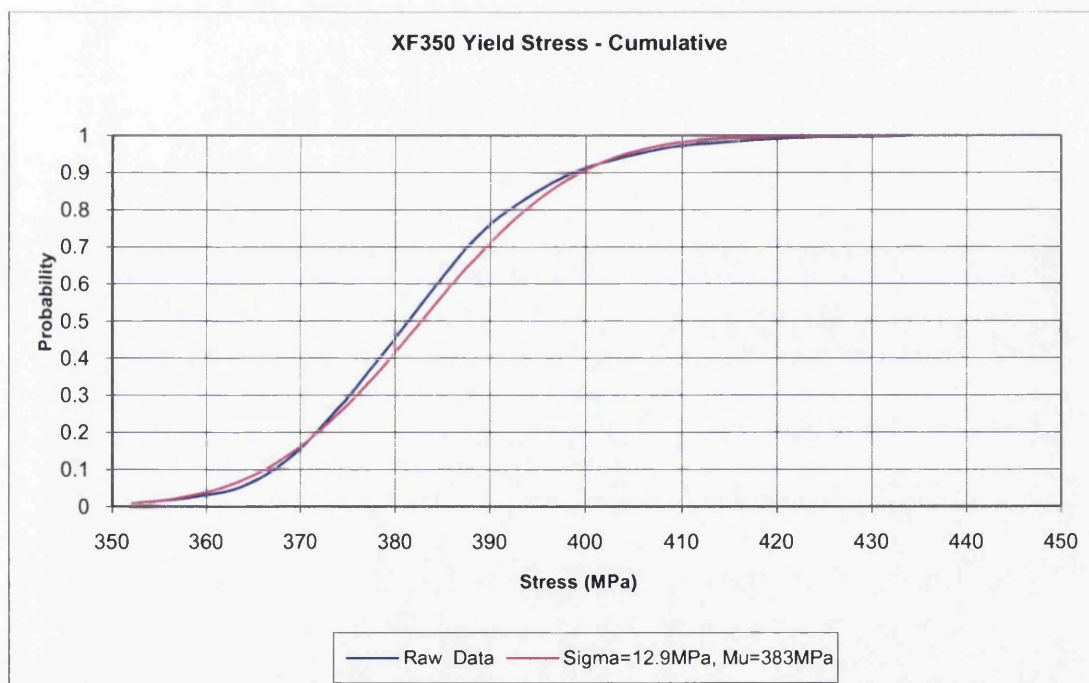
Figure 4.5. XF350 yield stress variability - cumulative

It can be seen that the population of XF450 is much closer to the LSL compared with XF350. With XF450 only 50% of the population has a yield greater than 20MPa of the LSL. As with the histograms, fitting a curve to the cumulative frequency graph has no benefit as so much of the data is missing.
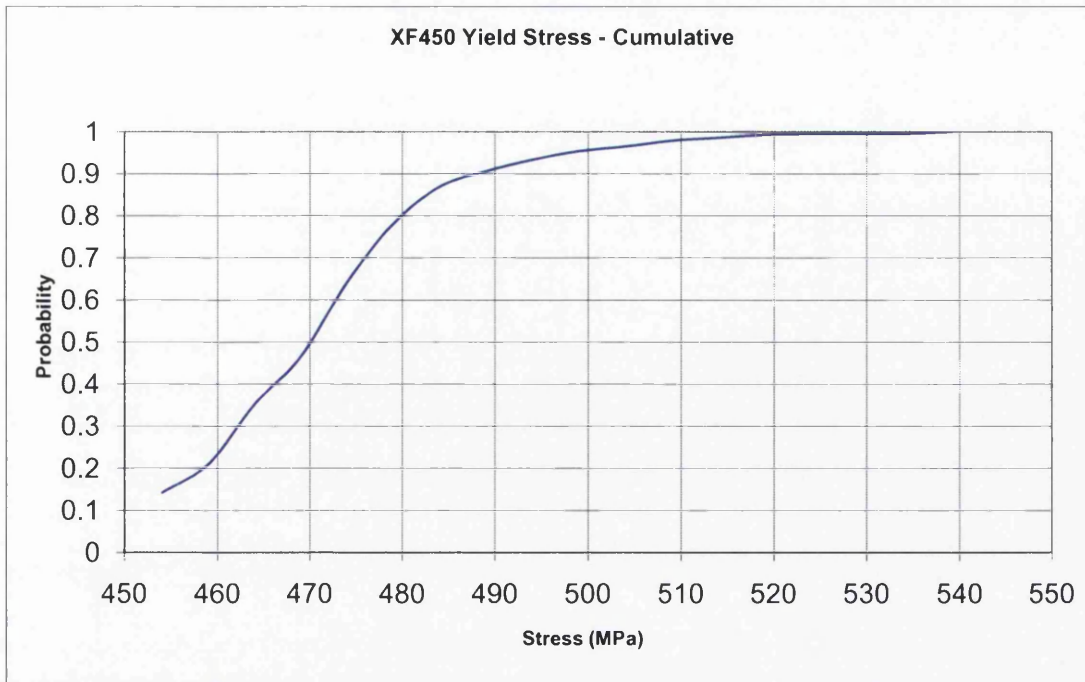
Figure 4.6. XF450 yield stress variability - cumulative

4.1.2 UTS variability

The distributions of UTS for both grades are closer to the fitted curves. While the closeness of fit for XF350 was not surprising, observing a reasonable fit for XF450 was surprising considering the nature of yield distribution. Another reason that this was unexpected is that studies suggest a close correlation between UTS and yield. Since the Yield strength for XF450 showed a significant skewness in its statistical distribution, it was assumed that the UTS graph would be similar.

Once again the histograms are displayed along with the "normally" distributed trend line showing values for the mean and standard deviation, these are illustrated in figures 4.7 and 4.8. The XF350 results are from the sample of 1055 coils used by JLR, while the XF450 are from a range of customers, as there was not enough data for this particular grade from one customer alone for statistical analysis.
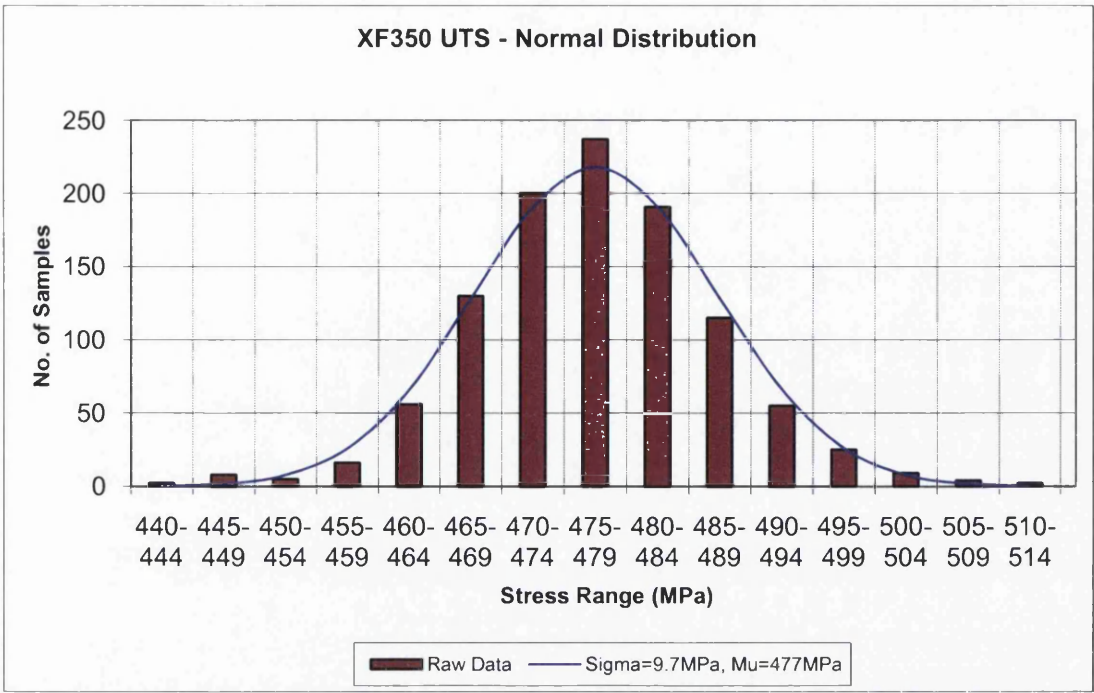
Figure 4.7. XF350 UTS variability
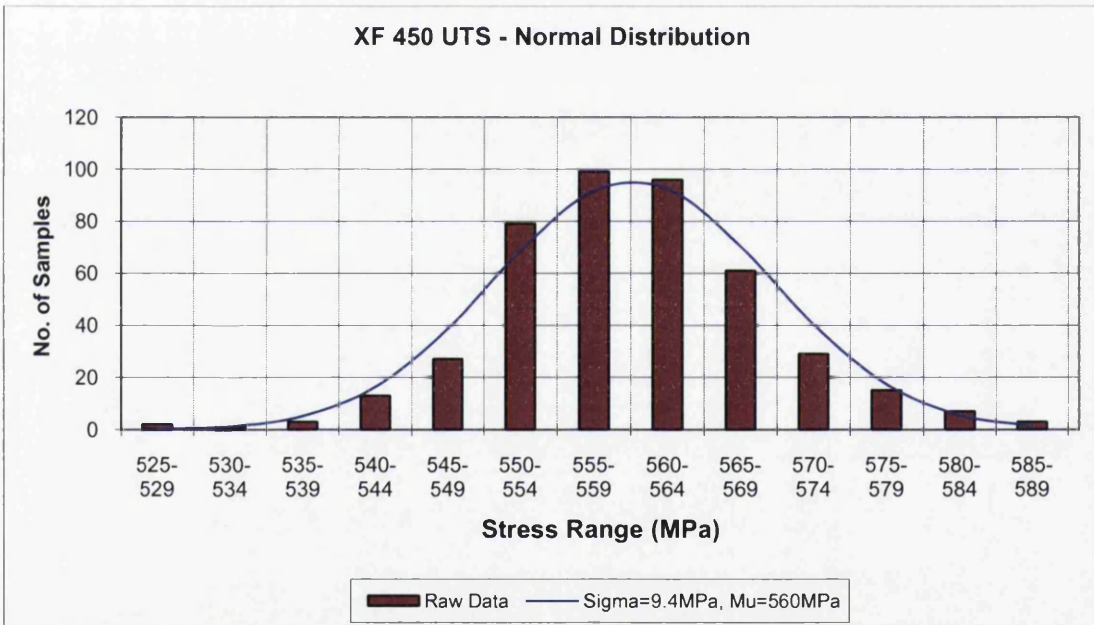
Figure 4.8. XF450 UTS variability

Both grades also show good correlation with the fitted cumulative distribution curve as can be seen in figures 4.9 and 4.10.
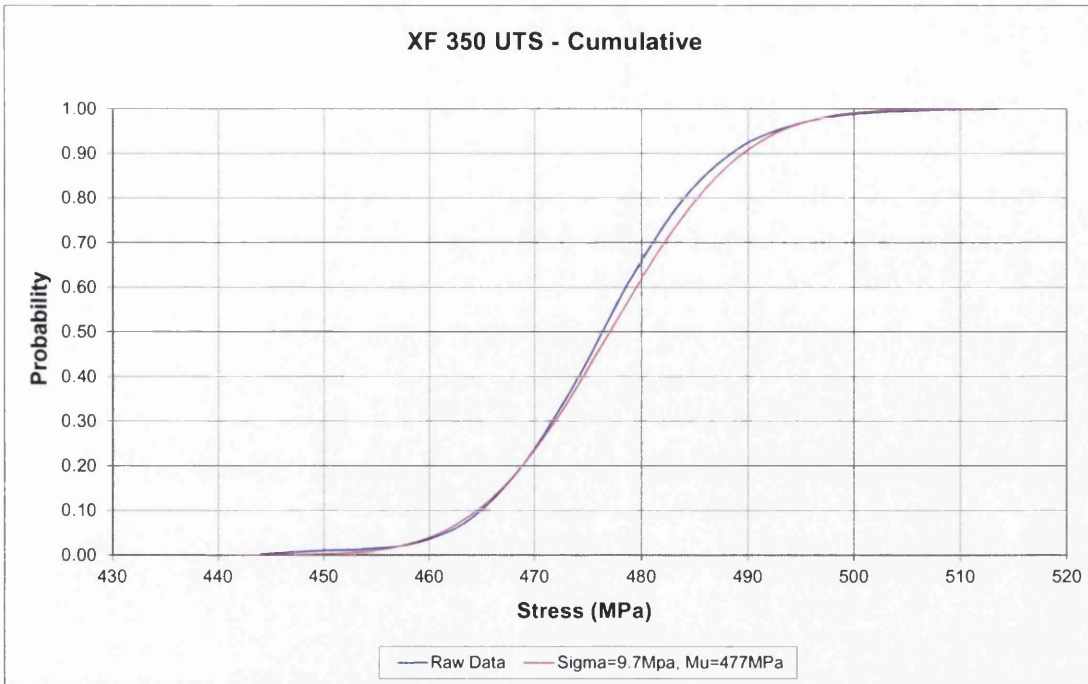
Figure 4.9. XF350 UTS variability - cumulative
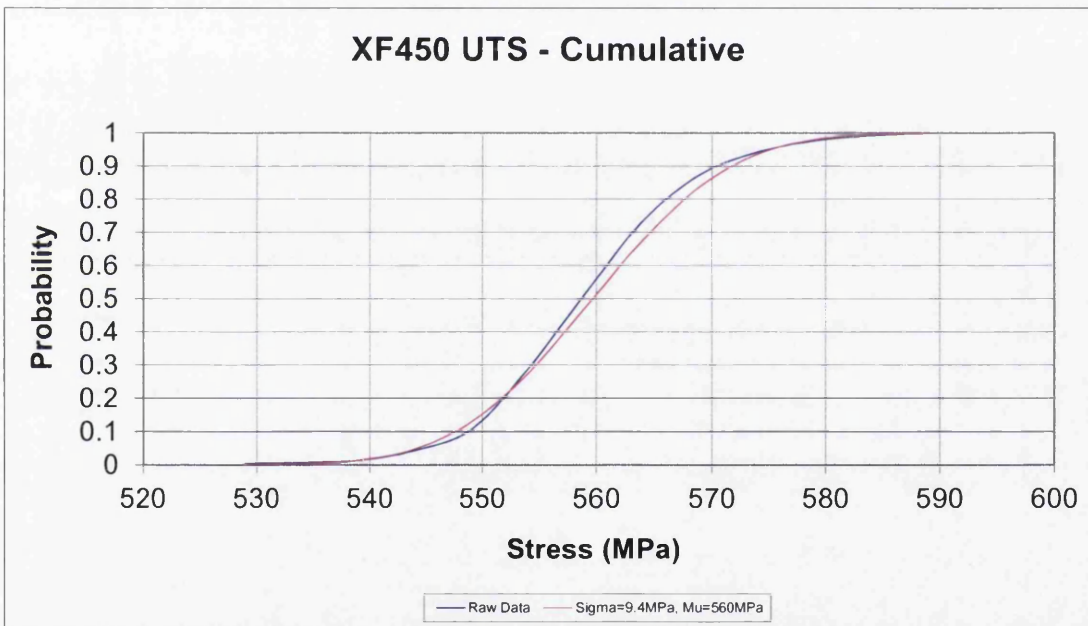
Figure 4.10. XF450 UTS variability - cumulative

It can be clearly seen that the calculated distributions represent the data well, and can therefore be used with confidence to aid in the robust design of new components.

4.1.3 Elongation variability

Elongation is one of the important properties that require consideration for predicting a material's potential for forming. A material with low elongation is less ductile and has limited capability for plastic deformation after and during forming or cold working. As a result, this may lead to premature failure in service. Understanding the variability or scatter in this property is therefore critical to achieving both reliable and robust designs.

It was found that the distribution of elongation data for XF350 (figure 4.11) closely followed a normal distribution curve, though XF450 was not so closely mapped (figure 4.12). This could be due to the relatively low number of results sampled, as it is commonly documented that normal distribution graphs are more accurate when there is a large amount of data to work with.
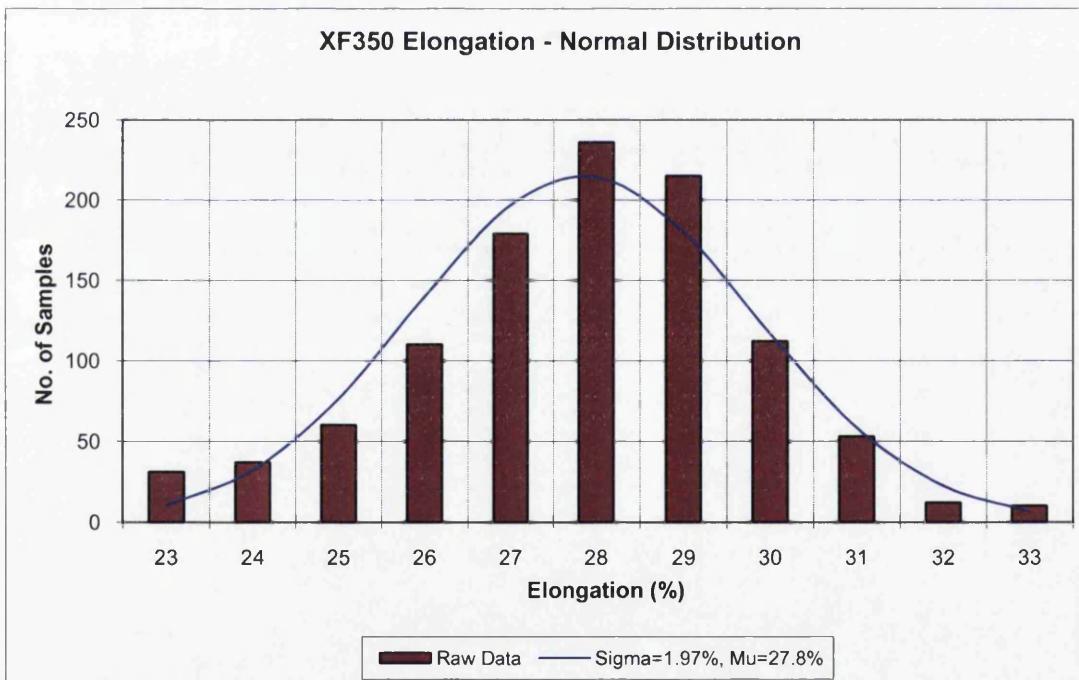
Figure 4.11. XF350 elongation variability
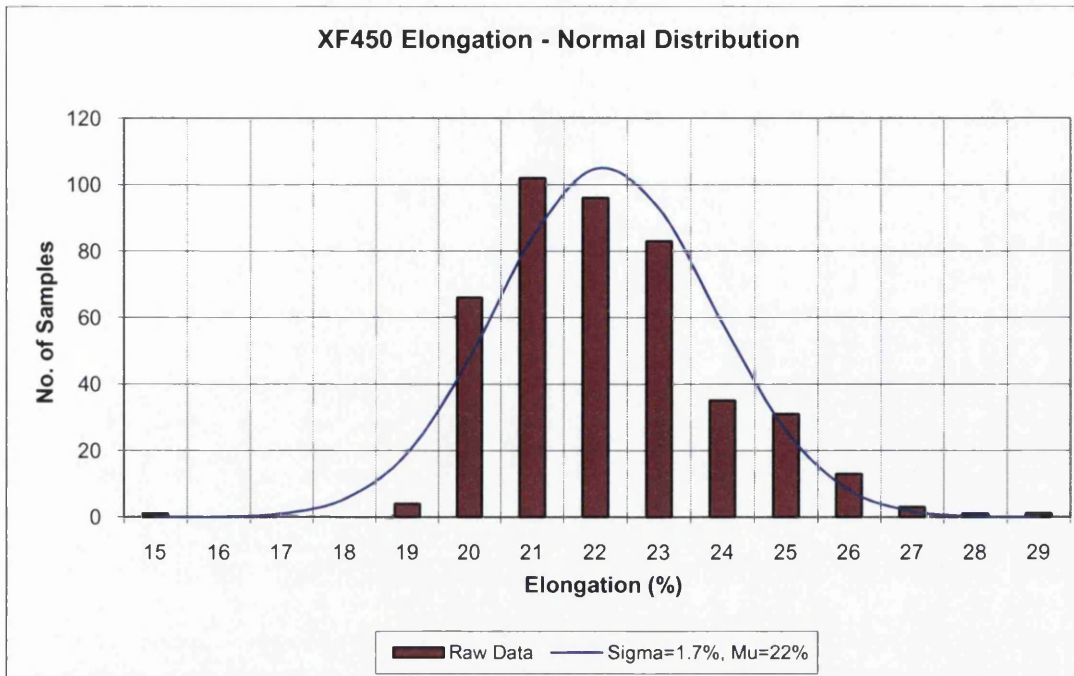
Figure 4.12. XF450 elongation variability

It can be seen that the ranges of elongation with both grades are large, where the LSL for XF350 is 23% and the LSL for XF450 is 20%. The reason for 5 coils of XF450 having less than 20% elongation in the graph shown above is due to the quantity of data available for this grade being low, it was necessary to include results from S460MC to the data set. S460MC is the nearest equivalent Euronorm grade for XF450. TSSP-UK manufactures this steel in exactly the same way as XF450, the only difference between them is that they have slightly different LSL values as described earlier in table 4.1.

This means that the 5 coils in the graph that have an elongation of less than 20% would have failed the criteria for branding as XF450, but they could still be supplied as S460MC. Apart from the 5 results mentioned, all other samples could have been branded as XF450, therefore including data for S460MC does not have a negative effect on the overall results.

The cumulative distribution graphs are shown in figures 4.13 and 4.14. By observing these results it seems that while the shape of the obtained data seems similar to the calculated distribution, the calculated curve seems to be offset slightly. However, the values for mean and standard deviation are sufficient for use in later work.
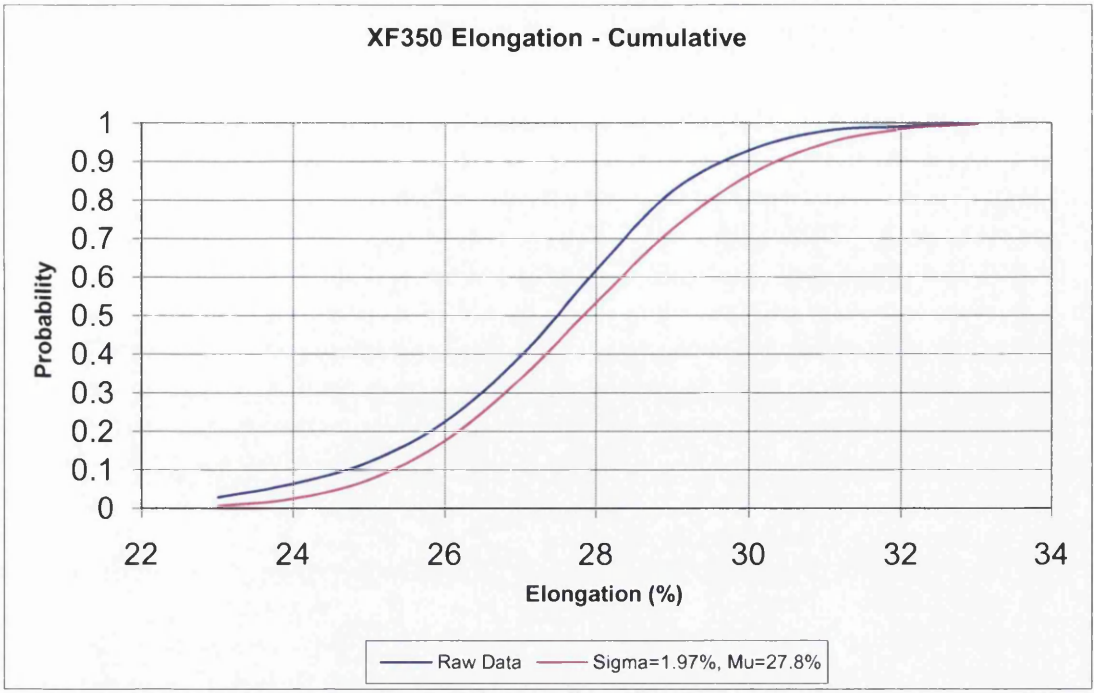
Figure 4.13. XF350 elongation variability – cumulative
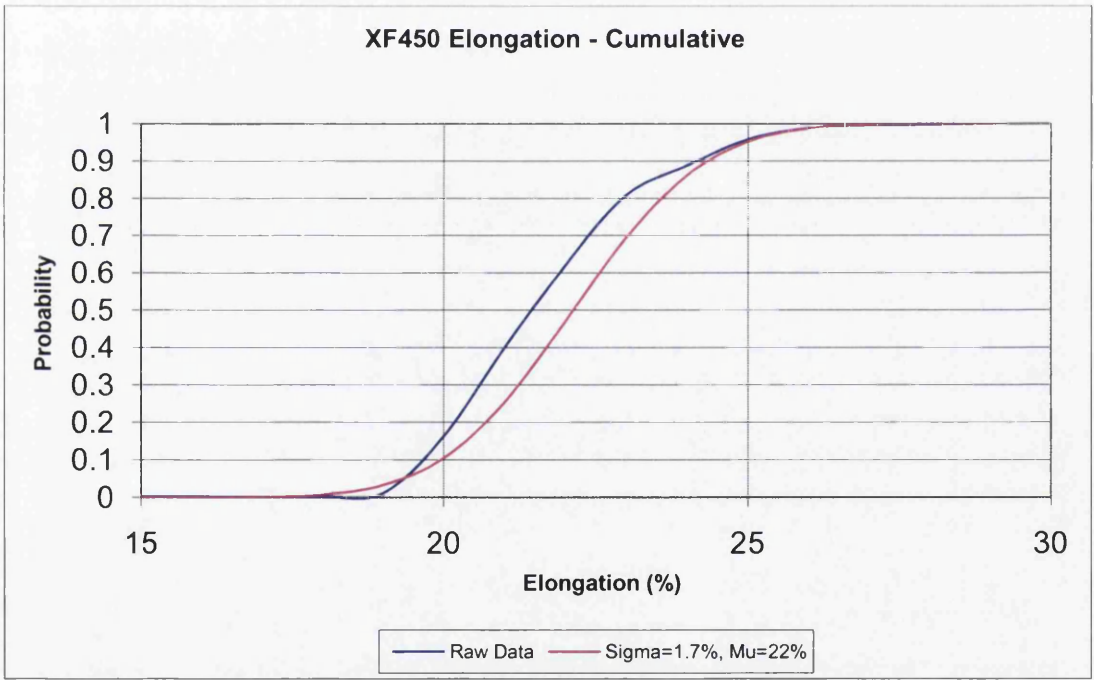
Figure 4.14. XF450 elongation variability - cumulative

4.1.4 Strip thickness variability

The data from gauge variability analysis gave results which at first were surprising, though after further investigation into the rolling process at the Port Talbot hot mill the results are backed up by sound evidence and theories. Slab is rolled through the roughing mill and comes out as a 35mm transfer bar, then the seven finishing mills have the job of producing anything between 1.4 & 18mm gauge strip products (figure 4.15).
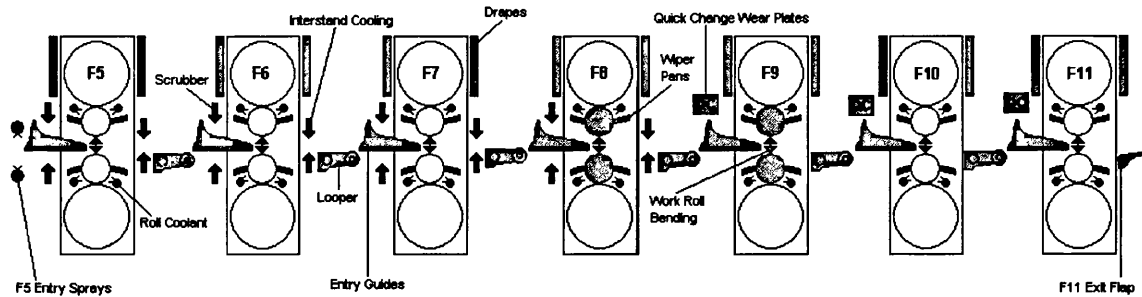
Figure 4.15. Port Talbot finishing mill

Since every hot mill only has a finite number of mills to roll a range of gauges, the smaller the amount of reduction performed on the transfer bar, the more accurate the finished product will be. Alternatively, it is much more difficult to achieve a large amount of reduction. As a result, it is established that thin gauges have a greater amount of dimensional variability compared to thicker gauges. Therefore, since dimensional accuracy of the strip deteriorates as the thickness is reduced, the variability in gauge measured in percentage terms is compounded and increases significantly for thinner strip products.

The samples used to perform gauge variability analysis were from the coil ends and hence represent one of the most variable (along with the front end) sections of the coil. The mid-section of the coils manufactured at Port Talbot are manufactured to extremely close tolerances, these fractional errors in gauge are not really worth considering. Note that the definition mid-section represents the vast majority of the coil. However components are also manufactured from the two coil ends, which show a fairly large amount of variability, thus the extent of variability must be defined.

There was only enough data available to perform a statistical analysis for S355MC, the data used for this section of work only represents strip products rolled at the Port Talbot hot mill – different mills will undoubtedly perform differently to one another. Due to the limited number of coils of identical thickness, In order to produce the graph below it was necessary to group some gauges together, hence the values on the x-axis show the average gauge for the sample in each group. i.e. the mean gauge for the category 1.5mm – 2.5mm was 2.25mm.

Standard Deviations in Gauge

$y = -0.0098x + 0.1003$

$y = 12.109x^{-1.513}$

Legend: SD (%) SD (mm) Power (SD (%)) Linear (SD (mm))
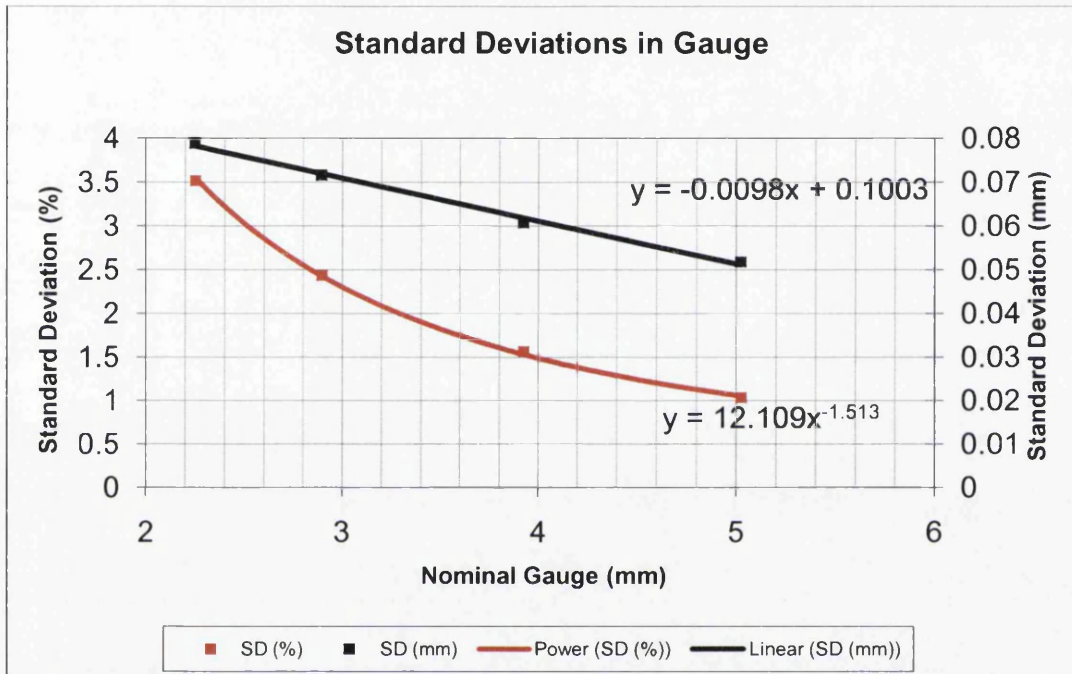
Figure 4.16. Statistical analysis of thickness

Either of the mathematical relationships between nominal gauge and standard deviation can be used to predict the variation in gauge across the range of gauges from 2mm-6mm with confidence. The graph in figure 4.17 shows how the variability is reduced with thicker gauges as it plots nominal gauge against measured gauge, the area between the two lines represents 99% of all data.

The reduction in gauge variability with thicker coils is clearly visible in the graph shown on the following page, and would be even more visible with a graph showing data with gauges of 10mm or more, however for automotive chassis applications only gauges between 2-6mm are relevant. Even though in theory 1% of the population is not represented in this graph, by checking the original data set very few results fall outside these lines. It is therefore safe to assume that the two

mathematical relationships for variability shown in figure 4.16 represent the data well, and using these along with a standard deviation of ±2.576 accounts for virtually all data, thus giving the upper and lower limits for gauge variability.
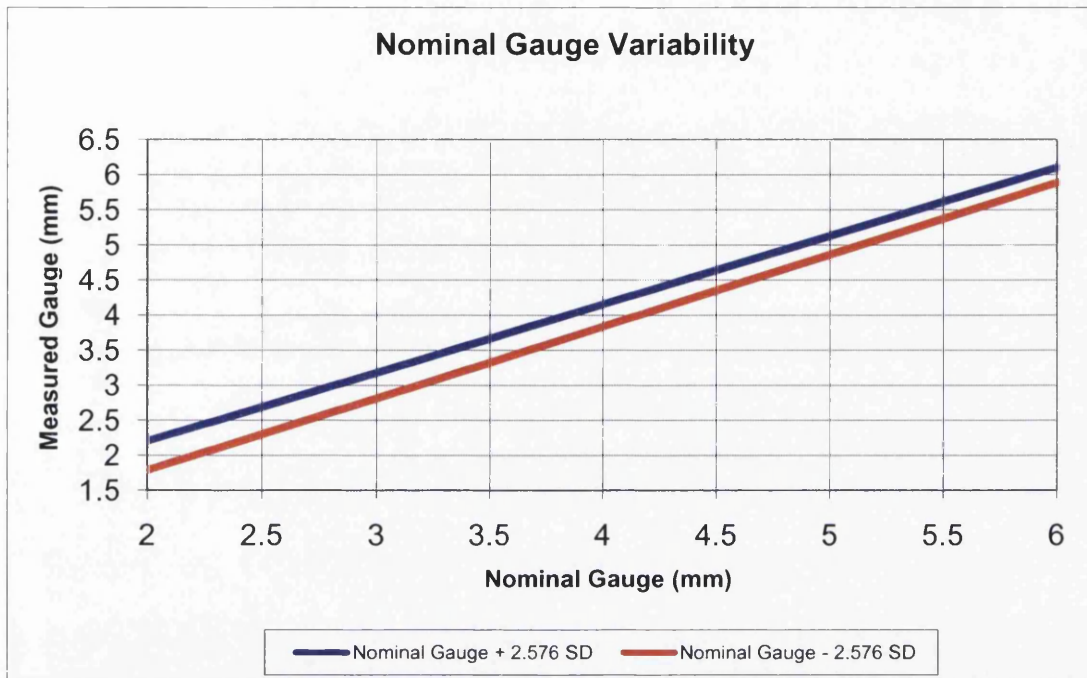
Figure 4.17. Statistical analysis of thickness – theoretical limits

However, it is not entirely safe to assume that these two lines account for all data, as material is sometimes supplied outside these limits. The only failsafe method that can be used is to use the tolerances detailed by BS EN 10051:1991 +A1:1997; to which both S355MC & S460MC must conform. The tolerances outlined by this document are shown previously in table 4.4. Note that S460MC has tolerances that are 15% more relaxed than S355MC. It is therefore recommended that table 4.4 should be used to determine worst-case possibilities for error in gauge. It has been observed that the vast majority of every coil is extremely close to the specified gauge, though the thickness of the two coil ends may vary up to the amounts specified in the standards. Figure 4.18 shows how table 4.4 corresponds to the statistical analysis performed from approximately 6000 samples of S355MC & XF350.

Nominal Gauge Variability
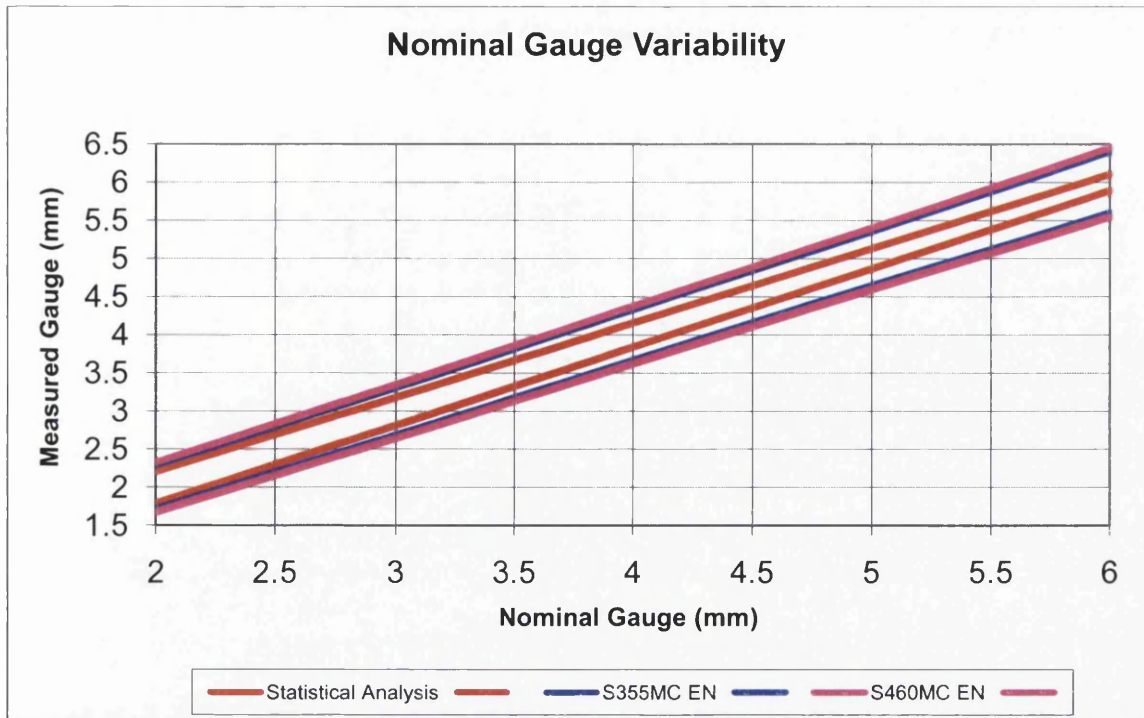
Figure 4.18. Theoretical and Euronorm limits for thickness

It can be seen that, at 2mm gauge, the data used to perform the statistical analysis shows almost as much variability as the maximum tolerance for Euronorm compliance, though at larger gauges the extent of variability is reduced. This may be partly due to the relatively low number of samples at larger gauges available to perform the analysis, hence using the Euronorm tolerances is the only safe method available to design robust new products. However, it is still thought that the durability does genuinely reduce at thicker gauges due to the reasons outlined earlier.

To highlight that the variability in material thickness is mainly limited to the coil ends, the graphs in figure 4.19 shows how the thickness of a coil can vary along its length. These coils are all specified as 3mm thick S355MC.
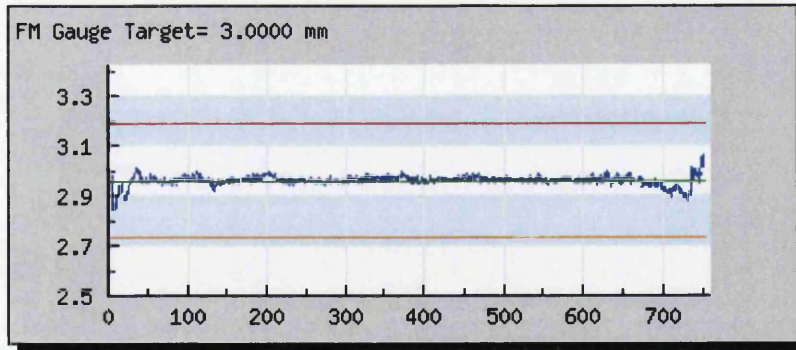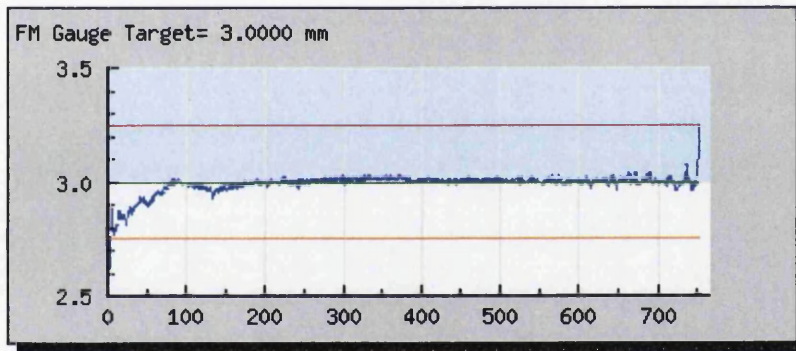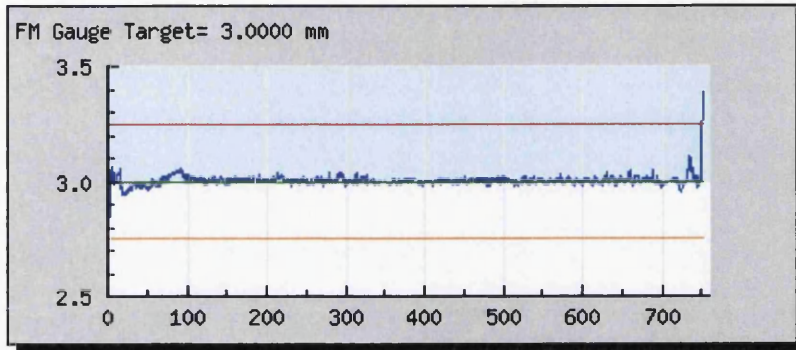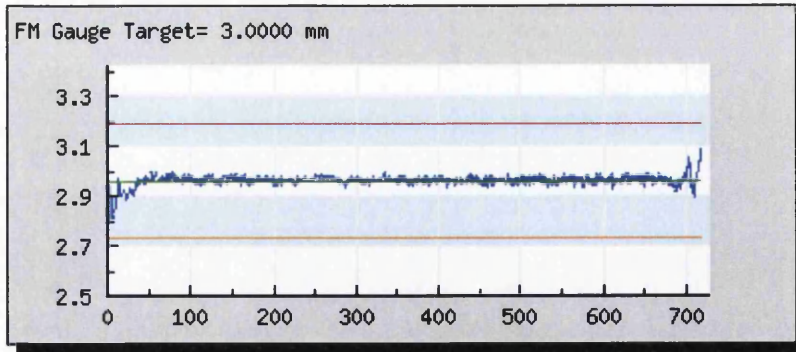
Figure 4.19. Typical thickness variability of 3mm S355MC

4.1.5 Correlation between mechanical properties

The correlation between UTS, elongation & yield can help determine the probability of a given sample of steel having mechanical properties in the favourable end of the spectrum on all three accounts. Alternatively it can also be used to predict obtaining a material in the unfavourable spectrum on all three accounts, as well as any combination in between. The graph below shows a clear linear correlation between UTS and yield, though there is a significant amount of scatter.
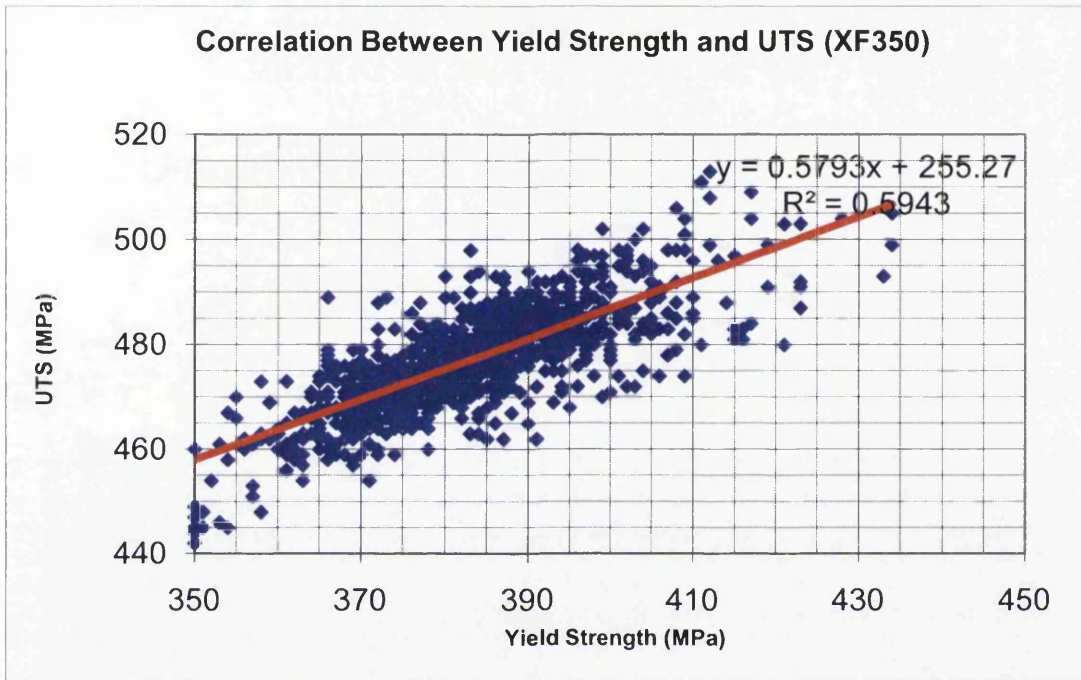
Figure 4.20. Correlation between UTS & yield (XF350)

The Pearson correlation coefficient for this relationship in XF350 is 0.77, which is a reasonable correlation. There can be no doubt that a linear correlation exists, as all samples with a yield higher than 410MPa have a UTS of at least 480MPa, both being well above the LSL for the material. Surprisingly, this is the only correlation that exists for the three mechanical properties studied for the two Tenform grades.

Despite this clear relationship, no such pattern exists for XF450 (or S460MC). This is shown in figure 4.21 where a marginal rise in UTS can be seen as the yield increases, but not enough to justify the existence of a correlation. This phenomenon cannot be accounted for by the extent of grade re-classification associated with this grade and constituent chemistry, all that can be deduced is that most samples have a UTS of between 540 & 580MPa regardless of the yield strength.
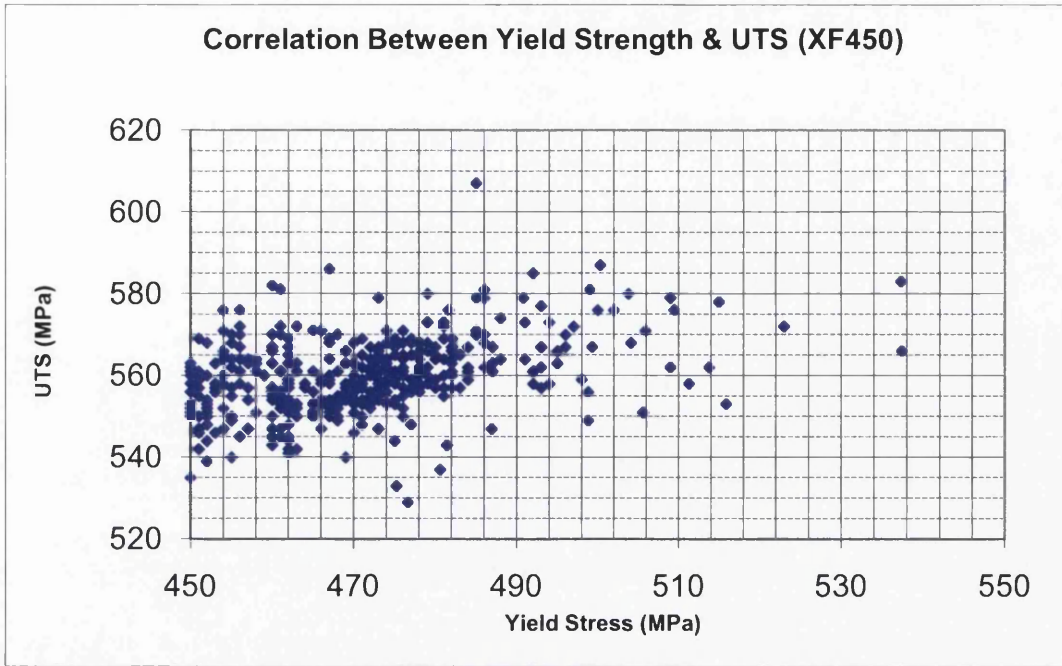
Figure 4.21. Correlation between UTS & yield (XF450)

There is also no relationship between any other combination of properties, as can be seen from the following four graphs in figures 4.22-4.25. It was expected that both UTS & Yield would be inversely proportional to elongation, though this study suggests no correlation and therefore a random distribution. This may be due to a large variation in the amount of temper rolling within the data set (where temper rolling can significantly alter the proof to ultimate strength ratio). Unfortunately no information is recorded and stored on the TSSP-UK temper mills for hot-rolled steel.
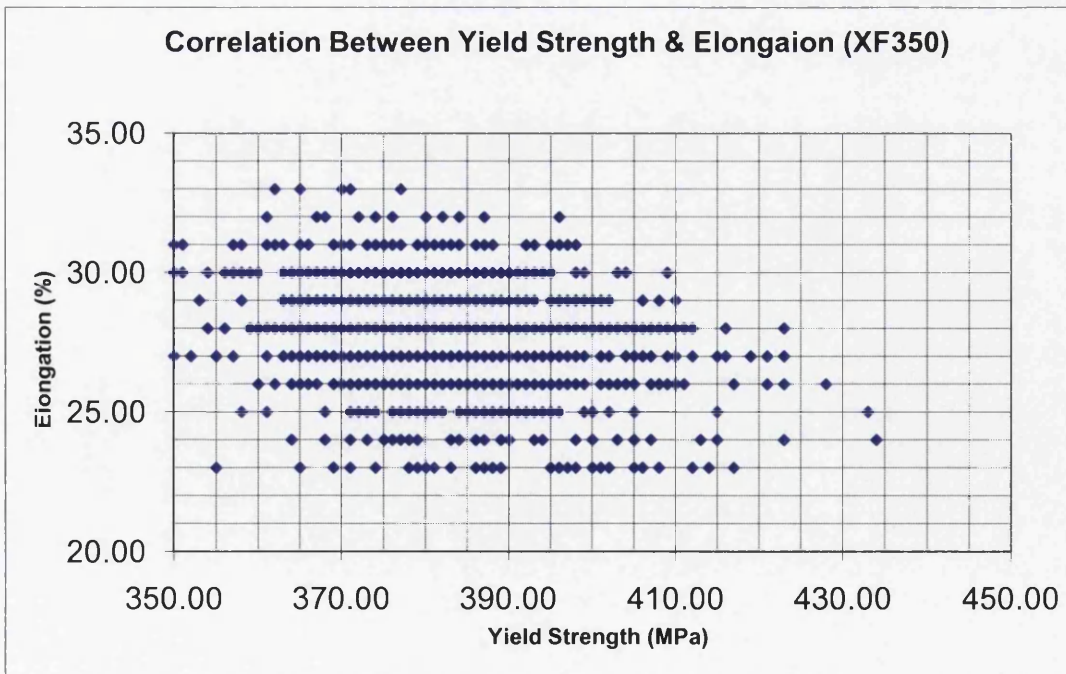
Figure 4.22. Correlation between elongation & yield (XF350)
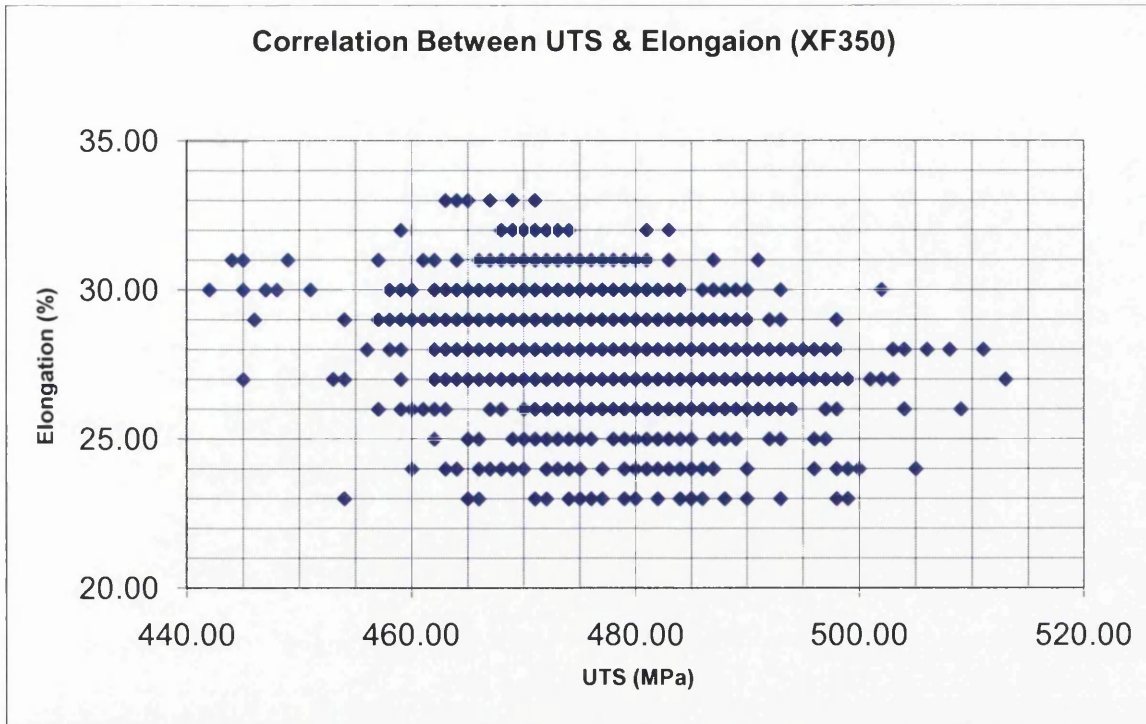
Figure 4.23. Correlation between elongation & UTS (XF350)
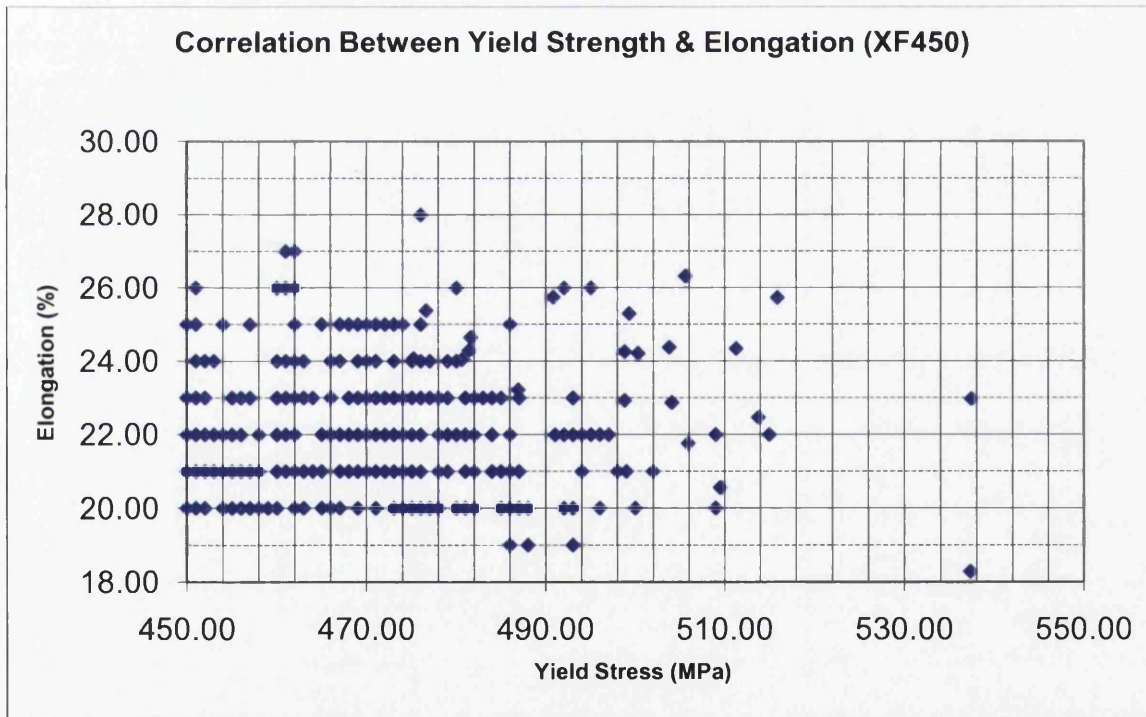
Figure 4.24. Correlation between yield & elongation (XF450)
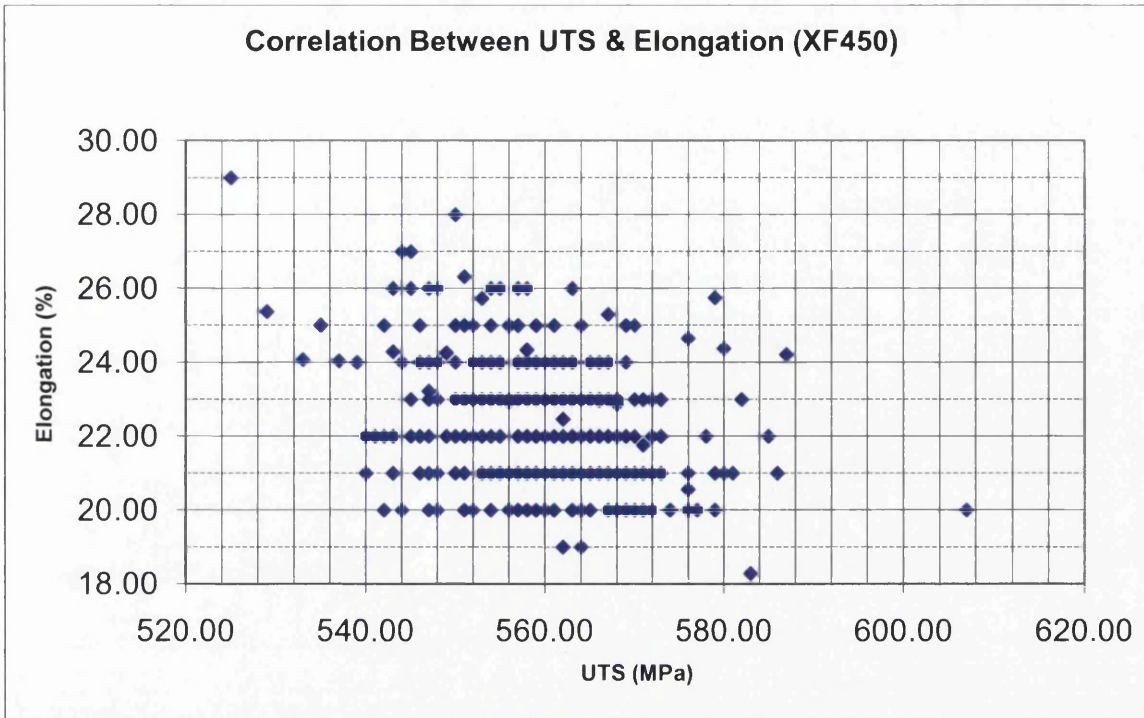
Figure 4.25. Correlation Between UTS & elongation (XF450)

4.1.6 Process capability

There are various methods of measuring and calculating process capability, though most, if not all use the Lower Specified Limits (LSL) and standard deviations of the parameters being studied. The TSSP-UK method used to define process capability, which is a common method used in other industries is defined as:

$$C_{pk} = \frac{\mu - LSL}{3\sigma}$$

TSSPUK aims to achieve a C_{pk} of 1.33:

$$\frac{4}{3} = \frac{\mu - LSL}{3\sigma}$$

$$4\sigma + LSL = \mu \quad \text{or} \quad LSL = \mu - 4\sigma$$

Note that a C_{pk} value of more than 1 indicates that the mean is more than 3 standard deviations from the LSL.

The equation for process capability, shown in the previous page has been used to calculate C_{pk} values for Yield, UTS and Elongation for XF350 & XF450 (including S335MC & S460MC). Using the definitions for standard deviation and normal distributions, the number of theoretical failures per 1000 were calculated and shown in table 4.5 below:

Table 4.5. Failure rates & C_{pk} values for tenform grades

Grade	Yield		UTS		Elongation	
	C_{pk}	Failures (%)	C_{pk}	Failures (%)	C_{pk}	Failures (%)
XF350	0.844	0.56	1.614	0.00	0.818	0.72
XF450	N/A	N/A	2.116	0.00	0.418	10.54

It was not possible to calculate the C_{pk} value for the yield strength of XF450, as the data set was not normally distributed. It is clear that the process capability for elongation of XF450 is very low, giving a theoretical 10.54% failure rate. Though this may seem extremely high it is not totally disastrous as it can be re-branded as S460MC, which has a relaxed elongation specification – though of course it needs to meet the other minimum mechanical property requirements for the grade. As a reference, the failure rates for various Cpk values are shown below.

Table 4.6. Projected failure rates for various C_{pk} values

C_{pk}	Failure Rate (%)
0.4	11.51
0.5	6.68
0.6	3.59
0.7	1.77
0.8	0.82
0.9	0.35
1.0	0.135
1.1	0.05
1.2	0.02
1.3	0.0048
1.33	0.0033

Hence with a TSSP-UK's target C_{pk} value of 1.33, the mean will be 4 standard deviations larger than the LSL, and the failure rate will be about 1 in 30,000

4.2 Understanding steel variability through analysis of un-pickled S355MC

A data set comprising measurements from 703 coils was compiled for this study. The chemistry of each individual coil was identified by the chemical analysis carried out on the cast from which the coil was rolled. Note that there may be slight variations between the chemistries of a cast and those of the tensile samples cut from the coils due to inhomogeneity. However with more than 700 data points, there is enough information to identify a trend, even in the event that discrepancy exists between some of the cast and strip chemistries.

To ensure consistency of measurement, all coils analysed in this study were not pickled. The pickling process increases the yield point of the material by approximately 20MPa due to elongation that occurs during levelling and therefore must be taken into consideration when looking at the distribution graphs. This may be counter-intuitive, as most would expect a work hardening effect. In reality all that happens during levelling is the stress-strain graph is smoothed, thus the "anchor point" for measuring yield strength is lost i.e the Yield Point Elongation (YPE) is removed.

The Port Talbot hot mill comprises of, amongst other things, a roughing & edging mill that rolls slabs into a 35mm transfer bar, followed by 7 finishing mill stands and a run out table, as shown in figure 4.26. Temperature data was recorded at various stages along the rolling process as well as at the reheat furnace, coil box, crop shears, run-out table and coiler.
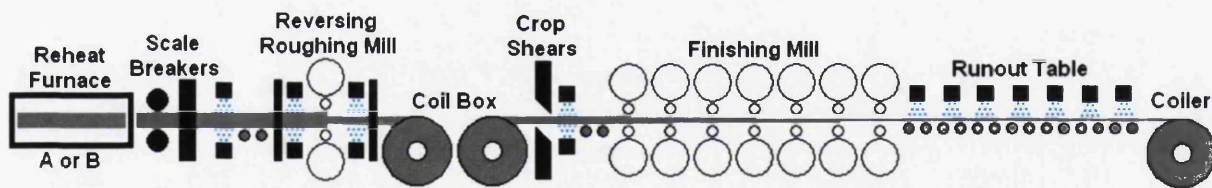
Figure 4.26. Sequence of processing steps at the Port Talbot hot mill

The maximum, minimum and average temperatures, as well as line speed, time between stands and ladle chemistry were measured and recorded at numerous stages along the manufacturing process. This data was subsequently paired with the pre-delivery mechanical test results to form the final data set for analysis. The statistical

96

distribution of each of these factors was then analysed, as well as their correlations to each other. Further statistical analysis then made it possible to establish the importance and influence of each factor with respect to achieving the desired mechanical properties in the end product.

Once the distributions of the mechanical properties, key steel processing data and chemistries were identified, the statistical analysis to determine the influence of each variable was undertaken. Early work involved grouping similar coils in terms of gauge and other variables in order to isolate the effect of numerous parameters. In this way only one factor was considered at a time, and, following which Pearson correlations were then calculated to identify potential relationships. Using this method of analysis, the variables that were found to have the most significant impact on the final mechanical properties were identified with the help of CART (Classification And Regression Tree) and CHAID Chi-squared Automatic Interaction Detector) models available in IBM's SPSS v17 and PASW Modeller v13 software.

After some evaluations it was decided that a CART model would be more suited to the data set than the alternative CHAID model. Since CHAID models perform multiple splits for each parameter, this results in the bottom-end of the models containing low populations in each node, and splits consisting of a population with fewer than 20 samples are normally regarded as unreliable. The CART model employed in this study was built manually to ensure sufficient numbers exist in each split and that each split was systematic and robust i.e. not picking up on small populations of unusual results, as may occasionally be the case for automatically generated models. Though the splits themselves are based on the automatic SPSS calculations

It was found that the yield strength, UTS and elongation results from the sample of 703 coils used for this study approximate to a normal distribution curve, as can be seen in the histograms in figures 4.27, 4.28 and 4.29. The mean and standard deviation for these distributions can also be seen in the figures. From these data it is clear that the values for yield stress are substantially greater than the minimum specified for this grade of material, this was to be expected as the coil were un-

pickled. As mentioned earlier, for consistency purposes only non-pickled coils that have not been through a leveller were considered for this study. The leveller has the effect of reducing the yield strength by around 20MPa. A mean yield strength of 423MPa for non-pickled coils means that very few of the samples contained in this study will fail to meet the relevant European Standards (Euronorms), should the customer require pickled steel.

As discussed earlier, a common measure to assess the performance of the production process for achieving the minimum specifications required for delivery is the process capability index (C_{pk}). Assuming a 20MPa drop in yield stress during pickling, with both other properties remaining the same, the C_{pk} values for each mechanical property upon delivery then become:

$$\text{Yield } C_{pk} = (402.99\text{-}355)/(3 \times 18.529) = 0.863$$
$$\text{UTS } C_{pk} = (487.44\text{-}430)/(3 \times 11.312) = 1.693$$
$$\text{Elongation } C_{pk} = (25.63\text{-}19)/(3 \times 2.313) = 0.955$$

These values are similar to those from the pickled coils manufactured in 2008. A C_{pk} value of greater than 1 means that the mean value is at least 3 standard deviations greater than the lower specified limit. Therefore, theoretically the failure rate should be less than 0.135%, as shown in Table 4.6.

It becomes obvious from this analysis that the variability in yield strength is greater than the variability in UTS, where the standard deviation in yield expressed as a percentage of the mean is 4.38%, the same calculation for UTS stands at only 2.32%. There is also a significant amount of variability in the elongation results, with a sizable sample lying close to the lower specified limit. Its mean value, however, lies at a healthy distance away from the minimum requirement.

Variability in thickness does not have such a predictable distribution as those for mechanical property parameters. It was found that the vast majority of the coil was manufactured to very tight tolerances. The only locations within the coils that had any thickness variability of note were the first and last few metres. On a coil that is

several hundred metres long, one can expect that on average more than 99% of the coil will have virtually no variability worth mentioning with regards to thickness.
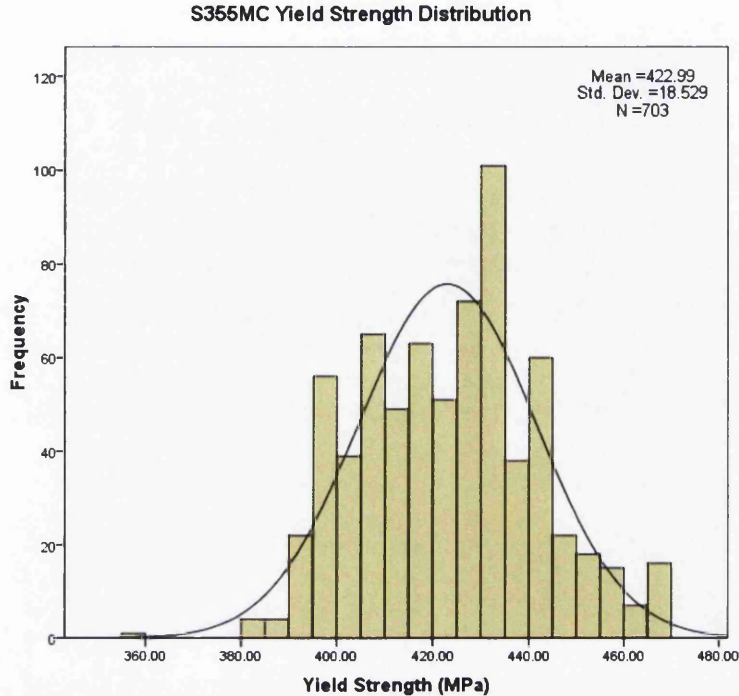
Figure 4.27. Yield strength histogram
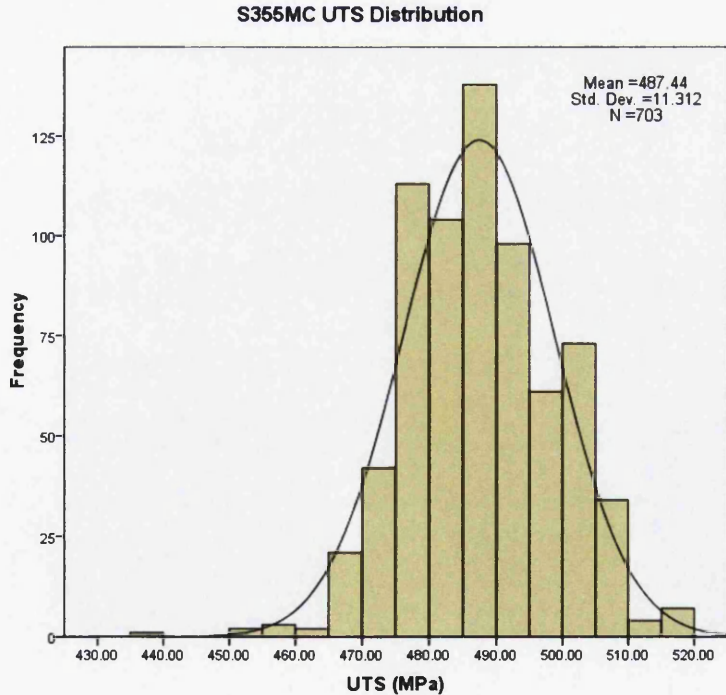
Figure 4.28. UTS histogram

99
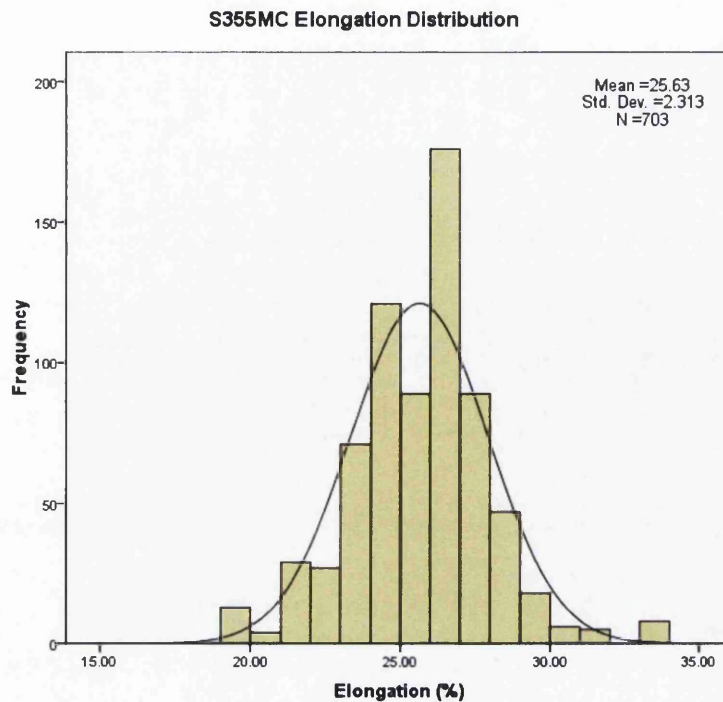
Figure 4.29. Elongation to failure histogram

End users should however note that the first and last few metres may exhibit some variability that are within the tolerances shown earlier in table 4. The distribution of this variability is extremely random and as such cannot be generalised by a standardised distribution curve. If parts are being made that may be sensitive to fluctuations in strip thickness, this can easily be resolved by cutting off a relatively small amount off both ends of the steel coil.

As previously, many different methods were used to investigate the root cause of the variability seen in figures 4.27, 4.28 and 4.29. The end result of that work is shown in the CART model shown later in figure 4.30. This model provides a systematic approach to identify why a coil may have properties at either the lower or higher end of the distribution curve. It was identified that a reasonably strong correlation exists between UTS and Yield Stress, as shown in figure 4.32.

It was therefore no surprise that the CART model showed similar sensitivity to the same variables for both strength properties. As such only one model was required to analyse both UTS and yield. By analysing these results it was pleasing to see that not many production variables had a significant effect on the end properties, leading to

100

suggestions that the process is well controlled and adapts well to producing coils of various thickness whilst using the same cast grade. However it was also surprising that certain parameters such as manganese and sulphur content did not have a significant effect, which will be discussed later.

Note that the CART model splits the original sample of 703 coils by parameters that were found to have a significant effect on the final mechanical properties. Balancing the split for each variable in the CART model required careful consideration. A split into 3 groups (high, medium and low) for each parameter would have been desirable to assess the influence of each parameter. However, this was not possible as dividing the population up too much would have resulted in low populations in each group, and give rise to unreliable results. The dual split that was used for the current study clearly differentiates the influence of each variable and therefore provides an adequately clear tool for describing the influence of each parameter.

The four most significant factors influencing the properties were found to be the strip thickness, the niobium and carbon content, and a combination of two processing variables. This singular processing variable is the difference in the mean surface temperature of a coil between the end of the roughing mill (RM) and the crop shears (CS), ΔT_{RM-CS}. The temperature drop is caused by delays in the coil box, where a significant drop in temperature of around 30°C or above was found to be detrimental to both the UTS and yield strength, however this phenomenon was only found to be significant in thinner gauge coils, as can be seen from the CART model. It was surprising to see that thicker coils were less susceptible to this strength reducing phenomenon. This is possibly due to the thicker coils having increased capacity for maintaining their core temperature and heat energy as compared with thinner products.

The patterns seen when analysing coil thickness and niobium content are very straightforward. Thicker coils tend to be slightly weaker and niobium has a clear strengthening effect. This was to be expected since the strengthening and grain refining properties of niobium are well documented. The analysis of other chemistry was not as definitive. This grade of material is sensitive to changes in carbon

content, though the extent of its sensitivity is masked by other variables. The last row of the CART model illustrates that higher carbon content nodes are generally stronger both in terms of UTS and yield in comparison to low carbon nodes, although this is not always the case.

The most notable exceptions occur in nodes 19 & 20, where the yield strength drops by 3.1MPa and the UTS drops by 1.1MPa. These anomalous results can be explained by investigating the data that comprise these two nodes. It was found that the mean values of other parameters critical to strength were favourable in nodes 19 as compared to node 20. i.e. the mean thickness was less and the mean values for niobium and manganese were greater. Since the CART model splits data by high and low values only, unfortunately a significant amount of variability still exists within each node. As the bottom tier in the CART model contain relatively few samples in each node, the mean values on occasions become less dependable and further investigation may be required.

Not all nodes are significantly different to each other, though the CART model has succeeded in its main objective, which was to investigate the root cause of the variability and define why coils may have mechanical properties close to the upper or lower specified limits. Nodes 20 and 25 highlight this well, where the two nodes are exact opposites in terms of strength critical chemistries and processing conditions. It can be seen that the two sets of data are statistically different to each other by the differences in their means being significantly greater than their standard deviations. This is true for both yield strength and UTS. All other nodes should theoretically, and very nearly do, lie between these two nodes in terms of strength.

Generally, the standard deviations reduce as we go further down each tier in the CART model, though in order to reduce the standard deviations further, the range of values within each parameter split would need to be reduced. i.e. a three or more way split. It can therefore be concluded that coils with yield strength and UTS values close to the lower specified limits are likely to have the following properties: low niobium and carbon content, thick gauge and a high temperature drop in the coil box. Strong coils are likely to have the exact opposite parameters to those previously described.

Figure 4.30. Yield stress & UTS CART model

It was thought that some parameters may have a greater effect on mechanical properties compared to others due to the extent of variability and control within that particular parameter. Therefore the statistical distributions of each parameter were analysed and calculated, and are shown in table 4.7. This information can be used to explain why the niobium content features so prominently in the CART model, and also why the manganese data, an element that is added for strength, could not be used to build a robust CART model. By analysing the standard deviations expressed as a percentage of the mean it is clear that manganese content is very well controlled within this grade of material, where the niobium content within the steel has a greater amount of variability.

The study does not suggest that manganese has no effect on mechanical properties, as it does provide strength. This research suggests only that S355MC material manufactured at TSSP-UK exhibits little variability in manganese content and as such the sensitivity to variability in the content of this element is low. For any pattern to emerge regarding the strength of S355MC in relation to manganese content, a much larger range of values would be required.

Table 4.7. Variability of key parameters

Parameter	Mean	Standard Deviation	Standard deviation (% of mean)
Carbon (%wt)	0.07005	0.004421	6.3
Niobium (%wt)	0.02230	0.001636	7.3
Manganese (%wt)	0.5049	0.02362	4.7
Sulphur (%wt)	0.006367	0.001338	21.0
$\Delta T_{RM\text{-}CS}$ (°C/K) (between roughing mill and crop shears)	31.23	9.833	31.5

One might look at these results and consider there to be a significant amount of variability in the sulphur content. Ultimately however, since the relative amounts are kept so low, and there are many times the required quantities of other elements present such as manganese to absorb and counteract the negative effect of this small amount of sulphur, this possibly has been discounted.

A parameter that also has a large amount of variability and does have a significant impact is the temperature drop between the rougher mill and the crop shears, with a

mean of 31.2°C and a standard deviation of almost 9.8°C, as can be seen in table 4.7 and figure 4.31, this parameter exhibits much greater relative variability than the other parameters.

The fact that there is so much variability in this particular process parameter serves as an underlying reason why it has such an effect on the final mechanical properties of these coils of steel. Although it is defined as the temperature drop between the rougher mill and the crop shears, the vast majority of this temperature drop is caused by delays in the coil box. Potentially procedures could be put in place to reduce the likelihood of such large drops of 40°C or more, thus giving an area of potential process improvement.

Roughing Mill to Crop Shears Temperature Drop Histogram
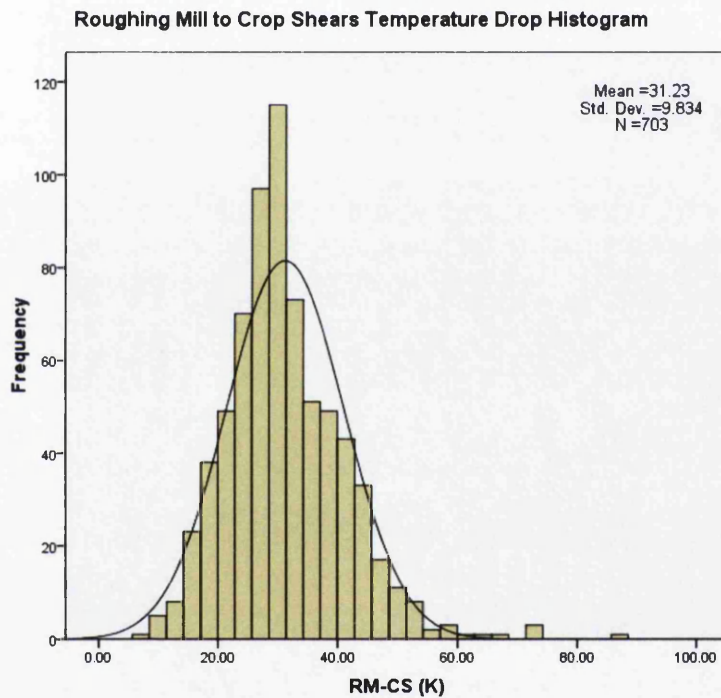
Figure 4.31. Coil box temperature drop histogram

A clear correlation exists between UTS and yield stress, as can be seen from figure 4.32, thus, as mentioned earlier, the fact that the CART model returns similar patterns for both comes as no surprise. It was expected that a negative correlation would exist between strength and elongation. If this was the case a CART model with the same criteria could have established a trend that would enable the prediction of elongation values. Unfortunately as can be seen in figure 4.33, no such correlation exists. Furthermore, no parameters were identified using the many statistical tools

utilised in order to identify a trend for predicting elongation. A general trend exists between strength and elongation when looking at all families of steels, though using only this grade of steel and the parameters previously outlined, as well as many others, no pattern was found to exist.
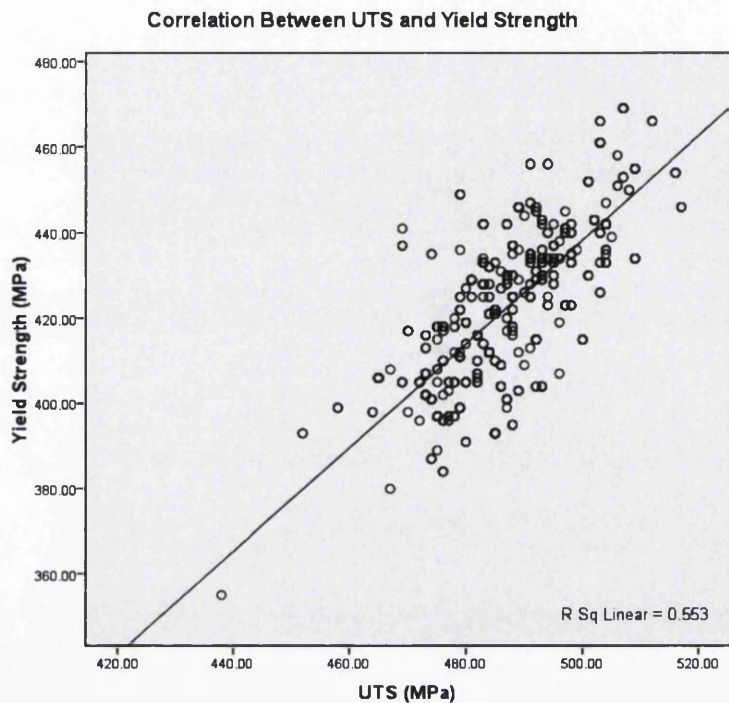
Figure 4.32. Yield strength & UTS correlation
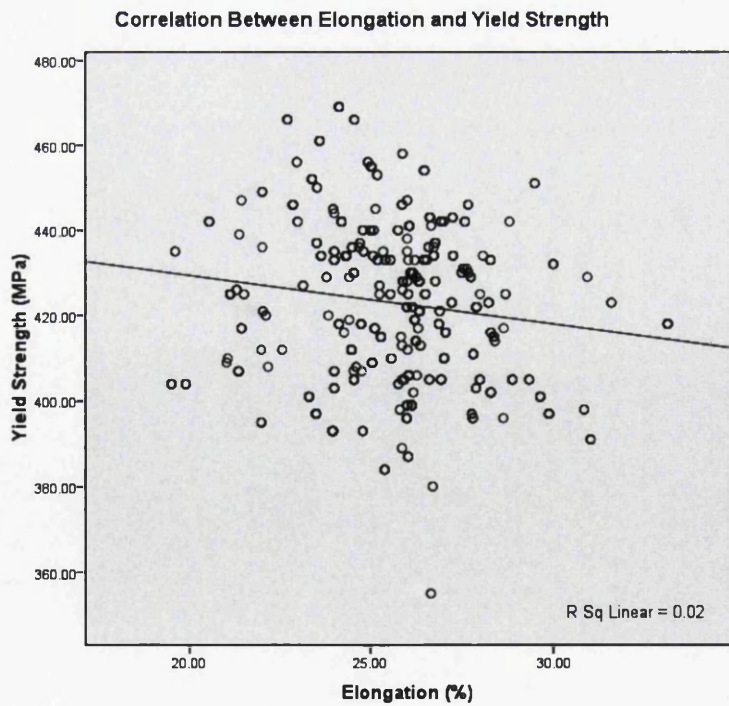
Figure 4.33. Yield Strength & elongation non-correlation

106

Chapter 5 – Fatigue properties of Tenform steel

5.1 Processing Fatigue Data

5.1.1 Comparison of x-axis and y-axis minimisation using least squares method

Before statistical processing of any fatigue data is carried out it is important to establish which curve fitting techniques are most suitable for this project. It was established during the literature survey that least squares fitting of the Basquin relationship was the most well known method of analysing SN data. Curve fitting of this type can be done in two ways, either by minimising the sum of the square of errors in the x-axis or alternatively the y-axis. This is covered in the literature review and the mathematical process was described in order to calculate A and b for the two methods to fit the curve shown below. Note that the same theory also applies when using stress amplitude, which is $\Delta\sigma/2$.

$$\Delta\sigma = A \cdot N_f^{\,b}$$

For this exercise an MS Excel spreadsheet was written which uses the theories described previously, the spreadsheet then generates values for A and b. For comparison of these two methods, the raw data for XF350 as used in the TSSP-UK catalogue was utilised. While the values for these two constants may differ slightly, the end results are extremely similar, with one curve virtually sitting on top of the other, as shown in figure 5.1.

Note that the 'Predicted N' curve uses x-axis offsetting and the 'Predicted Stress' curve uses y-axis offsetting. The Basquin relationship for these both are:

Predicted N: $\Delta\sigma = 1162.75\ N_f^{-0.0652}$

Predicted Stress: $\Delta\sigma = 1144.02\ N_f^{-0.0640}$
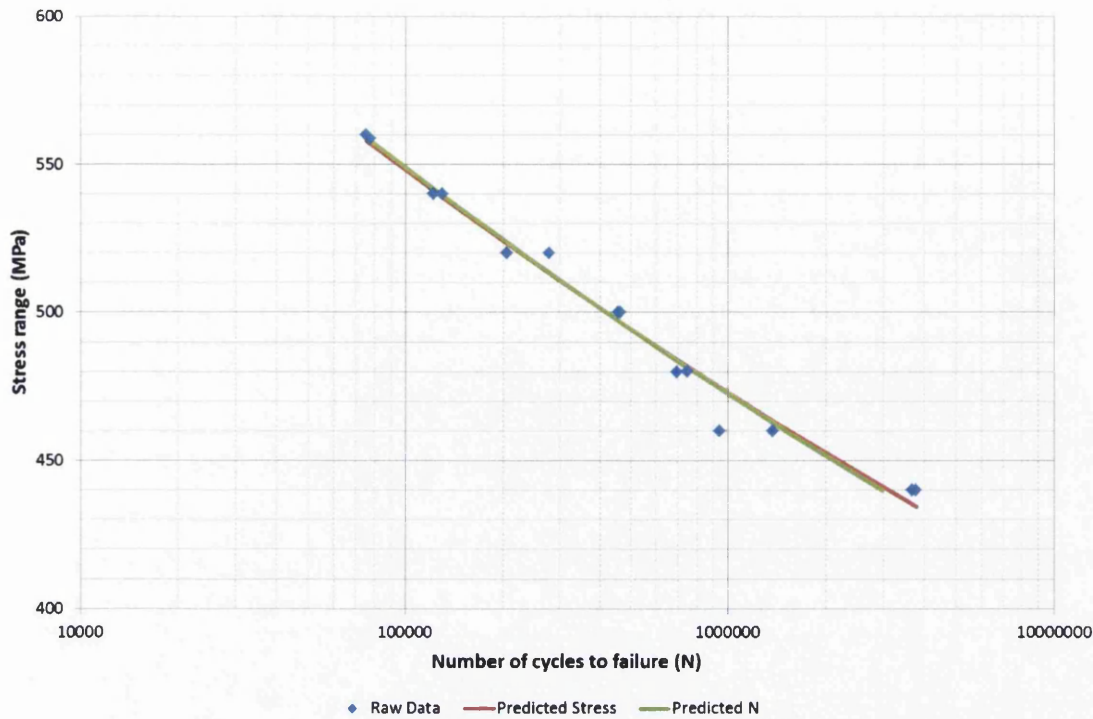
Figure 5.1. Comparison of the two least squares fitting methods

It is very subjective as to which method of offsetting is better, some may argue that x-axis offsetting is better, since whilst fatigue testing the input is stress and the result is the number of cycles to failure – hence the method aims to minimise the sum of the square of errors of results, not inputs. Normally of course the result would be plotted on the y-axis instead of the x-axis, but for historical reasons the graph is plotted with the input on the y-axis and will probably stay that way. The main thing that has been learnt from this exercise, which has been validated by checking the methods with other SN data, is that it makes little difference which method is utilised as both are very similar.

5.1.2 Scatter analysis of SN curves

While it has been proven that it makes little difference as to which method is deployed for curve fitting of the 50% survival (base) line, the statistical processing and curve fitting to determine other (i.e. 99% & 1% survival) curves shows a greater difference between each method. The two most common methods each have similarities, i.e. the first step is to define the standard error (which itself has more than one method – to be discussed later). One method finds the standard error in stress values, while the other finds the standard error in log N values.

Once these values are determined they are usually multiplied by a value of either 2.326 or 3 in order to determine 1% & 99% or 0.13% & 99.87% certainty of survival curves respectively. Note that with standard deviation values of 2.326 and 3, the population that lies between the two curves will be 98% and 99.74% respectively. Furthermore, 3 standard errors either side of the mean gives approximately 1 result in every 370 outside the expected range.

It is important at this time to note the difference between standard error and standard deviation. Depending on the literature read there are numerous definitions and explanations of their differences. Some use standard deviation theory and then call it standard error due to the way it is applied – i.e. a traditional standard deviation is calculated from numerous results with a single mean. With fatigue data processing we are calculating the "standard deviation" where the mean is not fixed and depends on the number of cycles where the specimen failed. Due to this difference it is sometimes called standard error, even though the equation for standard deviation is used. Excel defines its standard error as:

$$\sigma = \sqrt{\left[\frac{1}{n(n-2)}\right]\left[n\sum y^2 - \left(\sum y\right)^2 - \frac{\left[n\sum xy - \left(\sum x\right)\left(\sum y\right)\right]^2}{n\sum x^2 - \left(\sum x\right)^2}\right]}$$

Where standard deviation is defined as:

$$\sigma = \sqrt{\frac{\sum_{i=1}^{N}(x_i - \mu)^2}{N}} = \sqrt{\frac{N\sum_{i=1}^{N}x_i^2 - \left(\sum_{i=1}^{N}x_i\right)^2}{N}}$$

Note that the first equation, which is deployed when using the STEYX function in excel can only to be applied to calculate errors in y-axis values for each x-axis value in the regressed data set. TSSP-UK uses ANOVA within Excel, which is identical to the STEYX method where the x-inputs are log stress and y-inputs are log N. The result returns a standard error for log N, a multiple of this value can then be used to plot a new curve for any percentage survival rate desired.

The standard deviation formula can be used with the raw results, where no regression is required. Again a multiple of this value can be used to calculate any theoretical

survival rate. It can be seen that there are many data processing methods that are acceptable and all are widely used, the many variations are shown in the table below:

Table 5.1. Fatigue Data Processing Options

Least Squares Offsetting	Generation of Certainty of Survival Curves
Minimise sum of x-axis errors^2 (N$_f$)	Standard Deviation theory
	Standard Error theory (STEYX)
Minimise sum of y-axis errors^2 (σ)	Standard Deviation theory
	Standard Error theory (STEYX)

While it has been shown that there is little difference between minimising the sum of x-axis errors^2 (N$_f$) as compared to minimising the sum of y-axis errors^2 (σ), deciding on the most appropriate method for generating certainty of survival curves is the next step in this evaluation process. Although four possible combinations exist, we can ignore the possibility of using the STEYX method with y-axis offsetting, since this regression based method is more suited to the x-axis offsetting technique, where predictions are calculated in logs (fatigue also plotted in logs on x-axis).

Furthermore, using standard deviation theory with x-axis offsetting returns a smaller deviation value than the STEYX method, not only for this data, but for all fatigue tests carried out as part of this research. As can be seen in the next few paragraphs, as well as in figure 5.2, the most conservative options are the best approach for the purposes of this project.

Now that there are only 2 processing methods left to compare, the graph below illustrates the theoretical boundaries of six 'deviations' using the remaining two techniques. Figure 5.2 shows that there is relatively little difference between predicting the number of cycles to failure with the STEYX method, and predicting stress with the standard deviation method, although the standard error method (STEYX) is a little more conservative. Since one data point lies close to the 3SD/SE lines, it would be wise to come to the conclusion that the more conservative estimate is the best option to choose from.
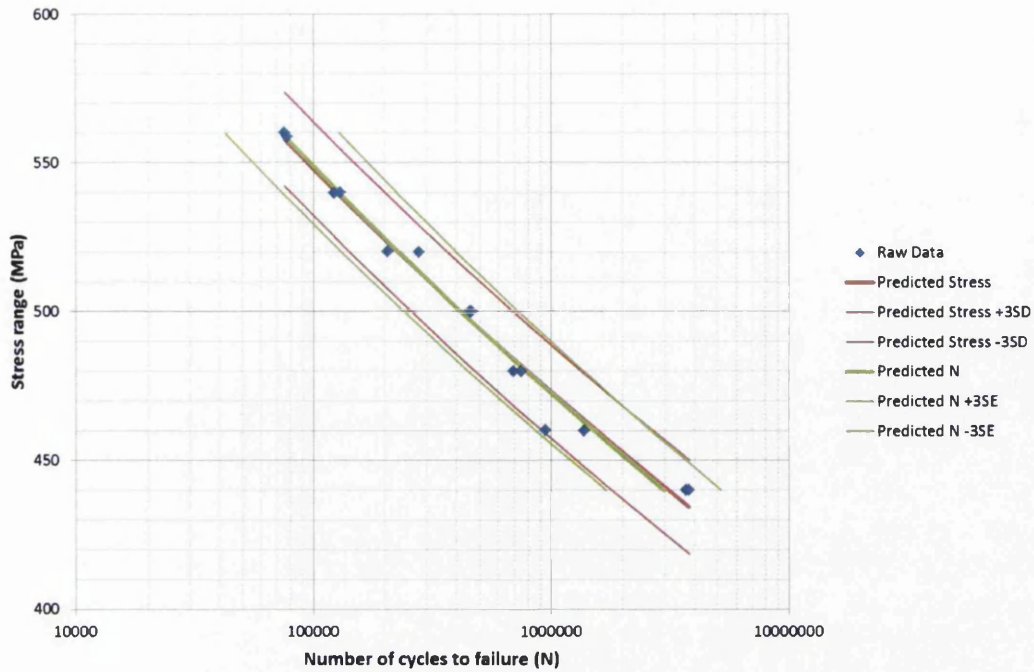
Figure 5.2. Comparison of the two least squares fitting methods with survival rate curves

Note that the thin green lines are not parallel in the graph above, though the red ones are – suggesting a fixed variability in stress range over the whole range of cycles. If the graph was drawn using a log-log scale the scenario would be reversed where the green lines would be parallel and the red lines would not. With only 14 data points it is difficult to give a concrete answer as to which method most accurately describes the statistical behaviour of the material, though as mentioned earlier, at this stage it may appear wise to take the conservative option.

5.1.3 Concluding the preferred statistical fatigue processing method

Even though all four data processing methods have proven to be similar, this comparison of the various methods has provided the tools necessary to decide upon which method to use for the purposes of this project. Since x-axis and y-axis least squares fitting give virtually identical results it has been decided that since the number of cycles to failure is the result and the stress range is the input, it is better to minimise the sum of the square of errors in the number of cycles.

This leaves only two further options, the standard error or standard deviation method. Since least squares fitting is a regression based method, it is logical to use a regression based method to plot the survival rate curves. This is exactly what the STEYX method provides. Furthermore it is slightly more conservative and as such is

111

preferred since fatigue data is highly variable. It is therefore concluded that least squares fitting using x-axis offsetting and STEYX method for determining survival rates is the most appropriate. This gives identical results to the current TSSP-UK method, though ANOVA within Excel is used to calculate the regression.

5.2 S-N Performance of Tenform Products

5.2.1 Background information

It was previously established that the most appropriate way to represent cyclic loading data is by using the Basquin relation in conjunction with x-axis offsetting for the least squares method, where upper and lower bound curves are calculated using the STEYX function within excel. All fatigue data within this section were collected from experimentation at TSSP-UK's Swinden Technology Centre (STC) at Rotherham, with the only exception being the R=0.1 data, which is part of the weld fatigue programme, which was undertaken at Cardiff University. Both grades of Tenform steel (XF350 & XF450) tested used the same specimen geometry as shown in figure 5.5. Note that the specimen was held by hydraulic grips at both ends. Images of the test equipment at STC are shown in figures 5.3 & 5.4, while images of the equipment at Cardiff University are shown in the chapter on weld fatigue.

Figure 5.3. Dartec Fatigue testing machine
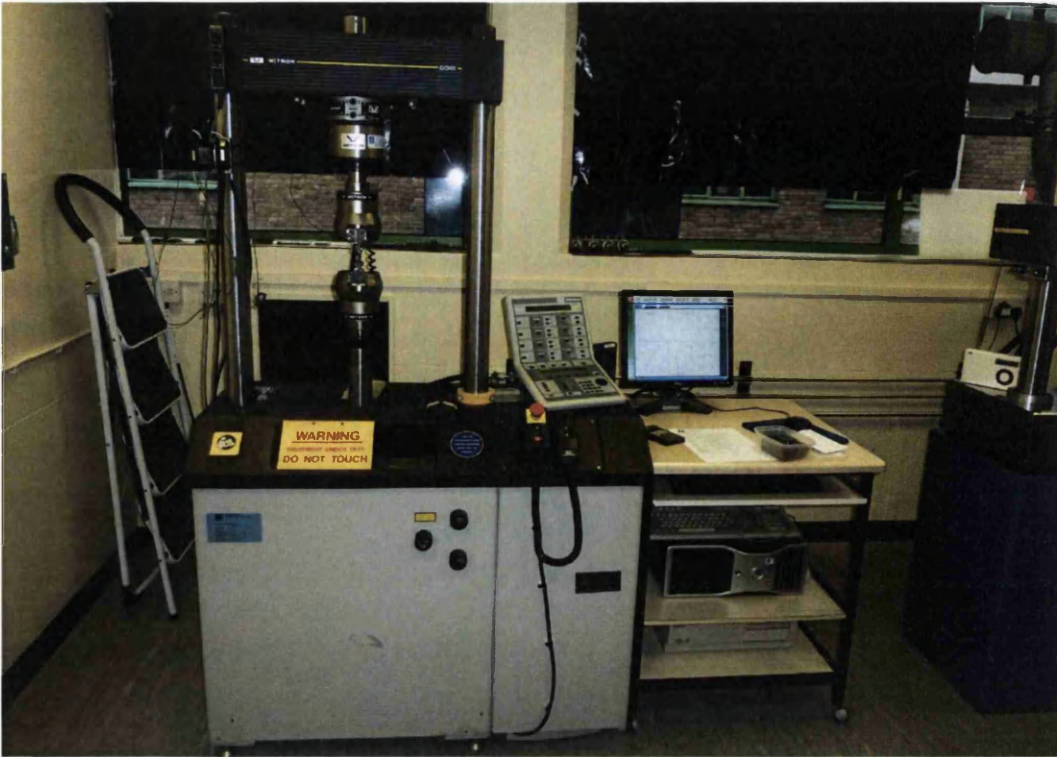
Figure 5.4. Instron Fatigue testing machine
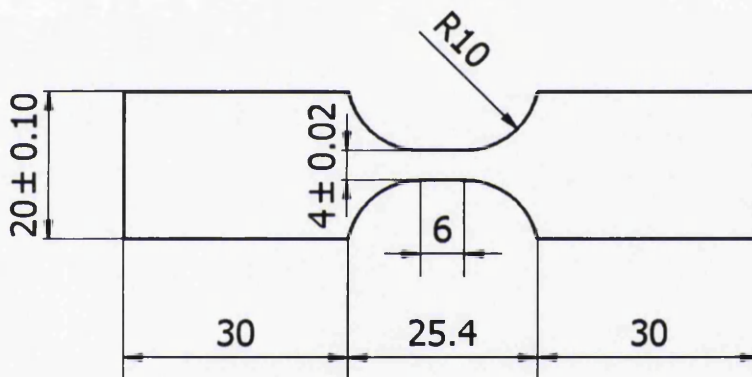
Figure 5.5. Fatigue specimen geometry

This section's aim is not only to define the fatigue properties of these grades of steel, but also to assess the effect of mean stress during cyclic loading. The behaviour of the material under various mean stresses is an important consideration for achieving accurate FE predictions. For most of TSSP-UK's products, the brochure will typically include fatigue data for R=-1. Automotive customers will want to be able to predict the performance of components under a range of various loading conditions, it is therefore essential to establish whether the Goodman, Gerber or Soderberg predictions are sufficient to provide reliable FE predictions.

Another important aspect of this chapter is to evaluate the likely effect of variability in tensile performance is on the cyclical behaviour of Tenform grades. It was shown in chapter 4 that a significant amount of variability existed in yield strength and UTS, it is expected that the statistical distributions of these properties will also have an impact on the consistency of fatigue properties within these grades.

Since the mechanical properties of the specimens that were used for the fatigue results displayed in the TSSP-UK brochure are unknown, it is essential to carry out some experiments whereby the range of possible fatigue performance properties can be estimated based on tensile performance. It may be the case that using standard errors for one fatigue curve is not sufficient to provide an accurate prediction of the range of possible fatigue behaviours within a single steel grade. These numerous factors are all taken into consideration within this chapter.

To summarise, this section contains S-N data for XF350 & XF450 at three R-ratios: -1, -0.5 and 0.05. The results from these experiments can be compared to the information contained within the TSSP-UK brochure, as well as the tensile behaviour of samples cut from the same coil.

5.2.2 XF350 S-N Curves

The pickled & oiled XF350 steel sheet used to produce the data for the following tables & graphs were all 3mm thick. Mechanical properties for the material evaluated in this section are shown in table 5.2, where table 5.3 shows the raw data following SN trials on this material, as well as the data used for the TSSP-UK brochure. All S-N curves displayed within this section are from longitudinally cut samples.

Table 5.2. Tensile data of fatigue specimens

Data Set Samples	Yield Strength (MPa)	UTS (MPa)	Total Elongation (%)
XF350 – Longitudinal	394.0	473.0	30.83
XF450 – Longitudinal	468.8	539.6	25.7

Numerous graphical representations are generated from the data in table 5.3, these include the fatigue curves of each, along with their Basquin exponents and coefficients. These are of particular interest for all automotive users, as well as the upper and lower confidence limits, or standard errors. These are illustrated in the graphs shown in figures 5.6, 5.7, 5.8 and 5.9 for each data set in the table.

Other S-N curves that are of interest are the comparison of the TSSP-UK brochure data and the recently tested STC data. It is fair to compare these two results directly as they are both for the same material tested longitudinally, this graph can be seen in figure 5.10. The final S-N graphical representation that is of interest is a plot of the Basquin least fit curves of all STC fatigue results on one set of axes, seen in figure 5.11. This allows direct visual comparison as to the effect of mean stress, which is discussed in greater depth in subsequent sections.

Table 5.3. XF350 S-N data

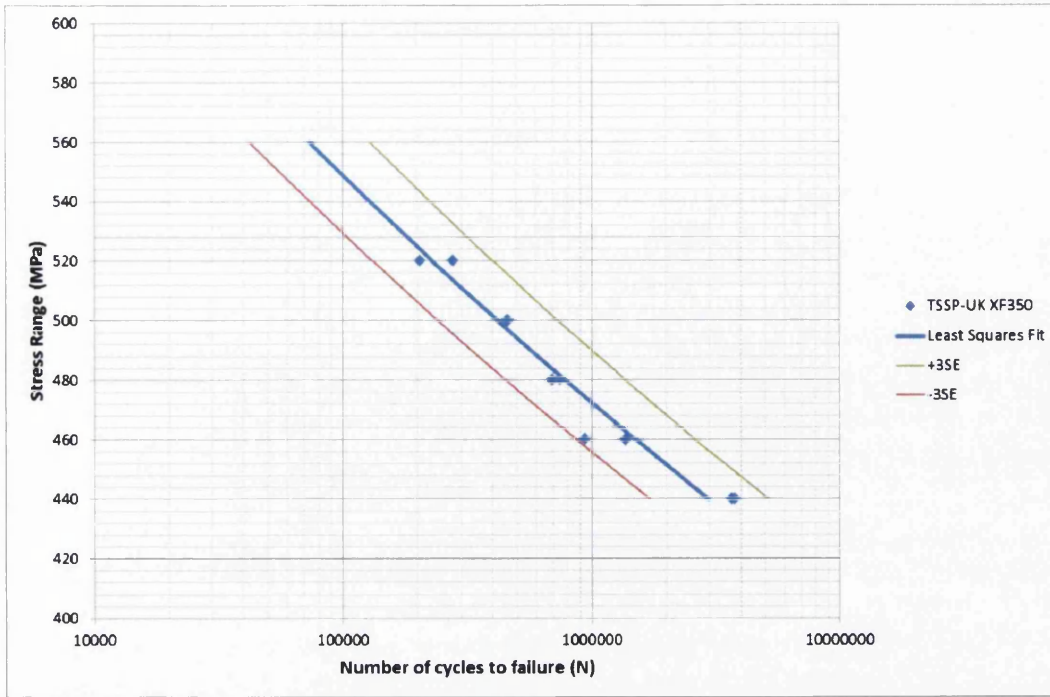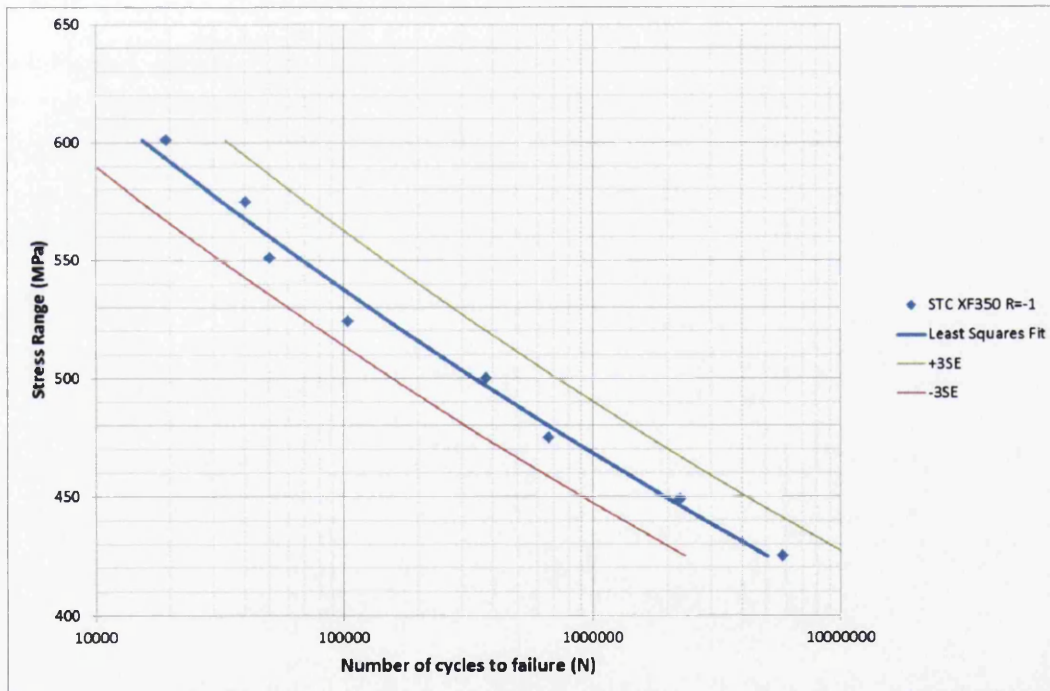| XF350 Brochure Data (R=-1)		XF350 STC Data (R=-1)		XF350 STC Data (R=-0.5)		XF350 STC Data (R=0.05)	
N (Cycles)	Stress Range (MPa)	N (Cycles)	Stress Range (MPa)	N (Cycles)	Stress Range (MPa)	N (Cycles)	Stress Range (MPa)
75490	560	19364	601	23383	525	258961	380
77430	559	40639	575	78658	500	308338	380
122255	540	50710	551	233229	474	902267	370
129846	540	104612	524	255268	475	1544845	360
205089	520	377152	500	482303	450	1792615	350
278521	520	670846	475			3160657	350
456311	500	2256272	449				
463300	500	5837477	425				
694805	480						
748026	480						
943374	460						
1370574	460						
3672039	440						
3777990	440						

Figure 5.6. TSSP-UK R=-1 S-N curve
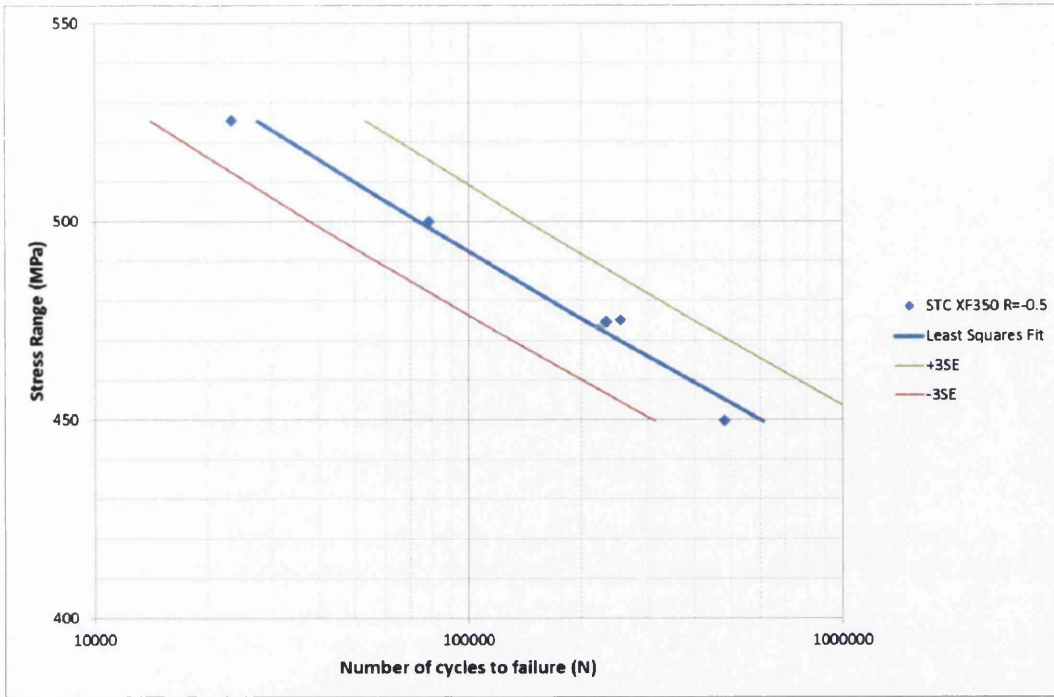

Figure 5.7. STC R=-1 S-N curve

116

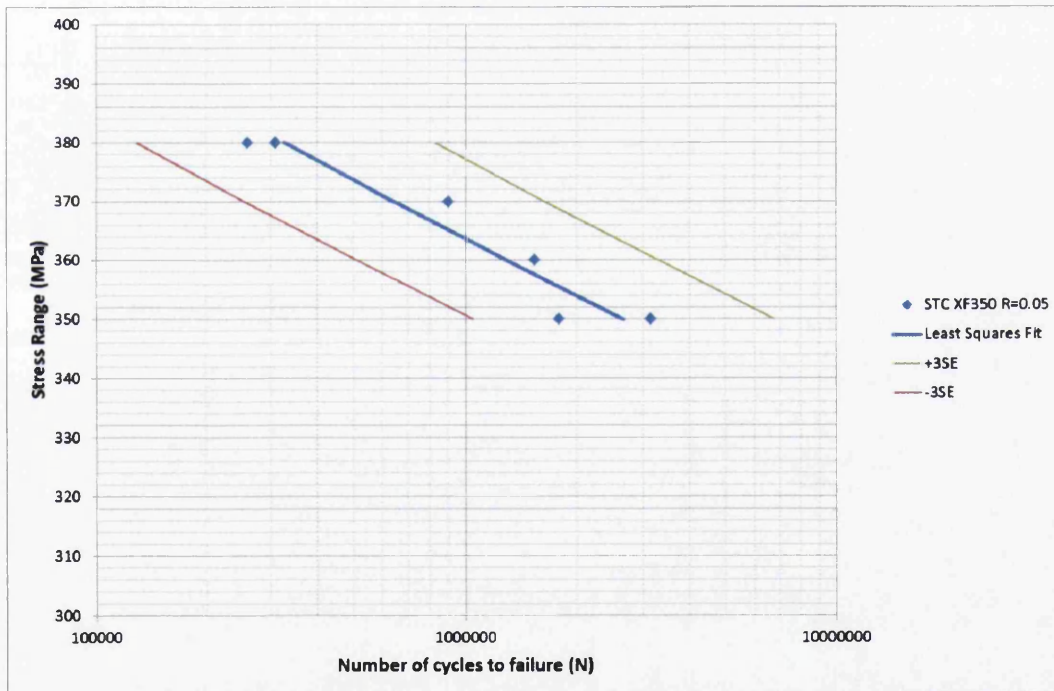Figure 5.8. STC R=-0.5 S-N curve

Figure 5.9. STC R=0.05 S-N curve

117
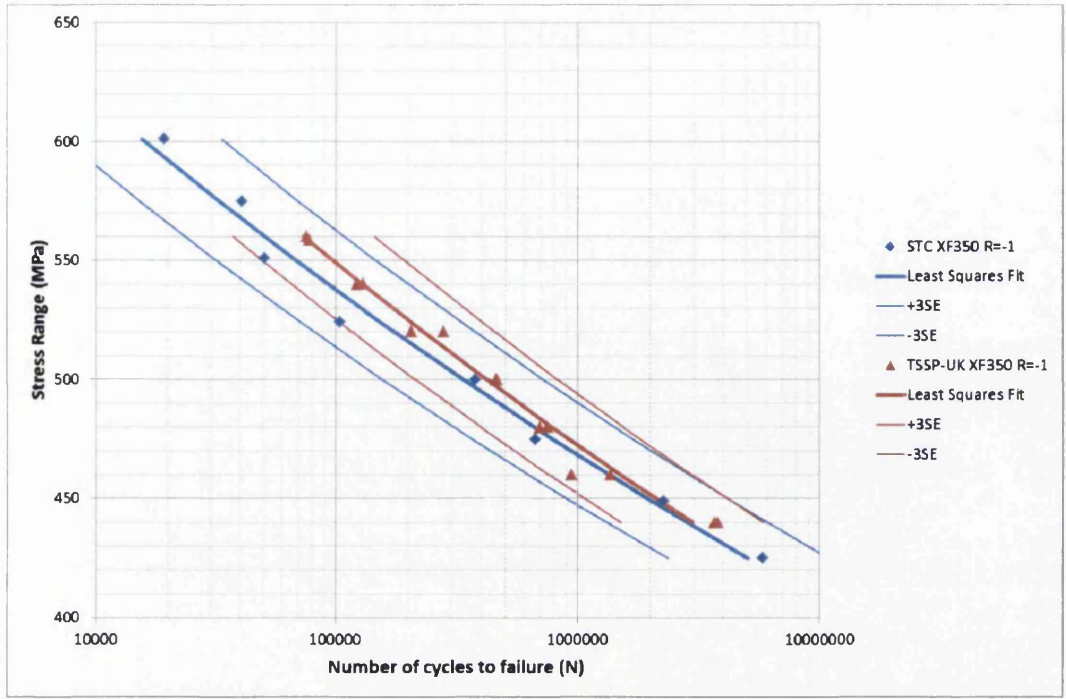
Figure 5.10. STC R=-1 & TSSP-UK R=-1 S-N curves
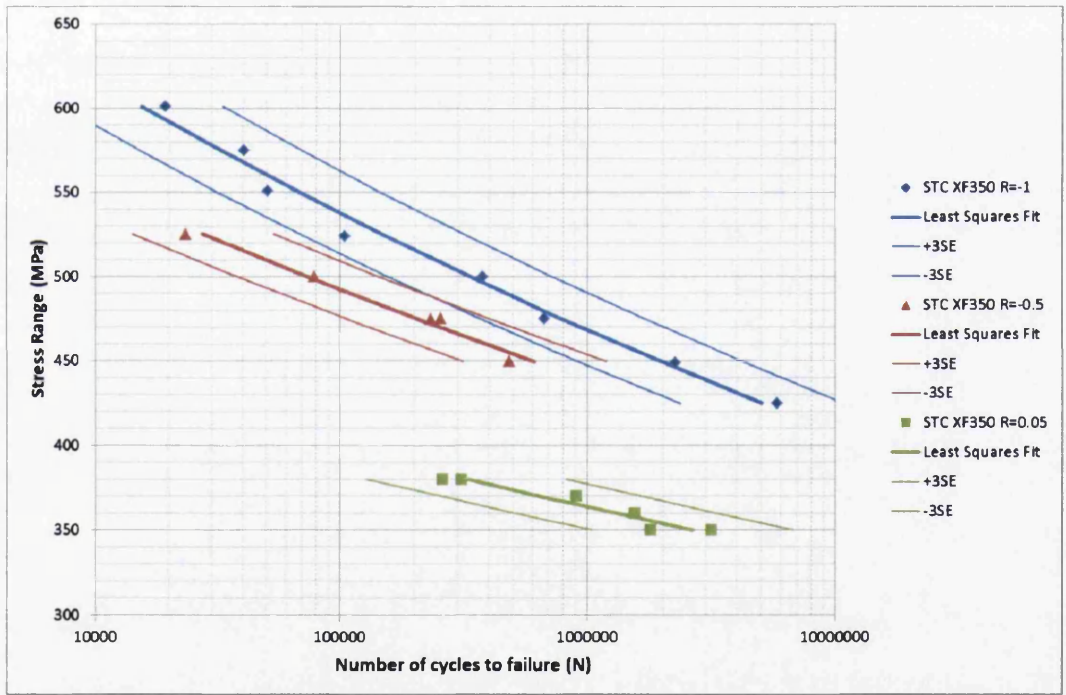
Figure 5.11. All STC XF350 S-N curves

118
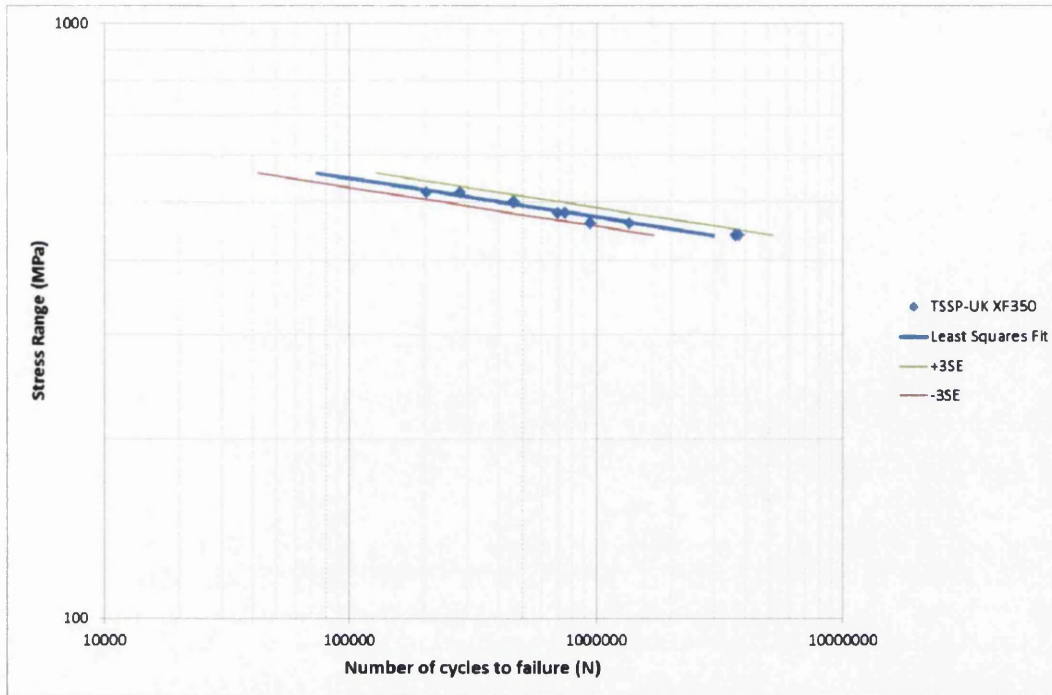
Figure 5.12. TSSP-UK R=-1 S-N curve as a log-log plot

The S-N curves shown in figures 5.6 to 5.11 provides numerous pieces of information which are essential for developing robust designs. Each graph on its own provides automotive users with crucial information that is required to engineer reliable components, but by analysing them simultaneously larger patterns of interest appear. Note that although the gradient of the graphs appear very negative, they are relatively 'shallow', the reason for this appearance may be due to the scale of the graphs. For this reason figure 5.12 was added to show the data from the TSSP-UK brochure results in a log-log plot, which some engineers & researchers prefer. It was however decided that a log normal plot was more usable since it made greater use of space and is more distinguishable.

By analysing figures 5.7, 5.8 and 5.9 it can be seen that increasing the mean stress during cyclical loading has two effects on this grade of material. One is the well published observation that higher mean stresses have the effect of reducing the stress range materials can withstand. This can also be observed by the fact that the Basquin exponent gradually reduces with increased mean stress. Hence the other observation that the gradient of the curves reduces with increased mean stress, i.e. the curves that represent data from higher mean stresses become more horizontal, this is especially visible by looking at figure 5.11 as well as the values for the Basquin coefficients in

119

table 5.4. Despite a pattern emerging regarding the nature of the S-N curves at various mean stresses, no pattern exists regarding the standard errors, where the average standard error for all tests stands at 0.1LogN.

It can be seen that despite the TSSP-UK brochure S-N data being much older than the recently tested STC material, both sets of results are comparable. This may be due to the fact that the STC tested material had a yield strength and UTS of 394MPa and 473MPa respectively, which is reasonably close to the mean for this grade of steel, as can be proven from the data in chapter 4.

Table 5.4. Processed XF350 S-N data

XF350 Data Set	Basquin Coefficient (A), (MPa)	Basquin Exponent (b)	Standard Error (logN)
Brochure Data (R=-1)	1162.8	-0.0652	0.0806
STC (R=-1)	1071.8	-0.0599	0.1106
STC (R=-0.5)	877.1	-0.0502	0.0964
STC (R=0.05)	624.8	-0.0392	0.1349

5.2.3 XF450 S-N Curves

The XF450 steel sheet used to produce the data for the tables & graphs in this section were all 3mm thick, however the steel was not pickled as the XF350 was. Table 4 shows the raw data following SN trials on this material, as well as the data used for the TSSP-UK brochure. All S-N curves displayed within this section are from longitudinally cut samples and are shown in figures 5.13-5.18.

The S-N graphs are displayed in the same fashion as the XF350 data in the previous section, with individual graphs for each curve as well as one showing 3 R-ratios on one set of axes and one graph comparing TSSP-UK brochure material to the STC tested material. Despite being in the same family of HSLA steels as XF350 (Tenform), the cyclical loading results for this grade of material are significantly different to their lower strength counterpart. The main surprise with this material was how the steel performed at a stress ratio of -0.5, with XF350 a gradual pattern existed with, whereby an increased mean stress resulted in a decreased stress range. With XF450 the R=-0.5 curve was very similar to the R=-1 curve. This can be seen in figure 5.18 and also by analysing the Basquin properties in table 5.6.

Table 5.5. XF450 S-N data.

XF450 Brochure Data (R=-1)		XF450 STC Data (R=-1)		XF450 STC Data (R=-0.5)		XF450 STC Data (R=0.05)	
N (Cycles)	Stress Range (MPa)	N (Cycles)	Stress Range (MPa)	N (Cycles)	Stress Range (MPa)	N (Cycles)	Stress Range (MPa)
91861	660	1027	800	36138	625	6089	500
97294	660	7466	700	75435	600	87737	475
135076	640	10080	700	80689	625	114306	475
188311	619	10364	700	126774	600	118950	463
256900	600	19829	675	160132	575	161634	463
269865	600	23242	675	174992	575	212014	450
366319	580	25341	675	274026	550	295439	450
1063671	559	30307	650	391971	550	2742363	425
1313171	540	33854	650	472325	525	4532575	437
1768188	540	36327	650	503613	525		
		62246	625				
		63657	625				
		90830	625				
		92245	600				
		98953	600				
		114185	600				
		159104	575				
		208608	575				
		278699	575				
		306595	550				
		312231	525				
		376640	550				
		435506	525				
		494290	550				

Table 5.6. Processed XF450 S-N data

XF450 Data Set	Basquin Coefficient (A), (MPa)	Basquin Exponent (b)	Standard Error (logN)
Brochure Data (R=-1)	1483.1	-0.0715	0.0896
STC (R=-1)	1345.6	-0.0702	0.1306
STC (R=-0.5)	1464.5	-0.0778	0.1163
STC (R=0.05)	635.2	-0.0264	0.2888

Comparing the properties of the STC tested material to those contained in the TSSP-UK brochure, it can be seen that the STC material has a reduced resistance to fatigue failure. This observation can be explained by the relatively low tensile properties. The yield strength and UTS were 469MPa and 540MPa respectively, whereas, if the material was pickled it would have a reduced yield strength, as mentioned previously in chapter 4.

Also mentioned in chapter 4 were the mean tensile properties upon delivery of these products, where although XF450 did not have a traditional bell curve for the distribution of these properties (for reasons detailed in chapter 4, such as re-grading of material resulting in a broken dataset), the mean for UTS stood at 560MPa. Combining this information with the fact that the yield strength would very likely be at the lower specified limit had the material been pickled, and it makes perfect sense that the fatigue properties were modest. This information also asks questions about the true fatigue properties of coils, given that variability exists in tensile properties. This is discussed in greater depth in subsequent sections.
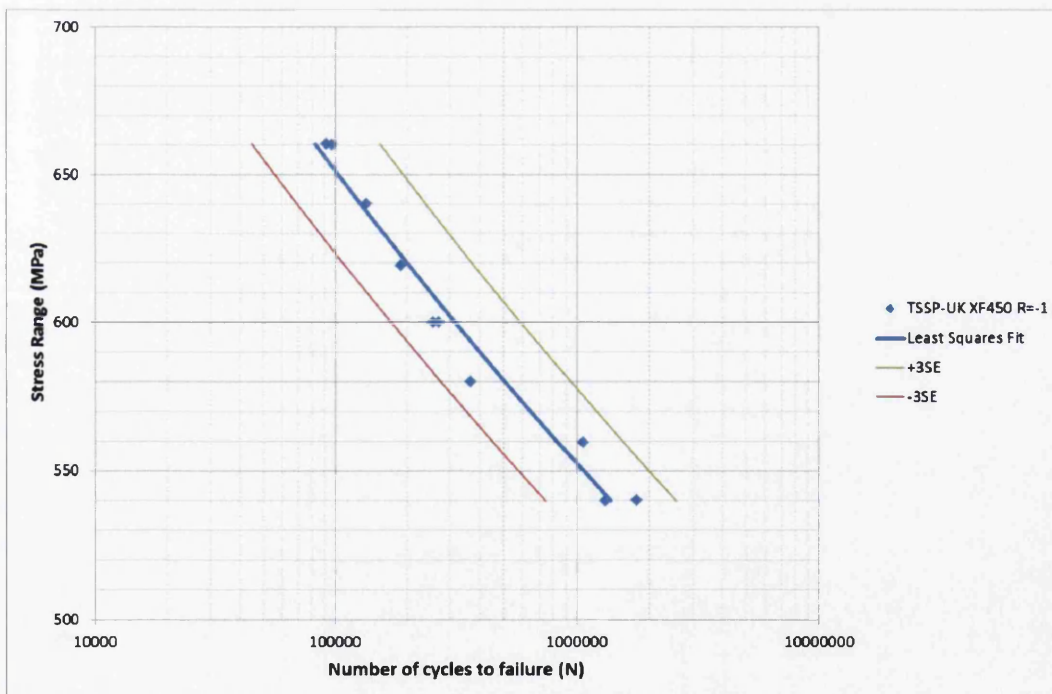
Figure 5.13. TSSP-UK R=-1 S-N curve
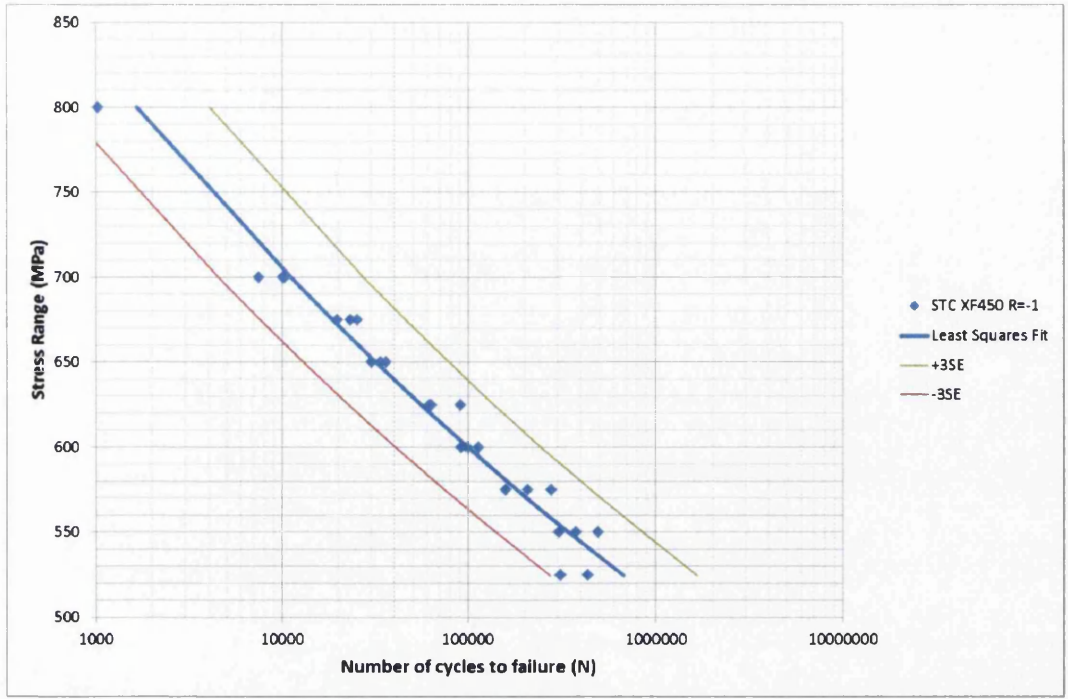
Figure 5.14. STC R=-1 S-N curve
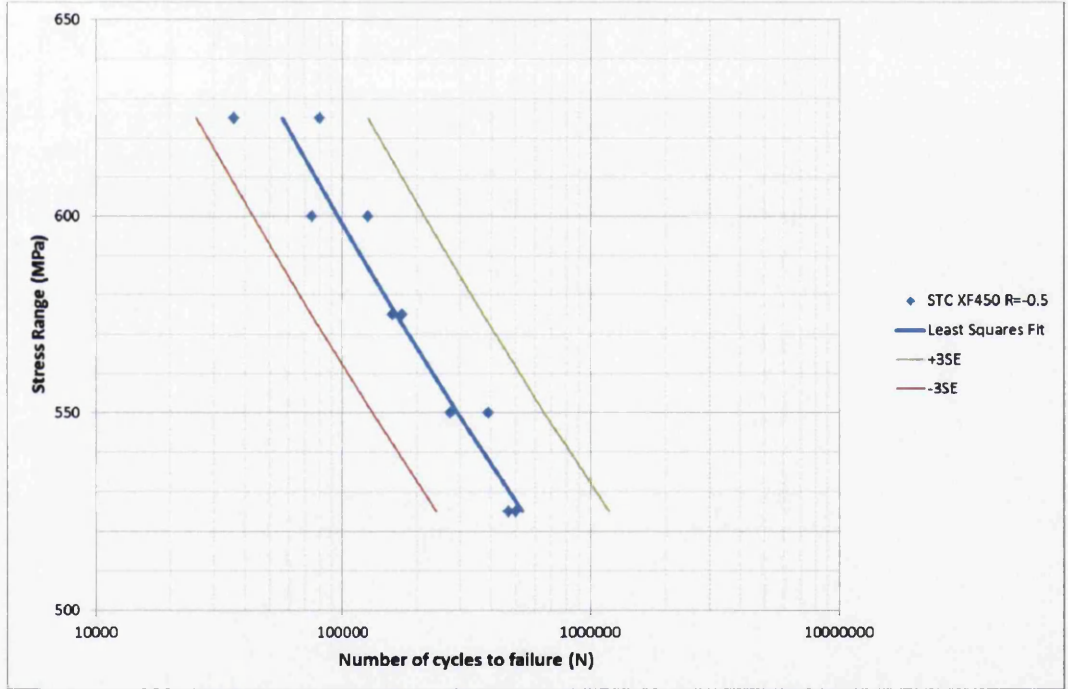
Figure 5.15. STC R=-0.5 S-N curve

123
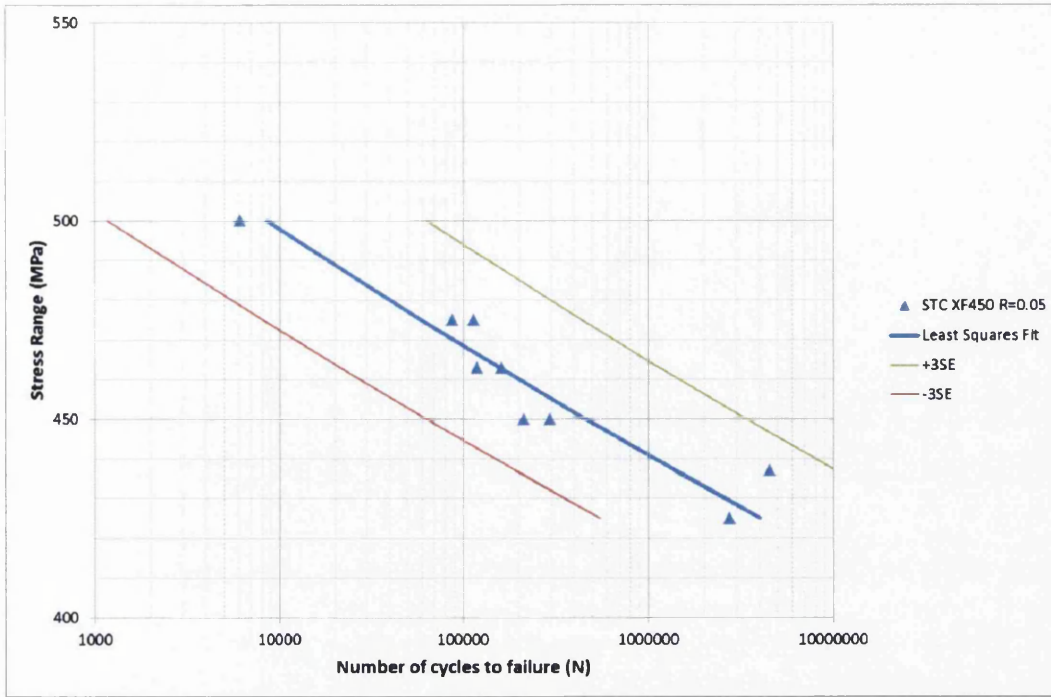
Figure 5.16. STC R=0.05 S-N curve
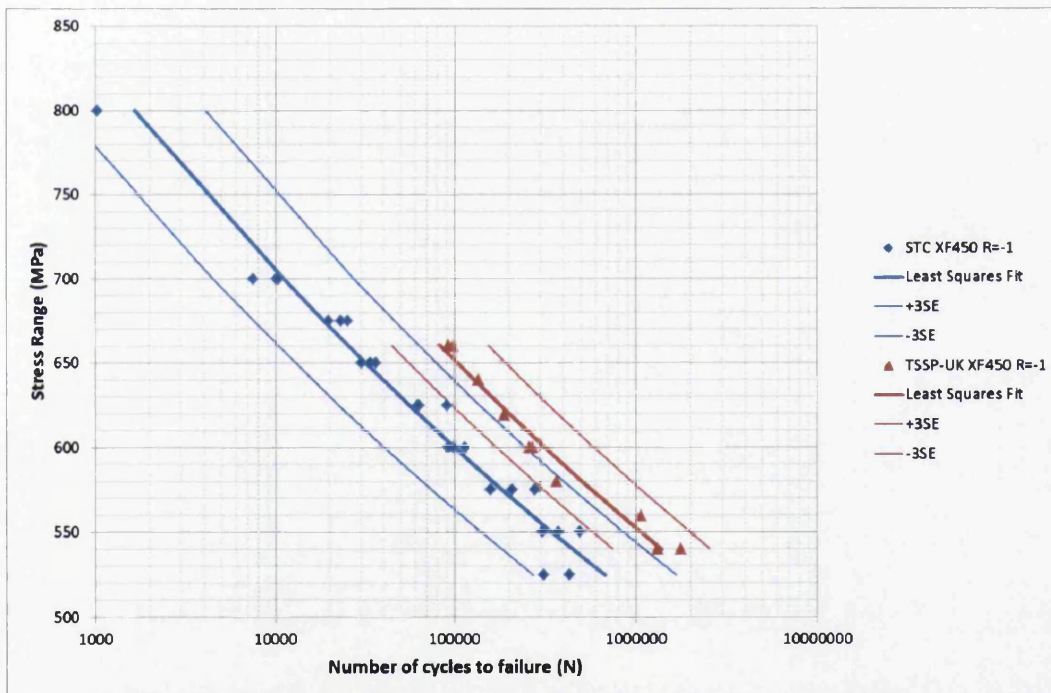
Figure 5.17. STC R=-1 & TSSP-UK R=-1 S-N curves

124
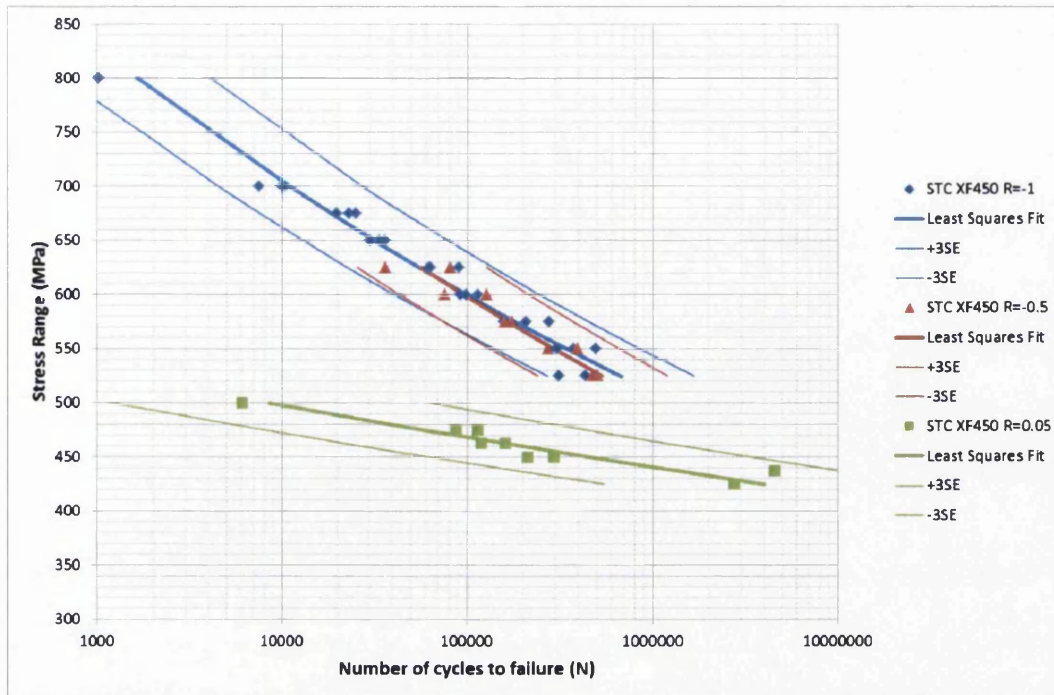
Figure 5.18. All STC XF450 S-N curves

5.3 Effects of mean stress on the fatigue behaviour of Tenform products

As fatigue testing is a time consuming and expensive operation, quite often S-N data for any given material may only be available for one single stress ratio, typically R=-1 or R=0.1. The actual loading conditions of structural automotive components associated with chassis and suspension may differ significantly from the fatigue data available for the material.

To combat this, modern FE packages normally utilise one of three methods to correct for the effects of mean stress. They are the Goodman, Gerber and Soderberg methods as described in the literature review. This section aims at identifying the true nature of Tenform material with regards to its performance at multiple stress ratios. This information can then be used to ensure that TSSP-UK customers are deploying the most accurate FE tools available in order to maintain product reliability.

Although the effects of mean stress can be displayed in numerous ways, the most common method now used is the Haigh diagram. These diagrams are capable of displaying many fatigue tests on a single pair of axes, thus hundreds of hours of fatigue experiments can be condensed into a single graph. The previous section

125

identified that the cyclical behaviour of XF350 was different to XF450 under various mean stresses, the Haigh diagram for each of these materials also highlights this difference. These can be seen in figures 5.19 and 5.20.
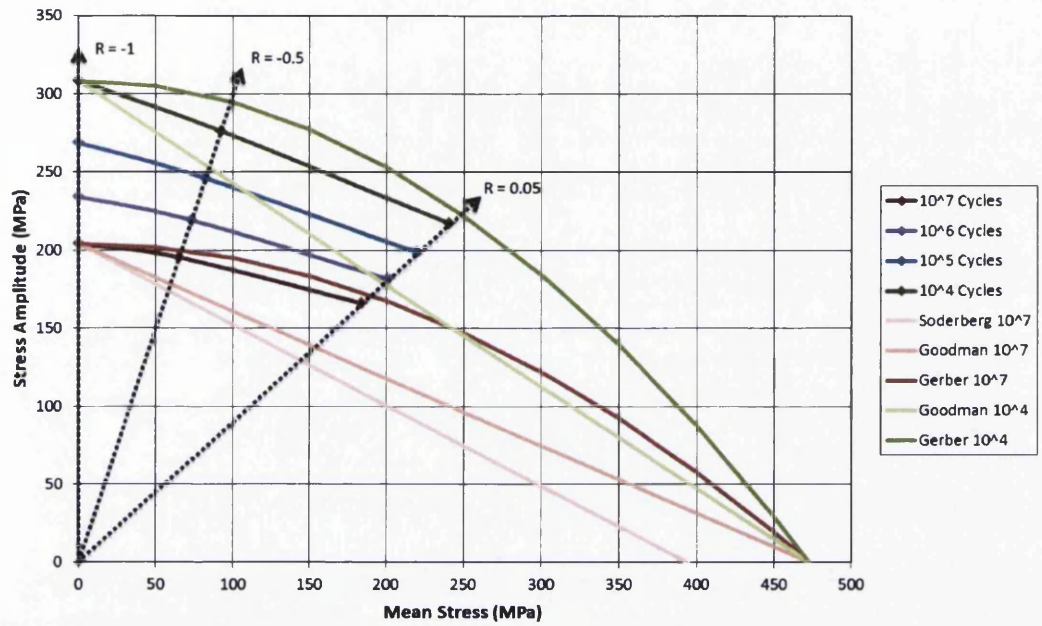
Figure 5.19. XF350 Haigh diagram
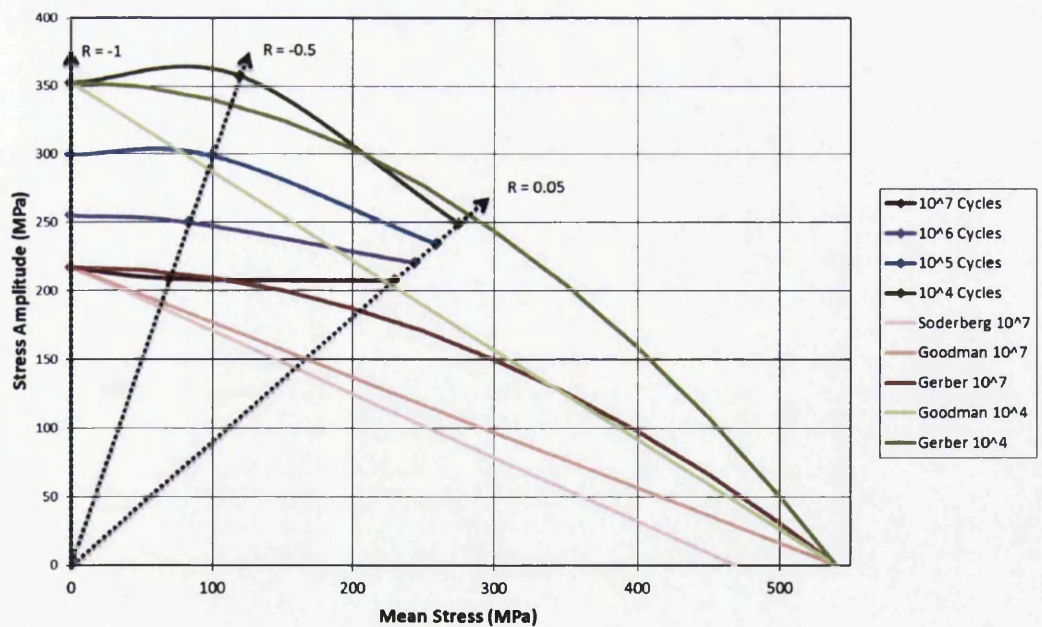
Figure 5.20. XF450 Haigh diagram

126

Before looking at the results themselves, it is important to explain the nature of each curve and what they represent. Using the least squares regression for each SN dataset, the stress range and subsequently the stress amplitude were calculated for lives of 10^4, 10^5, 10^6 and 10^7 cycles. In order to calculate what the theoretical mean stress would be at any given stress ratio, the three definitions for R-ratio, stress range and mean stress were used to assemble a new definition for mean stress based on the stress ranges and R-ratios only, this equation is shown below.

$$\sigma_m = \frac{\sigma_{max} + \sigma_{min}}{2} \ldots (1)$$

$$\Delta\sigma = \sigma_{max} - \sigma_{min} \ldots (2)$$

$$R = \frac{\sigma_{min}}{\sigma_{max}} \ldots (3)$$

Where:

σ_m is mean stress

σ_{max} is maximum stress

σ_{min} is minimum stress

$\Delta\sigma$ is stress range

R is fatigue stress ratio

From (3), we obtain:

$$1 + R = 1 + \frac{\sigma_{min}}{\sigma_{max}} = \frac{\sigma_{max} + \sigma_{min}}{\sigma_{max}} \ldots (4)$$

and

$$1 - R = 1 - \frac{\sigma_{min}}{\sigma_{max}} = \frac{\sigma_{max} - \sigma_{min}}{\sigma_{max}} \ldots (5)$$

Divide (4) by (5), we get

$$\frac{1+R}{1-R} = \frac{\sigma_{max} + \sigma_{min}}{\sigma_{max} - \sigma_{min}} \ldots (6)$$

Substitute (1) and (2) into (6), we obtain

$$\frac{1 + R}{1 - R} = \frac{2 \cdot \sigma_m}{\Delta\sigma}$$

Therefore, we derive the following relationship:

$$\sigma_m = \frac{1 + R}{2 \cdot (1 - R)} \cdot \Delta\sigma$$

The explanation above illustrates how the mean stress and alternating stress were calculated, thus this explains how the 12 data points were plotted on the graph i.e. 3 points for each fatigue life limit or four points for each stress ratio. The other four lines/curves on the graph are plotted using the definitions for the Goodman, Gerber and Soderberg methods as described in the literature review.

A number of conclusions can be drawn from these graphs, firstly it is clear that none of the mean stress correction methods accurately account for tests set at various R-ratios. Much of the literature on this subject suggests that the true effects lie somewhere between the Goodman and Gerber predictions. This is generally true for both materials tested in this study. Of all mean stress correction methods it is the Gerber that method provides the most accurate predictions for both materials, however engineers must be cautious when using this method. It can be seen from the graphs that Gerber tends to over-predict material capabilities, thus using this method may result in unreliable products if relying solely on this technique without cross referencing against other procedures.

What this information tells us is that in order to make accurate predictions regarding the cyclic behaviour of automotive products made of Tenform steel it is insufficient to only use data from a single R-ratio since all three mean stress correction methods return inaccurate predictions. By using the Goodman and Gerber techniques engineers may at least be reasonably confident that the true behaviour of the material more than likely lies somewhere between the two and therefore will have some kind of range to work within. Unfortunately, although the difference between the two in terms of stress amplitude may be relatively small, transferring this data into life predictions could give massively different results given that the gradient of many the fatigue curves generated as part of this project are fairly shallow.

Note that for the purposes of FE modelling, it was later required to obtain fatigue data at an R ratio of 0.1. Due to the fact that this data was obtained by testing on a different machine and location (Cardiff University), coupled with the fact that it was from a different coil (of the same grade, but similar tensile properties), it was decided not to show this data with the other Haigh diagram. However, since the calibration of both machines are up to date and the tensile properties were similar to

each other, the results plotted on a Haigh diagram ties in nicely with the general trend. This trend largely follows other literature that suggests Gerber may be the more accurate, though the true result lies somewhere between Goodman and Gerber. This can be seen in figure 5.21, where the data for the R=0.1 data may be seen in chapter 6.
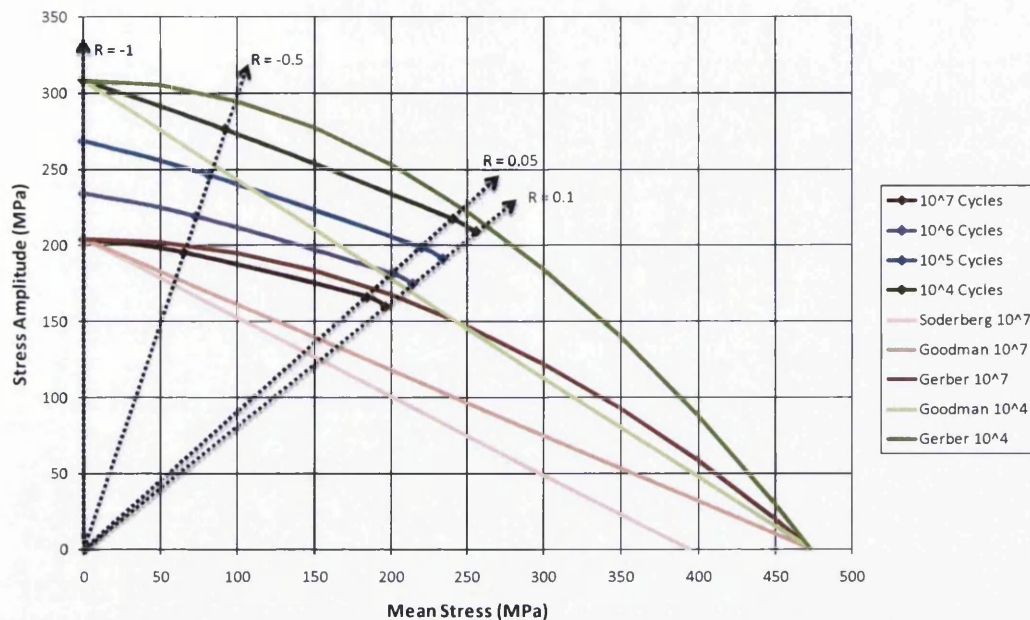
Figure 5.21. XF350 Haigh diagram with additional R-ratio

5.4 Variability in the fatigue performance of Tenform products

Chapter 4 identified that a significant amount of variability exists in the tensile performance of Tenform products, this section aims to identify what effect variability in yield strength and UTS has on fatigue performance. All Tenform grades within TSSP-UK have similar chemistries and thermo-mechanical processing routes, hence sometimes coils of XF450 that have chemical compositions significantly lower than the target and also suffer from low strength may be rebranded XF400. It is therefore reasonable to suggest that if a trend exists between tensile performance and fatigue performance between a range of Tenform products, then the same principles can be used to describe the variability within a single grade.

Three sets of samples were chosen for this work, they were selected to emulate similar ranges in tensile strengths as those in chapter 4. These three sets of specimens are transversely cut XF350, transversely cut XF450 and longitudinally cut XF450. Note that the longitudinally cut XF450 is the same data set that was

129

previously studied in this chapter. The processed and raw fatigue results are shown in tables 5.7 and 5.8 respectively, where the tensile data is shown in table 5.9.

Table 5.7. Processed fatigue data for variability study

Fatigue Variability Data Set	Basquin Coefficient (A), (MPa)	Basquin Exponent (b)	Standard Error (logN)
XF350 – Transverse (R=-1)	1059.2	-0.0625	0.2711
XF450 – Transverse (R=-1)	1489.4	-0.0735	0.1958
XF450 – Longitudinal (R=-1)	1345.6	-0.0702	0.1306

Table 5.8. Fatigue data for variability study

XF350 – Transverse (R=-1)		XF450 – Transverse (R=-1)		XF450 – Longitudinal (R=-1)	
N (Cycles)	Stress Range (MPa)	N (Cycles)	Stress Range (MPa)	N (Cycles)	Stress Range (MPa)
15401	550	839235	550	1027	800
1085076	450	203200	600	7466	700
71935	525	2464091	525	10080	700
363335	500	410671	575	10364	700
26158	550	226040	625	19829	675
112348	525	83118	650	23242	675
230077	475	40577	675	25341	675
444537	500	203388	600	30307	650
289743	475	127104	650	33854	650
1250886	450	300602	550	36327	650
1122962	425	21090	700	62246	625
				63657	625
				90830	625
				92245	600
				98953	600
				114185	600
				159104	575
				208608	575
				278699	575
				306595	550
				312231	525
				376640	550
				435506	525
				494290	550

Table 5.9. Tensile data of fatigue specimens

Data Set Samples	Yield Strength (MPa)	UTS (MPa)	Total Elongation (%)
XF350 – Transverse	399.7	474.3	27.9
XF450 – Longitudinal	468.8	539.6	25.7
XF450 – Transverse	502.2	549.6	22.5

From analysing tables 5.7 to 5.9 it is clear that a trend exists between tensile performance and fatigue performance. This is more easily seen in figure 5.22, where all three curves are separated significantly by their properties. Identifying the major contributor(s) to the difference in these fatigue curves will help us understand the correlation between the variability identified in chapter 4 and fatigue performance.
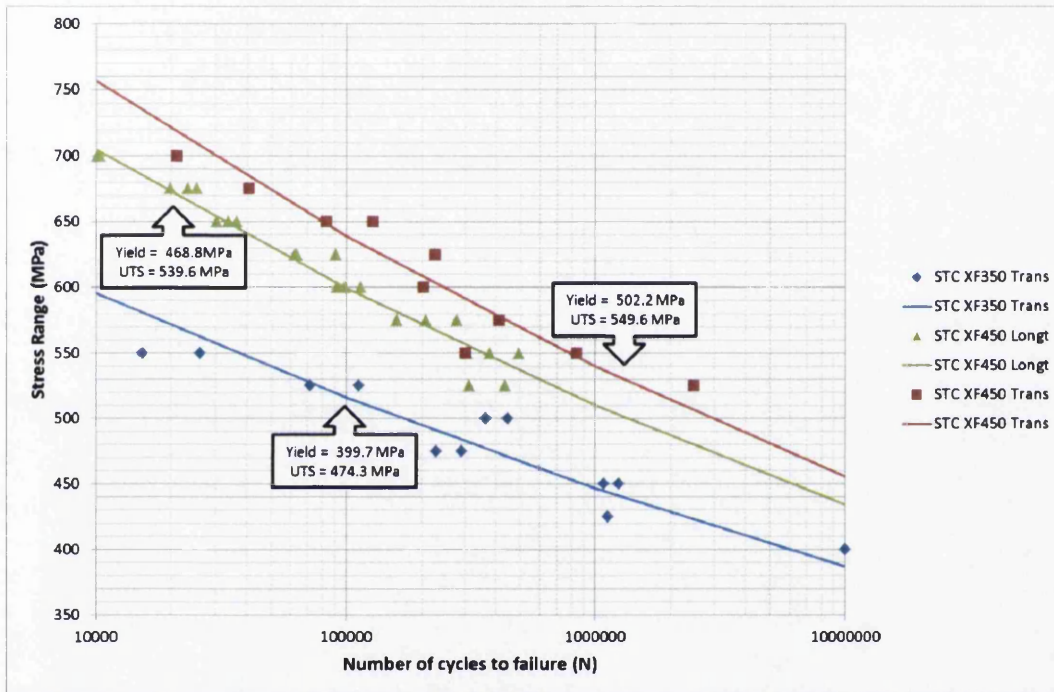
Figure 5.22. Three Tenform fatigue curves of varying tensile strengths

Although the three curves in figure 5.22 are not parallel, as an indicator it may be useful to modify the Basquin constant for the two XF450 curves by the proportional increase in their tensile properties over those of the XF350 transverse curve. The proportional increase in yield stress for longitudinal and transverse XF450 are 17% and 26% respectively, where for UTS they are 14% and 16%.

These percentage increases in yield strength applied to the Basquin constant of 1059.2 of the XF350 curve, as shown in tables 5.7 & 5.8, gives us constants of 1242.9 and 1331.5 for 14% and 16% increased respectively. This is done by simply

proportioning the Basquin constant by the differences in yield strength for longitudinal and transverse material respectively. The same methodology applied to the differences in UTS gives constants of 1205.6 and 1227.9. Figures 5.23 and 5.24 have been created by using these Basquin constants, where the Basquin exponent of transverse XF350 was used, which stands at -0.0625.

It can clearly be seen that altering the Basquin constant by the proportional increase in UTS, as shown in figure 5.24 gives very inaccurate results, this method greatly under-estimates the fatigue performance of transversely cut XF450. The predictions given by modifying the Basquin constant by the proportional change in yield stress however returns a fairly accurate representation of the true fatigue performance. Although the red and green curves are not perfect, they do seem to represent the data points reasonably well.
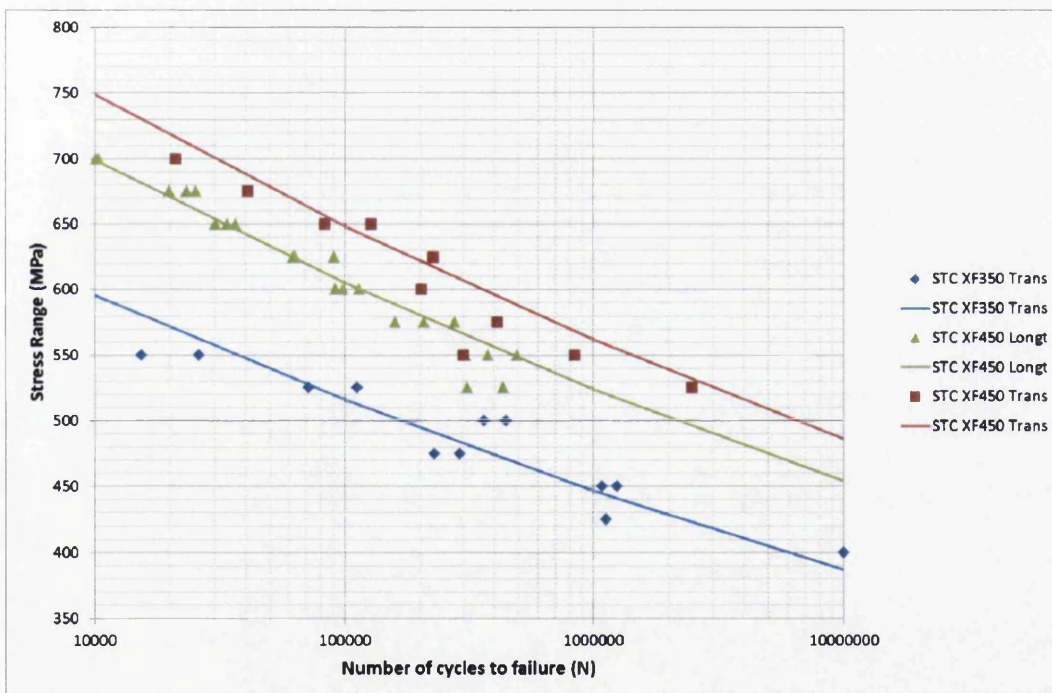
Figure 5.23. Curve prediction by proportioning Basquin constant to yield strength

Despite the fact that the method used in figure 5.23 produces reasonable predictions, it is systematically incorrect as a pure predictive tool. This is due to the fact that only the Basquin constant is modified and the exponent stays the same. In reality with stronger Tenform material, as well as the constant increasing as the tensile properties increase, the exponent also gets more negative. Thus the fact that all three curves are

parallel in figure 5.23 (if it was a log-log plot) tells us that this approach is only to be used as a tool for generalising the effects of yield strength and UTS on the fatigue properties of the material and not for outright prediction.
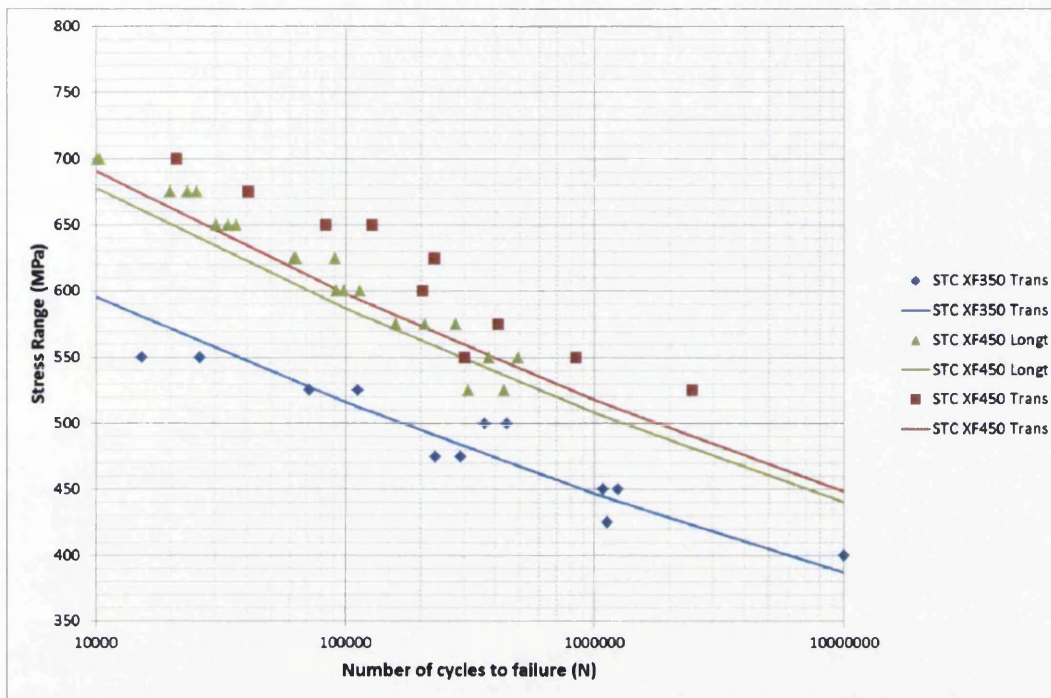
Figure 5.24. Curve prediction by proportioning Basquin constant to UTS

As a predictive tool, a more intricate system would have to be used that would offer predictions for the constant and exponent. Such a prediction is shown in the calculations below, and the results of those predictions are shown in figure 5.25. While this is not an in depth study to try and optimise predictions, it illustrates how generating predictions for both the exponent and constant could lead to a more accurate representation of how the variability in tensile properties are passed on to the fatigue properties of this family of material.

$$A_2 = A_1 \times \left(\frac{PS_2}{PS_1} + \frac{UTS_2}{UTS_1} \right)$$

$$b_2 = b_1 \times \frac{UTS_2}{UTS_1}$$

It was found that the predictions for the Basquin exponents using the technique shown above returned very accurate predictions for this batch of fatigue data, where the results for the constants were fairly close. It would of course be possible to

further optimise these predictions by employing techniques such as using random number generators, the solver function in excel, and building a multi-layer predictive model.

Figure 5.26 illustrates how much improvement is possible for predicting fatigue behaviour from tensile data by enhancing the complexity of the models, the purple line in particular has a very shallow gradient, thus highlighting the accuracy of the Basquin exponent calculation. This is in stark contrast to the steep negative gradients of the curves representing the simple yield strength proportioning method shown by the red and blue lines. If the coefficient prediction method was optimised for this curve, then the stress prediction would be virtually perfect.

Despite the clear opportunities that exist to improve on a fatigue prediction model, more data would be needed to be confident that the predictions made are accurate. This study is sufficient to conclude that for simple predictions it is fair to approximate that any variability in yield strength will result in a directly proportional change in fatigue performance.
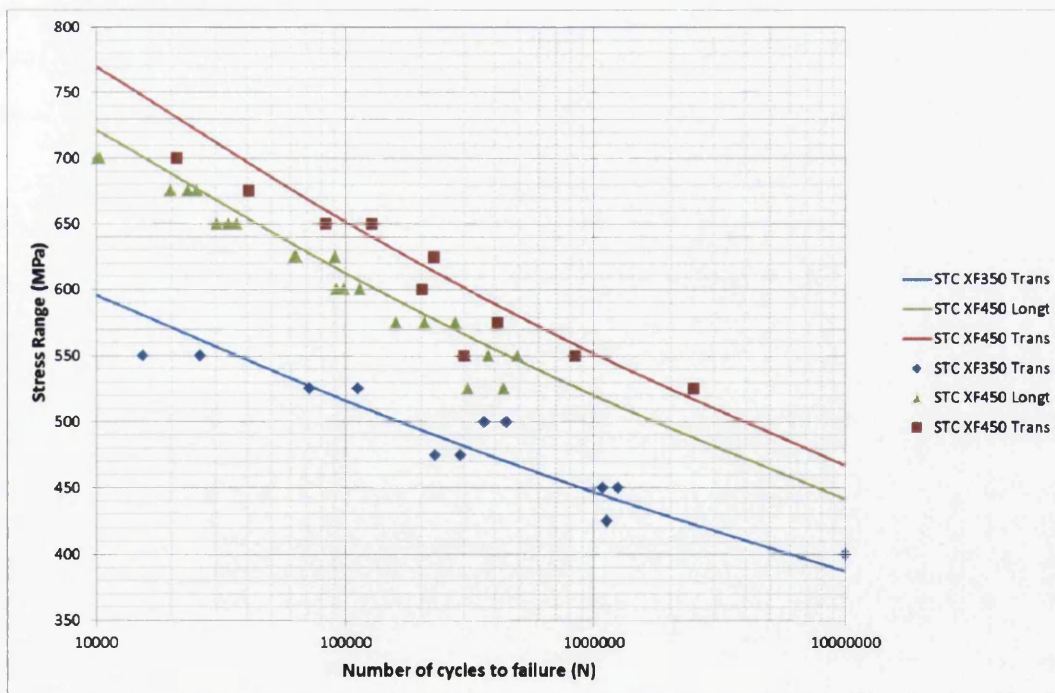
Figure 5.25. Curve prediction by modification of Basquin constants and exponents
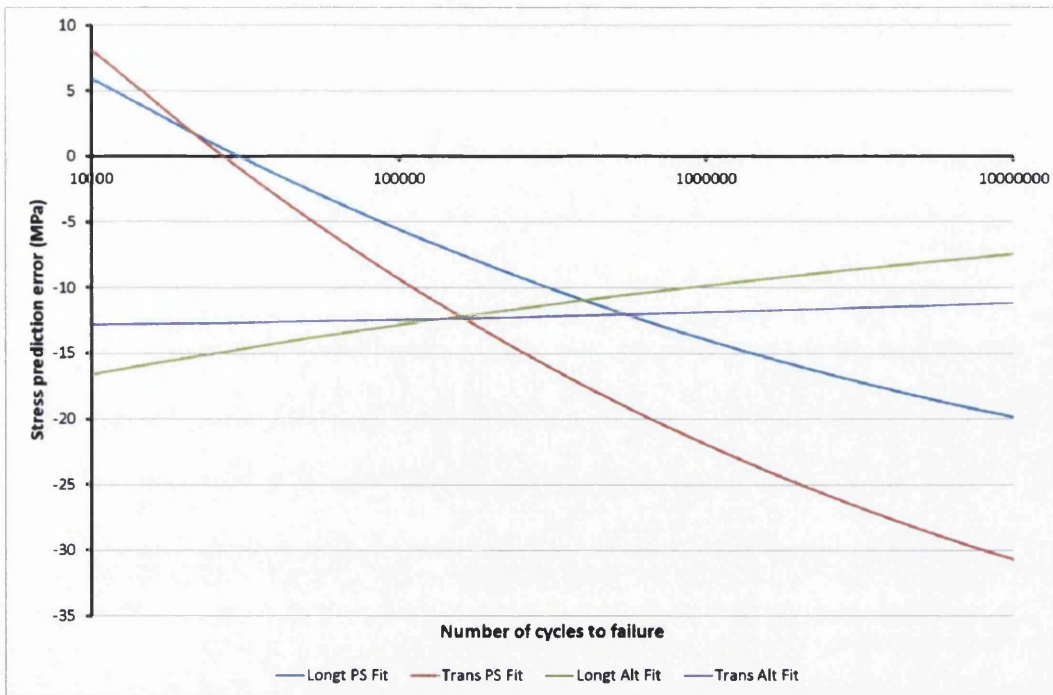
Figure 5.26. Stress prediction errors for curve fitting error

The correlation between yield strength and fatigue life can be explained in terms of microstructural characteristics. As discussed in the previous chapter, the major variables that contribute to yield strength variability are niobium content and heat losses in the coil box. These contributors can severely alter the grain size of the finished product, where for example, niobium forms carbides and nitrides which have extremely low solubility in austenite.

This means that micrometre-sized precipitates of NbC & NbN are virtually insoluble in steels at all processing temperatures and their location at grain boundaries helps prevent excessive grain growth. Excessive coil box temperature drops could cause complications further down the production route, including ferritic rolling, the need to preserve heat and thus latter cooling being reduced or switched off, as well as factors relating to poor shape.

Thus the relation between fatigue performance and yield strength comes as no surprise since the higher yield strength material will have a smaller mean grain diameter, as shown in figure 5.27. The principles considered in the literature in terms of finer grained material inhibiting stage I crack growth due to increased numbers grain boundaries acting barriers are testament to these observations.
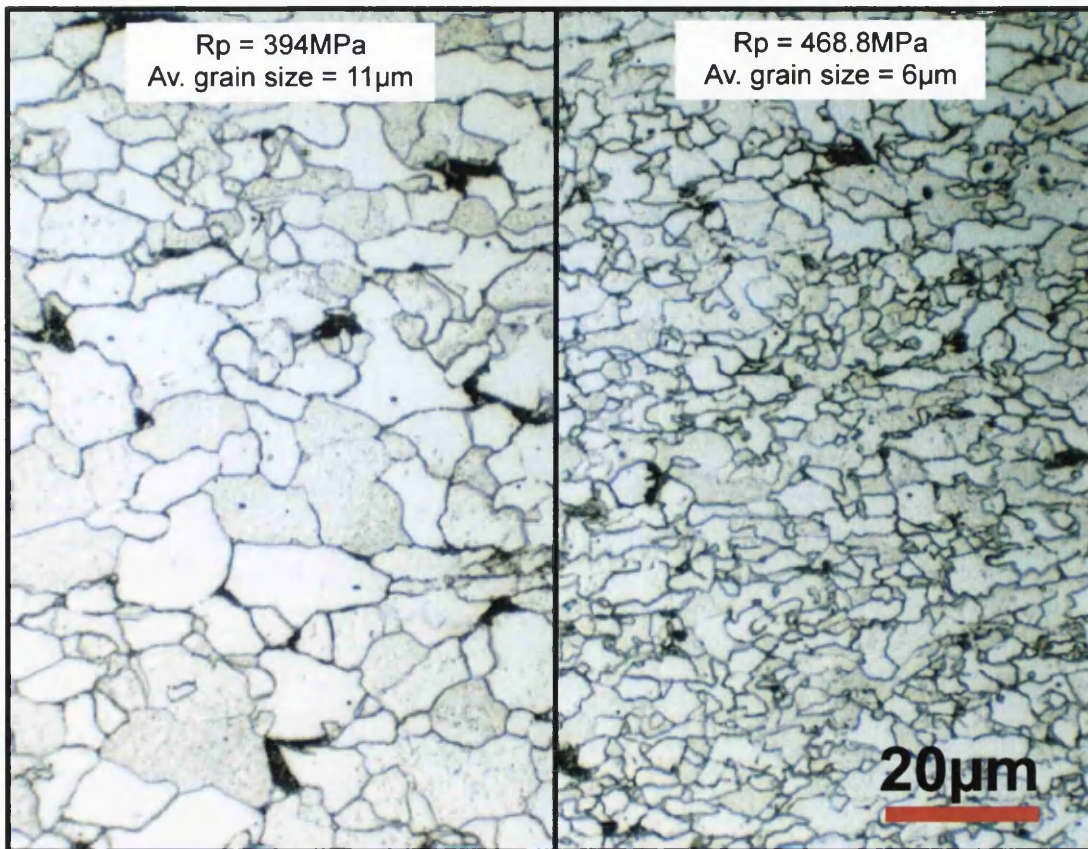
Figure 5.27. Correlation between grain size and Rp in Tenform products

It was observed that as per the literature, the crack path was indeed trans-granular and can be seen in figure 5.28. This confirms that grain boundaries form barriers to growth, which wouldn't be the case if cracks grew along grain boundaries. Furthermore, persistent slip bands were observed on the surface of failed coupons, where the depth of these regions were of the order of 50µm. Under closer inspection there were clear areas where enough slip occurred to form intrusions.

Low magnification micrographs of the slip bands on the surface, as well as high magnification of an intrusion are shown in figures 5.29 & 5.30 respectively. It can be seen that the slip band form at angles of around 45° to the loading direction and were found along the whole surface of failed specimens. Continuation of slip eventually generates intrusions, where the intrusions observed were of the order of 2-3µm

These observations link many of the conclusions of the project thus far. i.e. fatigue variability can be related to yield strength and grain size, which can be and explained in terms of crack growth, where the variability in yield strength is related back to processing variables in a quantitative manner in the previous chapter.
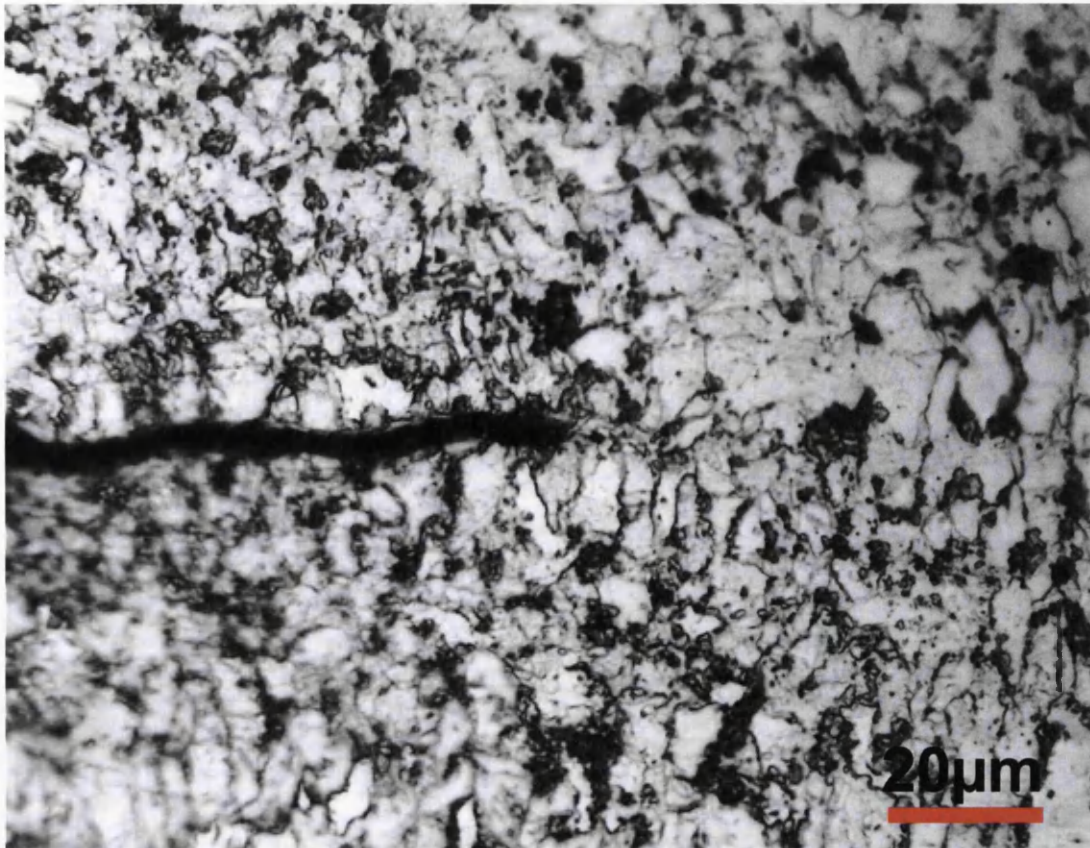
Figure 5.28. Trans-granular crack growth
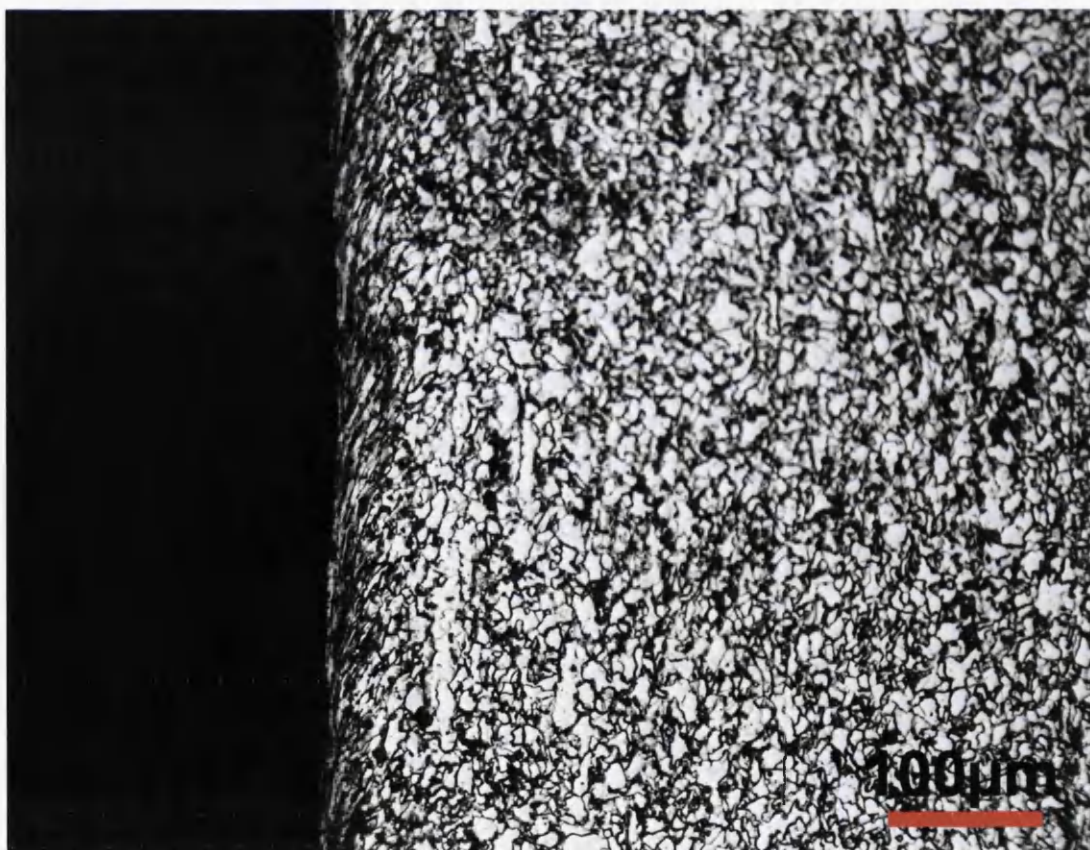
Figure 5.29. Persistent slip bands observes along the surface of a failed coupon

137
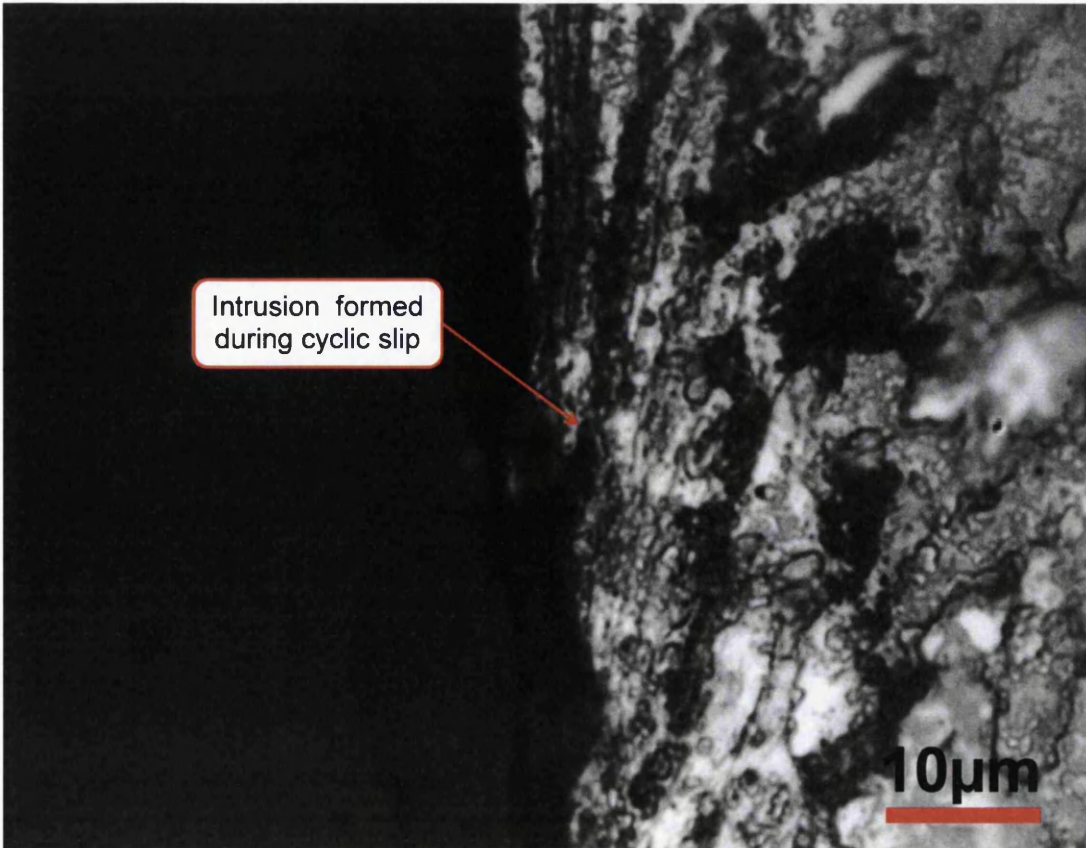
Figure 5.30. Intrusion formed during cyclic slip.

5.5 Repeatability of Tenform fatigue test results

Many of TSSP-UK's fatigue curves published in brochures, etc. typically have 8-12 data points to form a fatigue curve. From previous data in this chapter it is visible that for two apparently identical fatigue specimens tested at the same loading conditions there can be a huge amount of variability in their lives, unfortunately this is the nature of fatigue testing. An example of this phenomenon is shown in figure 5.31, where the two data points circled have the same applied load, but their difference in fatigue life is 1,368,042 cycles, or more applicable is equal to 0.2463 on a logarithmic scale. Despite this, it is always hoped that with enough data points the scatter will even itself out and the fatigue curve, as well as the statistical variation in results, or standard error, will give an accurate representation of the material.
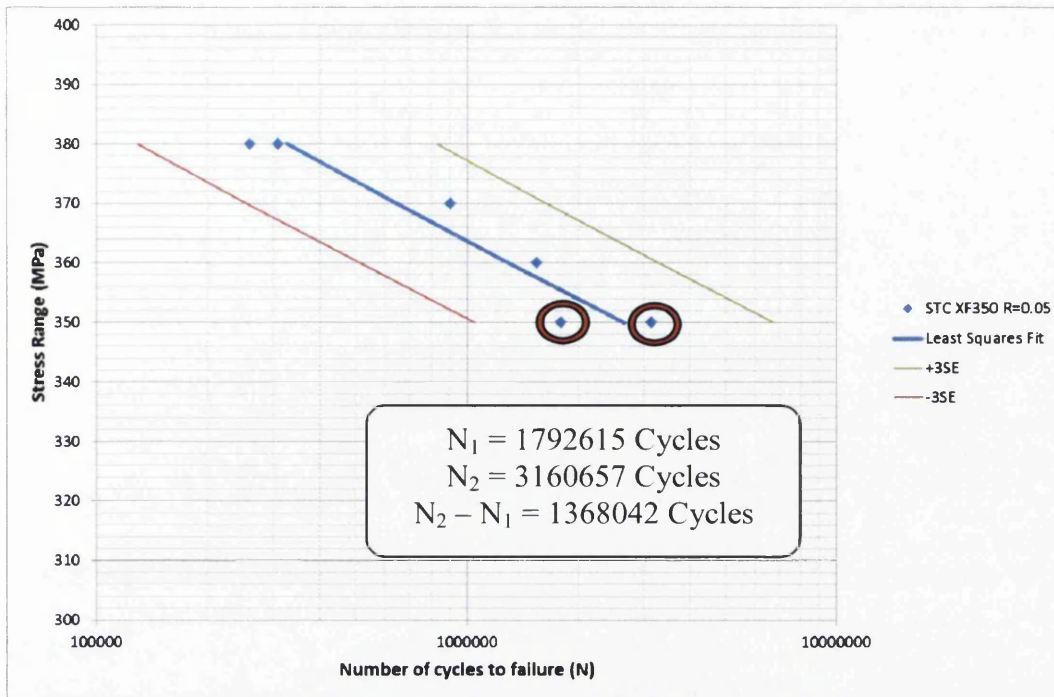
Figure 5.31. Variability of identical fatigue specimens

It is therefore important to establish how many data points are necessary to produce a fatigue curve that gives good repeatability and therefore an accurate description of the material's properties. In order to analyse this, three sets of data tested in an identical manner were created where all the material was sourced from a small section of sheet within a single coil. Thus three individual fatigue curves could be created, each of them consisting of 7 data points.

By doing this and comparing each of the three fatigue curves it is possible to establish how repeatable the tests are, not in terms of individual specimens, but in terms of the final fatigue curve as well as the standard errors. Not only will this study help identify if a single fatigue curve is sufficient to represent the performance of a coil with specific mechanical properties, it will also help to identify how many data points are required to be confident that a fatigue curve fully accounts for the statistical variability that inherently exists with this type of material structural performance testing.

Table 5.10 below shows the data that was gathered following the testing programme that was undertaken at Swinden Technology Centre. It can be seen that three results for fatigue life exists at each of the seven stress ranges. Also shown is the statistical information processed from this data, which is displayed in table 5.11.

139

Table 5.10. Three sets of fatigue data from longitudinally cut XF450

XF450 – Longitudinal Data Set 1 (R=-1)		XF450 – Longitudinal Data Set 2 (R=-1)		XF450 – Longitudinal Data Set 3 (R=-1)	
N (Cycles)	Stress Range (MPa)	N (Cycles)	Stress Range (MPa)	N (Cycles)	Stress Range (MPa)
10080	700	10364	700	7466	700
19829	675	23242	675	25341	675
33854	650	30307	650	36327	650
90830	625	62246	625	63657	625
92245	600	98953	600	114185	600
208608	575	278699	575	159104	575
494290	550	376640	550	306595	550

Table 5.11 Statistical information for three sets of fatigue data from longitudinally cut XF450

XF450 Longitudinal R=-1 Data Set	Basquin Coefficient (A), MPa	Basquin Exponent (b)	Standard Error (logN)
Data Set 1	1278.2	-0.0647	0.0909
Data Set 2	1300.2	-0.0664	0.0755
Data Set 3	1355.0	-0.0708	0.1127

Whilst from studying table 5.11 it may appear that all three curves are significantly different to each other, since the data set with the highest value for the exponent also has the most negative gradient, the predictions for all three fitted curves are extremely close to each other. By looking at figure 5.35 it is obvious that the curve fittings for each set are close to each other and as such no concerns may be raised regarding the accuracy of any of these curves in representing the performance of the material.

As an additional comparison, all three curves may be compared to the 'master curve' (figures 5.31-5.34) which contain all 21 data points. They are also compared to each other in figure 5.35. Once again they all appear to follow the reference curve very closely. The only area where any noteworthy discrepancy exists between the reference and partial data curves is when looking at the standard errors of each. The largest difference between the standard errors of the three curves exists between data set 1 and 3, which have log values of 0.0909 and 0.1127 respectively. Whilst this difference of 0.0261 is significant, it is compounded by the fact that the 50% survival curves for these two data sets are on different sides of the reference curve i.e. data set 1 rises above the master curve, where data set 3 lies beneath the master curve.

Despite these critical remarks, the overall variability between each of the curves of all the data sets, as well as their standard errors is not significant enough to cause any concern. Comparing the processed statistical information contained within table 5.11 to a Basquin coefficient and exponent of 1309.5 and -0.0672 along with a standard error of 0.0896, it can be seen that the data from the other curves do not deviate enough from these values to provide misleading information.

After considering all the relevant information it is concluded that if using identical specimens prepared in the same way and cut from the same location within a coil, despite fatigue data being very un-reproducible, fitted curves and will not vary greatly from one data set to another. Another important observation is that a curve using only 7 data points compares very well against a curve with 21 data points, and as such, as long as there are a reasonable spread of stress ranges and cycle counts, ranging from about 10^4 up to 10^7, then this should give very usable information for characterising the fatigue properties of strip steel.
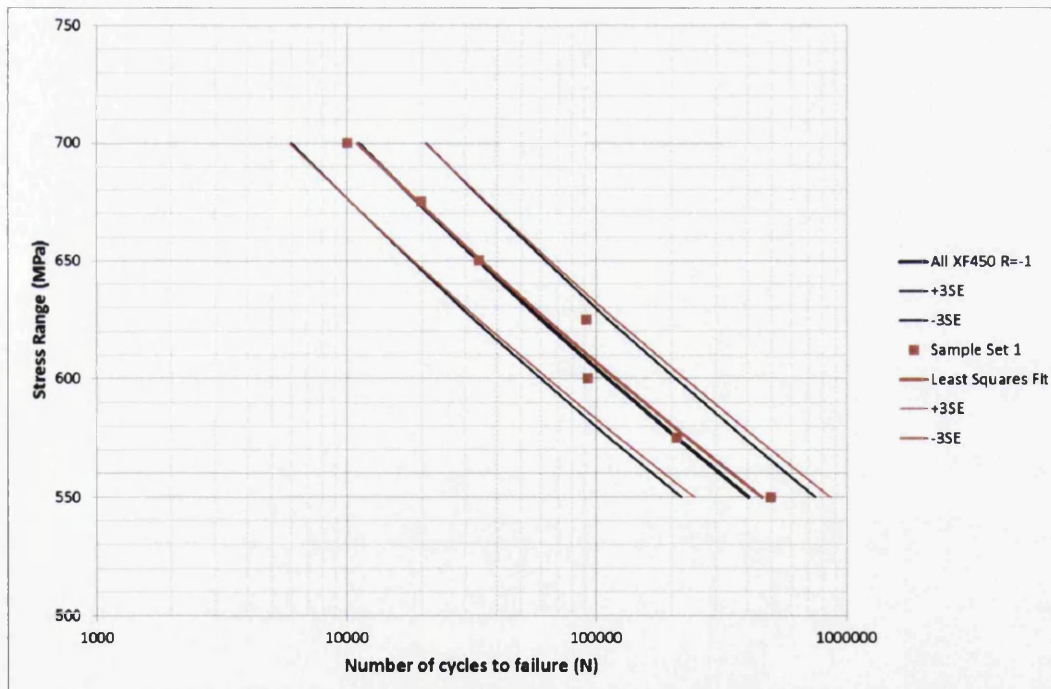

Figure 5.32. Data set 1 compared to the baseline curve
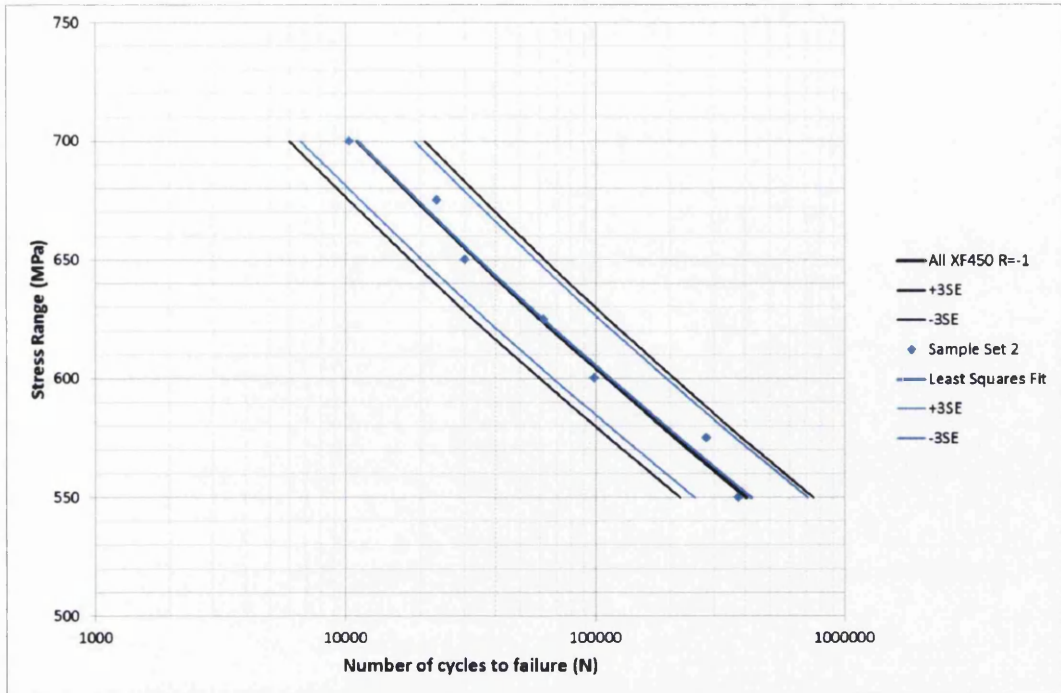
Figure 5.33. Data set 2 compared to the baseline curve
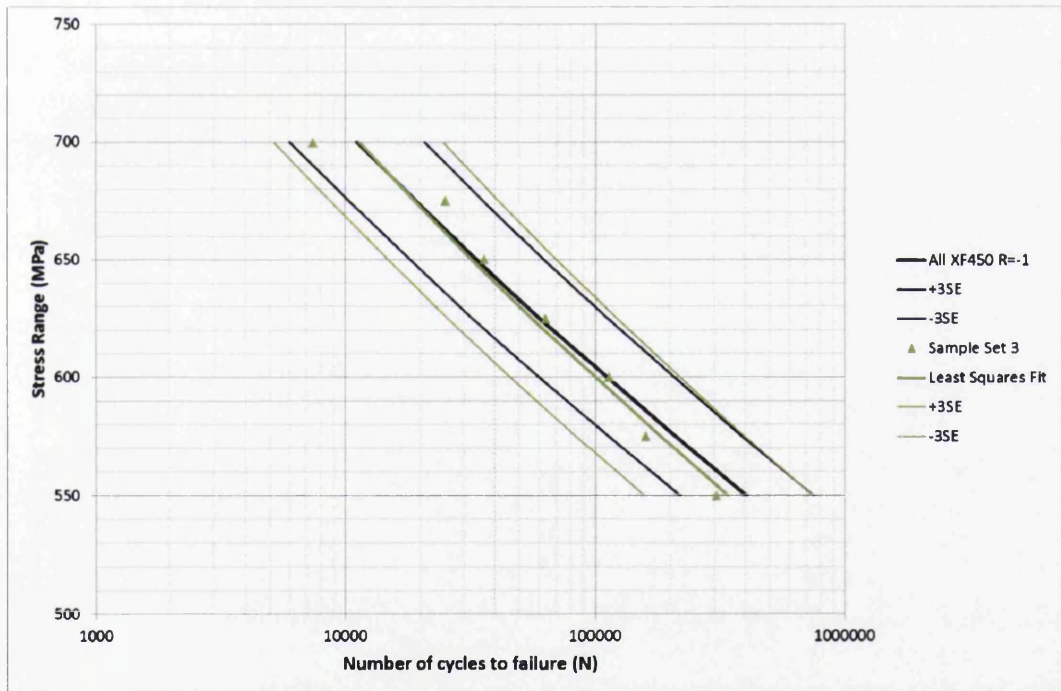
Figure 5.34. Data set 3 compared to the baseline curve

142
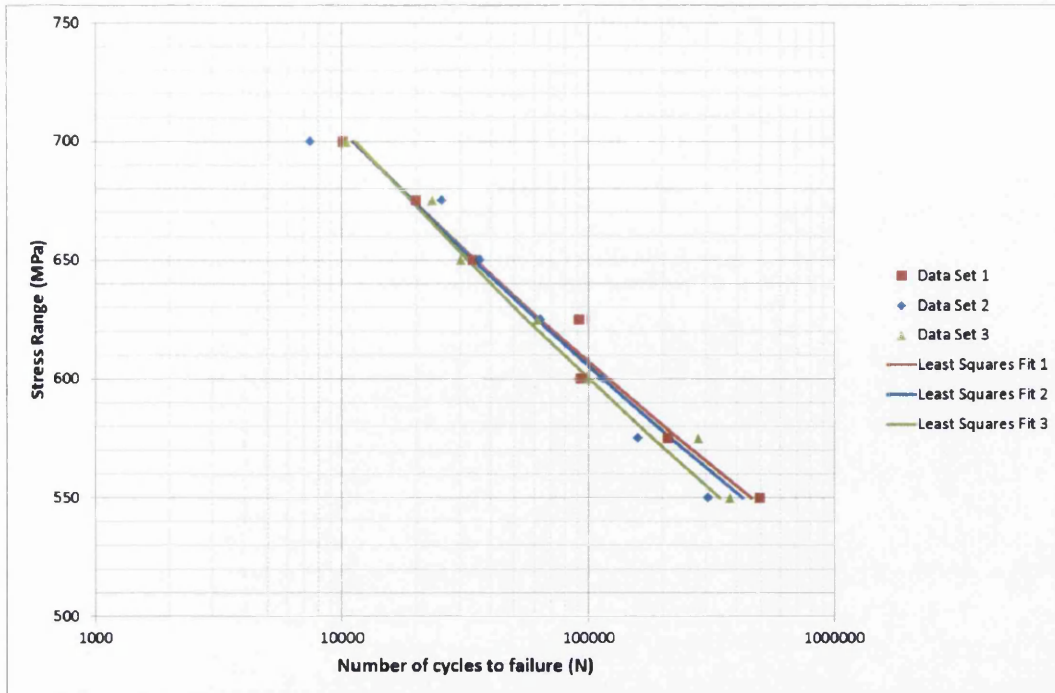
Figure 5.35. Comparison of data sets 1, 2 and 3

143

Chapter 6 – Weld Performance

6.1 Tensile performance of MIG/MAG & TIG welds

In order to compare the tensile performance of MIG & TIG welds, 80mm tensile samples of S355MC were prepared and cut in half prior to welding. The samples were butt welded on both sides, one was MIG welded using Bohler EMK 6 wire, and the other was TIG welded using Elga Elgatig 100 rods. Details of both consumables are listed below in table 6.1.

Table 6.1. Welding consumables data

Welding Consumable	Chemical Composition (Typical - Wt%)			Mechanical Properties (As-welded argon shielded)		
	C	Si	Mn	R_e (MPa)	R_m (MPa)	A (%)
Bohler EMK 6 (MIG)	0.08	0.90	1.45	≥420	500-640	≥24
Elga Elgatig 100 (TIG)	0.08	0.90	1.50	≥460	≥530	≥22%

It can be seen that the chemical composition and mechanical properties for both welding consumables are very similar. The mechanical properties for both are significantly greater than the base material, and as such, the tensile specimens did not fail at the welds for either welding method. It was promising to see that the tensile strength of the welded coupons were very similar to the un-welded substrate, where the effective tensile strength of each coupon (based on parent material cross-sectional area) are shown below in table 6.2.

Table 6.2. Tensile strengths of welded/un-welded coupons

Data Set Samples (Longitudinal)	Yield Strength (MPa)	UTS (MPa)	Total Elongation (%)
Un-welded XF350	379.93	467.80	28.82
TIG welded XF350	378.18	457.91	11.97
MIG welded XF350	384.38	466.46	12.48

The difference in extension is probably attributed to the extra material that is deposited in the weld that resists the necking that normally occurs in the centre of the work piece. It can be concluded from table 6.2 and figures 6.1 & 6.2 that the weld quality and filler material is appropriate for the substrate material, and as such the

fatigue data gathered from this chapter can be regarded as being sourced from welds that are fit for purpose. This theory is reflected by the fact that recalculating the stress/strain curve based on a 70mm gauge length (nominal 80mm – 10mm weld) does not bring the elongation values back to that of the substrate.
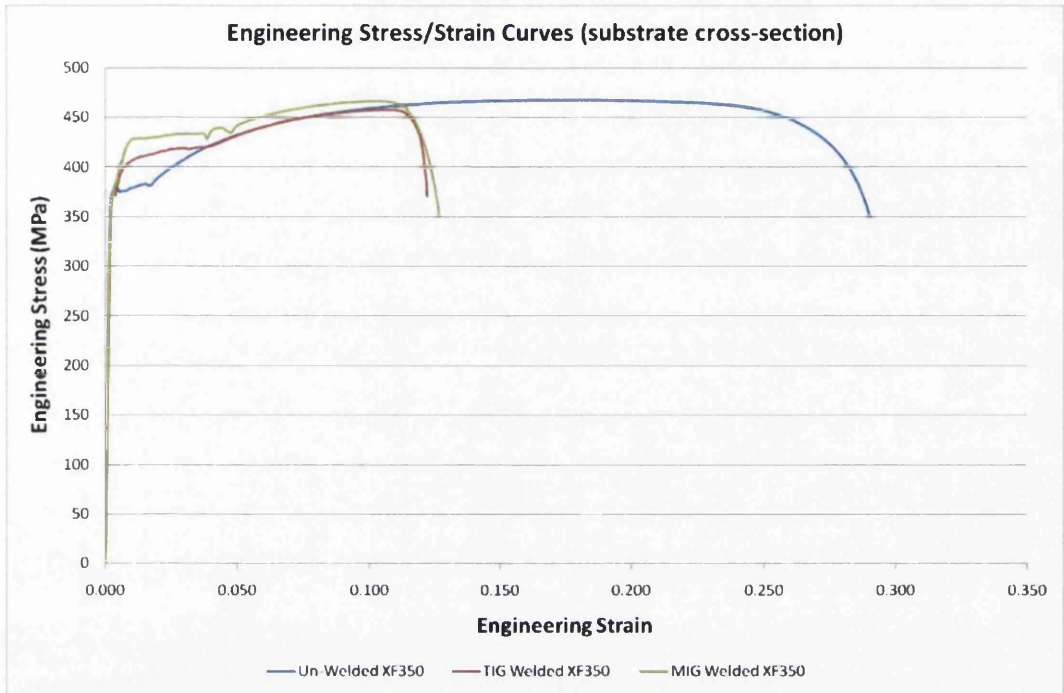
Figure 6.1. Tensile performance of MIG/TIG welded S355MC
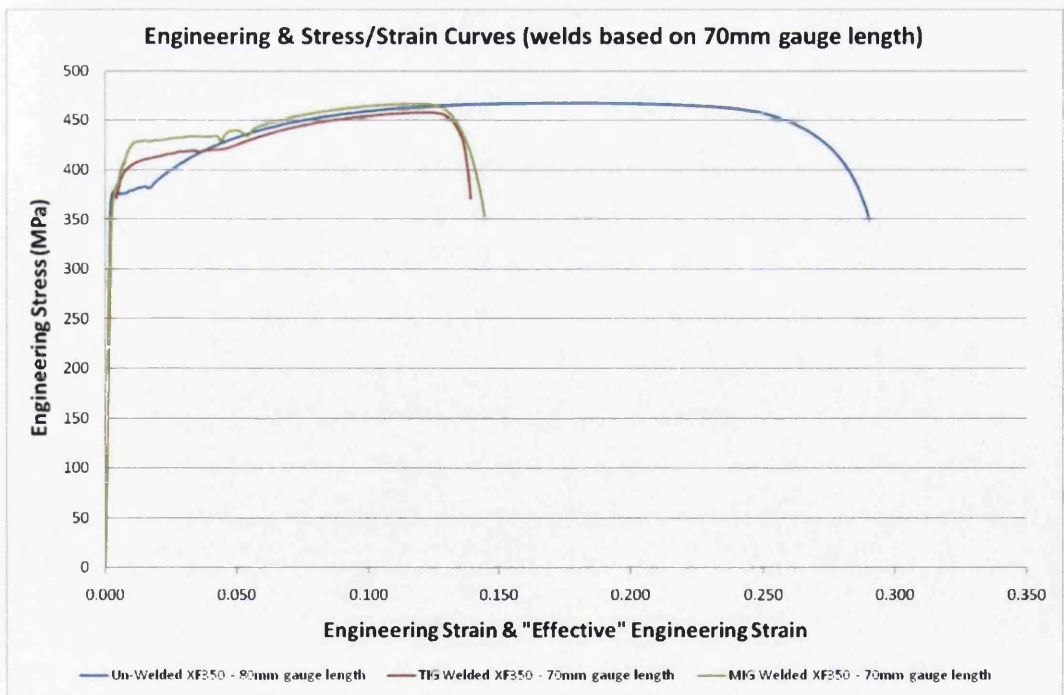
Figure 6.2. Tensile performance of MIG/TIG welded S355MC – 70mm gauge length

Micrographs were taken of the failure zone, as well as the Heat Affected Zone (HAZ) and compared to micrographs of the base material. These can be seen in figures 6.3 & 6.4. The microstructure of the base material is fairly uniform throughout, where the mean grain size is around 11μm. The areas immediately to either side of the welded filler/substrate material or HAZ showed a microstructure that was similar to the base material prior to welding, suggesting minimal damage was inflicted to the material from the large amount of heat applied during welding.

This is especially true of MIG/MAG welds, where the heat affected zone was relatively small. The microstructures found in the HAZ were a ferrite/pearlite mix, identical to the substrate, the only difference being the slightly less consistent grain size, where more variation existed compared to the mean 11micron grains found in the base material.
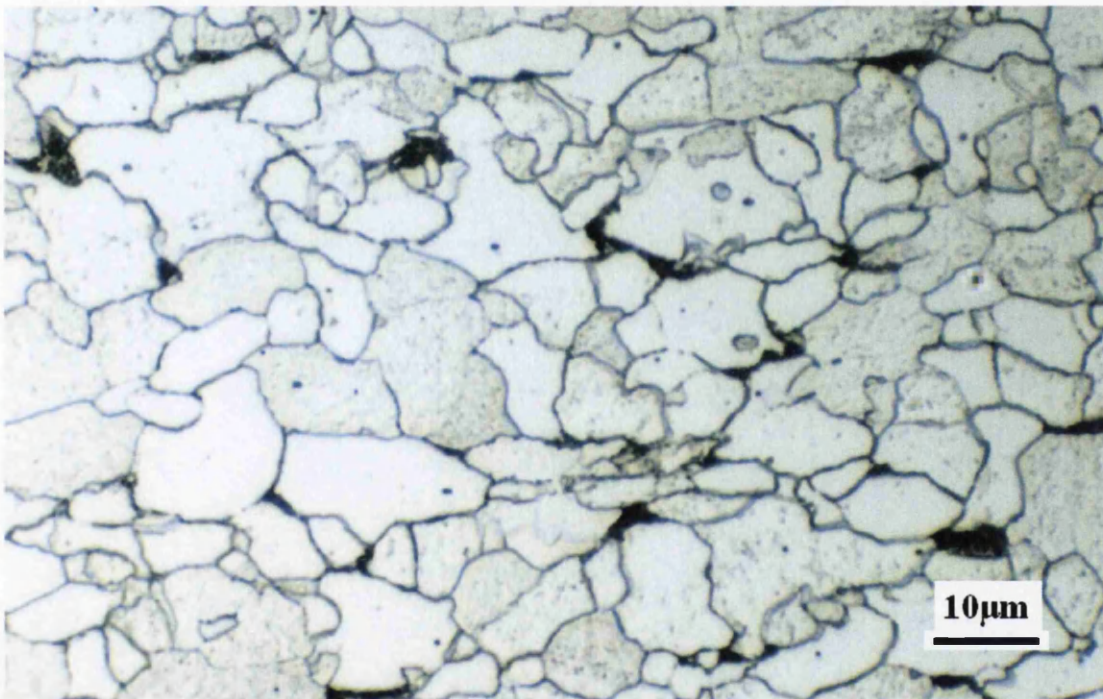
Figure 6.3. Base material micrograph (S355MC)

Even though similar consumables in terms of chemistry and mechanical properties were used for both welding methods, the microstructures of TIG and MIG welds were shown to be significantly different to each other. The MIG/MAG welds had a straight-forward microstructure of primarily polygonal ferrite and perlite, while many variants of ferrite existed in TIG welds, some of which resembled the structures of bainite and martensite more than those of the more common forms of ferrite.

146
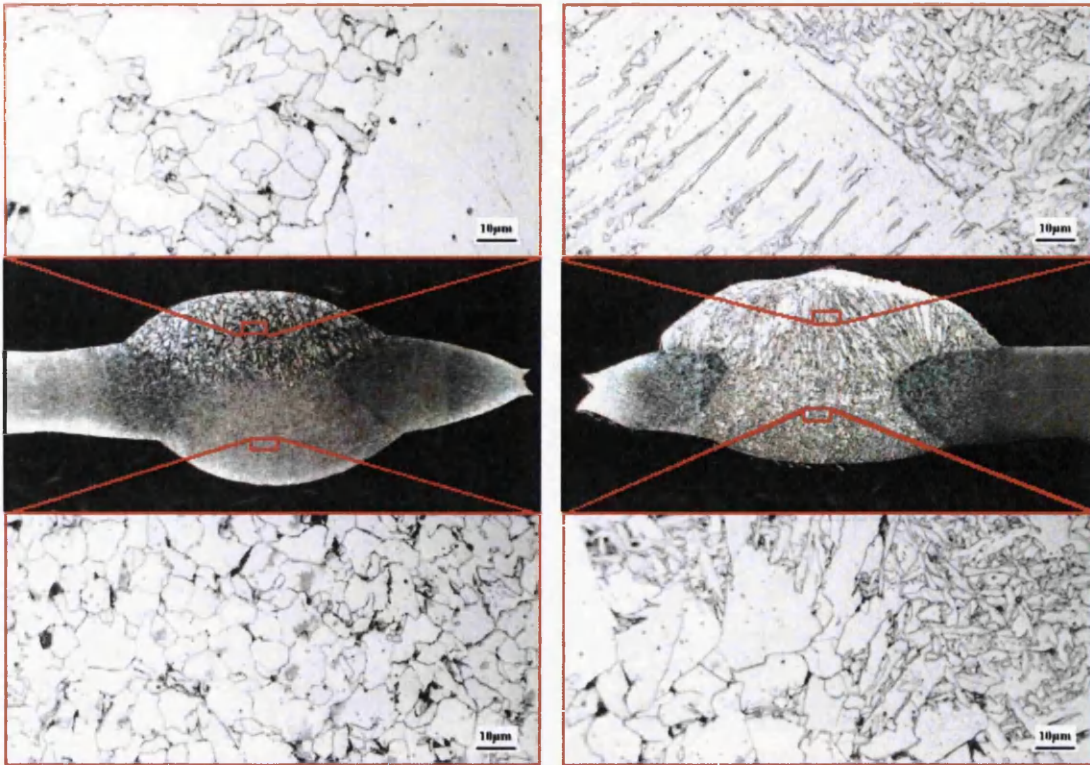
Figure 6.4. Micrographs of MIG(left)/TIG(right) welded S355MC

In addition to the differences between MIG and TIG welds, it is clear that the first pass has a different microstructure to the second pass. For MAG welds, the second pass has a fine uniform structure, and the first has a very irregular pattern of fine and course grains of ferrite, along with perlite. TIG welds however include numerous form of ferrite, these include fine grains of acicular ferrite, as well as inconsistent patterns of fine and course ferrite grains, and widmanstatten ferrite (also known as aligned side plate ferrite or intra-granular nucleated bainite).

These observations are consistent with those of Bhadeshia & Honeycombe [53]. Larger microscopic images at a reduced magnification of 500 times are shown of the welded regions in figures 6.5, 6.6, 6.7 and 6.8, as these show a larger area, and more of the microstructure, hence the variability in microstructure can be seen.
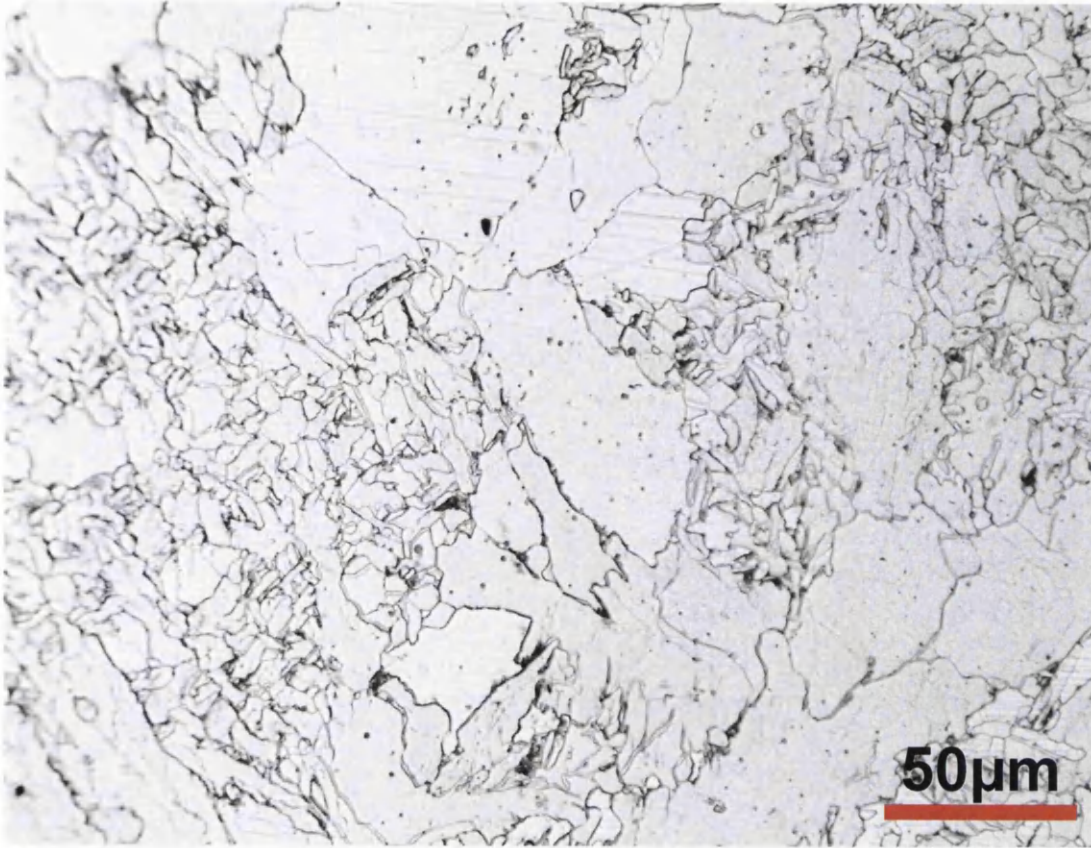
Figure 6.5. Top section of MIG weld
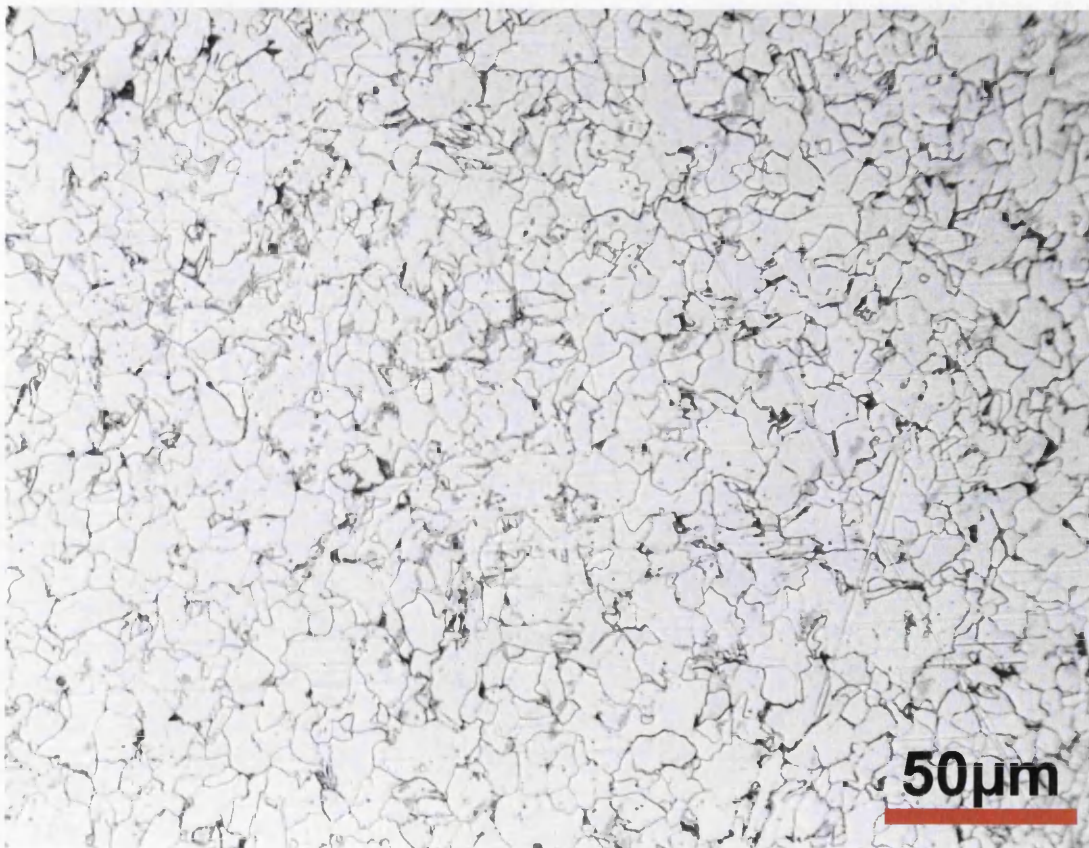
Figure 6.6. Bottom section of MIG weld

148
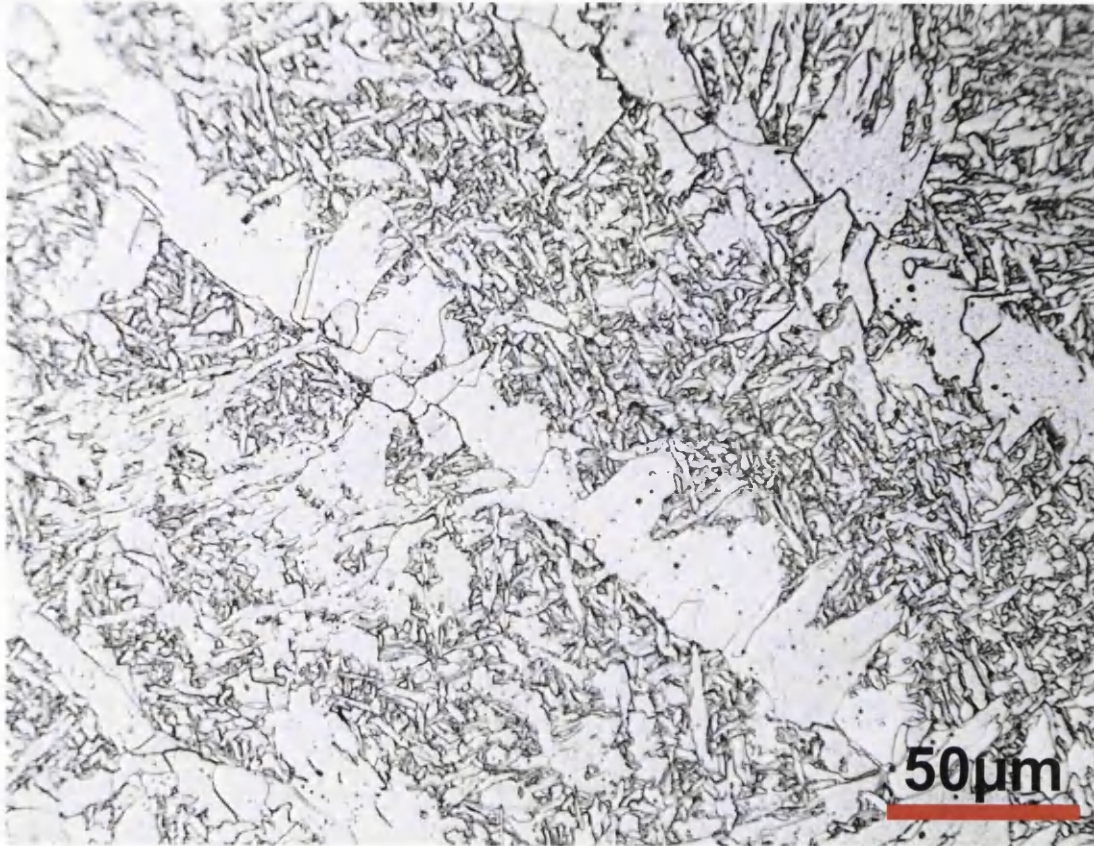
Figure 6.7. Top section of TIG weld
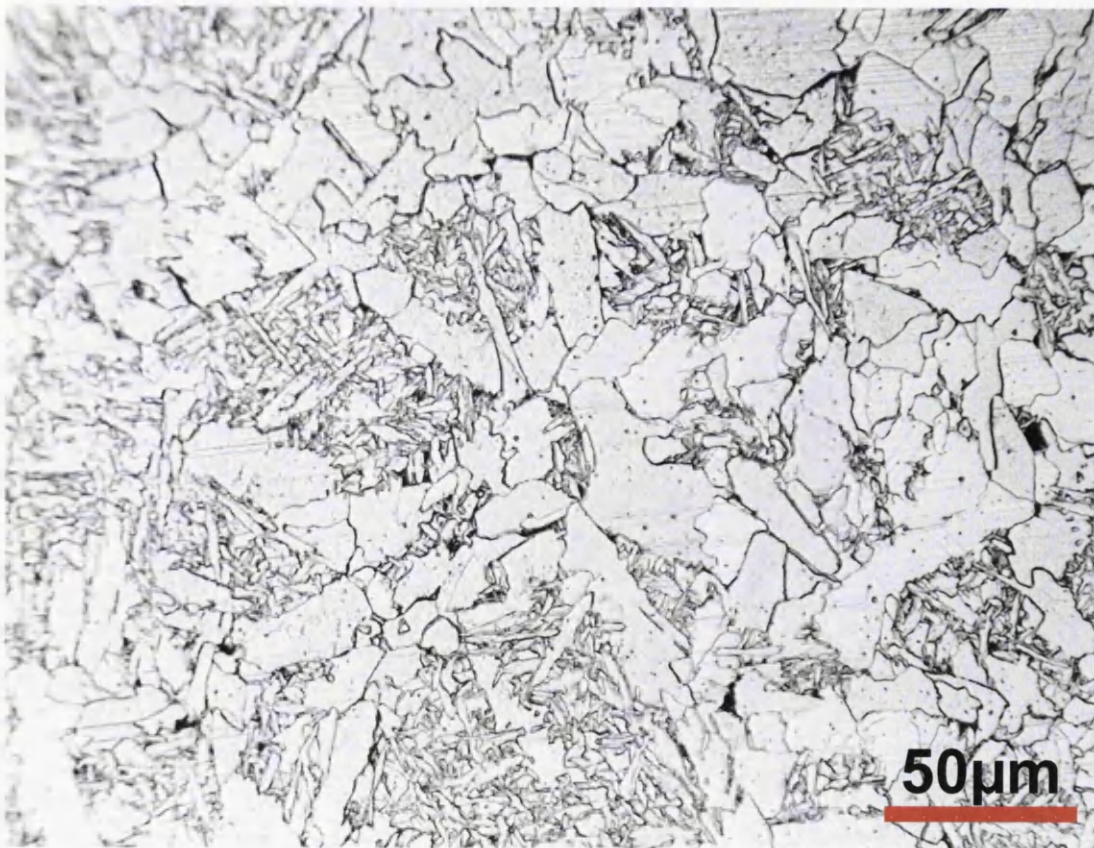
Figure 6.8. Bottom section of TIG weld

149

6.2 Weld fatigue coupon design

It was determined that the fatigue testing of welds should be carried out at Cardiff University. The equipment at this university had yet to be used to test this type of material, let alone welds, therefore deciding upon appropriate geometry and ensuring secure fitment of specimens to the test equipment was the first task in hand. After inspecting the machinery, the final specimen geometry, along with the design of the clamping plates were decided upon and are shown in figures 6.9 & 6.10, followed by the whole assembly in figure 6.11.

The specimen geometry shown complies with the relevant British and international standards, where guidelines are laid out for transition radius, cross-sectional area of the parallel region and machining tolerances. These standards are:

BS 3518-3: 1963 Fatigue Testing – Part 3: Direct stress fatigue tests
ISO 1099:2006 Metallic materials – Fatigue testing – Axial force-controlled method

Designing the specimen to have a large enough radius to comply with these standards and also be compatible with the test equipment was not easy, and although the final design complies with the two standards shown above, it does not comply with the ASTM standard shown below:

ASTM E 466 Standard Practice for Conducting Force Controlled Constant Amplitude Axial Fatigue Tests of Metallic Materials

Figure 6.9. Weld fatigue specimen geometry

The ASTM standard requires a radius of eight times the test section compared to only twice the section for the ISO standard. To comply with this the only practical solution was to reduce the width of the test section. In this case, a test section of less than 20mm did not seem sufficient for the testing of welds, thus complying with the ISO standard seemed sufficient, especially since a FE evaluation of the stress concentrations were undertaken and included in chapter 3.

Figure 6.10. Clamping plate geometry

151

Figure 6.11. Weld fatigue assembly

Note that the figures above show drawings of the un-welded "baseline" specimens. For the welded specimens, in order to eliminate the often negative effect that weld start/stop has on fatigue behaviour, it was decided that a rectangular "blank" should be made first, then subsequently cut and welded, as shown in figure 6.12. This could then be machined and the specimen would include a continuous weld in the centre, with no start/stop locations.

Figure 6.12. Welded "blank"

152

Note that the design of the test coupon and clamping plates specifies that the centre hole for the pin connection in the coupon is larger than those of the clamping plates, this is in order to ensure that the load is applied through the entire contact area between the specimen and the plates. Applying the load this way should ensure an as even as possible stress distribution through the specimen. With this configuration it is crucial to ensure that the frictional clamping resistance is large enough to prevent any slipping occurring between the specimen and plates.

The first step for this exercise is to evaluate the clamping force of each bolt. The minimum strength of bolts is specified in BS EN ISO 898-1:2009, where an M8 bolt with an 8.8 specification has a yield strength and UTS of 21,200N and 29,200N respectively. Gedore, a tool manufacturer recommends a torque of 24.931Nm [54], thus supplying a clamping force of 16,539N. This clamping torque would theoretically put the bolt into a tension that is 78% of the yield strength, though these values are only applicable for a thread friction of $\mu=0.14$. any changes in the coefficient of friction would result in a different clamping force. As a reference for possible alterations to the bolting assembly in the future, the ISO specifications, along with Gedore's recommendations are shown in tables 6.3 and 6.4 respectively.

Table 6.3. ISO bolt strength specification

BS EN ISO 898-1:2009 Mechanical properties for selected metric fasteners							
Metric Bolt Classification	Thread Pitch (mm)	Proof and ultimate tensile loads (N)					
		8.8		10.9		12.9	
		Proof	Ultimate	Proof	Ultimate	Proof	Ultimate
M6	1	11,600	16,100	16,700	20,900	19,500	24,500
M8	1.25	21,200	29,200	30,400	38,100	35,500	44,600
M10	1.5	33,700	46,400	48,100	60,300	56,300	70,800
M12	1.75	48,900	67,400	70,000	87,700	81,800	103,000

Table 6.4. Gedore bolt torque specification

Gedore technical specifications for metric bolts with friction value $\mu = 0.14$							
Metric Bolt Classification	Thread Pitch (mm)	Axial spring tension (F_{SP}) and applied tightening torque (M_A)					
		8.8		10.9		12.9	
		F_{SP} (N)	M_A (Nm)	F_{SP} (N)	M_A (Nm)	F_{SP} (N)	M_A (Nm)
M6	1	9,011	10.247	12,671	14.410	15,205	17.292
M8	1.25	16,539	24.931	23,258	35.059	27,909	42.070
M10	1.5	26,336	49.450	37,034	69.540	44,441	83.440
M12	1.75	38,401	86.320	54,001	121.38	64,801	145.660

Thus, given that the assembly includes 10 bolted connections, the total clamping load using Gedore's recommendations would be R = 10 × 16539 = 165,390N. It can be seen that the fatigue coupon has a cross section of 20mm × 3mm in the failure region, i.e. the cross-sectional area is 60mm^2 or $6 \times 10^{-5}m^2$. The maximum stress that the material is likely to experience during cyclic loading is in the region of 350MPa, thus the total static frictional resistance needs to be greater than the load required to apply 350MPa of stress to the fatigue specimen. The applied force can be calculated as shown:

$$\sigma = F/A$$

$$F = \sigma A$$

$$= (350 \times 10^6) \times (3 \times 10^{-5}) = 21,000N$$

Where the static friction for a coefficient of friction, $\mu = 0.14$:

$$F = \mu R$$

$$F = 0.14 \times 165,390 = 23,155N$$

Although the static frictional resistance is not a great deal larger than the applied load there is no reason for concern, since the value applied for the coefficient of friction is typical lubricated sheet steel. Increasing the value of 0.14 by degreasing and/or roughing with emery cloth should not pose any problems. If any slippage does occur, then table 6.4 may be consulted and the size and/or quality of the bolt may be altered.

6.3 Fatigue performance of MIG/MAG & TIG welds

After overcoming numerous challenges associated with the fatigue testing of MIG and TIG welds, the programme was finally completed in July 2012. The testing was completed on two separate machines at Cardiff University, this did not make any difference as both used the same specimen design and the same 20mm pin connection. Both machines were calibrated and therefore there are no concerns over accuracy. The larger of the two machines is a Mayes, and the smaller one is a Servocon machine.

Despite being smaller, even the Servocon machine was more than adequate for the task, with a maximum permissible load of 100kN, where the maximum load used as part of this project stood at around quarter of that value. The Mayes machine is

capable of an applied load of 500kN, thus both machines were very comfortable carrying out this work. Most of the testing however was carried out on the smaller of the two machines due to scheduling of other project work. Images of these two machines can be seen in figures 6.14 and 6.15.

Some of the challenges encountered along the way were both software and hardware related. In regards to software, there were some initial difficulties in detecting that specimens had failed, which did not pose a problem in the daytime as I was there to witness the failure and stop the cycle count, though unfortunately when specimens failed in the middle of the night there were instances where the counter kept running, therefore giving unreliable data that had to be discarded.

The successful solution to this problem lay in programming the machine to power off when the error between the desired load and actual load rose above a certain level. The only major hardware problem encountered was due to using unidentified material for the manufacture of pins to secure the specimens to the test rig. This did not pose any problems initially, though after many millions of cycles of loading, one eventually gave way mid test resulting in that particular test being abandoned. The failure was a textbook fatigue failure of a circular cross-section, complete with beach-marks as can be seen in figure 6.13.

Figure 6.13. Failed pin
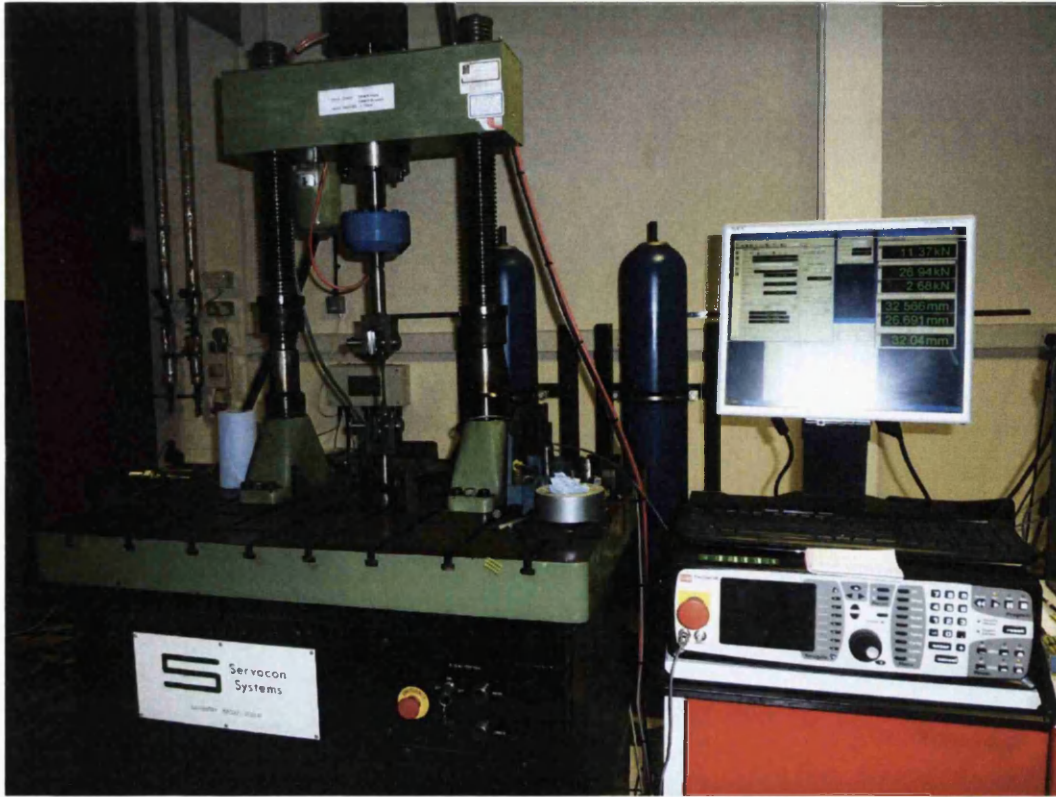
Figure 6.14. Servocon fatigue testing equipment

Figure 6.15. Mayes fatigue testing equipment

156

For the un-welded coupons, the failure mode was consistent with a mechanism documented be Schijve [12]. This mode of failure begins in the tensile mode (max normal stress) and final fracture ends with failure in the shear mode (max shear stress at 45°), where these angles of fracture are consistent with Mohr's circle theorem. An image of the fractured surface, as well as the illustration by Schijve are shown in figures 6.16 & 6.17. It is also an interesting observation that crack initiation occurred at the corner where the grains have 2 free surfaces, and hence little support compared to grains in the mid-thickness of the material.
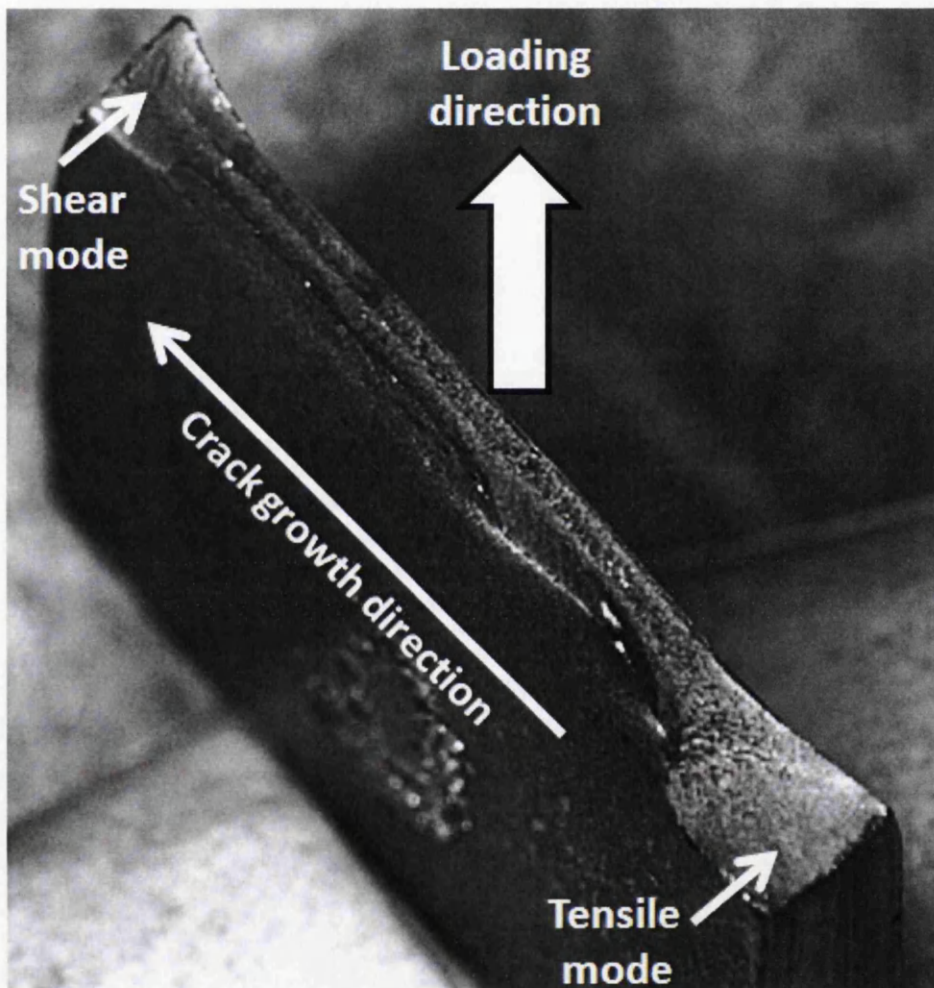
Figure 6.16. Transition of crack growth from tensile mode to shear mode in XF350
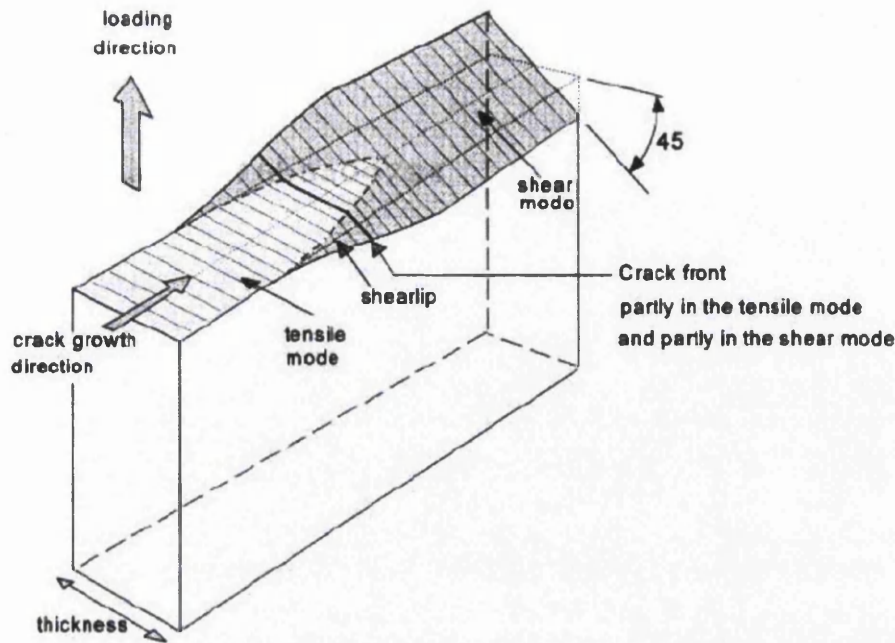
Figure 6.17. Transition of crack growth from tensile mode to shear mode

Once the initial problems were ironed out, apart from the pin failure, the testing programme went smoothly and the data collected from the experiments are shown in table 6.5.

Table 6.5. XF350 weld S-N data

XF350 Un-welded Data (R=0.1)		XF350 MIG Data (R=0.1)		XF350 TIG Data (R=0.1)	
N	Stress Range (MPa)	N	Stress Range (MPa)	N	Stress Range (MPa)
10436	400	25300	370	38401	370
127804	390	35907	360	41926	300
262684	380	76486	350	185046	250
299791	370	57718	330	279338	200
395361	360	62723	310	2074143	170
687415	350	168432	250	2143069	150
2163092	340	236438	200		
		604761	150		

The data in the table above was then statistically processed and the curve fitting information derived from this work is shown in table 6.6 below. Note that this information may lead to the conclusion that the performance of MIG and TIG welds are vastly different. The analysis of this data alone does not tell the whole story, and further investigation is required into the nature of the curves and of each individual specimen in the data set.

158

Table 6.6. Processed XF350 weld S-N data

XF350 Data Set	Basquin Coefficient Exponent (A), MPa	Basquin Exponent (b)	Standard Error (logN)
Un-welded Data (R=0.1)	597	-0.0385	0.3154
MIG Data (R=0.1)	11012	-0.3213	0.1313
TIG Data (R=0.1)	2845	-0.2019	0.2344

Four graphs (figures 6.18-6.21) are used to display the information shown in tables 6.5 and 6.6. Individual graphs are shown for each of the fatigue curves, this is so that the standard error curves may be clearly distinguishable, which may not have been the case if they were included in figure 6.21, which includes the 50% survival curves for all three data sets. What is clearly noticeable from these curves is that welding by any of these methods has a huge detrimental effect on the fatigue performance of the steel strip. However, the difference between the two is a little more intricate than purely observing the curves on the graphs, as will be discussed later.
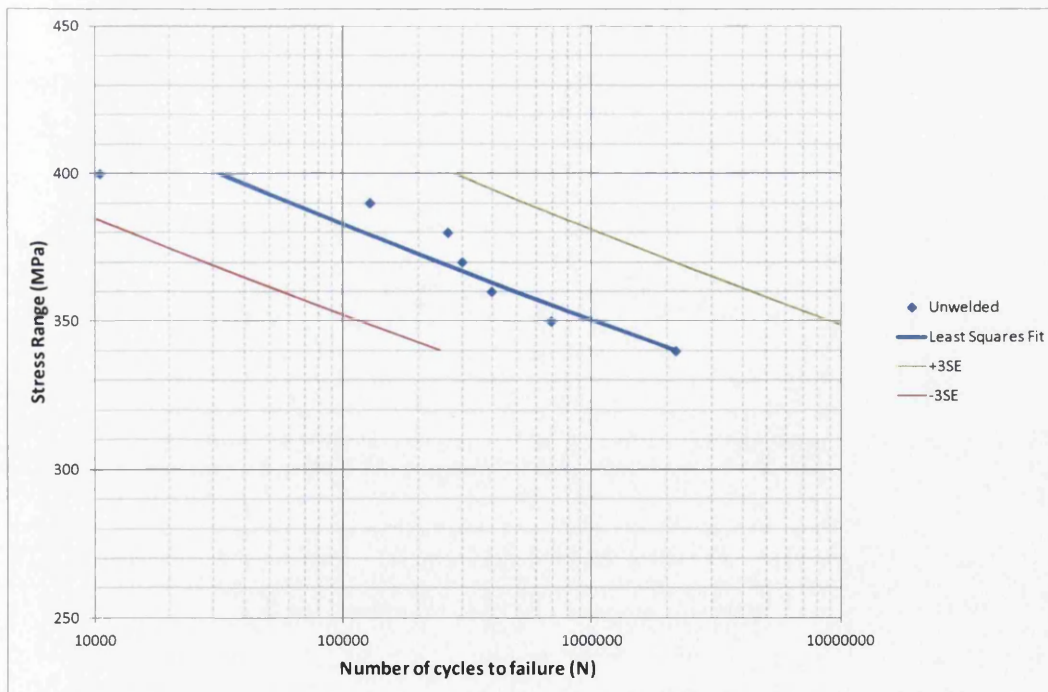
Figure 6.18. Baseline un-welded SN curve

159
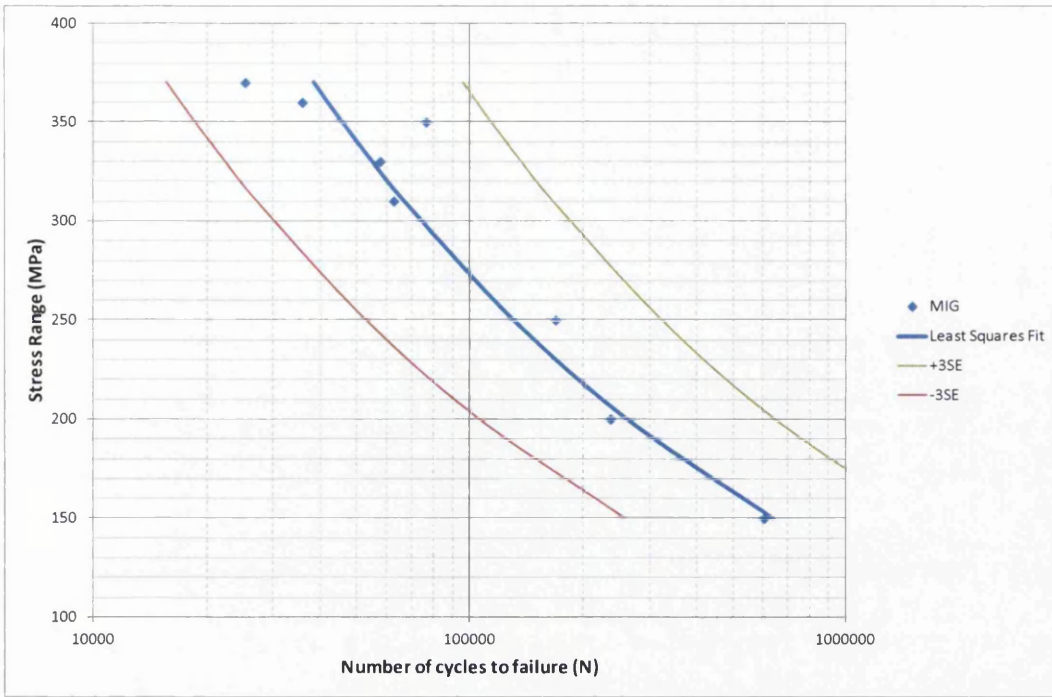
Figure 6.19. MIG welded SN curve
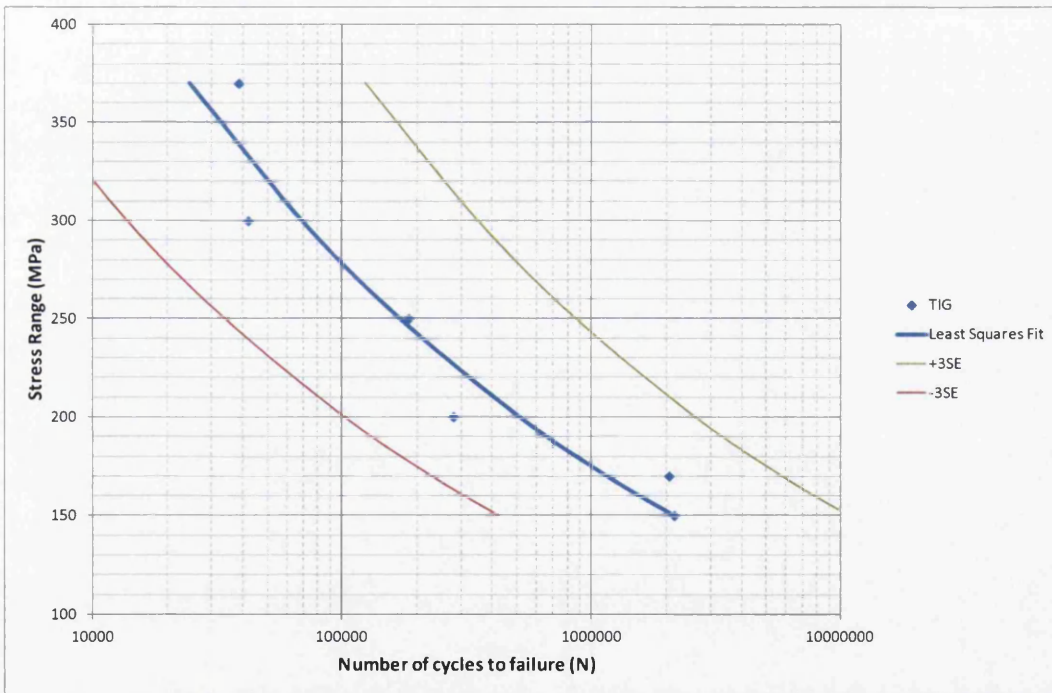
Figure 6.20. TIG SN curve

160
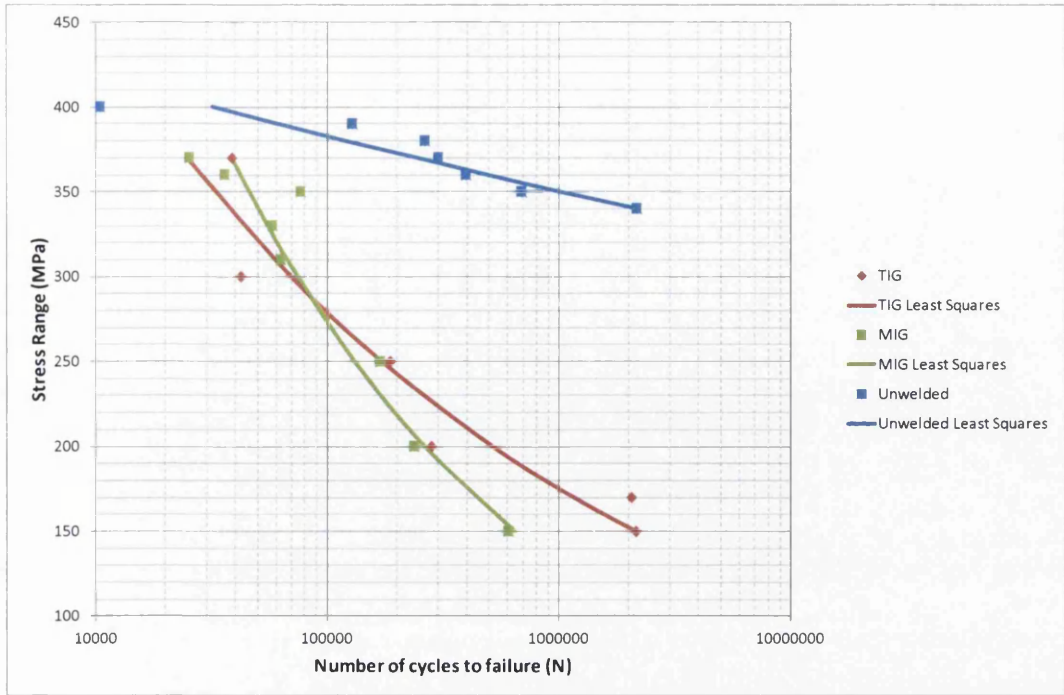
Figure 6.21. MIG, TIG & un-welded SN curves

The reduction in fatigue life of welded coupons does not come as a surprise, as Maddox [20] outlined design rules for various welds geometries subject to cyclic loading. Weld's were grouped into categories where a butt weld of this type falls into group C, as shown in figure 6.22.

| Full penetration butt weld joining plates of equal width and thickness made from both sides or from one side onto consumable insert or temporary non-fusible backing. | Weld overfill dressed flush and welds proved free from surface breaking and significant embedded flaws by appropriate NDT. Any misalignment blended with slope 51 in 4. | 4.1 | C | Because of extremely demanding NDT requirements, this type is only recommended for use in exceptional circumstances and certainly not in structural work. Recognition of this results in choice of Class D for dressed flush seams in pressure vessels. | |

Figure 6.22. Category C weld as described by Maddox.

Fatigue properties for this class of weld can be seen in table 6.7, where the R-ratio used to generate this information was set at 0. The constants refer to the equation shown on the next page below. As d is the number of standard deviations $a\Delta^d = A$. The final equation is a re-arranged variant that allows generation of an S-N curve.

Table 6.7. Fatigue properties of a class C weld.

Curve (class C)	m	Δ	A	S_0 (N/mm^2)
Mean			1.08×10^{14}	102
Mean-1SD	4.0	0.657	6.75×10^{13}	89
Mean-2SD			4.22×10^{13}	78

161

$$S^m N = a\Delta^d$$

$$S^m N = A$$

$$S = \sqrt[m]{A/N}$$

Surprisingly, this curve represents the weld S-N curve for any grade of steel, irrespective of the substrate microstructure or filler material. This may not be the case now, as a greater number of filler materials exist for today's AHSS & UHSS. However, this equation should be a good representation of the HSLA material used as part of this project. The only problem with this data is that it is set for an R-ratio of 0, and in order to convert it to other R-ratios using Goodman or Gerber, the fatigue data at a ratio of -1 would be required. The results of this calculation are plotted in the graph in figure 6.23.
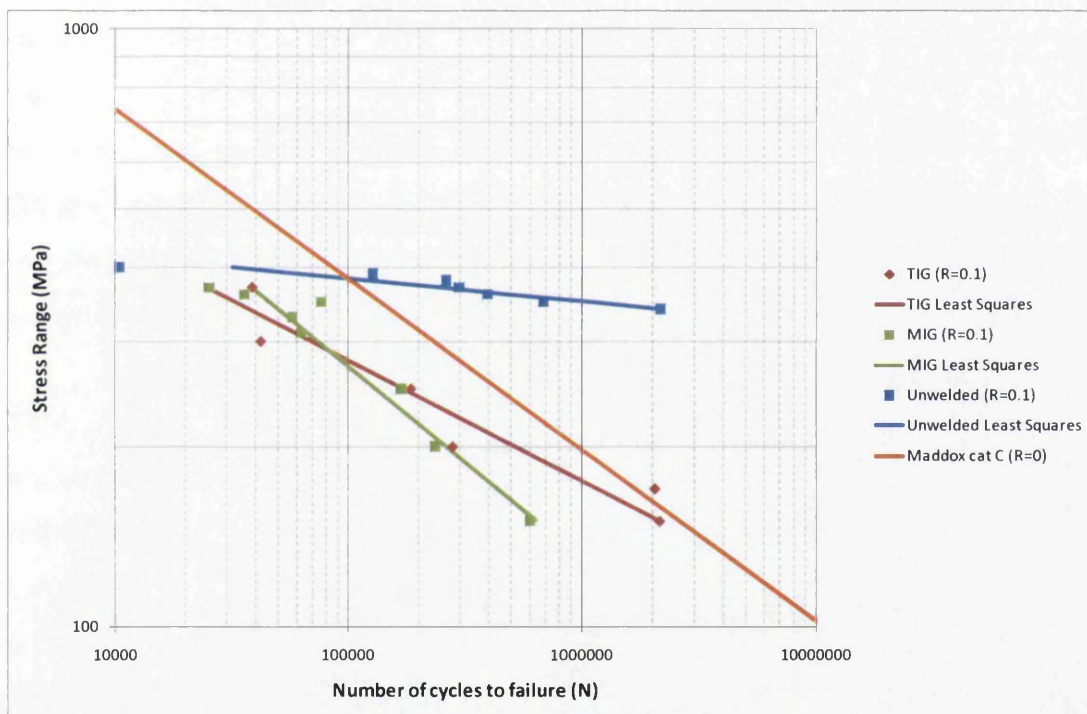
Figure 6.23. MIG, TIG, un-welded & Maddox SN curves.

Although the curve generated by Maddox's date may look slightly different, it does tie in with the experimental results. The gradient of the curve is very similar to the experimentally obtained MIG curve, and the position of the curve would be shifted to the left by moving from a higher mean stress with an R ratio of 0.1, compared to the ratio of 0 that this curve represents. Moreover, in this case, as the low cycle strength will be limited by the substrate (~400MPa), thus the curve is probably very representative of a MIG weld with S355MC/XF350 as a substrate.

162

The vast difference in the performance of welded coupons versus un-welded variants can be explained by the Digital Image Correlation (DIC) results, as can be seen in figure 6.24. DIC images track the movement of a speckle pattern that had been sprayed on to the surface of the material, from which it can calculate the strain. This image shows how applying a load below the yield point of the material, which should only give a strain of around 1833 microstrains actually results in strains of 3000 microstrains or more due to the stress concentrations at the base of the weld. It can be seen from the colour scale that the main body of the specimen is experiencing the expected level of strain of around 1833 microstrains that was calculated given the loading conditions, cross-sectional area and modulus of elasticity for this material.

Note that there are two spots on the image that have given erroneous results due to an unknown optical error, which could be caused by numerous factors such as dust particles, slight paint loss etc. This does not deter from large stress concentration that has been identified here, and there can be no doubt that this is the primary reason for the poor fatigue performance compared to un-welded specimens. This factor alone can be considered far more significant than any metallurgical changes to the substrate in the heat affected zone, or the microstructure of the weld itself.

This image of a MIG weld can be considered to be a typical sample of this joining method. In fact the aesthetic and geometric appearance of all MIG welds in the collection of coupons were reasonably similar to each other, with relatively little variability in terms of distribution of filler material. This is due to the perfectly constant wire speed that is pre-set when performing MIG joining, as will be discussed later.

It may also be noted that the stress/strain concentration seems to be one-sided, with the highest strain readings taken on the bottom half of the weld. This is on the static clamped side of the coupon, where a tensile load is applied from the top. This observation is not coincidental as every single fatigue test for both MIG and TIG welding types gave failures on this bottom section of the weld.
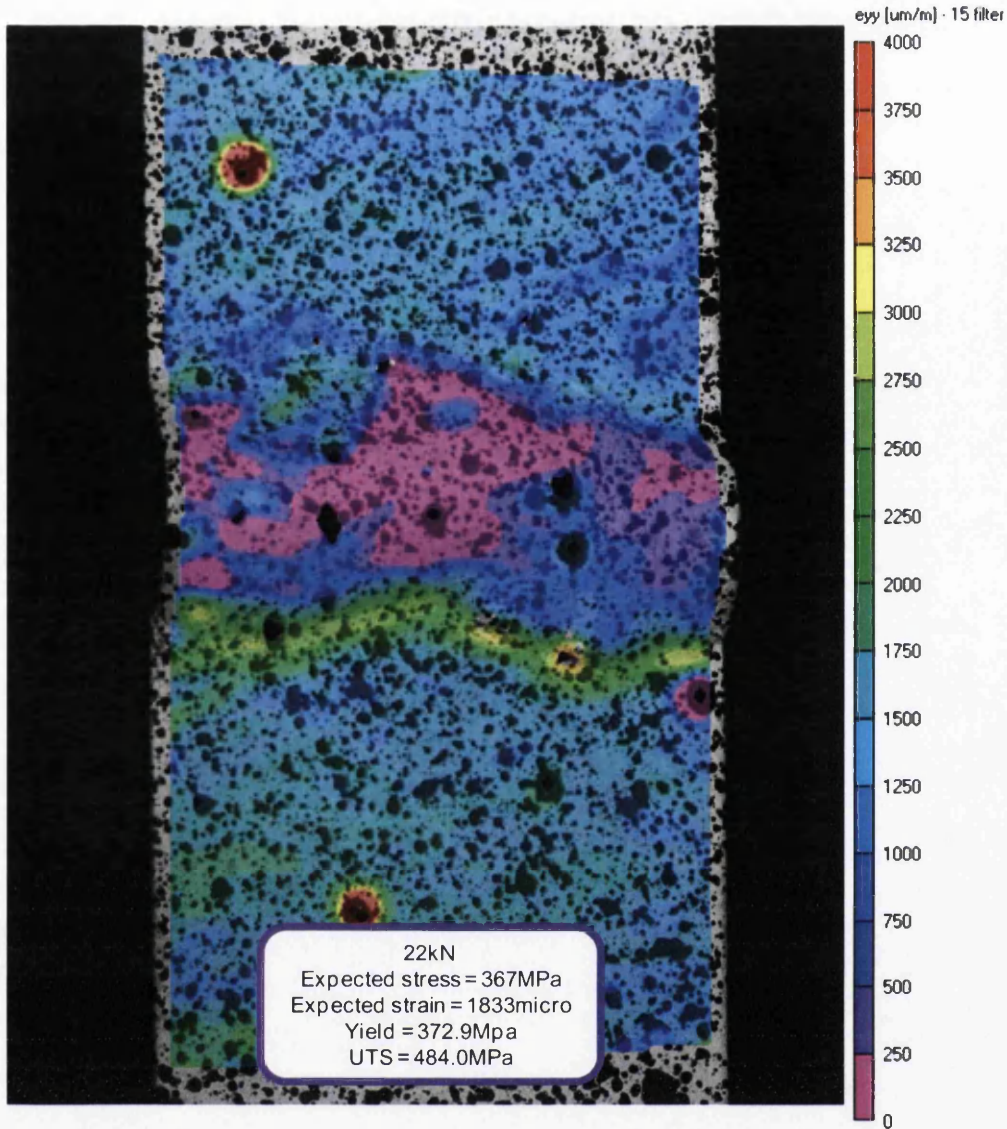
Figure 6.24. DIC image of a MIG weld

By analysing the standard errors of the SN curves for both welding methods, it is clear that the performance of the MIG welds were more consistent than those of the TIG welds. This is also reflected in the appearance of the welds, where practically all the MIG welds had a similar appearance to that shown in figure 6.25. Due to the increased complexity of TIG welding, the welds were far more variable. Some had a highly raised profile where the filler material was added, where others were far flatter in appearance. This is especially visible in figures 6.25-6.28.
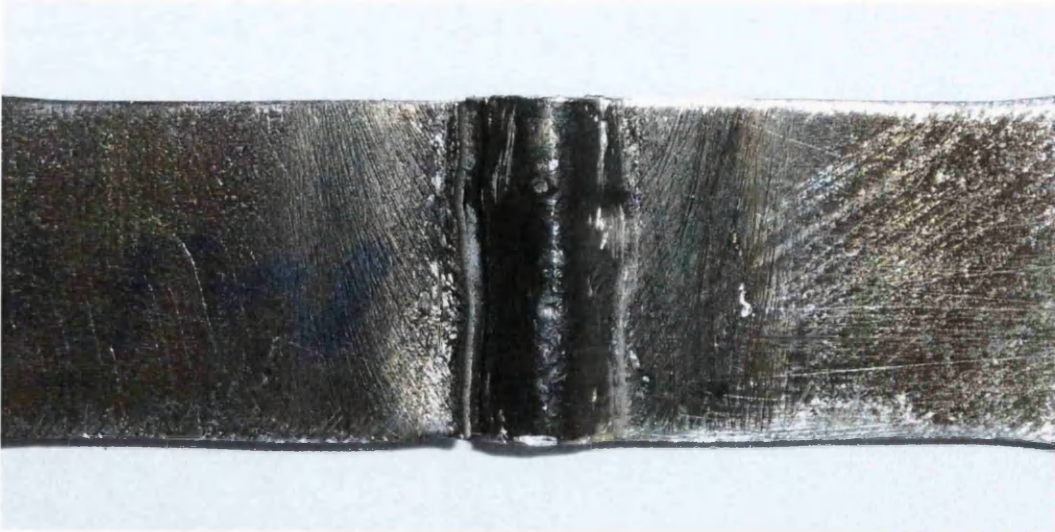
Figure 6.25. MIG weld failure
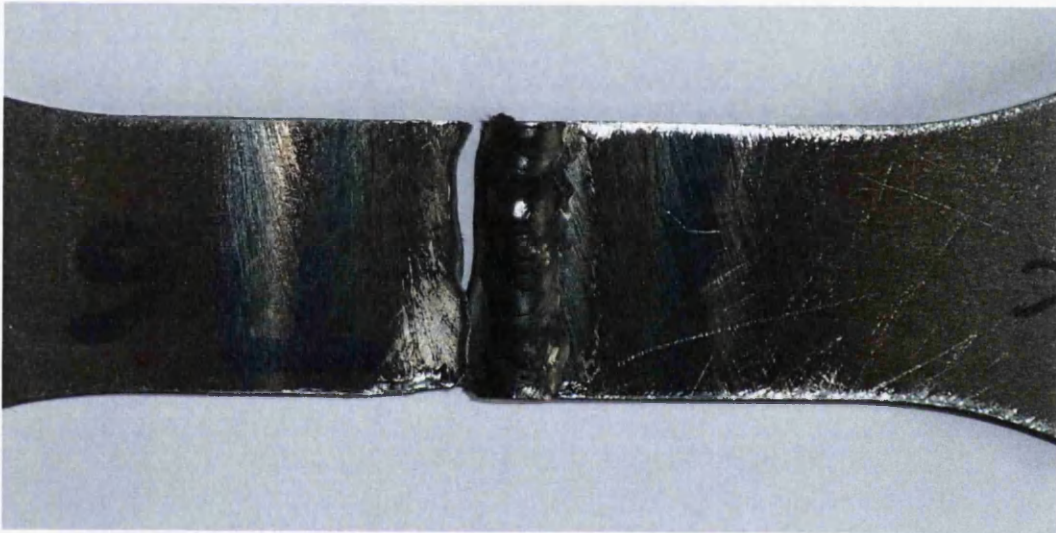
Figure 6.26. Under-performing TIG weld Failure

Figure 6.27. Over-performing TIG weld Failure

At first glance it may seem by analysing figure 6.21 that TIG welds have a better overall performance, though in reality the fatigue performance has more to do with the weld geometry rather than the welding method and resultant microstructure. This conclusion is possible since towards midway through the testing programme a trend was identified and accurate predictions were made purely based upon the geometry and aesthetic appearance of the weld.

Every TIG weld which had a raised or domed profile such as shown in figures 6.26 and 6.28 had fatigue lives which were below the 50% survival curve, whereas the welds with a lower, almost flat profile with neat tie-in at either side of the welds, as shown in figures 6.27 and 6.28 had lives exceeding those predicted by the 50% survival curve. It is thought that this is due to the weld toes having high levels of stress concentration, and are the main contributors to crack initiation, rather than any disturbance caused to the original coupon microstructure, or properties relating to the filler material.

It is perfectly understandable that the TIG welds exhibit more variability than the MIG welds, as the operator has to coordinate the addition of filler material with one hand whilst simultaneously creating a fusion pool using the other arm. MIG welding on the other hand can be done single handed since the wire feed is automatic and combined within the fusion process. Thus the profiles of the MIG welds were all fairly similar, whereas the geometrical properties of TIG welds were significantly different from one coupon to another.
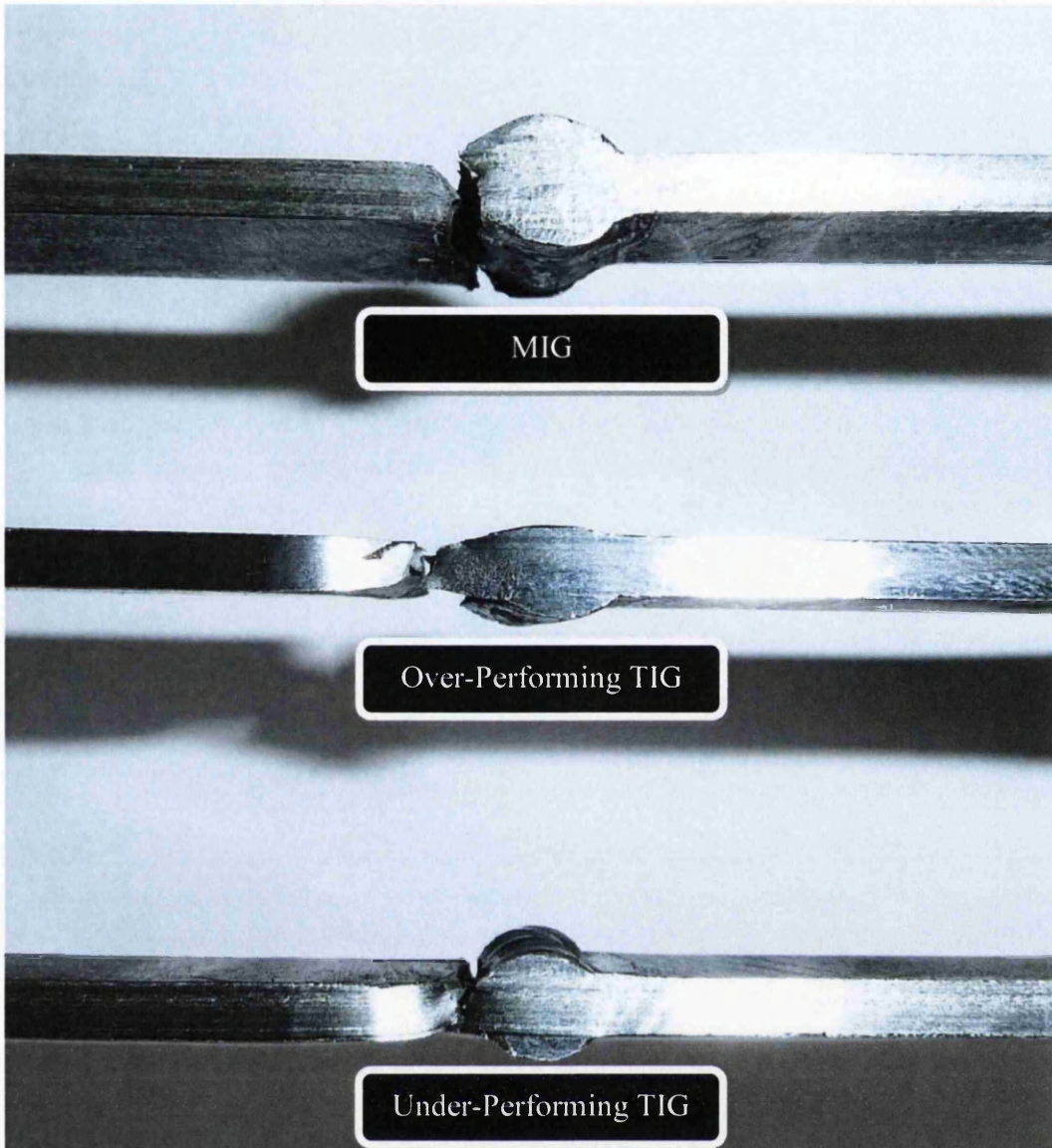
Figure 6.28. Weld profile comparison

Whilst there can be no doubt as to the influence of the weld geometry on the fatigue properties of this material, it is difficult to come to a final conclusion as to which welding method potentially gives the best weld performance. By analysing the individual results of each specimen, it appears that both MIG and TIG weld fatigue results are similar to each other given that the profiles of the welds in each coupon are also similar. However with increased potential to achieve flatter weld profiles with TIG welding, it appears that for a robust product a very carefully executed TIG weld would be a better option than its MIG counterpart.

Maddox also documented information on the effects of weld geometry on fatigue with the same conclusions. It can be seen in figure 6.29 that poor profiles are severely detrimental to fatigue performance, where accompanying data for that graph is shown in figure 6.30.
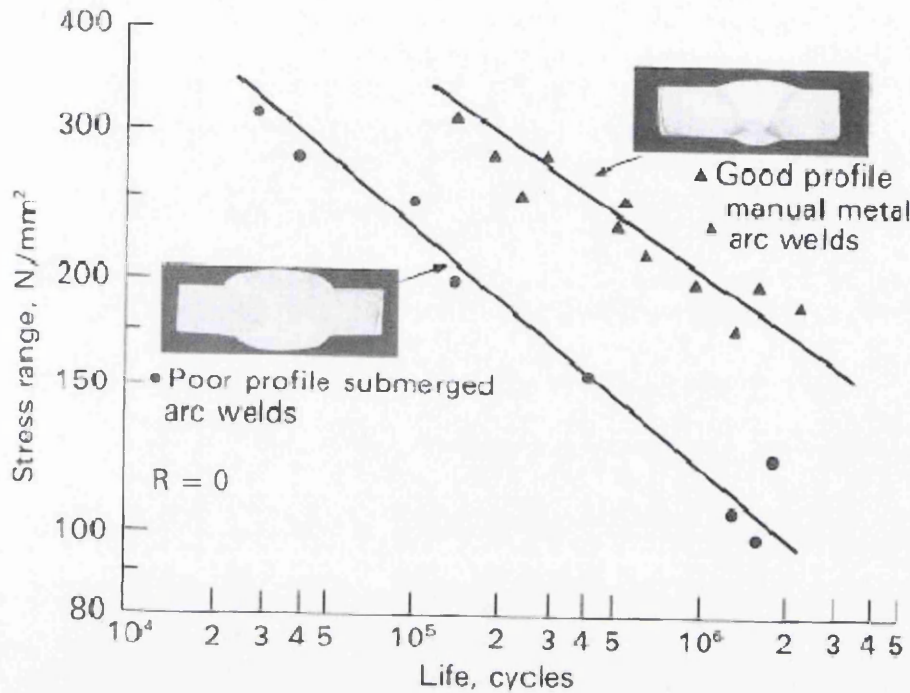
Figure 6.29

Detail	Sketch of detail and mode of fatigue cracking	Fatigue strength (R = 0) N/mm²	
		10⁵ cycles	2 × 10⁶ cycles
Transverse butt welds with good profile		355	155
Transverse butt weld with poorer profile (including submerged-arc)		260	116
Transverse electron beam butt weld		310	155
Transverse butt weld on a permanent backing strip		260	100

Figure 6.30

Again, this phenomenon can be related back to fatigue crack initiation & propagation theory, where at high stresses a large fraction of the total fatigue life comprises of stage I and II crack growth, where at low stress levels the majority of the fatigue life is determined by the crack initiation period. It can be seen from figure 6.31 from Schijve that the crack initiation period is heavily influenced by surface characteristics, where any stress concentrations will shorten this period and hence have a detrimental effect on the high cycle fatigue life.
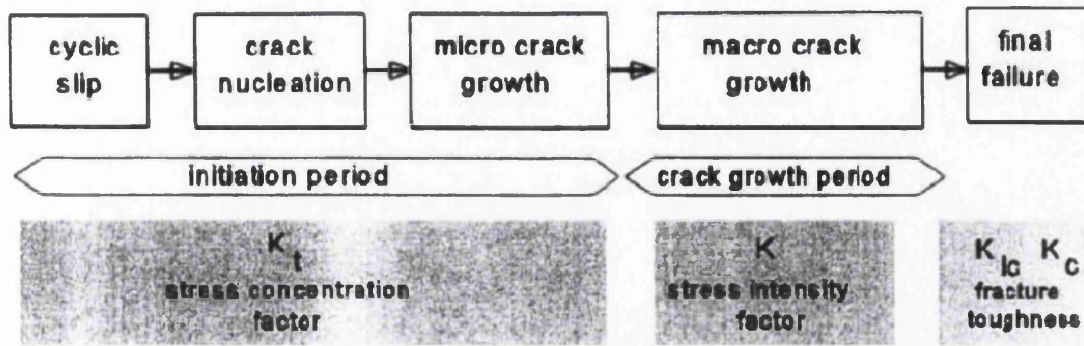
Figure 6.31. Different phases of fatigue life and relevant factors.

One question raised by this work which is not possible to answer without further research is whether grinding welds to a flat surface on both sides would result in increased fatigue resistance and also more consistent performance. Even though it is not possible to answer this question with any certainty, through the results obtained within this project, it is suspected that doing so would have a significantly positive effect on fatigue life.

Another question raised is, by grinding the welds would the two welding methods give similar results after grinding, or would the difference in their microstructures come into effect once their geometrical properties were nullified? What this research has told us is that TIG welding can potentially offer us improved fatigue resistance over MIG welding, given that the process is optimised and executed with either a great deal of skill or automated with settings that would allow a flat weld profile such as seen in figure 6.27.

In order to avoid welds such as the one shown in figure 6.26 a number of factors must be considered. Firstly the amperage has to be sufficient to provide a turbulent weld pool in which adequate mixing of the parent and filler material occurs. Too much heat on the other hand could result in the weld burning through the material, especially for thinner materials, this is commonly referred to as weld blow through. One factor that is certainly causing the undesirable domed profile is the feeding of filler material being too quick. Not only does this cause a build up of material, which leads to stress concentration at the base of the tie-in regions, but it also absorbs some of the energy that should have been used to create a turbulent weld pool as

previously discussed. This parameter, along with the welding/line speed are two of the factors which cause the most variability for manual TIG welding.

The reason that these two are the main contributors to variability, and that the welding amperage is a consistent parameter is that typically a welder will optimise the heat setting on practice pieces before welding components and this setting will remain fixed for the duration of the procedure. Having said that, the welding speed also affects the amount of heat introduced, since a fast line speed allows little time for fusion to occur and heat to build up, this can result in a very narrow fusion area and a lack of penetration. If all these parameters can be optimised and executed with a high level of skill.

6.4 FE evaluation of weld geometry

After noting that weld geometry is a highly influential factor in determining the fatigue properties of welds, it was decided to carry out FE evaluations on the effects of geometrical deviances on fatigue coupons. This evaluation helps us understand the physical test results and confirms the previous hypothesis. The assessment was carried out by applying a load which equates to a theoretical stress of 350MPa in the same manner as that shown for the un-welded sample in chapter 3. Stress predictions are made for both Von-Mises and normal stress in the direction of the applied load, where the predictions for both are similar.

The first task was to evaluate the failed specimens and note the geometries of specimens that over-performed and under-performed the 50% survival curve. The geometries of such specimens can be simplified to the drawing shown in figure 6.32. Whilst this model is basic and does not show the striation patterns of the weld it represents the overall geometry very accurately. Note that the better of the two welds is both wider and flatter. What this model cannot show is the quality of the tie-in on the weld base, which tended to be better on the flatter welds, and as such this evaluation only stands to assess the effect of the basic geometry. The FE evaluations follow in figures 6.33 – 6.36.
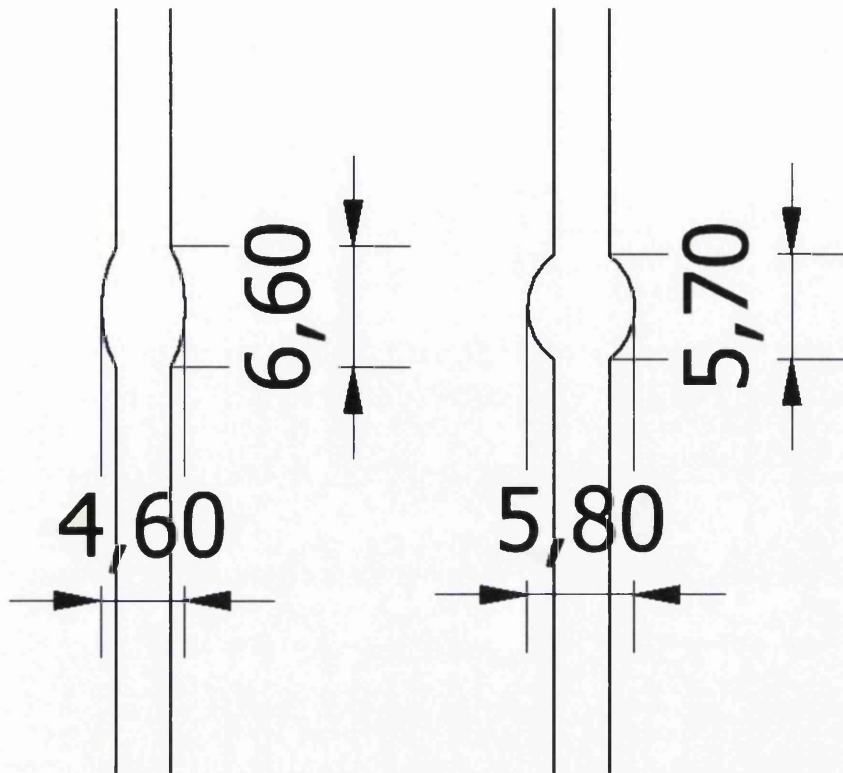
Figure 6.32. Geometries of over-performing weld (left) and under-performing weld (right)

It can be seen that both the Von-Mises and normal stress predictions show stresses of around 360MPa and 372MPa for the flatter and higher profile welds respectively, where the location of the stress concentrations in both are at the base of the tie-in at the edge of the coupon. This stress concentration goes some way to explaining the deviations from the 50% survival curves, though it is believed that the quality of the tie-in regions are also a contributing factor, where the flatter welds tended to have very neat tie-in's and the more domed like geometries could at times appear more jagged in appearance.
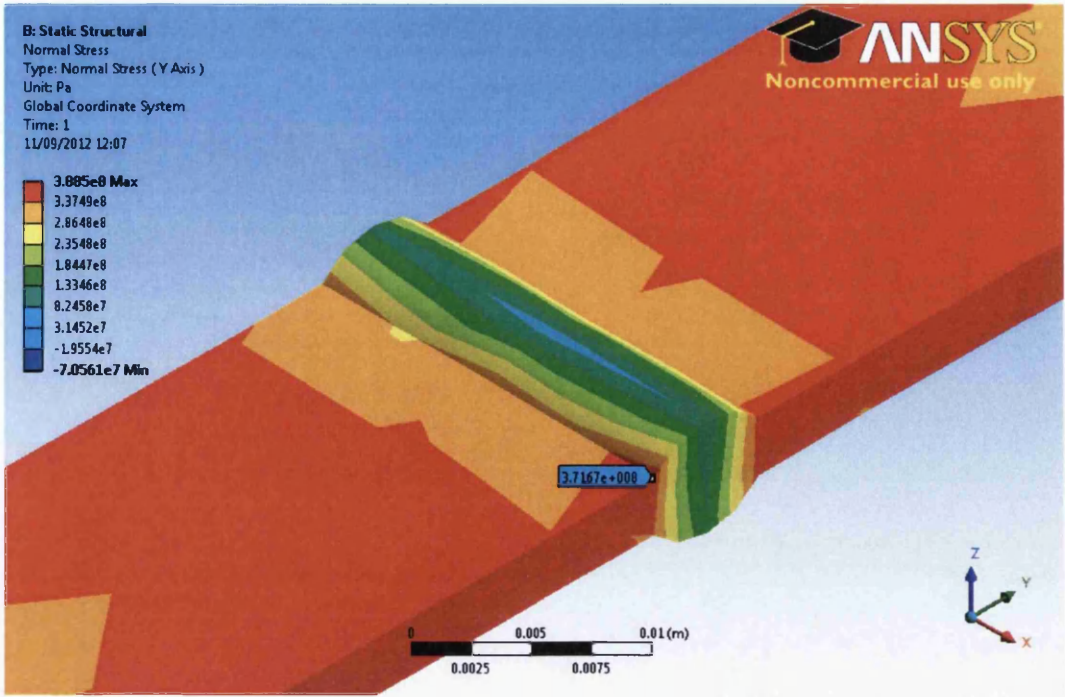
Figure 6.33. Normal stress in a poor weld
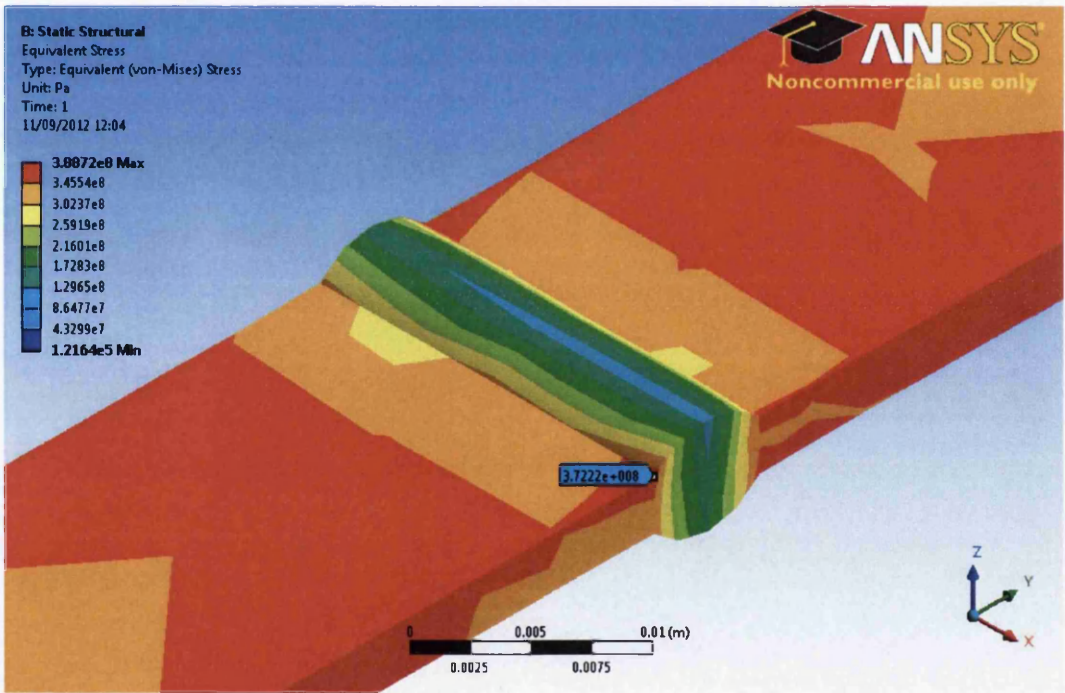
Figure 6.34. Von-Mises stress in a poor weld
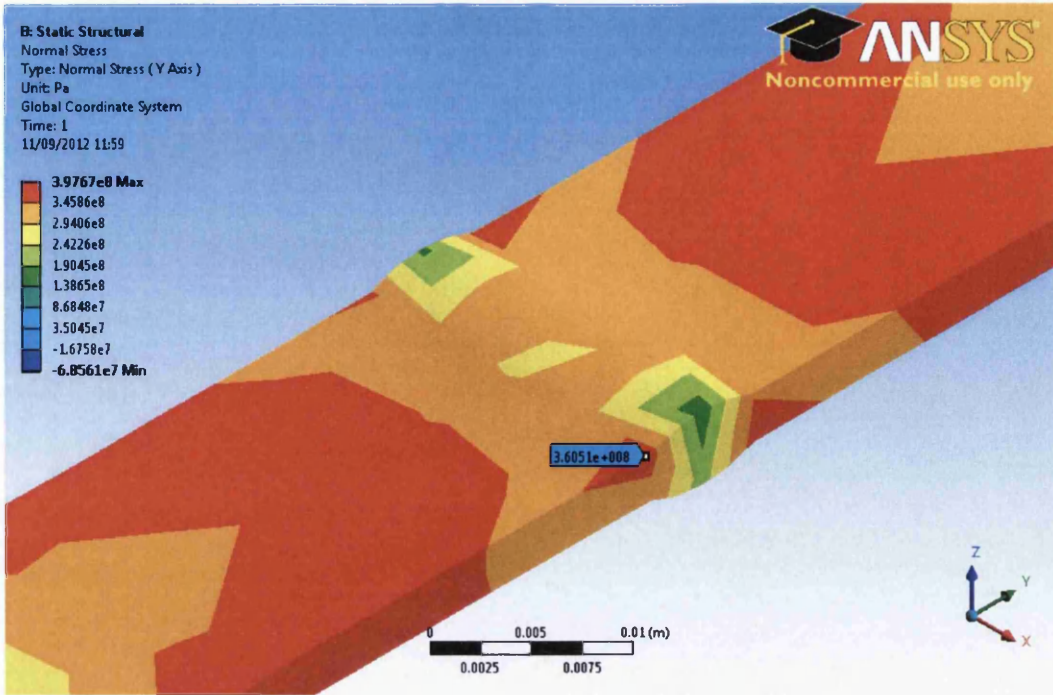
Figure 6.35. Normal stress in a good weld
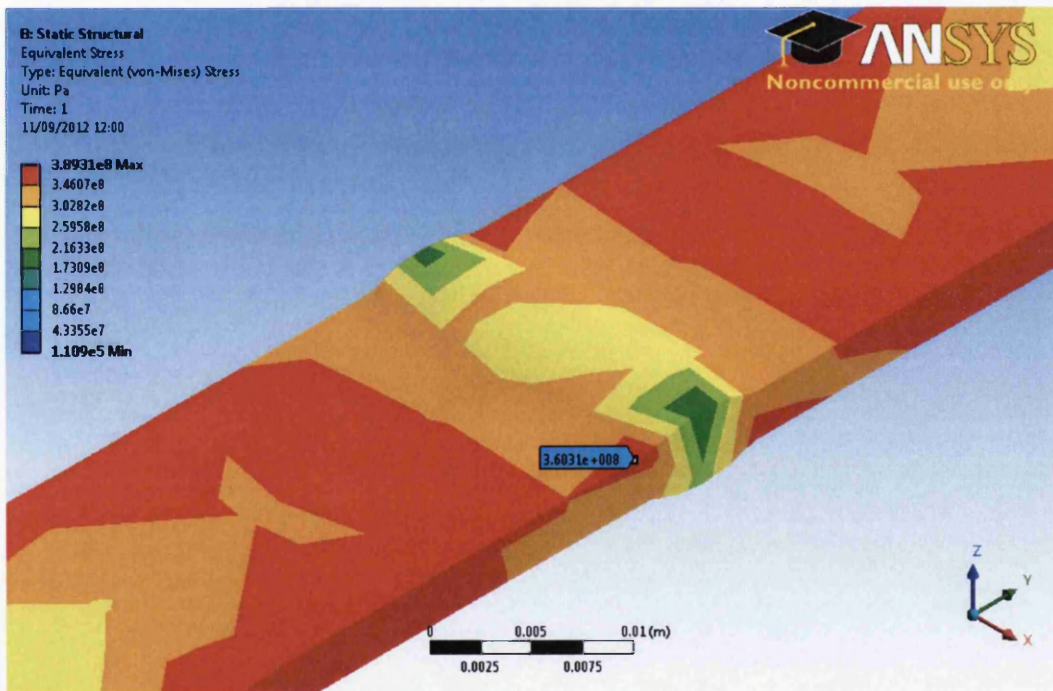
Figure 6.36. Von-Mises stress in a good weld

Chapter 7 – Effect of material variability on a top hat structure

7.0 Introduction

After gathering numerous data sets on fatigue performance, tensile property variability and strip thickness variability, it is now possible to analyse the effect of these factors on the overall structural performance of a manufactured structure. In this case the component is a top hat structure tested by a former Tata Steel EngD research engineer, D Thomas [55]. The structure is made of XF350, and is geometrically similar in terms of its thickness and cross section to many structures found in the automotive chassis sector. Engineering drawings of this structure can be seen in figures 7.1, 7.2 and 7.3 where this particular batch of steel had yield strength, UTS and elongation values of 394MPa, 473MPa and 30.8% respectively.

19 x spot welds @ 27.5mm pitch
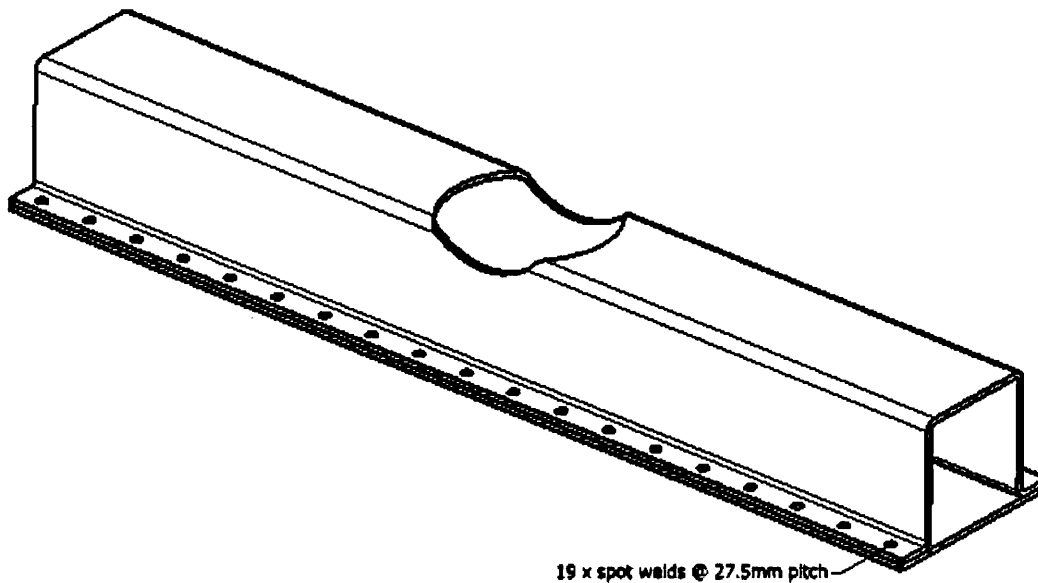
Figure 7.1. 3D illustration of the top hat structure

With the potential for variability in mechanical properties, as well as the strip thickness, the dimensions shown in figure 7.2 are of course subject to change, therefore these dimensions are only valid for the nominal 3mm strip thickness. As well as being in possession of a great deal of material property data for this structure, the fatigue performance is also documented and can be seen in table 7.1.

By using the material data from previous chapters, it is hopeful that a strong correlation exists between FE based predictions using ANSYS commercial software and the data shown in the table. Once the FE model is capable of returning accurate

174

predictions, the model created may be used to evaluate the effects of material property data being at the upper and lower specified limits for this grade of material.
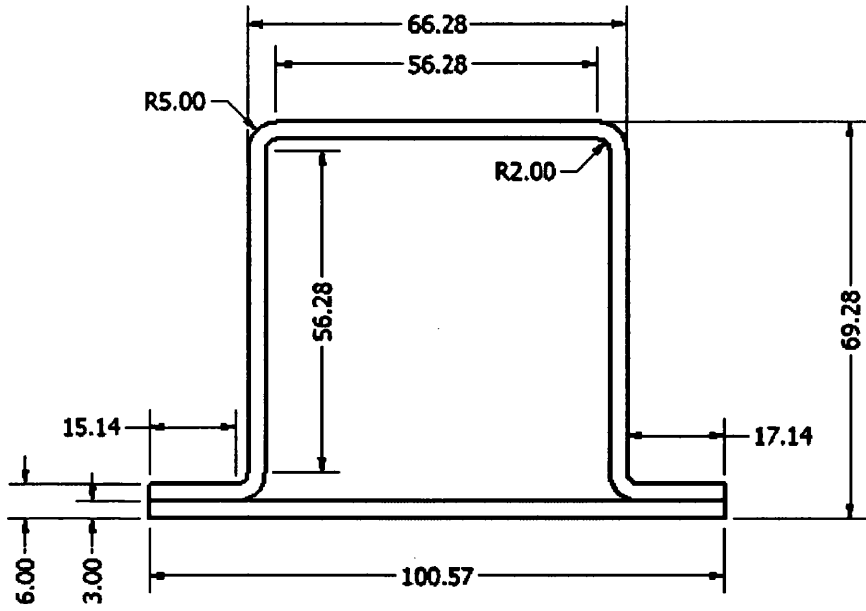
Figure 7.2. Top hat cross-section
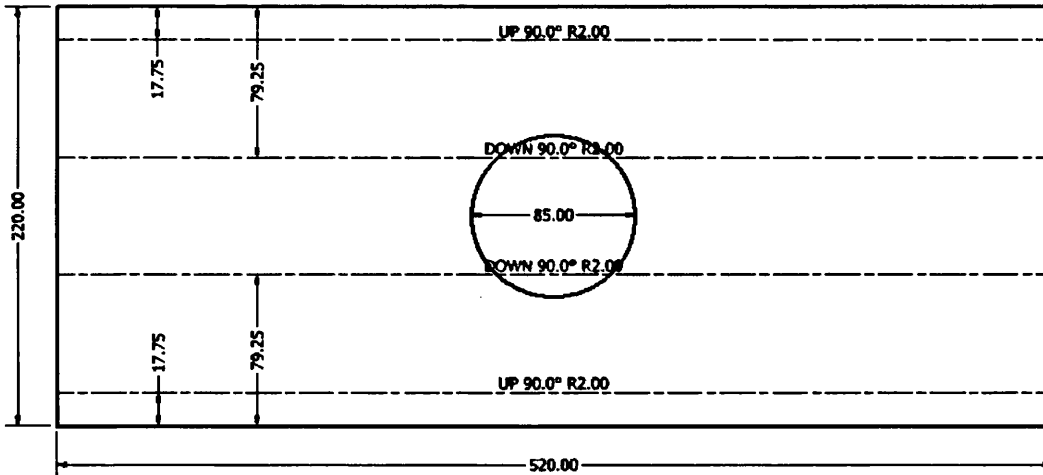
Figure 7.3. Top hat sheet metal folding specifications

Table 7.1. Top hat physical test fatigue data

Load (kN)	Number of Cycles to Failure	
	Least Squares Prediction	Test Life
20kN	472,669	467,395
22kN	242,532	225,000
24kN	131,890	137,333
26kN	75,309	93,000
28kN	44,825	38,000
A=129292 (N)	b=-0.14284	SE=0.070564

The fatigue curve for the top hat structure can be seen in figure 7.4 below. This curve is only representative of material that has yield strength, UTS and elongation values of 394MPa, 473MPa and 30.8% respectively, as mentioned earlier. Furthermore, any deviation from the nominal strip thickness of 3mm will render this curve inaccurate unless provisions are made to account for these changes.
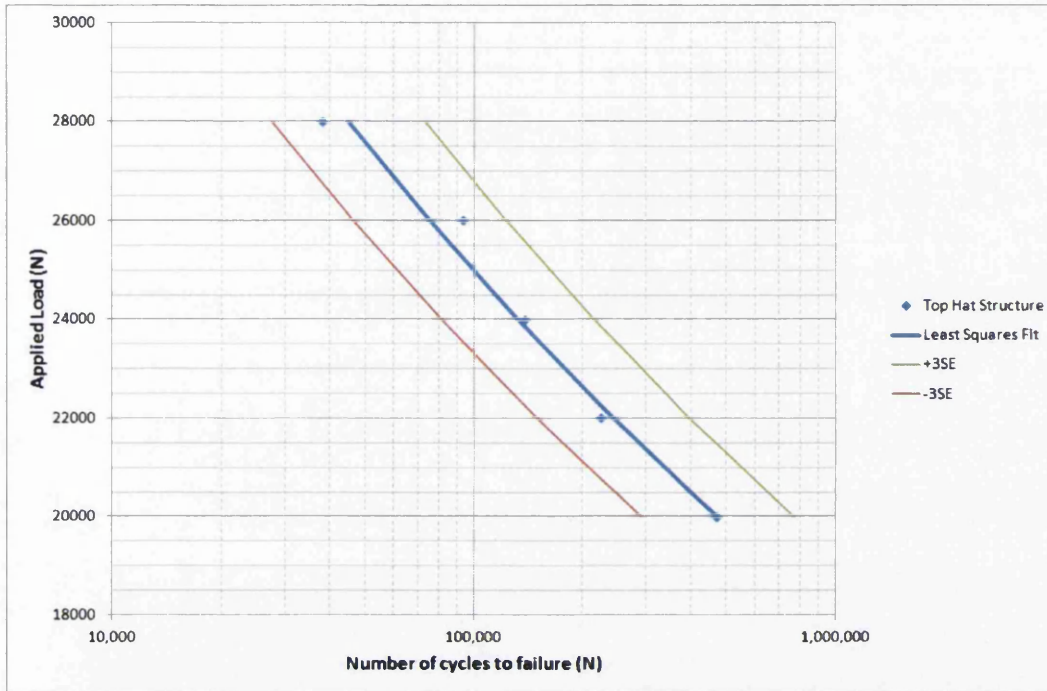
Figure 7.4. Top hat fatigue curve

Accounting for the change in structural performance due to inconsistency in strip thickness poses little difficulty, as the thickness of the material is directly proportional to the fatigue performance during axial loading. The major difficulty lies in accounting for other variabilities such as tensile properties, where it is known that these prameters do affect fatigue performance, though the extent of which are difficult to quantify. As a result of this, certain presumptions will have to be made during the course of this chapter, all of which are consistent with other findings as part of this work.

7.1 Effect of strip thickness variability

7.1.1 Strip thickness and second moment of area

In addition to a components resistance to fracture during loading etc., it is also of interest to understand the resistance to bending, or the stiffness of a component. The stiffness can be defined as flexural rigidity, which is the modulus of elasticity multiplied by the second moment of area (E × I). As the modulus is fixed, the only variable which will influence the rigidity is the thickness of the material, as such it was decided to investigate the relationship between changes in strip thickness due to processing variability and the second moment of area.

The relationship between variations in component geometry and its second moment of area (or area moment of inertia) is a complex one. Any correlation that exists between these two parameters can only be applied to the specific part analysed, since so many geometrical factors have to be taken into account. For general cross sections a trend does exist, i.e. the second moment of area of a rectangular section is shown below:

$$I_{XX} = \frac{bd^3}{12}$$

Where:

I_{XX} = cross sectional second moment of area, as measured from neutral x-axis (mm^4).
b = cross-sectional breadth, or width (mm).
d = cross-sectional depth, or height (mm).

From this we can see that doubling the width merely doubles the second moment of area, doubling the depth however increases the second moment of area by 8 fold. The added difficulty when assessing the effect of such a parameter is the need to establish the new geometry with fluctuations in the strip thickness. This is not as easy as first imagined, as simply making the whole component 0.15mm thicker all round in order to account for steel that is 0.3mm over the specified thickness is not an accurate way of accounting for this change.

Probably the best way of estimating the new geometry is by analysing the production method and ensuring the same manufacturing steps are carried out with the new

thickness of steel, i.e. the folding locations of the top hat structure in figure 7.3 should not change, despite the material being thicker. Assuming the bottom sheet is cut to the new size top hat structure (which it would have been with these hand made samples, but may not be in an automated sequence), then the new geometries of the top hat structures conforming to the minimum and maximum euronorm specifications are shown in figures 7.5 and 7.6.

With the detailed dimensions of the top hat with the nominal 3mm strip thickness shown in figure 7.2, along with the upper and lower tolerances shown in the two figures on the next page, there is enough information to calculate the second moment of area for each cross-section and hence evaluate the effect of material thickness variability on the structural stiffness of this particular component. It must be remembered that this is in effect a case study, and as such results from this analysis are only relevant to this structure and are not transferrable to any other part. The section properties of any component are unique, and a separate study has to be carried out for each individual part.
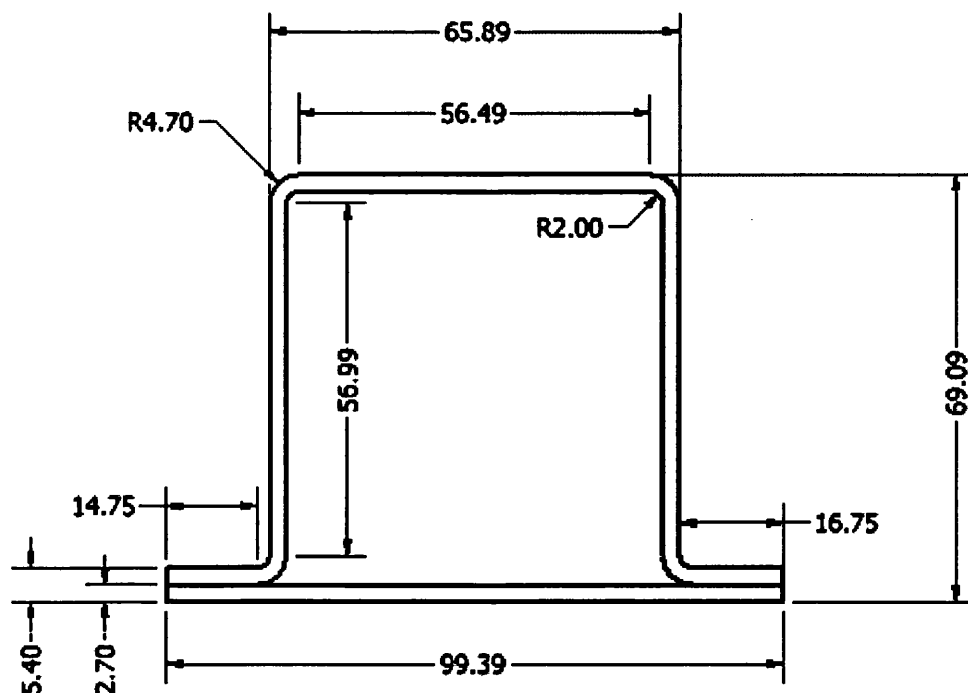
Figure 7.5. Top hat cross-section for 2.7mm thick strip steel
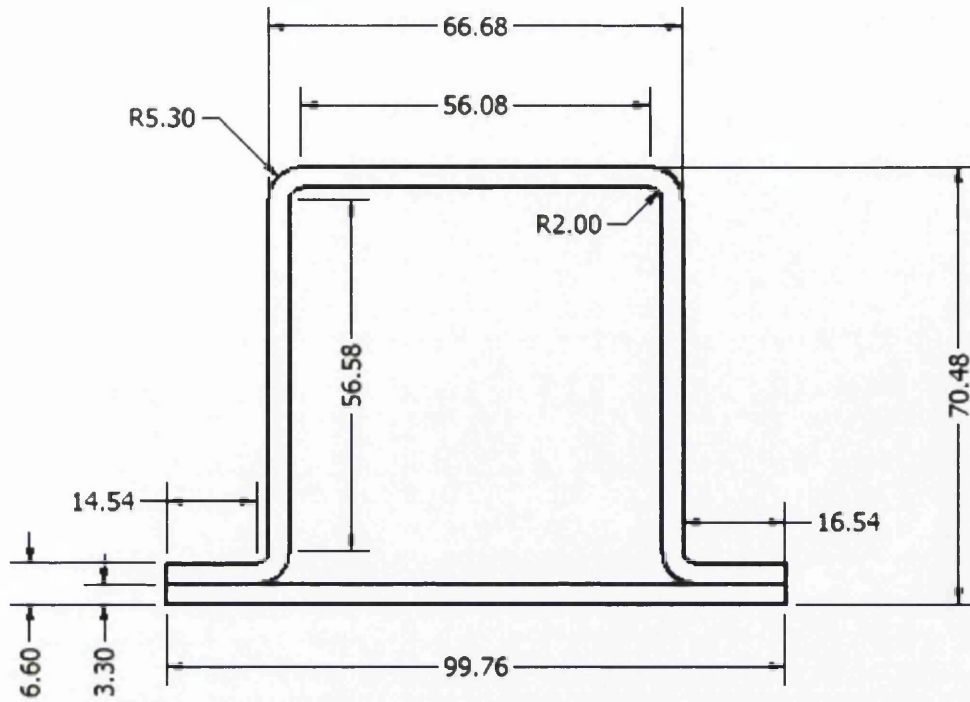
Figure 7.6. Top hat cross-section for 3.3mm thick strip steel

In order to calculate the second moment of area for these sections, the principles of this area property needs to be defined and understood, once this is done the cross sections can be broken up into regular shaped sections and calculated individially. The overall second moment of area can then be worked out by using the parallel axis theorem.

The second moment of area of any geometry can be described mathematically as:

$$I_{xx} = \int y^2 \cdot dA$$

Where dA is an elemental area as shown in figure 7.7.
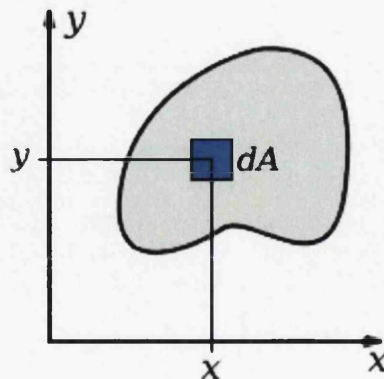
Figure 7.7. Elemental area

179

In order to calculate the second moment of area for the top hat structure, ther cross-section will be broken up into common geometric shapes wich have second moment of area equations which can be easily looked up in engineering handbooks. The only geometrical shape that is not generally easy to find is a semi-circle, thus is described from first principles below:

$$I_{XX} = \int y^2 \cdot dA = \int_0^\pi \int_0^r \left(y_{cg} - \sin\theta\right)^2 \cdot dr \cdot rd\theta$$

$$I_{XX} = \frac{(9\pi^2 - 64)r^4}{72\pi}$$

We also need to be able to define the centre of mass for a semi-circle:

$$y_{cg} = \frac{\int y \cdot dA}{A}$$

$$y_{cg} = \frac{\int_0^\pi \int_0^r r \cdot \sin\theta \cdot dr \cdot rd\theta}{\frac{1}{2}\pi \cdot r^2} = \frac{4r}{3\pi}$$

Thus with all the necessary information, the calculation of the structure's second moment of area can begin, where the cross-section is broken up into 8 regular sections, two of which are negative areas which are added to counteract the fact that two semi-circles are added. By using negative areas, the sum of the calculations along with the parallel axis theorem enable us to build a semi circular tube.

The geometry of these sections are shown in table 7.5, which can be used to help identify how the section is broken up. Tables 7.2, 7.3 and 7.4 show the calculations for I$_{GG}$ and Ah^2, which are necessary components in order to use in the parallel axis theorem prior to calculating the second moment of area. Figure 7.8 shows how the cross-sections are broken up into regular shapes for calculation (nominal gauge used as example):
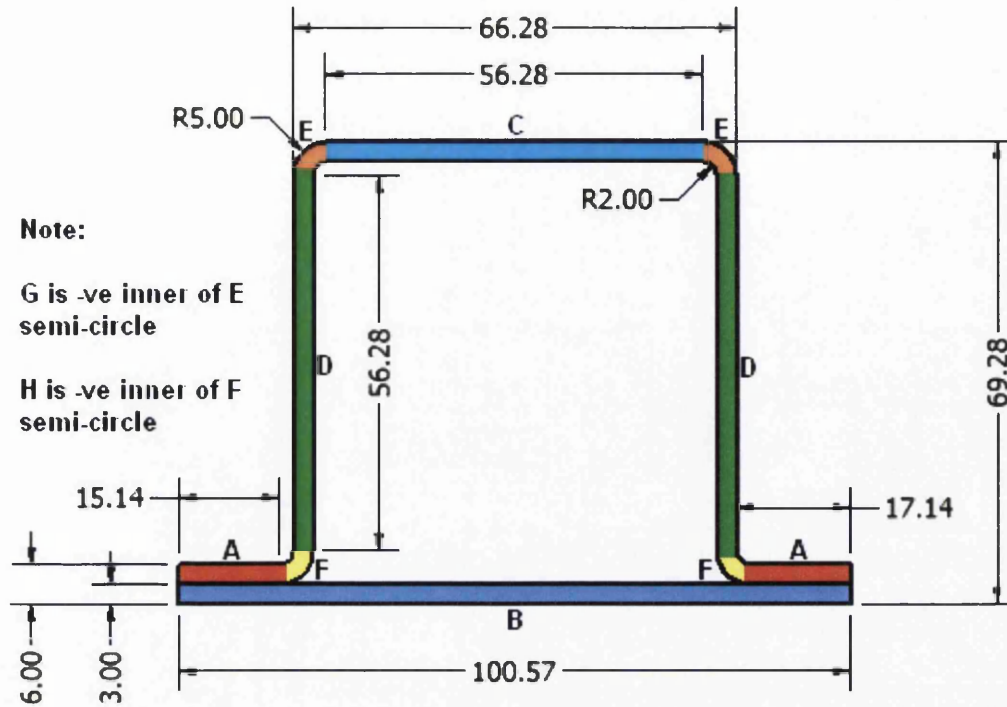
Figure 7.8. Sections for second moment of area calculation

Table 7.2. Nominal thickness second moment of area calculation

Section	A (mm^2)	y (mm)	Ay (mm^3)	h (mm)	Ah^2 (mm^4)	I$_{GG}$ (mm^4)
A	90.84	4.50	408.78	23.90	51875.06	68.13
B	301.71	1.50	452.57	26.90	218269.31	226.28
C	168.84	67.78	11443.98	39.38	261876.28	126.63
D	337.68	36.14	12203.76	7.74	20246.05	89131.72
E	78.54	66.40	5215.21	38.01	113442.61	68.60
F	78.54	5.88	461.65	22.52	39827.68	68.60
G	-12.57	65.13	-818.43	36.73	-16955.02	-1.76
H	-12.57	7.15	-89.86	21.25	-5672.19	-1.76
Sum	1031.02	N/A	29277.64	N/A	682909.76	89686.44

Table 7.3. Minimum thickness second moment of area calculation

Section	A (mm^2)	y (mm)	Ay (mm^3)	h (mm)	Ah^2 (mm^4)	I$_{GG}$ (mm^4)
A	79.65	4.05	322.58	24.14	46421.72	48.39
B	268.35	1.35	362.28	26.84	193342.01	163.02
C	152.52	67.74	10331.91	39.55	238556.45	92.66
D	307.75	35.40	10894.21	7.21	15990.39	83293.00
E	69.40	66.38	4606.95	38.19	101231.17	68.60
F	69.40	5.41	375.11	22.79	36032.83	68.60
G	-12.57	65.24	-819.82	37.05	-17247.22	-1.76
H	-12.57	6.55	-82.32	21.64	-5884.98	-1.76
Sum	921.93	N/A	25990.90	N/A	608442.36	83730.75

Table 7.4. Maximum thickness second moment of area calculation

Section	A (mm^2)	y (mm)	Ay (mm^3)	h (mm)	Ah^2 (mm^4)	I$_{GG}$ (mm^4)
A	95.96	4.95	475.02	24.23	56321.81	87.09
B	329.21	1.65	543.19	27.53	249437.00	298.76
C	185.06	68.83	12737.96	39.65	290999.99	167.95
D	373.43	36.89	13775.76	7.71	22220.35	99621.14
E	88.25	67.43	5950.46	38.25	129133.34	68.60
F	88.25	6.35	560.42	22.83	45977.27	68.60
G	-12.57	66.03	-829.74	36.85	-17066.65	-1.76
H	-12.57	7.75	-97.40	21.42	-5768.33	-1.76
Sum	1135.03	N/A	33115.67	N/A	771254.79	100308.6

Table 7.5. Top hat section geometry

Section	Radius (mm)			Breadth/width (mm)			Depth/height (mm)		
	Nom	Min	Max	Nom	Min	Max	Nom	Min	Max
A	N/A	N/A	N/A	30.28	29.5	29.08	3	2.7	3.3
B	N/A	N/A	N/A	100.57	99.39	99.76	3	2.7	3.3
C	N/A	N/A	N/A	56.28	56.49	56.08	3	2.7	3.3
D	N/A	N/A	N/A	6	5.4	6.6	56.28	56.99	56.58
E	5	4.7	5.3	N/A	N/A	N/A	N/A	N/A	N/A
F	5	4.7	5.3	N/A	N/A	N/A	N/A	N/A	N/A
G	2	2	2	N/A	N/A	N/A	N/A	N/A	N/A
H	-2	2	2	N/A	N/A	N/A	N/A	N/A	N/A

Note that in tables 2, 3 and 4, the calculation for h is:

$$h = |\bar{y} - y|$$

Where:

$$\bar{y} = \frac{\sum Ay}{\sum A}$$

The parallel axis theorem then states that:

$$I_{XX} = \sum I_{GG} + \sum Ah^2$$

Applying this theorem to the three tables gives us the following values for the second moment of area for the three cross sections:

Table 7.6. Second moment of area chages due to thickness variability

Strip Thickness (mm)	Percentage change in gauge from nominal thickness	Second Moment of Area (mm^4)	Percentage change in I$_{xx}$ from nominal thickness
2.7	10%	692,173mm^4	-10.4%
3.0	-	772,596mm^4	-
3.3	10%	871,563mm^4	12.8%

182

Thus a 10% reduction in strip thickness has resulted in a 10.4% decrease in the component bending stiffness (or flextual rigidity EI), although a 10% increase in strip thickness has resulted in a 12.8% increase in the second moment of area. It can be seen from these results that the correlation between thickness and stiffness is non-linear, whereas for other components with different geometries the correlation may be more dramatic, with small increases in thickness resulting in large changes in stiffness.

7.1.2 Development of accurate FE modelling techniques

In order to build and develop an accurate FE model of the top hat structure, many intricate factors had to be considered. As with any FE modelling, applying accurate boundary conditions are paramount to obtaining close correlations with physical test results. This sounds easier than it appears, as contact surfaces may have a certain amount of friction that are hard to quantify and supports may move slightly whilst applying loads. FE analysis of fatigue includes additional complications as the user may wish to simulate a loading condition which is at a different R-ratio to the material data that he or she wishes to use.

This is the case for this project, where the physical data for the top hat is at R=0.1, which is also what ratio is to be modelled, though the material data in the TSSP-UK brochure is at R=-1. It is desirable to use the R=-1 data since it is what TSSP-UK's customers will have available to them without carrying out any expensive fatigue testing of their own. When using material data that is not at the same R-ratio as what is being modelled, the FE software has to perform a mean stress correction.

Within ANSYS mean stress correction be done in three different techniques, they are the Goodman, Gerber and Soderberg methods and are also detailed in the literature review. A screen shot of the ANSYS engineering data input selection for this parameter is shown in figure 7.9. Note that once a method is selected, it is highlighted as shown by the green line as shown in the figure. The curved line above the green line is the Gerber method and the straight line beneath is the Soderberg method.
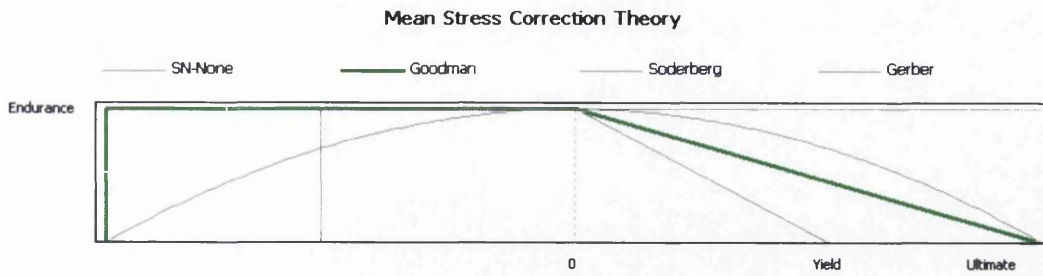
Figure 7.9. ANSYS mean stress correction options

Another consideration is the meshing properties, the meshing parameters were optimised, where details of the mesh can be seen in figure 7.11, and the final mesh can be seen in figure 7.10. Note that the part was meshed from a solid model drawn in Autodesk Inventor. The final consideration was the application of boundary conditions, where it was decided to also insert the loading blocks into the assembly and apply a frictionless surface between the blocks and the top hat structure.
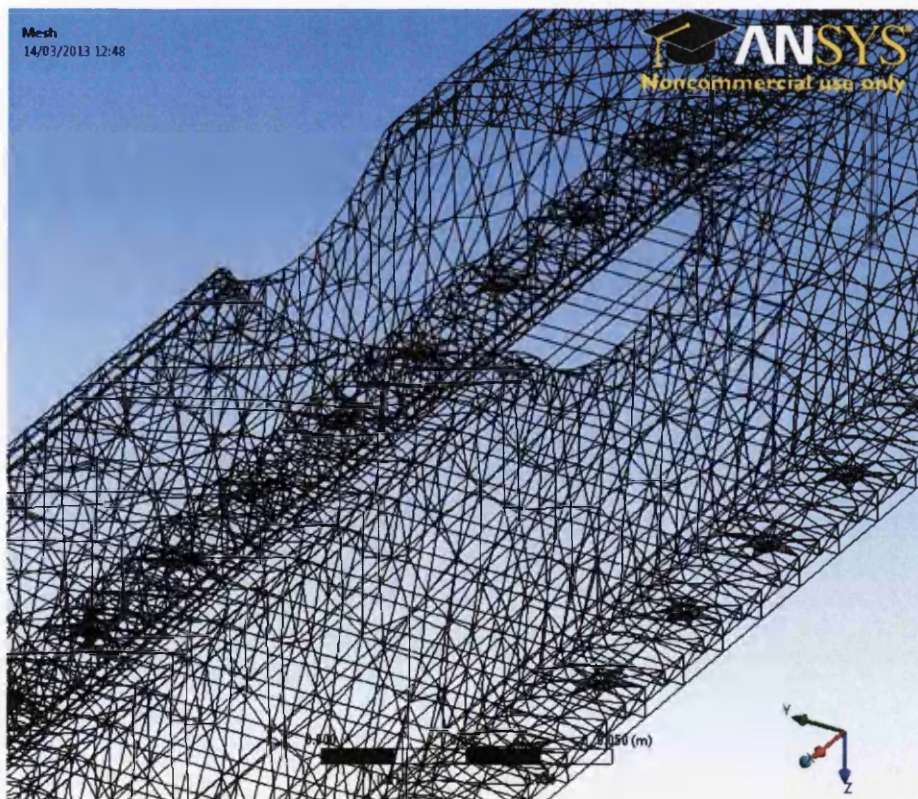
Figure 7.10. ANSYS mesh

184

As the loading conditions for the physical top hat structure were designed to be in the elastic region, all modelling work carried out was linear with the assumption that no plastic deformation occurs. Adaptive mesh refinement was used, which was found to optimise the mesh size around the more complex parts of the structure very well. Other data in terms of properties of the mesh are also shown in figure 7.11.

Details of "Mesh"		⥕
Defaults		
Physics Preference	Mechanical	▼
Relevance	0	
Sizing		
Use Advanced Size Function	Off	
Relevance Center	Medium	
Element Size	Default	
Initial Size Seed	Active Assembly	
Smoothing	Medium	
Transition	Fast	
Span Angle Center	Coarse	
Minimum Edge Length	1.3154e-003 m	
Inflation		
Use Automatic Inflation	None	
Inflation Option	Smooth Transition	
Transition Ratio	0.272	
Maximum Layers	5	
Growth Rate	1.2	
Inflation Algorithm	Pre	
View Advanced Options	No	
Advanced		
Shape Checking	Standard Mechanical	
Element Midside Nodes	Program Controlled	
Straight Sided Elements	No	
Number of Retries	Default (4)	
Extra Retries For Assembly	Yes	
Rigid Body Behavior	Dimensionally Reduced	
Mesh Morphing	Disabled	
⊞ Defeaturing		
Statistics		
Nodes	39355	
Elements	20287	
Mesh Metric	None	

Figure 7.11. ANSYS mesh properties

Numerous attempts were made to try and develop one of the three mean stress correction methods to return accurate fatigue life estimations for the top hat structure, though none were successful, thus it was later decided to carry use the R=0.1 data provided in the previous chapter. Attempts at evaluating the safety factor and fatigue life for one loading condition using the Gerber method are shown in figures 7.12, & 7.13. It can be seen that the fatigue life estimation of 9.182×10^6 cycles is far greater than the actual life of 467, 395 cycles for a 20kN load on the top hat structure.
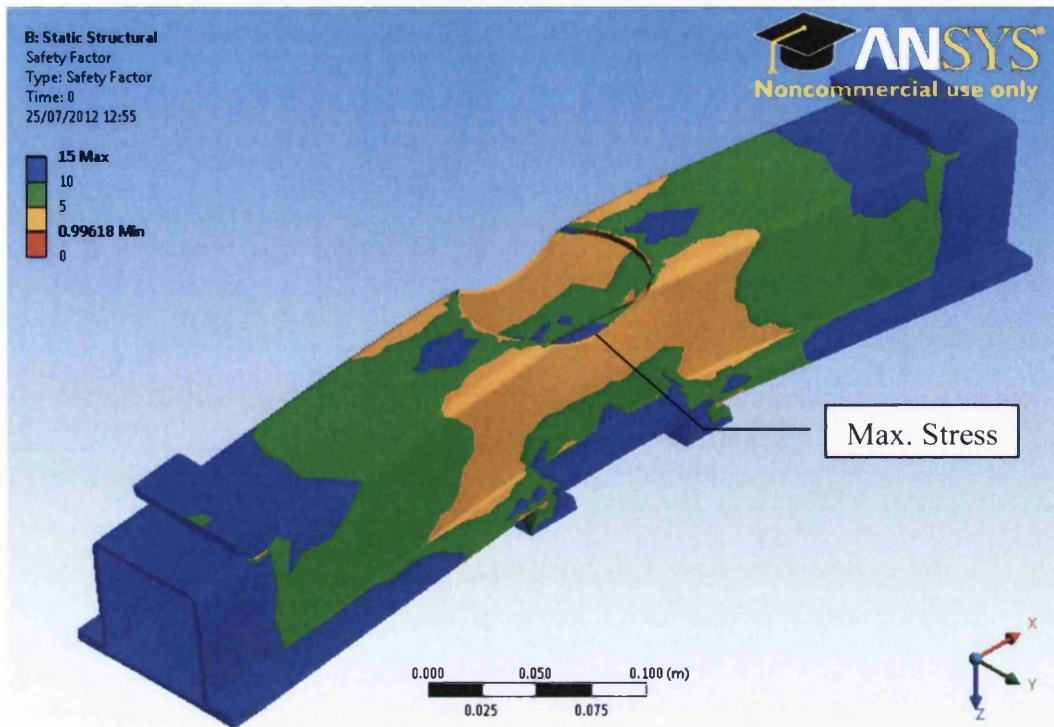
Figure 7.12. Gerber safety factor prediction for 20kN load

One area where the FE prediction proved successful is how it correctly identified the area in the structure where cracks would initiate and propagate, where the safety factor in this region is shown to be 0.99618. As this value is below 1, it predicts that failure would occur in this region before 10^7 cycles, which is the run-out applied in the software in this case.

At first glance the life expectancy model does not provide much information, as it shows up mainly in blue. This is due to the fact that the safety factor is close to 1, where only a small area of the structure is likely to fail within 10^7 cycles. However, it does predict failure at 9.182×10^6 cycles, hence the fact that it is very close to being 10^7 where the run-out applies. As mentioned earlier, this value is significantly greater ($\times 20$) than the actual value of nearly half a million cycles from the physical test results, and thus deemed inaccurate. This is not a surprising result since earlier chapters identified that the Gerber method for mean stress correction was an optimistic method, constantly over-predicting material capabilities. Despite the fact that it is flawed in the sense that it over-predicts performance, we should also be mindful that it is perhaps the most accurate method available if data at the correct R-ratio is not available.

186

B: Static Structural
Life
Type: Life
Time: 0
25/07/2012 12:54

1e7 Max
9.9056e6
9.8121e6
9.7195e6
9.6278e6
9.537e6
9.447e6
9.3578e6
9.2695e6
9.182e6 Min

Max. Stress
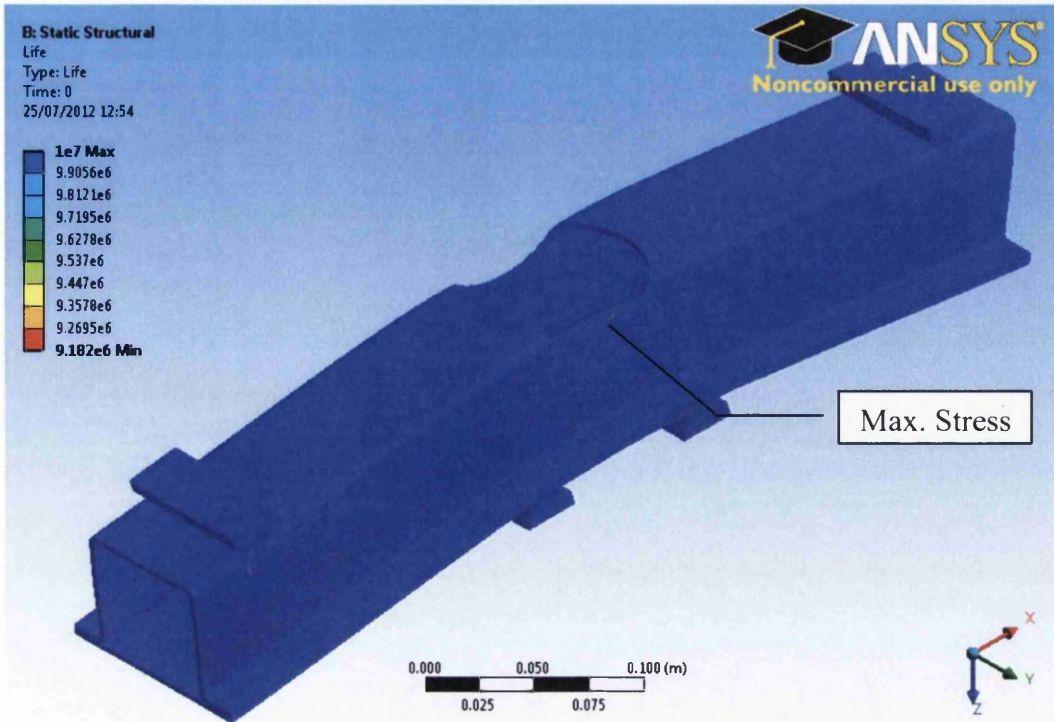
Figure 7.13. Gerber fatigue life prediction for 20kN load

In order to generate more accurate predictions two feasible options exist, we can
either use another mean stress correction method such as the Goodman method or we
can input data of the same R-ratio as we are simulating in the FE model. Changing
the model to a Goodman prediction is as easy as a click of the mouse, whereas
gathering new fatigue data is an expensive and time consuming process. Fortunately
the work carried out in chapter 5 on weld fatigue served a dual purpose and has
allowed the un-welded R=0.1 data to be used in this chapter.

As well as changing the mean stress correction method, changes can be carried out to
the way ANSYS makes calculations by modifying the engineering data. Normally
engineering data is not something that is subjective, though due to the many options
that ANSYS has for reading fatigue data, it is something that requires careful
consideration. Fatigue data input is in tabular form, where numerous interpolation
options are available to calculate values between the data points. The engineering
data input screen can be seen in figure 7.14.

Theoretically the raw fatigue data could be used, though since ANSYS wants to 'join
the dots' this option would be unwise and would result in a zig-zag fatigue 'curve'.

187

By far the best option was to use the 50% survival least squares curve and using the Basquin exponent and coefficient to backwards calculate what the stress would be at 10,000, 100,000, 1,000,000 and 10,000,000 cycles.

Once the information is fed into the database, ANSYS also requires information on how interpolation is carried out between those data points, where three options are available. All options are straight line based, though plotted on different axes. Those options are log-log, log-linear or simply linear. By choosing the log-log interpolation along with applying the data points in the manner previously described, the engineering data should not only read the same data points as the Basquin curves processed as part of this project, but ANSYS will interpolate the data points to read the same result for any loading condition.

Once all the information is fed into the database and the interpolation technique is decided upon, all that is required to do is to state the R-ratio that the fatigue information has come from. If a mean stress correction is required, then ANSYS will have a reference point. Note that in this project, when mean stress correction was used the engineering data input was at R=-1, but any R-ratio may be used. As long as the yield strength, UTS and R-ratio are stated it provides the software with enough information to work out an alternative S-N curve at different mean stresses.

One other problem may arise by using mean stress correction in this way, since both Goodman and Gerber methods require the tensile data i.e. the yield strength and UTS, varying these values will result in different fatigue predictions. In this case the tensile data that was used were the mechanical properties of the actual coil of steel that the top hat structures were made of. TSSP-UK customers may be using the catalogue data which only specifies minimum strengths, or alternatively JLR may be able to use mean values provided to them through this project. Of course, as seen in previous chapters, any tensile data that is used will be subject to variability from one coil to another.
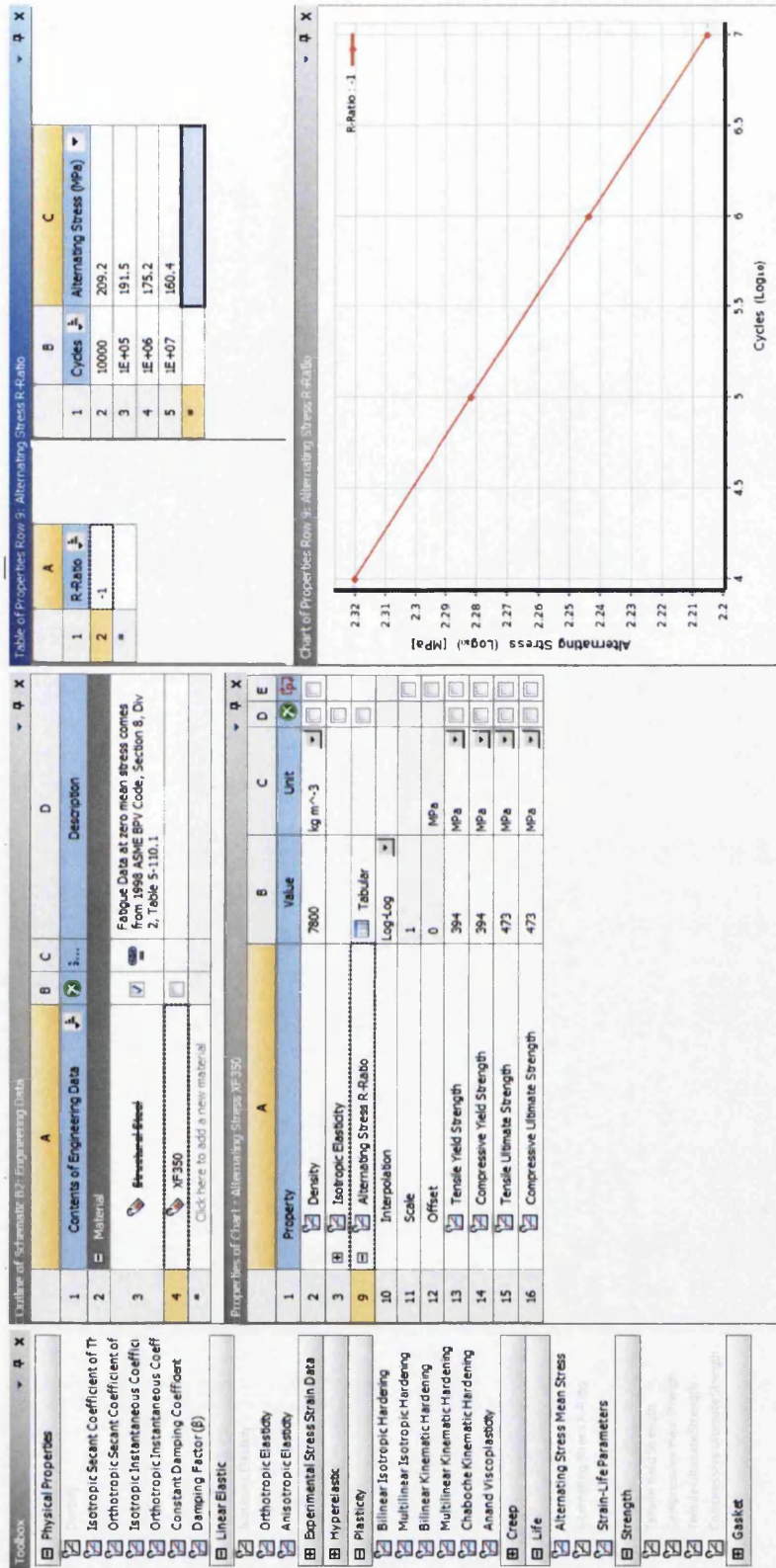
Figure 7.14. Engineering data imput options

By applying the engineering data in this way, Goodman, Gerber, and predictions with no mean stress corrections were completed. Life and safety factor predictions were carried out for a range of loads. The results for 20kN loads are shown in figures

7.15-7.18, for the Goodman and no mean stress correction methods respectively, which complement the Gerber predictions shown in figures 7.12 & 7.13.

It is instantly visible by both the fatigue life and safety factor predictions that, as expected, the results for the no mean stress correction method by deploying SN data at the same R-ratio as what is simulated results in predictions which lie between the Gerber and Goodman. What came as a surprise was the sheer difference between all three methods. For a 20kN load the life predictions for Gerber, Goodman and no correction method were 9,182,000, 37,859 and 3,739,000 cycles respectively. It can be seen that the prediction obtained by not using any mean stress correction method is of the same order of magnitude as the Gerber method, giving strength to the suggestion that the Gerber method is possibly more accurate than Goodman. Though once again we see that it is the most optimistic of all methods, thus relying on Gerber would be a risky option for any design engineer and designing to these specifications without adequate safety factors could lead to catastrophic failure of components in service.

In contrast, the Goodman method seems so conservative that the danger of working to these specifications may result in over engineering. At a time when vehicle mass is at the forefront of automotive manufacturers design criteria, this would be very undesirable. The difference in the predictions returned by Goodman and Gerber are at their most apparent when studying the safety factor predictions, with the Gerber method predicting a minimum safety factor that is close to 1, whereas the Goodman safety factor is 0.8.

In order to have a fairer idea of the difference between the three simulation techniques this model was processed with the same loading conditions as the physical top hat, i.e. 20, 22, 24, 26 and 28kN. For some of these loads and for certain mean stress correction techniques no prediction could be obtained, as either the applied load was too little and an infinite life was predicted (Gerber), or the load was too large and the prediction was less than 10,000 cycles, thus no fatigue reference was available (Goodman). Thus, in certain situations an increment of 1kN was used in order to provide enough information for graphical representation. This information is shown in table 7.7.
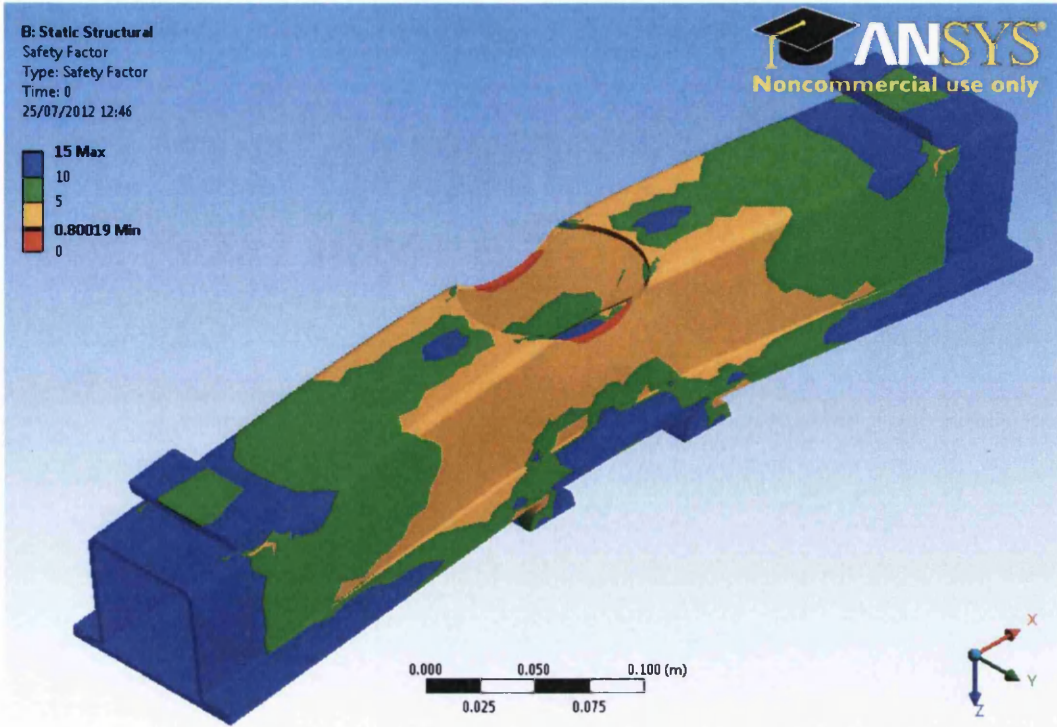
Figure 7.15. Goodman safety prediction for 20kN load
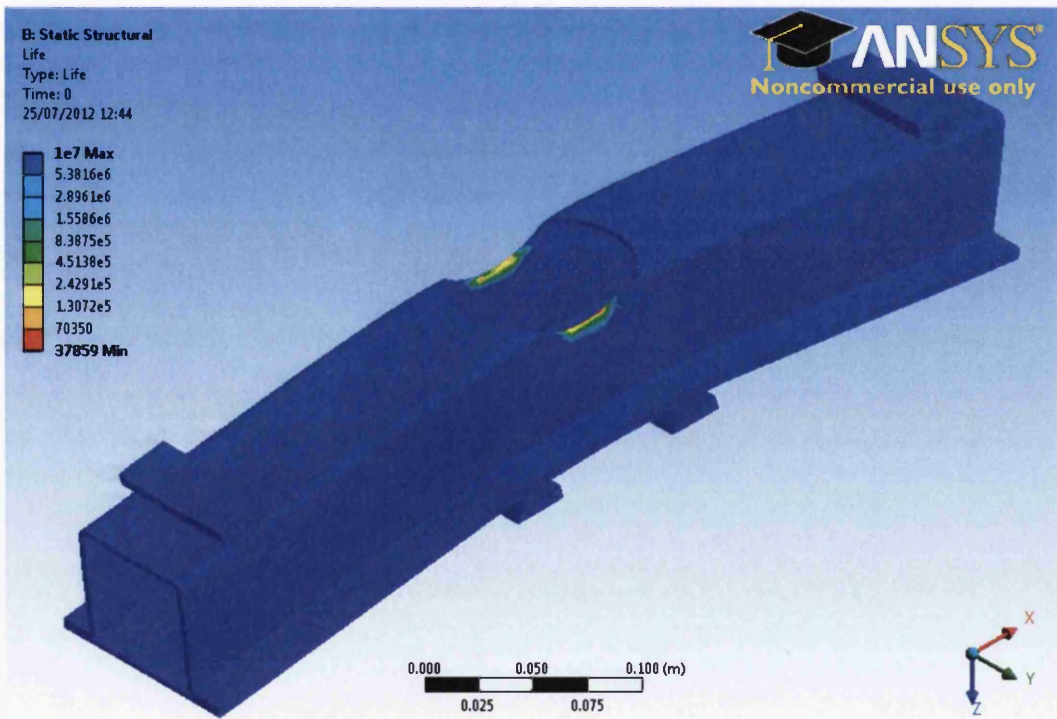

Figure 7.16. Goodman fatigue life prediction for 20kN load

191
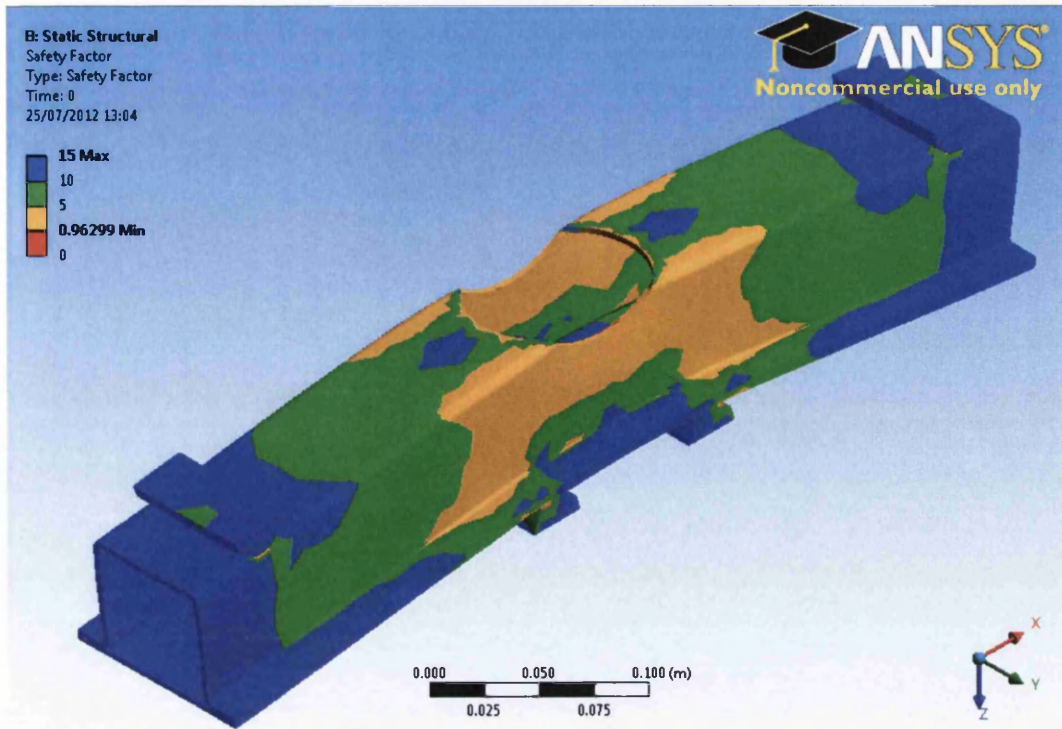
Figure 7.17. No mean stress correction safety factor prediction for 20kN load
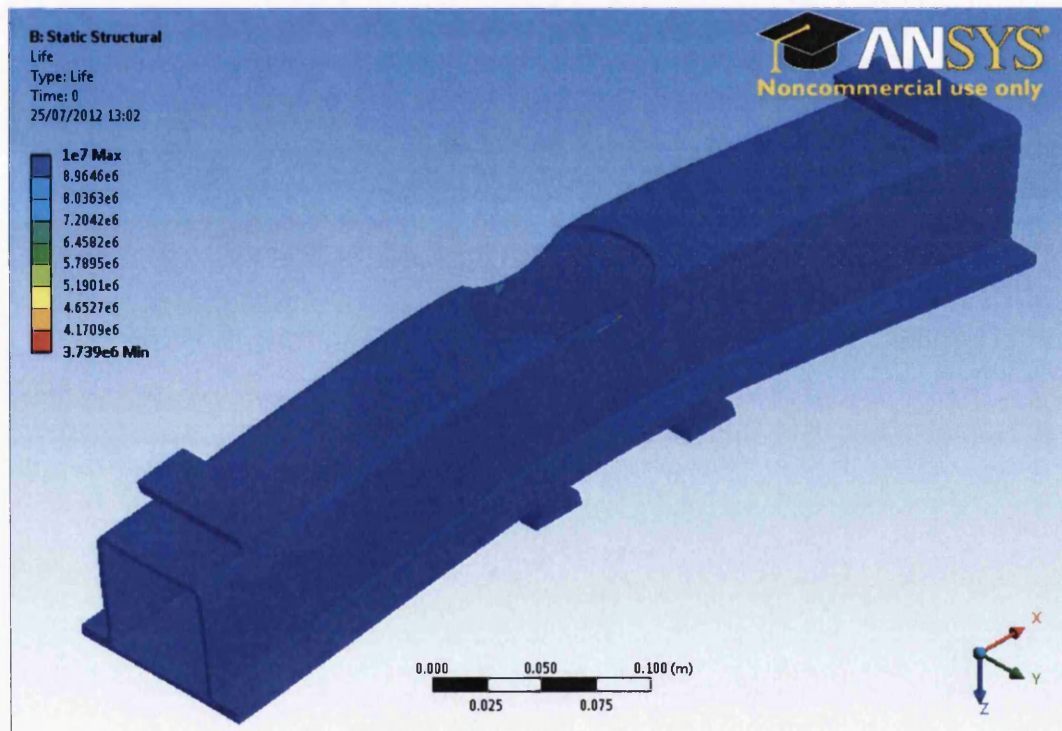
Figure 7.18. No mean stress correction fatigue life prediction for 20kN load

Table 7.7. Force-life data for various mean stress correction techniques

No mean stress correction		Goodman		Gerber	
Load (kN)	Life	Load (kN)	Life	Load (kN)	Life
20	3739000	20	37859	20	9182000
22	313940	22	0	22	1003100
24	32788	24	0	24	111300
25	11323	26	0	26	11955
		28	0	28	0

Note that after the first load of 20kN, the Goodman method predicted a life of zero cycles, as the stress was larger than what Goodman predicts the material is capable of. The range of life predictions available is between 10,000 and 10,000,000 cycles, anything less or more than these two values is predicted as either infinite or zero life respectively. It was decided that it was not necessary to simulate the structure at loads lower than 20kN using the Goodman method, even though doing so would have enabled a curve to be generated for figure 7.19. The reason for this is that, as the maximum load it can withstand in the simulation is 20kN, it is obviously not a good method for achieving accurate predictions, especially since this is the lowest load applied during physical testing.

With the Goodman method clearly proving to be inaccurate purely by analysing the information in the table, it is only the Gerber and no correction methods that need to be assessed. Having said this, it is still recommended to carry out a Goodman prediction in such cases, as it provides a safe level to work from where it gives engineers a good idea of how to design reliable products, though not necessarily finely and robustly engineered products. It was understood from previous chapters that the Goodman method is a conservative approach, though it is unfortunate to discover through this work just how conservative the method is. It was originally thought a relatively small difference existed between all three methods.

If this had been the case and Goodman was only marginally conservative, then it would have provided a perfect tool to enable products to be designed carefully without over engineering. Products could then be fit for purpose and safe from fatigue failure, yet light-weight without the need for large safety factors. With these

findings it can only be recommended that the Goodman method should only be used as a reference, with further work required to establish how much more the material/component is safely capable of.
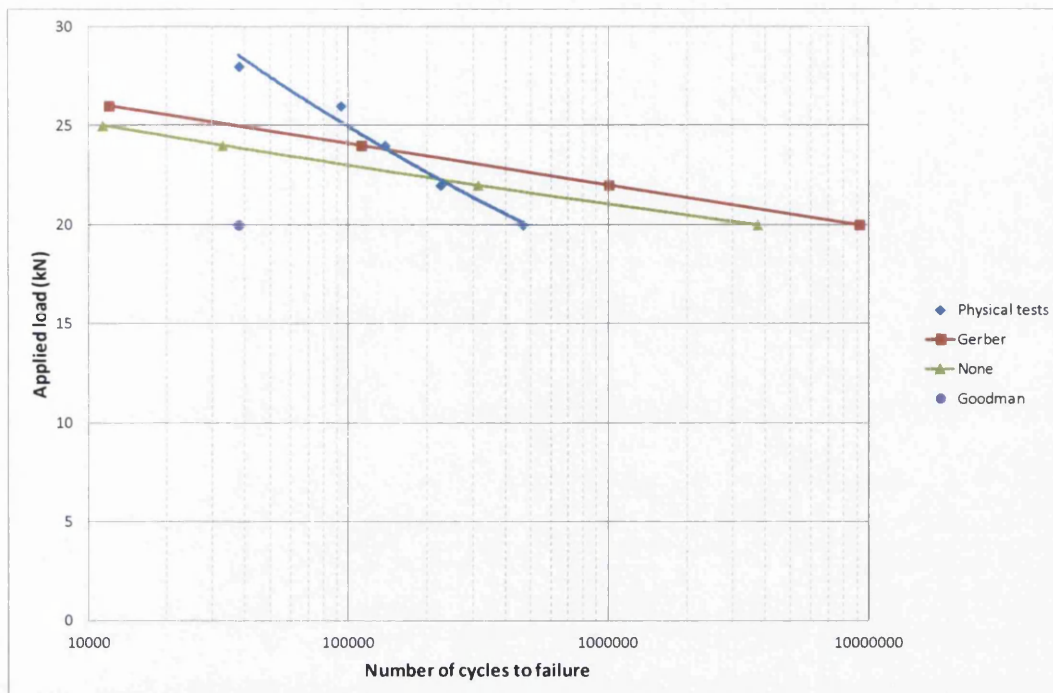
Figure 7.19. F-N results for various mean stress correction techniques

After concluding that the Goodman method is inaccurate by purely looking at the information in table 7.7, further work is needed to establish how accurate the Gerber method is at correcting data from different R-ratios. By looking at the table there appears to be a significant difference, though at least the results are in the same order of magnitude as the un-corrected data. In reality the correlation between the two can be regarded as reasonably good. The reason that the difference between the two may appear large in tabular form is that the fatigue curve for this material is rather shallow, thus a small change in stress results in a large change in fatigue life. Thus the difference in an applied load for two samples with very different fatigue lives can be very little. In contrast, a small change in applied load can give significantly different life predictions.

This tells us that if no data is available at the R-ratio required then the Gerber method may be used in order to achieve a reasonable degree of accuracy. This must however be done with caution, since even though the predictions are reasonably

194

accurate, they are over-predictions of the structures' capability. The difficulty then lies with how is the degree of over prediction quantified and how is it possible to ensure reliability when using a method known to give artificially high predictions of fatigue life. The answer to such a question may be subjective, but at least an additional Goodman simulation would help provide some answers by providing a range of best and worst case predictions.

Another observation that is apparent when studying figure 7.19 is how sensitive the physical structure is to changes in the applied load as compared to the FE model. The FE model has the kind of gradient you would expect from the structure given the gradient fatigue curves obtained from coupon tests. Even though the FE prediction curves have quite a shallow gradient (as per the fatigue coupon curves), the physical test results give a very steep curve.

One possible explanation for this is that the FE model assumes even distribution of stress on both sides of the structure. In reality due to very small imperfections in geometry during manufacturing and alignment during testing it becomes increasingly likely that the structure would suffer greater loading on one side. Cracks will initiate and propagate sooner on that side than the FE model suggests.

7.1.3 Correlation between strip thickness and fatigue performance

Now that reasonably accurate predictions are possible in regards to the structural performance of the top hat, which is made from XF350, the necessary tools are in place for further structural analysis to proceed (although issues with Basquin exponent remain). Combining these FE techniques with variability data obtained in previous chapters enables us to assess how changes in key delivery condition data may affect structural integrity. Possibly the most obvious variable that could be accounted for in these FE evaluations is the strip thickness, where it was identified during previous work that for 3mm XF350 strip a variability of +/- 0.3mm is permitted and experienced. Thus by using FE modelling it is possible to see the effect of this variation on the stresses within the product as well as the knock on effect it has on the fatigue behaviour and subsequent safety factor of the component.

Figures 7.20, 7.21 and 7.22 show the stresses in the top hat structures for strip thicknesses of 3mm, 2.7mm and 3.3mm respectively. Note that these structures have cross sections as previously described in this chapter, where the folds were kept in the same locations, i.e. the manufacturing process was kept the same with only the material thickness changing. Other cross-sections would be possible by, for example, simply adding or subtracting to or from the nominal cross-section. This would have resulted in different FE predictions, though it was felt that keeping the folds in the same location gave a more accurate picture of what may occur in a high volume production line. Note that the following FE images all have an applied load of 20kN.
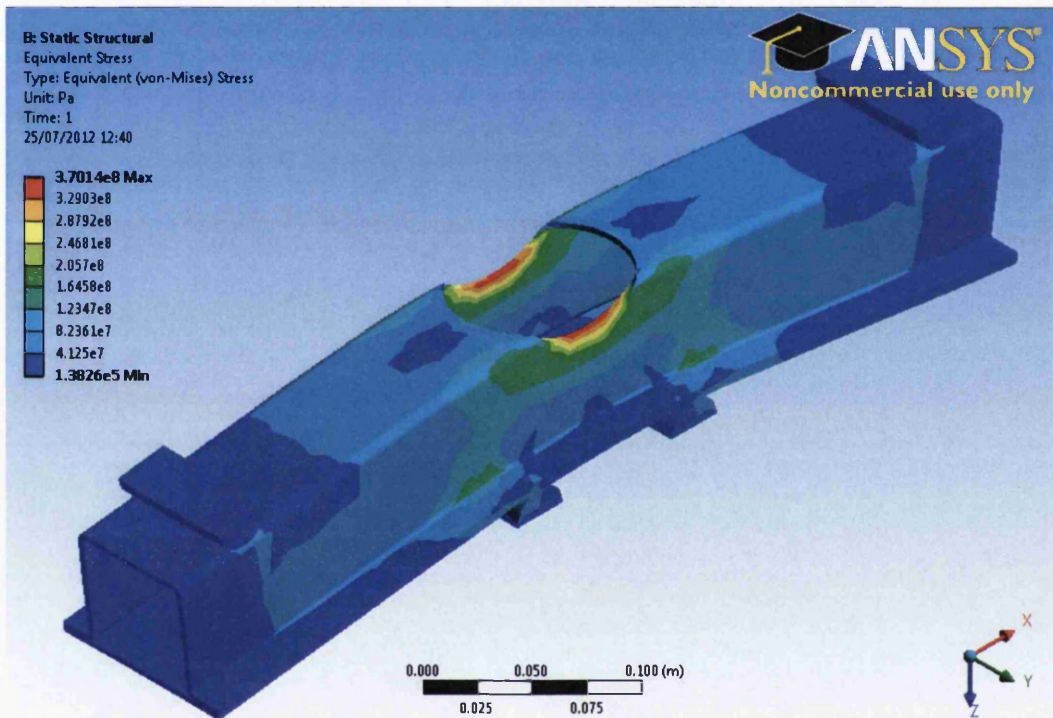
Figure 7.20. Stresses within a 3mm top hat structure
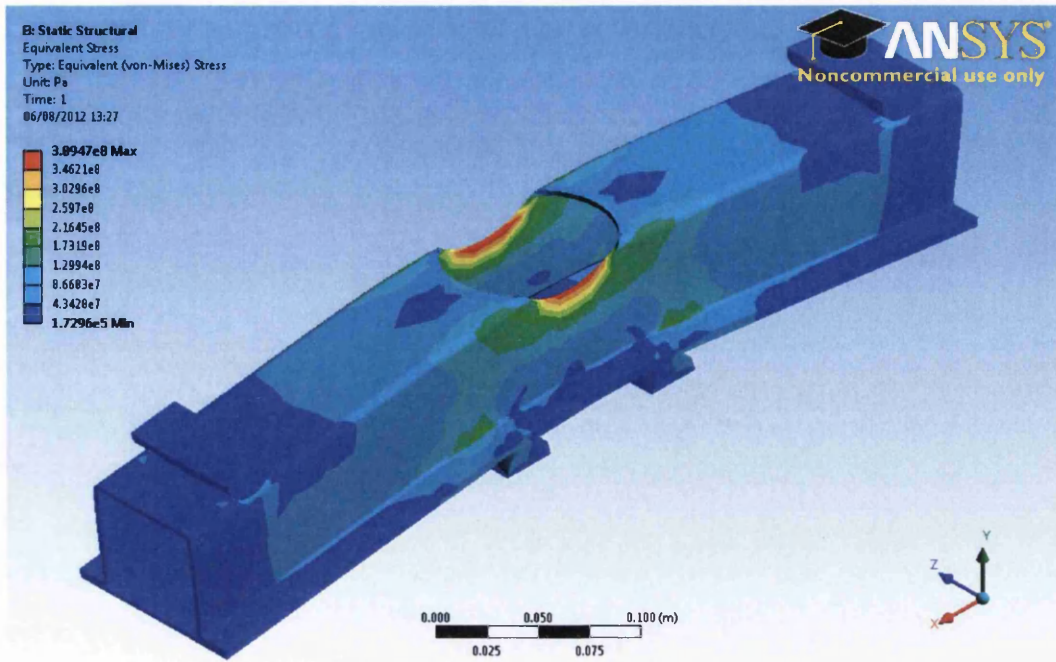
Figure 7.21. Stresses within a 2.7mm top hat structure
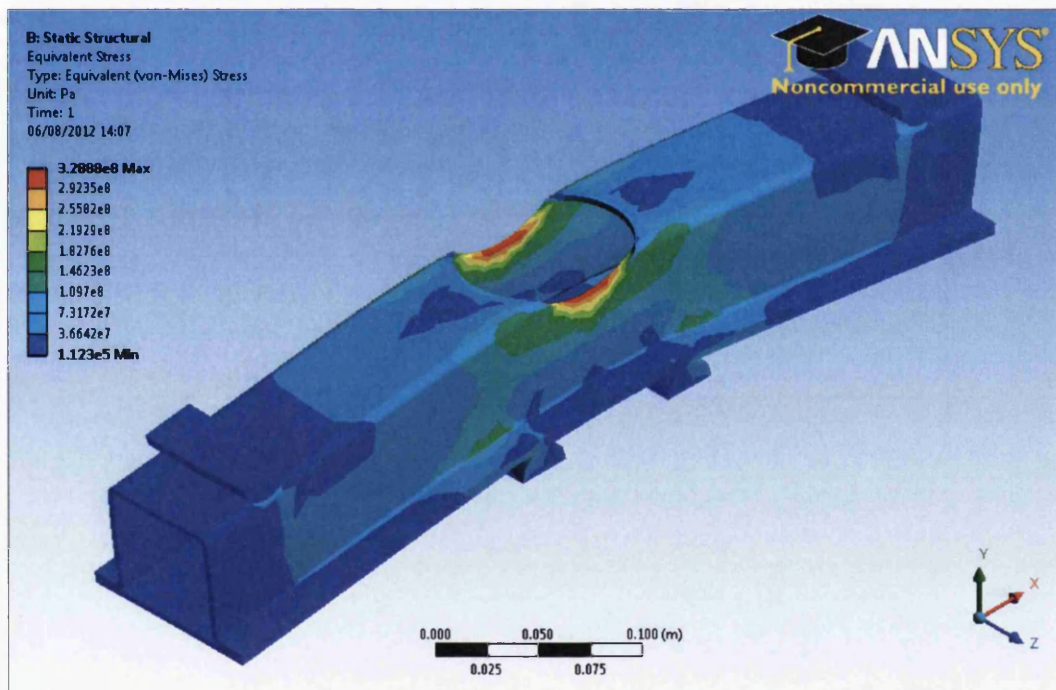
Figure 7.22. Stresses within a 3.3mm top hat structure

Three very different predictions are returned by the FE model for Von-Mises stress. The maximum stress for the nominal 3mm structure is predicted at 370MPa, which although larger than the minimum strength permitted for this grade of material (350MPa), it is at least smaller than the actual yield strength of 394MPa tested for this coil of steel. Whilst these two values are not vastly different, by contrast, the

197

stress in the 3.3mm structure is only 329MPa. It was originally expected that the difference in stress between the 3.3mm structure and the 3mm structure would be the same as the difference between the 2.7mm and 3mm structures, though this is obviously not the case. As with the second moment of area study, the relationship between stress and thickness is non-linear and the sensitivity of structures to changes in strip thickness needs to be assessed on a case by case basis.

With the stress predictions complete, obtaining fatigue life predictions was possible by using the fatigue tool and inputting R=0.1 data obtained from previous work into the engineering data. The life predictions for 2.7mm and 3.3mm are shown in figures 7.23 and 7.24 respectively, and the prediction for the nominal 3mm top hat was previously shown in figure 7.18.
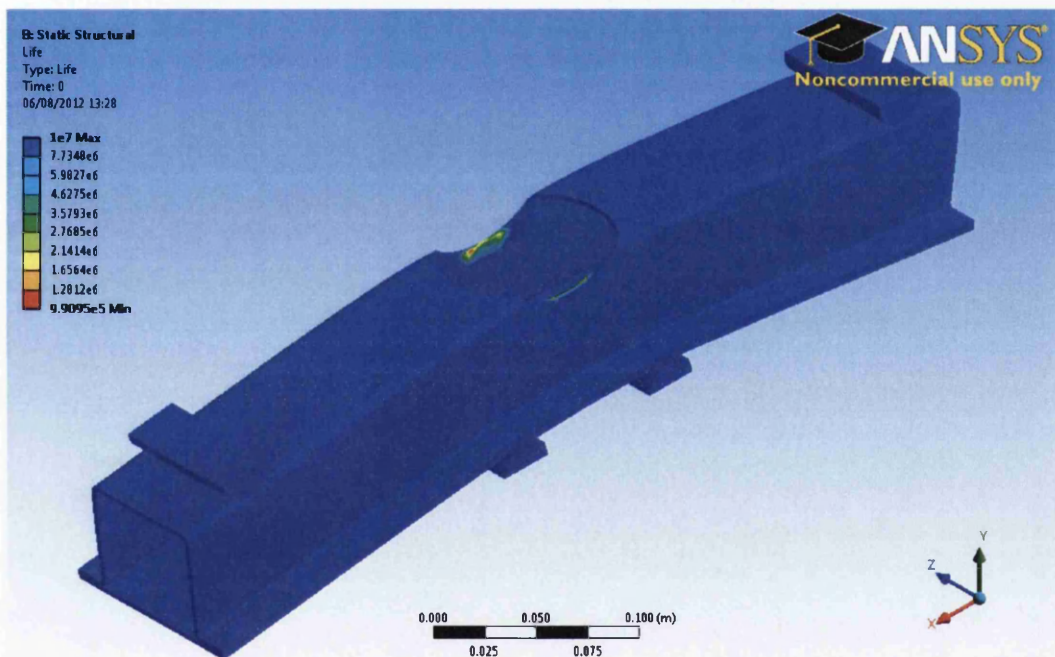
Figure 7.23. Fatigue life of a 2.7mm top hat structure

It can be seen that the fatigue life predictions at a load of 20kN are vastly different to each other. The 2.7mm top hat has a fatigue life of almost 1 million cycles, whereas the stress in the 3.3mm structure is not large enough to cause failure within 10 million cycles, thus is shown in red. The nominal 3.0mm structure was predicted to last 3,739,000 cycles.
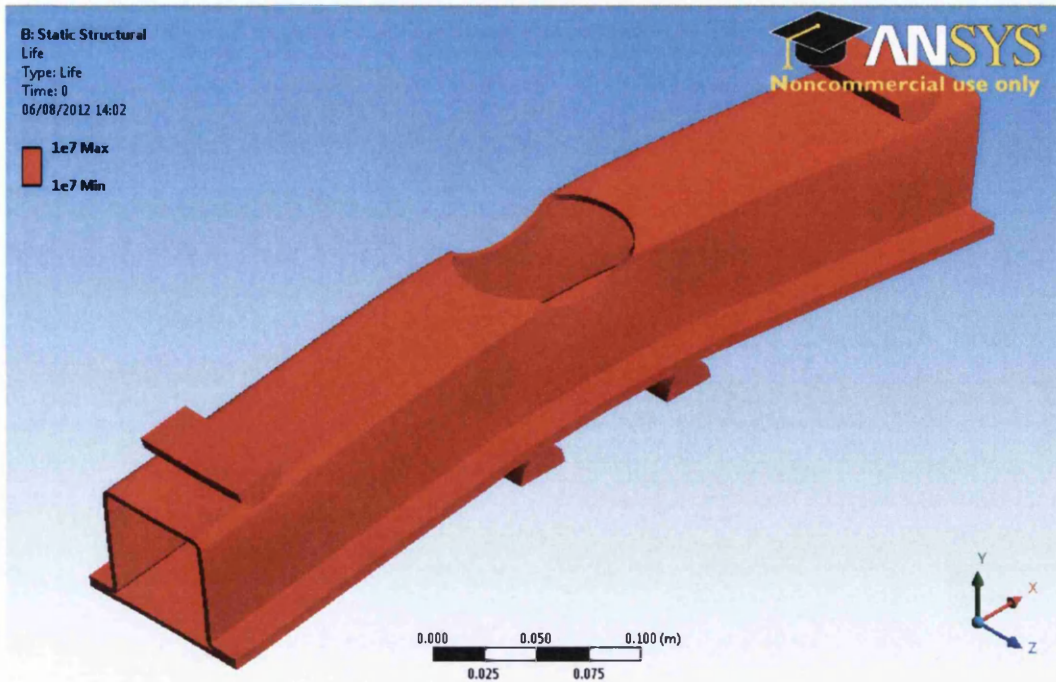
Figure 7.24. Fatigue life of a 3.3mm top hat structure

The contrast in fatigue life predictions between under and over-gauge components aligns with what one would expect for such a part, since the von-mises stress levels were considerably lower in the 'over-sized' structure. All that is possible to learn from figure 7.24 is that is that the 3.3mm structure at 20kN gives us a life that is classed as a 'run-out', comparison of these structures is only possible after other simulations are carried out with different applied loads.

Also, as figure 7.24 only shows that the structure will not fail within 10 million cycles, the safety factor results for this loading condition possibly tells us more about their differences in structural performances (figures 7.25 & 7.26). While the under-sized structure has a safety factor of 0.9152, the 3.3mm structure's safety factor stands at 1.0838. As this figure is greater than 1 it does not predict failure within the fatigue limits set within the engineering data.

In order to obtain a full picture of the effects of strip thickness variability on fatigue life the CAE model was run, with, where possible, the same applied loads as the physical specimen. Where it was not possible to obtain results due to the load being too large or too little, a smaller load increment was used. Note that it is only possible to achieve a prediction between 10,000 and 10,000,000 cycles with the applied

engineering data. With the 3mm structure a 26kN load returned a result of 0 cycles for life, even though it would not in reality be 0, but since the stresses were more than what the material is capable of withstanding for 10,000 cycles, the prediction is returned as zero. In this case it was decided to use a 1kN increment, i.e. 25kN in order to obtain enough information for graphical representation. These results are shown in table 7.8

Table 7.8. Top Hat fatigue life for various strip thicknesses

3.3mm		2.7mm		3.0mm	
Load (kN)	Life	Load (kN)	Life	Load (kN)	Life
20	Inf.	20	990950	20	3739000
22	6792100	22	83983	22	313940
24	703620	23	26385	24	32788
26	88561	24	-	25	11323
28	12851	-	-	-	-
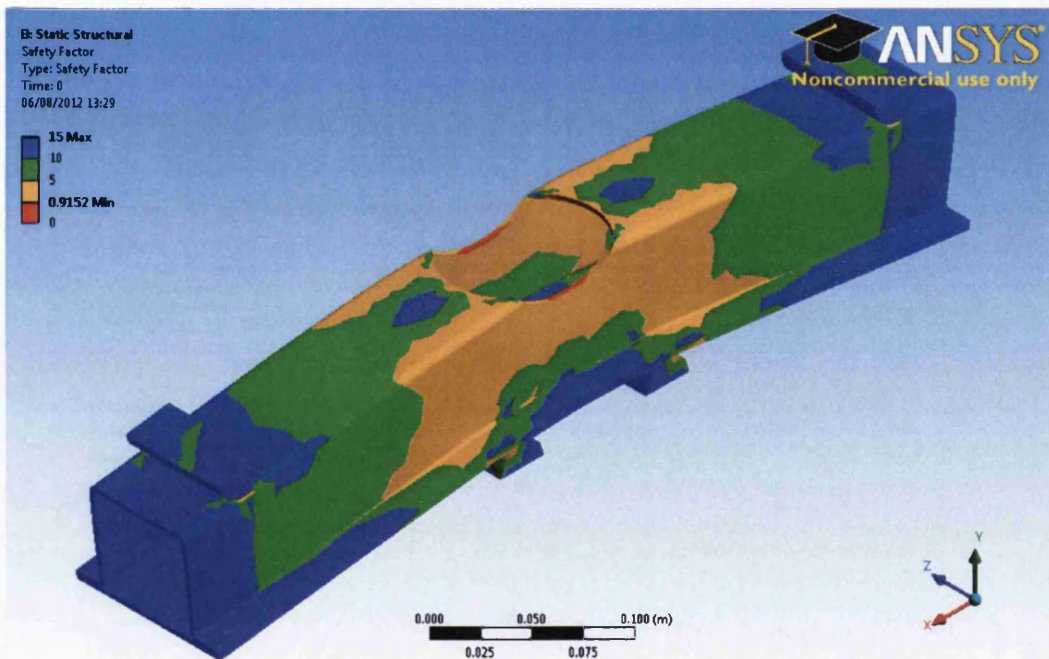
Figure 7.25. Safety factor of a 2.7mm top hat structure
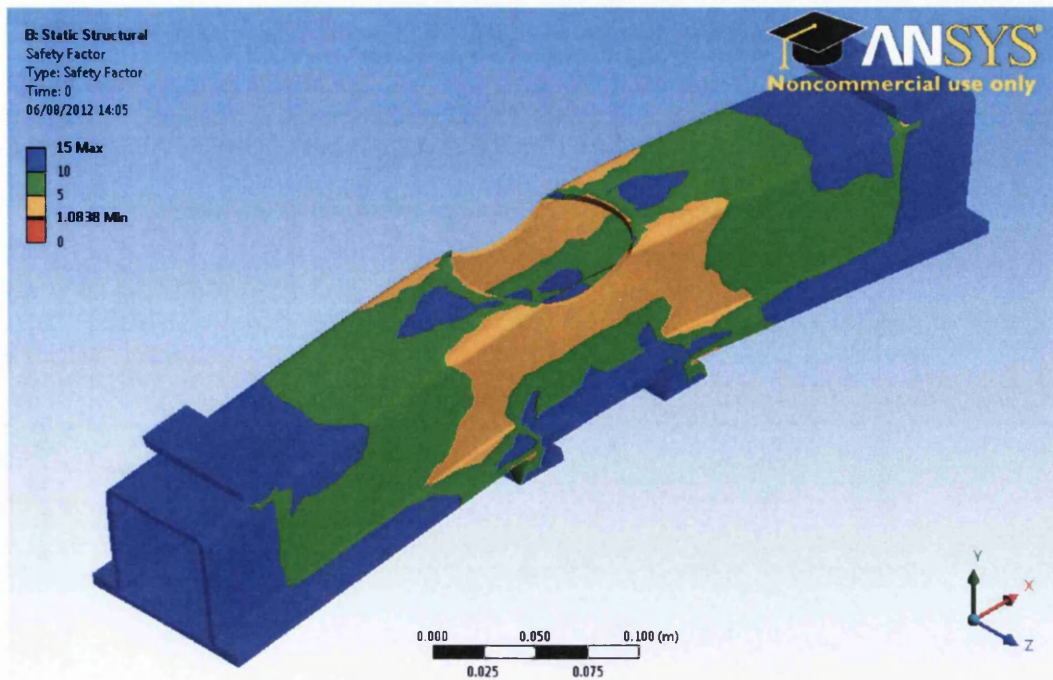
Figure 7.26. Safety factor of a 3.3mm top hat structure

The information in table 7.8 is shown in graphical form in figure 7.27, where it can be seen that, unexpectedly, the difference between the oversized and undersized structures are not symmetrically spaced from that of the nominal thickness of 3.0mm. This was discussed earlier when looking at the 20kN results in isolation. One possible reason for the two lines appearing asymmetrical from the 3mm line is that there is also asymmetry in the second moment of area results, this would certainly have a knock on effect on the stresses in the structure, and in turn on the fatigue behaviour of the component.

The nature of the asymmetry in this case is quite pleasing, since the structure appears fairly insensitive to reductions in strip thickness and more sensitive to increases. The reason this is a positive observation is that it was originally feared that decreases in thickness would lead to large detrimental chances in performance and possibly lead to unreliable products. It is therefore comforting to see the relatively small change in performance following a 0.3mm decrease in strip thickness.

These results are however specifically for this particular structure and as such may not be typical of other components manufactured from this material. As such, this study stands as an example of what must be contemplated when assessing the

201

structural performance and durability of new designs. Each new design needs a similar assessment on a case by case basis.
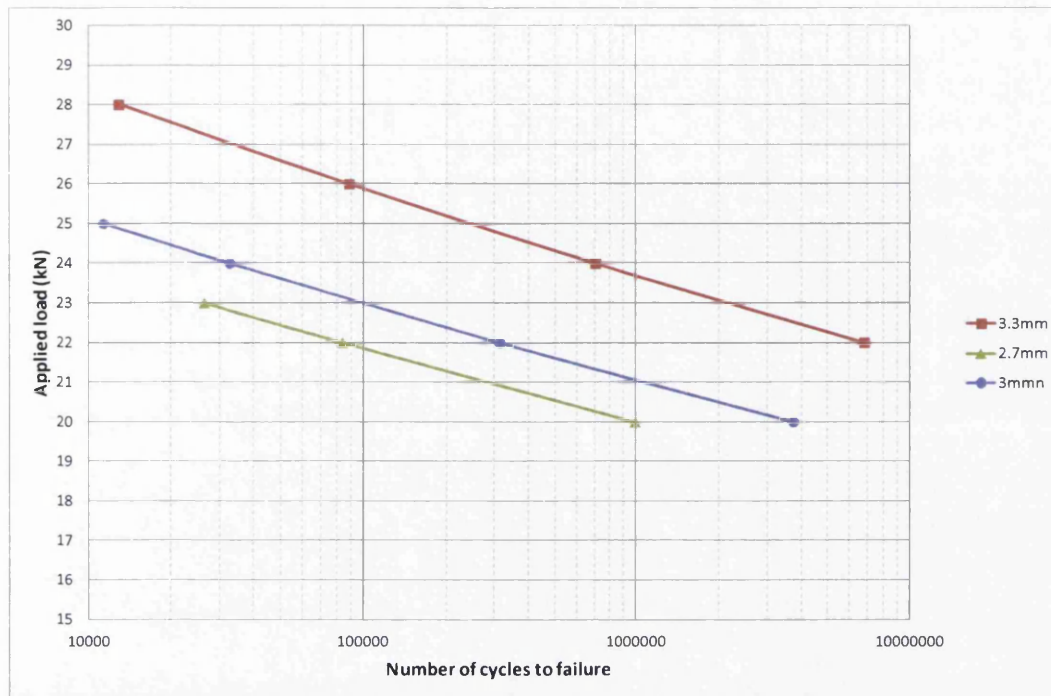
Figure 7.27. Top Hat fatigue life for various strip thicknesses

7.1.4 Effect of other variables on the top hat structure

Other variables which may affect the structural performance of the top hat are the variables in thermomechanical rolling conditions and ladle chemistry that resulted in variabilities in the tensile behavior from one coil to another. From previous work the amount of variability experienced is well documented within this project, though the overall effect of those variables on the overall performance of structures is largerly unknown. Work carried out in chapter 5 identified that there is a definitive correlation between tensile behaviour and fatigue performance within this grade and wider family of steels, though the exact nature of the relationship between the two is impossible to tell without much more data.

Unfortunately it is outside the budget and timescale of this project to perform enough tests to obtain data that would be sufficient for such a study, as such an assessment would require at least several hundred sets of data such as that seen in chapter 4. A reasonable prediction was however achieved by simply modifying the Basquin

constant in line with the proportional change in yield strength. This simplistic approach did seem reasonably accurate for the fatigue data contained within this project, though it would be by no means guaranteed to work using other data, as much more work is needed to confirm the accuracy of this hypothesis.

The added difficulty of modifying fatigue data to coincide with variations in tensile data is how to establish a datum. The fatigue data in the TSSP-UK brochure did not quote what the tensile performance was for the coil that the coupons were manufactured from, where later on it was established that it had similar fatigue performance to a coil with a yield strength and UTS of 394MPa and 473MPa respectively. The only complication with using these tensile results as a datum is that it was identified that, as with all fatigue coupons, a stress concentration existed within the specimens used for testing. It was previously documented that it is virtually impossible to eradicate the stress concentrations that exist within dog-bone type specimens and as such the curves obtained from the results will be slightly lower than what the material can handle in reality.

If we want to use the Basquin proportioning technique for estimating the worst possible fatigue performance of this material i.e. material, with the weakest permissable yield strength of 350MPa, then we would multiply the Basquin constant by 350/394 = 0.888. To make it more accurate and not under estimate the materials strength we should first increase the Basquin constant by 8%, which is the stress concentration as identified in previous FE simulations. The original and new statistical fatigue data for the top hat structure using the proportioning method are shown below in table 7.9, with the force – life curve shown in figure 7.28.

Table 7.9. Modified statistical fatigue curve data for 350MPa yield strength steels

Parameter	394MPa yield Strength	350MPa yield Strength
A	129292	124042
b	-0.14284	-0.14284
SE	0.070564	0.070564
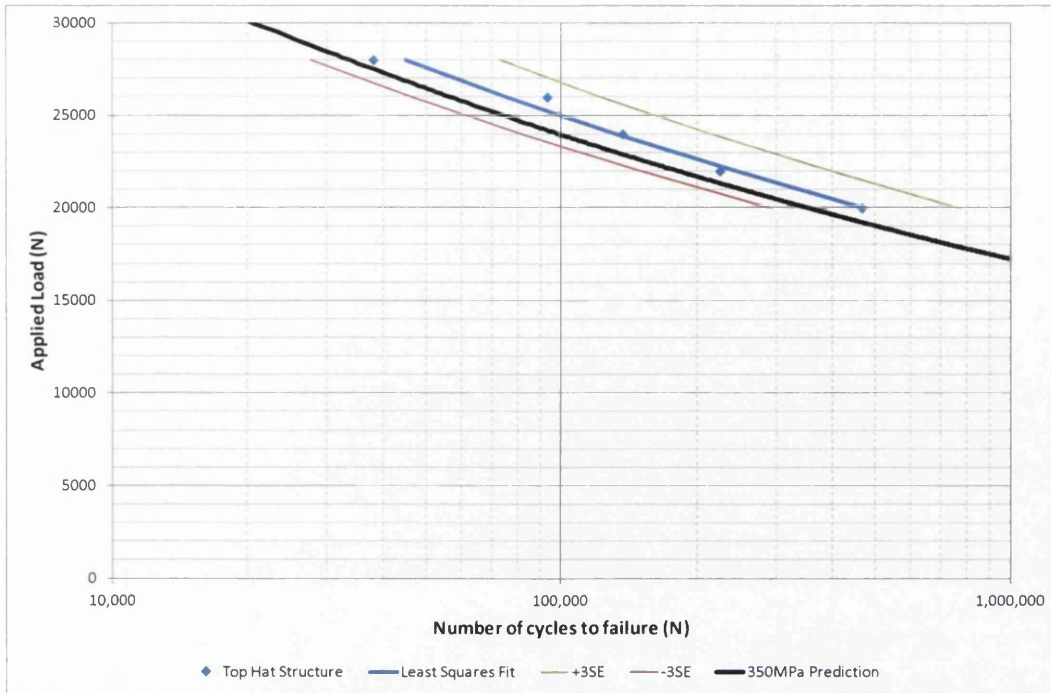
Figure 7.28. Modified fatigue curve for 350MPa yield strength steels

Note that the black line in figure 7.28 is only an estimation of the true fatigue performance of XF350 if it is supplied with its minimum permissable strength delivery condition of 350MPa. This estimation is based on the evidence gained through this project and appears reasonably accurate for the data set contained within. The fact that the curve for this condition lies within three standard errors of the original curve is good news since it appears designing to this curve is robust enough to cope with material variations. The bad news is, this curve is also subject to variation, where it is likely that the value for standard error will be very similar to the the original curve. Of course this is hypothetical, though the signs that inconsistencies in material production does not result in the new predicted 50% survival curve falling outside three standard errors of the original is encouraging.

The only other concern is that material which is close to the worst case scenarios for material thickness and strength i.e. 2.7mm and 350MPa may result in unreliable structures. The likelihood of such an occurrence is low since very few coils within TSSP-UK are delivered with strength values close to the LSL, also the statistical probability of finding a section of coil which is 0.3mm under gauge is very low, and as mentioned in previous work, this is always at the ends of the coils. Thus the

probability of the two happening in unison on a particular part is very low, although none the less possible.

It can be seen that the life predictions in figure 7.27 show that the 2.7mm structure shows stress level capabilities of around 1kN less throughought the whole life range as compared to the 3mm structure. Factoring this into the results shown in figure 7.28 (by moving the black line down by 1kN) and the fatigue curve for the very worst case scenario would lie virtually on top of the -3SE curve. Thus for an entirely reliable product it would be advisable to design products with a margin of six standard errors, three to deal with the unpredictable nature of the fatigue behaviour of metals and another three to allow for variabilities from one coil to another due to manufacturing inconsistencies.

Chapter 8 – Conclusions and Further work

8.1 Conclusions

The chapters contained within this project, both individually and collectively have provided data and information that enables design engineers to account for the sources of variability within TSSP-UK Tenform products, thus providing the crucial tools necessary to achieve robust and reliable designs. Furthermore, the major contributors to these sources of variability have been identified and their influence quantified, which will assist the steel industry in producing more consistent grades of steel in terms of their mechanical properties. As a correlation exists between fatigue performance and yield strength, the variability in fatigue performance could then be directly attributed to processing parameters which impact on the final microstructure of HSLA products.

The effects of these sources of variability were also trialled on a top hat specimen, and the fluctuation in performance, due to the inconsistencies of numerous factors, quantified. As CAE modelling is now an integral part of the automotive design and engineering process, provisions are also made for achieving accurate FE modelling of components made from TSSP-UK material. The major findings of this project are as follows:

- The fatigue performance of HSLA steels analysed as part of this project are directly proportional to yield strength, which in turn can be attributed to grain size. The major contributors to yield strength variability were determined from large data sets of thermo-mechanical production information coupled with test certificates.
- CART statistical modelling has been used successfully to analyse and assess the causes and effects of processing variables on the mechanical properties of hot-rolled S355MC steel. The conclusions drawn from this model are included below.
- The variability in the niobium content of the steel caused a greater variability in mechanical properties than any other element. This may be due to two factors; the strengthening and grain refining properties of niobium, and also the fact that it is the least well controlled of the main alloying elements.

- Coil box delays that caused mean surface temperature losses of 30°C or more were solely responsible for a 10.7MPa mean yield strength reduction on coils less than 3mm thick. This can be attributed to the slow cooling that occurs in this part of the mill, thus impacting on cooling rates further down the production route and hence much of the potential for grain refinement is lost.

- Apart from the coil box temperature drop, all other processing parameters were found to be statistically well controlled, and their variability did not affect the mechanical properties.

- As expected, given similar chemistries and processing conditions, thicker coils were shown to be weaker than thinner products.

- Coils less than 3mm thick were proven to be vulnerable to strength reduction caused by heat losses between the crop shears and roughing mill. Potentially this could be improved by reducing delays in the coil box.

- The tramp element content was sufficiently low in all coils studied in order to avoid any strength issues relating to unwanted elements.

- None of the parameters considered were found to significantly influence elongation values.

- As a whole, little variability exists in the desired thickness of coils, with the vast majority of the length of coils being manufactured to close tolerances. However the coil ends did show fluctuations which are in line with the relevant euronorm standards. The extent of the fluctuations were in some cases as much as the maximum and minimum values permissible, and as such, end users must be aware of this.

- It was found that the effects of loading XF350 at various R-ratios could not be accurately predicted using either the Goodman or Gerber mean stress correction techniques. The true behaviour of the material lies between the two.

- Despite knowing that the true behaviour of XF350 lies between Goodman and Gerber, this does not aid in accurate FE predictions, as the difference between the two is large.

- Reasonably accurate FE predictions are made possible by using fatigue data of the same R-ratio that was performed during physical testing.

- The fatigue properties of XF350 in the TSSP-UK brochure were very similar to XF350 tested at STC with a yield strength of 394MPa. Therefore using this data poses a risk, as coils with yield strengths close to the lower specified limit of 350MPa are likely to have reduced lives.

- In contrast to the previous conclusion, it is likely that the fatigue lives in TSSP-UK brochures are 'under-sold', as the coupons used to produce the results exhibit significant amount of stress concentrations due to their dog-bone shape. Despite this inherent flaw, it is difficult to design this feature out, as a reasonable surface area is needed for clamping the coupons and there are further complications when using pinned connections. However the level of stress concentration within the coupons may be reduced but not eradicated in the future by using a new geometry. This should provide a more accurate representation of TSSP-UK's material in terms of fatigue performance.

- The effect of changes in material thickness on the performance of structures is difficult to predict as it impacts on many factors which have a non-linear relationship with fatigue performance. The locations of folds during fabrication can change, and factors such as the second moment of area will change in fashions which are not easily predicted as they have a higher order contribution to geometrical changes. As a result no general theory can be applied and thus must be assessed on a case by case basis.

- Material supplied on a worst-case scenario basis in terms of tensile properties and thickness is likely to have a fatigue curve which lies very close to the -3SE curve from the brochure data. As a result it would be wise to allow account for this and allow a further 3SE from this curve in order to ensure reliability.

- Welding of any method is severely detrimental to fatigue performance.

- Despite the very different microstructures formed following MIG and TIG welding, their fatigue properties are relatively similar, although there is possibly more scope for improving upon the performance of TIG welds by optimising the settings and welding process.

- TIG welds were found to be more variable than MIG welds, this is due to the increased difficulty and additional manual controls. An automated process for both should however reduce the amount of variability shown in this study,

208

where it would be expected that both would show similar levels of fluctuation in performance.

- The geometry of TIG welds were found to influence the fatigue performance of coupons, where flatter shallower welds performed better than those more dome-like in appearance. This is also validated by FE modelling. The flatter welds also appeared to have better tie-in regions, which further improve their performances.

- The stress concentrated region within welded coupons which was identified by FE modelling, coincides with the crack initiation points indentified during testing. The true stress concentrations at these locations are likely to be higher than the model predicted due to imperfections and blemishes which are unaccountable in the model.

- Key variability factors that must be accounted for in new designs include: variability in yield strength and UTS which have a knock on effect to fatigue performance, changes in elongation values affecting formability, strip thickness inconsistencies, and variable weld performance. The statistical variations of which are well documented within this project.

8.2 Further Work

As this project drew to a close it became apparent that it would be beneficial to both the steel and automotive industries to explore other avenues in terms of how various criteria affect the performance of automotive structures. Also, as TSSP-UK are beginning to commercialise new Advanced High Strength Steels, it would be beneficial to carry out a similar evaluation of those grades of steel. Of course this would need to occur once these grades of steel have been in production for a reasonable amount of time, as large amounts of data are necessary to carry out such an evaluation.

It is fortunate that Tata Steel continue to invest in research within this subject area, where work is already underway on evaluating the effects of corrosion on fatigue for both welded and un-welded steel sheet. This work will broaden the knowledge gained from this project, as an understanding of how capable components are at maintaining their structural integrity after ten or more years in service is another

important step in developing a comprehensive understanding of variability in performance. On welds, further work needs to be carried out on quantifying the effects of geometrical changes that were reported in this work, where it may be possible to greatly enhance performance by grinding excess material away. Grinding can be done very easily on butt joints but not so easily on fillet joints, thus understanding this technique for enhancing weld performance requires much consideration.

It is documented within this thesis that a correlation exists between tensile and fatigue data. These observations would only be valid for the single family of steels considered as part of this project which have a ferrite/pearlite microstructure. It would be beneficial to both the steel and automotive industries to understand how mechanical properties correlate with fatigue performance across a wider range of products, which may include microstructures consisting of bainite, martensite and retained austenite.

Reference List

[1] Collins J A. Failure of materials in mechanical design: analysis, prediction, prevention. *Wiley* (1993)

[2] Thomas D J, Whittaker M T, Bright G W, Gao Y. The influence of mechanical and CO_2 laser cut-edge characteristics on the fatigue life performance of high strength automotive steels. *Journal of Materials Processing Technology.* **211**, [2], 263-274 (2011)

[3] Dieter George E. Mechanical metallurgy. *McGraw-Hill* (1989)

[4] Benham P P, Crawford R J, Armstrong C G. Mechanics of engineering materials. *Longman* (1996)

[5] BS EN 10149-2:1996 Specification for hot-rolled flat products made of high yield strength steels for cold forming - Delivery conditions for thermomechanically rolled steels

[6] Askeland D R. The science and engineering of materials. *Pws Pub Co.* (1988)

[7] Callister W D. Materials science and engineering: an introduction. *Wiley* (2002)

[8] Keeler S. The science of forming – measuring n value. *PMA Metalforming Magazine.* 60-61 (June 2007)

[9] Goodman J. Mechanics applied to engineering. *Longmans, Green and Co.* (1904)

[10] Sendeckyj G P. Constant life diagrams – a historical review. *International Journal of Fatigue.* **23**, 347-353 (2001)

[11] Lee Y, Pan, J, Hathaway R, Barkley M. Fatigue Testing and Analysis: Theory and Practice. *Butterworth-Heinemann.* (2005)

[12] Schijve J. Fatigue of structures and materials. *Springer* (2008)

[13] Campbell F C. Elements of metallurgy and engineering alloys. *Elsevier* (2008)

[14] Manson S S, Halford G R. Fatigue and durability of structural materials. *ASM International* (2005)

[15] Stephens R I, O, Fatemi A, Stephens R R. Fuchs H O. Metal fatigue in engineering. *Wiley* (2000)

[16]   Bannantyne J A, Comer J J, Handrock J L. Fundamentals of metal fatigue analysis. *Prentice Hall* (1989)

[17]   Timings R. Fabrication and welding engineering. *Newnes* (2008)

[18]   Jubb J E M. Undercut or toe groove - the cinderella defect, *Metal Construstion*. **13,** [2], 94 (1981)

[19]   Ertmer   J.   Setting   the   correct   parameters.   Available: http://www.thefabricator.com/ArcWelding/ArcWelding_Article.cfm?ID=186 0. Last accessed 10 April 2009. (2008)

[20]   Nguyen T N, Wahab M A. The effect of weld geometry and residual stresses on the fatigue of welded joints under combined loading. *Journal of Materials Processing Technology*. **77,** 201–208 (1998)

[21]   Balasubramanian V, Guha B, Swamidas A S J, Seshadri R. Infuences of shielded metal arc welded cruciform joint dimensions on toe crack failures of pressure vessel grade steels. *Engineering Failure Analysis*. **7,** 169-179 (2000)

[22]   Maddox S J. Fatigue strength of welded structures. *Woodhead* (1991)

[23]   George P M, Pillai N, Shah N. Optimization of shot peening parameters using Taguchi technique. *Journal of Materials Processing Technology*. **153,** 925–930 (2004)

[24]   Gao Y, Yao M, Shao P, Zhao Y. Another mechanism for fatigue strength improvement of metallic parts by shot peening. *Journal of Materials Engineering and Performance*. **12,** [5], 507-511 (2003)

[25]   Tekeli S. Enhancement of fatigue strength of SAE 9245 steel by shot peening. *Materials Letters*. **57,** 604–608 (2002)

[26]   Hammersley G, Hackel L A, Harris F. Surface prestressing to improve fatigue strength of components by laser shot peening. *Optics and Lasers in Engineering*. 34, 327-337 (2000)

[27]   Asquith D T, Yerokhin A L, Yates J R, Matthews A. Effect of combined shot-peening and PEO treatment on fatigue life of 2024 Al alloy. *Thin Solid Films*. **515,** 1187–1191 (2006)

[28]   Pilkey W D, Pilkey, D F. Peterson's stress concentration factors. *Wiley* (2008)

[29]   Ghosh A. Secondary steelmaking: principles and applications. *CRC Press* (2000)

[30] Marique C. Tramp elements and steel properties: a progress state of the European project on scrap recycling. *La Revue de la Métallurgie.* **95**, [4] 433-441 (1998)

[31] Wilshire B, Homer D, Cooke N L. Technological and economic trends in the steel industries. *Pineridge Press* (1983)

[32] Sperle J O, Trogen H. Influence of yield ratio on the fatigue strength of steel sheet. *Scandinavian Journal of Metallurgy.* **18**, 147-154 (1989)

[33] Aichbhaumik D. Steel variability effects on low cycle fatigue behaviour of high strength low alloy steel. *Mettalurgical Transactions A – Physical Metallurgy and Materials Science.* **3**, 269-278 (1979)

[34] Wang Z T, Zhang S H, Xu Y, Luan G F, Bai G R. Experiment study on the variation of wall thickness during dieless drawing of stainless steel tube. *Journal of Materials Processing Technology.* **120**, 90-92 (2002)

[35] Greitzer E M, Spakovszky Z S, Waitz I A. Heat transfer through a plane slab. Available:http://web.mit.edu/16.unified/www/FALL/thermodynamics/notes/ node117.html. Last accessed 2 May 2009. (2008)

[36] Kays W M, Crawford M E, Weigand B. Convective heat and mass transfer. *McGraw-Hill* (2005)

[37] Fukumoto Y. Reduction of structural ductility factor due to variability of steel properties. *Engineering Structures.* **22**, 123-127 (2000)

[38] Blackmore P A. Statistical variability in strain-life materials data. *SAE 2005 Transactions Journal of Materials and Manufacturing.* 696-707 (2005)

[39] Thomas J J, Perroud G, Bignonnet A, Monnet D. Fatigue design and reliability in the automotive industry. *Fatigue Design and Reliability.* **23**, 1-11 (1999)

[40] Johanssen P. Extrapolation of load histories and spectra. *Fracture & Fatigue of Engineering Structures & Materials.* **29**, 201-207 (2006)

[41] Klyatis L M, Klyatis E K. Development common problems of reliability application in the automotive and other industries. *SAE 2008 Reliability and Robust Design in Automotive Engineering.* 2008

[42] Yang K, El-Haik B S. Design for six sigma. *McGraw-Hill Professional* (2009)

[43] Pyzdec T, Keller P A. The Six sigma handbook. *McGraw-Hill Professional* (2009)

[44] Smith R E. Controlling sources of variability in stainless steel piping. *Metal Progress*. **112**, [2], 42-48 (1977)

[45] Parkinson D B. Robust design by variability optimization. *Quality and Reliability Engineering International*. **13**, 97-102 (1997)

[46] Zhang Y, Zhu P, Chen G. Lightweight design of automotive front side rail based on robust optimization. *Thin-Walled Structures*. **45**, 670-676 (2007)

[47] Kumar A, Prasanth N B, Keane A J, Slahpar S. Robust design using Baysian Monte Carlo. *International Journal for Numerical Methods in Engineering*. **73**, 1497-1517 (2008)

[48] Hsu J, Awano M, Hayahsi K, Kunihiro A, Yasin A. An approach on robust design optimization of side impact crash analysis using FEM and DFSS. *SAE 2008 Reliability and Robust Design in Automotive Engineering*. 79-83 (2008)

[49] Trem R. The future of automaking: tailor welded blanks. Available: http://weldingmag.com/consumables/news/wdf_10713/. Last accessed 11 May 2009. (2004)

[50] Fourlaris G, Ellwood R. Jones T B. The reliability of test results from simple test samples in predicting the fatigue performance of automotive components. *Materials and Design*. **28**, 1198-1210 (2007)

[51] Heuler P, Klätschke H. Generation and use of standardised load spectra and load–time histories. *International Journal of Fatigue*. **27**, [8], 974-990 (2005)

[52] Heuler P, Bruder T, Klätschke H. Standardised load-time histories - a contribution to durability issues under spectrum loading. *Materialwissenschaft und Werkstofftechnik*. **36**, [11], 669–677 (2005)

[53] Bhadeshia H K D H, Honeycombe R W K. Steels: Microstructure and Properties, Third edition. *Butterworth-Heinemann* (2006)

[54] Gedore torque setting and frictional resistance recommendations for fasteners. Available: http://www.gedoreuk.com/pdf_files/410-421_gedoreuk_2108577_Kat_GTC_UK_GPK_09.pdf. Last accessed 10th October 2011

[55] Thomas D J. Characterisation of steel cut edges for improved fatigue property data estimations and enhanced CAE durability. *Swansea University Engineering Doctorate Thesis* (2011)